Microstructure investigation by means of X-ray computed tomography : application to fine-grained clastic rocks

Hugo Saur

THÈSE

UNIVERSITÉ DE PAU ET DES PAYS DE L'ADOUR

École doctorale des Sciences Exactes et leurs Applications

Présentée et soutenue le 17 mars 2022

par **Hugo SAUR**

pour obtenir le grade de docteur
de l'Université de Pau et des Pays de l'Adour
Spécialité : Géosciences

Étude des microstructures par tomographie à rayons X : application aux roches clastiques à grain fin

Microstructure investigation by means of X-ray computed tomography: application to fine-grained clastic rocks

MEMBRES DU JURY

RAPPORTEURS

• Veerle CNUDDE	Professeur / Ghent University, Utrecht University
• Patrick LAUNEAU	Professeur / Nantes Université

EXAMINATEURS

• Jean-Paul CALLOT	Professeur / Université de Pau et des Pays de l'Adour
• Claire FIALIPS	Docteur, Expert / TotalEnergies SA, Pau
• Olivier LACOMBE	Professeur / Sorbonne Université

DIRECTEURS

• Charles AUBOURG	Professeur / Université de Pau et des Pays de l'Adour
• Peter MOONEN	Professeur / Université de Pau et des Pays de l'Adour

À mon père, Jean-Louis Saur

Remerciements

Je tiens tout d'abord à remercier Veerle Cnudde et Patrick Launeau d'avoir accepté d'évaluer ce travail et d'y avoir apporté des remarques constructives. Je remercie également Jean-Paul Callot, Claire Fialips et Olivier Lacombe d'avoir accepté de participer au jury. Claire et Olivier, je vous remercie aussi pour votre implication dans les comités de thèse annuels.

Je voudrais remercier mes deux directeurs de thèse, Charles Aubourg, professeur à l'UPPA ainsi que Peter Moonen, professeur à l'UPPA et directeur de la plateforme d'imagerie DMEX. Je vous remercie pour votre enthousiasme, de m'avoir encouragé et de vous être rendus disponible tout au long de ce parcours doctoral. J'ai sincèrement apprécié travailler avec vous.

Je tiens à exprimer toute ma gratitude aux responsables de mes précédents masters, Didier Néraudeau, professeur à l'Université de Rennes 1 ainsi que Laurie Barrier, maître de conférence à l'Université de Paris – Institut de Physique du Globe de Paris.

Je remercie l'ensemble des membres de l'équipe CRG du LFCR pour leur sympathie et leur disponibilité. Merci notamment à Stephen de m'avoir guidé dans le traitement des données EBSD. Merci à Chengyi de m'avoir aidé avec MATLAB et Python. Je voudrais remercier Nicolas pour son aide à la compréhension des microstructures et d'avoir accepté de participer à mon dernier comité de thèse. Je remercie également Cédric et Guilhem pour leur implication dans le volet enseignement de mon doctorat. Merci à Bertrand pour la préparation d'échantillons et à Marie-Laure d'avoir facilité la partie administrative durant ces trois années.

De même, je remercie l'ensemble des membres de la plateforme d'imagerie DMEX. J'adresse notamment mes remerciements à Pascale pour l'initiation à la microtomographie à rayons X et au traitement d'image. Un grand merci également à Hannelore et Tiphaine. Je remercie Maxime de m'avoir aidé dans la mise en place des connexions réseau.

Mes remerciements vont aussi à Christian Laborderie et Olivier Maurel pour leur initiation à la méthode des éléments finis.

Je remercie le projet E2S UPPA et TotalEnergies pour le financement de cette thèse ainsi que l'ensemble des partenaires du projet E2S UPPA.

Enfin, mes plus chaleureux remerciements vont à ma mère Nathalie, mon frère Lucas et ma sœur Anastasia. L'aboutissement de ces années de travail a été rendu possible grâce à vos encouragements, votre soutien et votre affection.

Résumé

L'étude de la microstructure des roches est indispensable pour nos enjeux contemporains et futurs en matière d'énergie, d'ingénierie et de construction. D'autre part, cette étude permet de caractériser les processus de déformation géologique ayant conduit à l'état actuel des unités lithologiques. Les roches clastiques à grain fin, communément appelées "shales" en anglais, représentent environ deux-tiers de l'ensemble des roches sédimentaires. Les données 3D relatives aux grains de silt ou clastes inclus dans la matrice argileuse et poreuse de ce type de roche sont peu fréquentes. Ces données sont pourtant cruciales pour comprendre les propriétés anisotropes à l'échelle macroscopique mais aussi pour évaluer l'état de déformation de la matrice rocheuse. Mieux connaitre la microstructure de ces roches permettrait d'être prédictif quant à leurs propriétés mécaniques ou physiques indispensables pour les applications du secteur de l'énergie par exemple. La tomographie à rayons X (XCT) est une technique non destructive permettant d'obtenir une image 3D de la microstructure d'un objet. Une caractérisation géométrique directe des constituants des roches clastiques à grain fin est envisageable grâce à cette technique. Sur la base d'images XCT, cette thèse vise d'abord à développer des aspects méthodologiques pour étudier la fabrique de forme 3D des clastes ainsi que leur distribution spatiale. Ces aspects sont élaborés à partir de la méthode des moments d'inertie qui est appliquée sur les grains segmentés des images 3D numériques. Nous présentons ensuite des applications sur des roches à grain fin possédant une fabrique sédimentaire et sur des roches à grain fin déformées présentant une fabrique d'origine tectonique. Le premier volet applicatif de la thèse s'intéresse à une même unité lithologique ayant enregistrée différentes quantités de déformation. Des échantillons du bassin sud-pyrénéen et des échantillons issus d'un affleurement historique dans les Appalaches centrales ont été collectés. Nous apportons de nouvelles données sur l'évolution de la forme 3D des grains et des pores à l'échelle micrométrique et sur leur agencement dans la matrice rocheuse en fonction de la déformation. Les données obtenues permettent de discuter des mécanismes de déformation à l'échelle du grain des différentes phases minéralogiques. Cependant, la petite taille des échantillons imagés par XCT (≤ 2 mm de diamètre) soulève la question de la représentativité de ces analyses. Sur le chantier sud-pyrénéen, certains échantillons sont étudiés de manière plus approfondie pour vérifier l'homogénéité des résultats. Nous y montrons que les données XCT complètent les mesures indirectes pétrophysiques en permettant de décrire et de localiser les sous-fabriques intégrées dans une mesure globale de la fabrique. Les limites apparaissent lorsque la dimension caractéristique des structures de déformation avoisine la taille de l'échantillon imagé par XCT. Dans le second volet applicatif, des échantillons provenant de systèmes turbiditiques du bassin sud-pyrénéen sont analysés. Ces systèmes, lorsque déformés en tectonique compressive, présentent l'avantage d'enregistrer la même quantité de raccourcissement différemment exprimée dans les unités lithologiques qui les constituent. Les résultats obtenus à partir de la forme des clastes sont comparés à nos mesures magnétiques globales de la fabrique et montrent une bonne cohérence. La méthodologie présentée dans ce travail peut s'étendre à d'autres types de milieux poreux et granulaires pour une meilleure compréhension de l'influence de l'anisotropie structurale sur leurs propriétés macroscopiques et leur comportement mécanique.

Mots-clés : Imagerie à rayons X, Microstructure, Grains de silt/clastes, Orientation préférentielle de forme, Anisotropie, Distribution spatiale, Fabrique magnétique, Déformation.

Abstract

The study of the microstructure of rocks is essential for our contemporary and future challenges in energy, engineering and construction. Furthermore, this study allows us to characterize the geological deformation processes that led to the current state of geological formations. Fine-grained clastic rocks, commonly called "shales", represent about two-thirds of all sedimentary rocks. 3D data concerning silt-sized grains or clasts embedded in the porous clay-rich matrix of this type of rock are relatively scarce despite the fact that these data are crucial to understand the anisotropic properties of these rocks at the macroscale but also to evaluate the deformation state of the rock matrix. A better understanding of the microstructure of these rocks would allow us to predict their mechanical or physical properties, which are essential for applications in the energy sector, among others. X-ray computed tomography (XCT) is a non-destructive technique providing a 3D image of the microstructure of any object. A direct geometric characterization of the constituents of fine-grained clastic rocks is possible with this technique. Based on XCT images, this thesis aims first to develop methodological aspects to study the 3D shape fabric of silt particles and their spatial distribution. The moments of inertia of segmented grains from 3D digital images are used for this development. We then present applications on fine-grained rocks with a sedimentary fabric and on deformed fine-grained rocks with a tectonic fabric. The first application part of the thesis focuses on the same lithologic unit having experienced different amounts of deformation. Samples from the South Pyrenean Basin and samples from a historical outcrop in the Central Appalachians were collected. We provide new data on the evolution of the 3D shape of grains and pores at the micrometer scale and their arrangement in the rock matrix with respect to the deformation intensity. The obtained data allow discussing the deformation mechanisms at the grain scale of the different mineralogical phases. However, the limited size of the imaged samples by means of XCT (≤ 2 mm diameter) raises the question of the representativeness of these analyses. On the South Pyrenean site, some samples are studied in more detail to evaluate the homogeneity of the results. We show that the XCT data complement the indirect petrophysical measurements by providing access to localized sub-fabrics that are integrated in a bulk measurement of the rock fabric. The limits are reached when the characteristic length of the deformation structures are on the order of the sample size imaged by XCT. In the second application part, samples from turbiditic systems of the South Pyrenean basin are analyzed. These systems, when deformed in compressive tectonic settings, record the same amount of shortening differently expressed in the various siliciclastic matrices. The results obtained from the shape data of the clasts are compared to our bulk magnetic fabric measurements and show a good consistency. The methodology presented in this work can be extended to other types of porous and granular media for a better understanding of the influence of fabric anisotropy on their macroscopic properties and mechanical behavior.

Key words: X-ray imaging, Microstructure, Silt-sized grains/clasts, Shape preferred orientation, Anisotropy, Spatial distribution, Magnetic fabric, Deformation

Table of contents

1 Introduction

1.1 General context and motivation

Geomaterials are key players in our contemporary energy challenges. Efficient and sustainable energy production requires a fine characterization of geomaterials in order to offer reliable projections on their use. This characterization allows to better constrain numerical models and is essential for CO_2 sequestration and nuclear waste storage projects.

This thesis is integrated in the "Characterization of geological reservoirs" team of the Laboratory of Complex Fluids and their Reservoirs (LFCR) and more particularly on the thematic focused on the study of matrix damage in reservoir rocks. Based on a multi-technique and multi-scale approach (from the field scale to the micrometric or nanometric scale), the general objective of this thematic is to characterize the fabric of reservoir rocks. Rock fabric corresponds to the geometrical arrangement of its consituants. It focuses on the size, shape and shape preferred orientation (SPO) of grains and pores, the crystallographic preferred orientation (CPO) of grains and the spatial distribution of all the constituents. The characterization of the rock fabric allows to better understand the deformation processes as well as the petrophysical and mechanical properties of rocks (Mendelson and Cohen, 1982; Hobbs, 1985; Launeau et al., 1990; Launeau and Robin, 1996, 2005; Lüneburg et al., 1999; Dürrast and Siegesmund, 1999; Brosch et al., 2000; Přikryl, 2001; Borradaile and Jackson, 2004, 2010; Baud et al., 2005; Passchier and Trouw, 2005; Kern et al., 2008; Klinkenberg et al., 2009; Cnudde et al., 2009; Kaufhold et al., 2013; Siegesmund and Dürrast, 2014; Almqvist and Mainprice, 2017).

In order to validate our new methodological approach, we chose siliciclastic rocks (with some additional carbonate content) that are ubiquitous in geological reservoirs systems. We emphasize here on fine-grained clastic rocks that are commonly grouped in the "shale" term. Shales represent two-thirds of the sedimentary rocks on the Earth (Nichols, 2009; Milliken, 2014). Shales are essential to many energy applications, in geotechnic and in the evaluation of technical and seismic risk. These rocks present a more or less pronounced degree of physico-chemical compaction related to their burial. They are composed of silt-sized grains or clasts (quartz, calcite and feldspar) embedded in a porous and carbonaceous clay matrix (Ougier-Simonin et al., 2016). Various well-established techniques allow characterizing the fabric of pore space in these rocks such as the anisotropy of P-wave velocity (Kaarsberg, 1959; Vernik and Liu, 1997; David et al., 2007) or the combination of anisotropy of magnetic susceptibility (AMS) with high-pressure ferrofluid and mercury injections (Esteban et al., 2006). Likewise, standard AMS measurement allows to retrieve the 3D crystallographic fabric of paramagnetic clay minerals (Parés, 2015). Techniques based on X-ray diffraction (X-ray pole figure goniometry or synchrotron X-rays) or neutron diffraction are also used to determine the crystallographic fabric of phyllosilicate minerals (van der Pluijm et al., 1994; Wenk and Houtte, 2004; Wenk et al., 2020). Crystallographic and shape fabrics of clay minerals are closely related (Valcke et al., 2006; Wenk et al., 2010). The AMS is particularly interesting because it allows to decipher discrete fabrics linked to intimate deformations processes of the rock matrix (Aubourg et al., 1991). However, standard AMS data measured in low field and at room temperature hardly provide the fabric of minerals with a negative magnetic susceptibility such as the diamagnetic quartz and calcite. We should note that techniques were developed to isolate the respective contributions and fabrics of diamagnetic and paramagnetic minerals (Schmidt et al., 2007; Issachar et al., 2018; Elhanati et al., 2021). In the case of quartz, this mineral does not possess an intrinsic magnetocrystalline anisotropy (Hrouda, 2007). Hence, the study of its fabric by means of AMS is less relevant. Fabric of silt-sized diamagnetic grains

(calcite and quartz) and paramagnetic grains (pyrite) is often hidden in the bulk signal of AMS. Their crystallographic fabric can be studied be means of Electron Backscatter Diffraction (EBSD) based on two-dimensional polished sections (Valcke et al., 2006). Similarly, the shape fabric determination of these components relies on the use of two-dimensional destructive techniques such as electronic or optical microscopy. In addition, this type of analysis only allows the study of a limited number of clasts or grains and does not provide sufficiently robust quantitative data. Although we can combine two-dimensional data with multiple orthogonal or non-orthogonal sections to obtain the bulk shape fabric (Launeau and Cruden, 1998; Robin, 2002; Launeau and Robin, 2005), a direct three-dimensional geometric measurement allows to avoid possible approximations. Most importantly, two-dimensional data may miss some particular structures in the rock, which is not the case with a true 3D technique. Silt-sized grains of calcite and quartz do have an impact on the anisotropic properties of fine-grained rocks at the macroscale and three-dimensional quantitative data of their shape and SPO at the microscale is needed. It is therefore necessary to use complementary techniques to study them.

X-ray computed tomography (XCT) is a non-destructive technique that can provide the three-dimensional image of a rock's microstructure (Raynaud et al., 1989). This technique has been successfully applied in geosciences (Ketcham and Carlson, 2001; Ketcham, 2005a; Carlson, 2006; Baker et al., 2012; Cnudde and Boone, 2013). However, this imaging technique, which allows to obtain a direct geometrical measure of a petrofabric, has been preferentially used on igneous, metamorphic and coarse-grained sedimentary rocks. The study of Voltolini et al. (2011) on igneous rock samples has proven the capability of XCT to investigate rock fabric and its anisotropy. The determination of the shape fabric of clasts in fine-grained sedimentary rocks is still poorly documented, although X-ray instruments are more powerful and a sufficiently large number of clasts can be extracted by means of XCT. Thus, this technique offers the opportunity to study the 3D microstructure of weakly deformed fined-grained rocks (shales) to highly deformed ones (slates).

1.2 Aims of the thesis

1.2.1 General objective

Based on XCT images acquired at the DMEX imaging center at the University of Pau (UPPA), the general objective of the thesis is built along two main axes:

- A methodological axis. This axis relies on developing tools to study the 3D shape preferred orientation (3D-SPO) and arrangement of particles (here grains and pores) embedded in a rock matrix. This development includes the study of shape-based data and point distribution data of the particles. This development presents individual or bulk analysis that are further explored by subset or subvolume analysis. We also provide a method to assess the representativeness of the shape fabric data. In addition, a method to study the 3D spatial distribution of grains, similar to the 2D method of Fry (1979), is emphasized.

- An application axis that concerns the use of the developed tools to characterize fine-grained rocks imaged by means of X-ray imaging. This axis is subdivided into two parts:
    1. The first is intended to explore the evolution of the same shale matrix subjected to a lateral strain gradient (**Sigüés** and **Lehigh Gap** case studies presented in the next section)
    2. The goal of the second part is to explore various clastic rock matrices of a turbiditic system that have been subjected to the same deformation regime (**Hecho** case study).

Either a lateral compressive regime of "Layer Parallel Shortening" or LPS (Mitra and Yonkee, 1985; Weil and Yonkee, 2009) or a combined regime of a lateral compaction and shearing. The effects of the latter can be observed on the limb of a folded structure.

The results obtained by this 3D-SPO analysis are compared to the AMS measurements that are mainly sensitive to the clay fraction of our studied rocks. XCT allows having an individual approach of the petrofabric of quartz and calcite grains as well as pores while the AMS provides a bulk (i.e. global) approach of the clay fraction. It should be noted that such a comparison (XCT versus AMS) to characterize the petrofabric of igneous or metamorphic rocks have already been presented in the literature (Schöpa et al., 2015; Sayab et al., 2017). One can note, for example, application cases on unconsolidated fine-grained rocks of tsunami deposits (Falvard and Paris, 2017; Paris et al., 2020) or an application on the Callovo-Oxfordian argillite from eastern part of France (David et al., 2007). In the latter study, the resolution of the XCT images was quite low and did not allow a precise analysis of the silt grains embedded in the clay matrix. The joint use of the two techniques remains, to our knowledge, poorly documented in the case of consolidated fine-grained rocks.

In this thesis, we will focus our attention on silt-sized grains recognizable in the XCT images of consolidated fine-grained rocks. Silt-sized grains have a diameter between 4 µm and 63 µm (Nichols, 2009). Sand-sized grains from the finer fractions (between 63 µm and 250 µm in diameter) will be also studied but generally less represented. These types of grains will be selected during the image processing of the XCT datasets and analyzed during the subsequent post-processing. The post-processing of the data from the image processing software was not yet developed at the beginning of this thesis. An important part of the work was therefore devoted to the development of tools for the analysis and quantification of the XCT data.

In addition, we will present a preliminary version of mechanical deformation simulation of clasts in a matrix. The aim of this approach is to validate the data of their spatial distribution, shape attributes and SPO observed in natural cases. This should allow us to better constrain our results obtained on the main case studies. Moreover, it is a way to better understand the macroscopic physical properties of fine-grained clastic rocks.

Because of the use of XCT and the range of studied rocks, this thesis has both academic and industrial interests. From an academic point of view, we will be able to discuss the intimate mechanisms of natural deformation of clasts in fine-grained rocks of fold-and-thrust belt systems. More specifically, we will focus on the role of stress driven dissolution-precipitation and rigid rotation processes associated with the development of cleavage. Cleavage remains one of the most common deformation structures in the upper crustal rocks. We will be able to compare the contribution of a bulk measurement of the petrofabric such as AMS with that of an individual measurement using XCT. We will also be able to see how to link the microscopic deformation to the macroscopic one. From an industrial and engineering point of view, the quantification of the 3D-SPO and the spatial distribution of particles in geomaterials, granular and porous media is very important. The study of weakly deformed fine-grained rocks is crucial for multiple energy applications at different stages (exploration, exploitation and production). A good knowledge of the mechanical strength of fine-grained rocks is necessary to evaluate the stability of boreholes (Baud et al., 2005; Ulm et al., 2005; Schuster et al., 2021) or areas of weakness in the upper crust. At higher temperature (>200°C) and with the ductile deformation processes of metamorphism, fine-grained rocks become slates with lower porosity, higher mechanical strength, and better structural homogeneity. These metamorphic rocks are also important in engineering and as rocks for building activities (Siegesmund and Török, 2014; Wenk et al., 2020; Cárdenes et al., 2021).

1.2.2 Three main study sites

In order to apply the XCT on natural cases, we worked on three main sites. Two of them are located in the Jaca basin (Southern Pyrenees). These first two sites are geographically located in the Roncal valley that crosses orthogonally the major structures of the South Pyrenean fold-and-thrust belt. The **Sigüés** site is located at the southern end of the valley and corresponds to the outermost domain. The two areas of the **Hecho** site are located in the internal domain of the fold-and-thrust belt. The third is a historic and well-known geological site in the Appalachian Mountains (**Lehigh Gap**, USA).

- The **Sigüés** site (Aragon, Spain) in the South Pyrenean foreland basin permits to study fine-grained rocks that present all stages from sedimentary compaction to intense tectonic deformation that overprints the sedimentary fabric. This site, already studied for several years, allows monitoring the evolution of the rock fabric in very homogeneous lithologies, and a priori, not subjected to a temperature gradient. This site integrates the first part of the application axis of the thesis.

- The **Hecho** site (Aragon, Spain) includes two sampling areas in the same basin but further north where deformed turbiditic systems outcrop. It aims at characterizing the response of multiple siliciclastic matrices to a deformation either of the LPS type or related to a folding. This site integrates the second part of the application axis of the thesis.

- The **Lehigh Gap** site (Pennsylvania, USA) is part of the fold-and-thrust belt of the central Appalachians. It is a historic site to study the imprint of a tectonic deformation in fine-grained rocks. We are returning to this site because it has some similarities with the **Sigüés** site but also many differences, especially in the conditions of metamorphism. As a result, the **Lehigh Gap** historical site fits into our first part of the thesis application axis.

1.3 Outline of the thesis

- In **Chapter *2***, we will present the state of the art regarding X-ray computed tomography and the main axes of research that use this technique in fine-grained rocks. We will also briefly review the methods used to characterize the shape fabric of grains in rocks.

- **Chapter *3*** will be devoted to the methodology developed in this thesis and the analytical techniques used. We will see how to characterize the shape of grains in 3D, how to study and quantify their arrangement and how to evaluate the finite strain from their spatial distribution. The method that combines X-ray image and Finite Element Method will also be explained.

- **Chapters *4*** and ***5*** will present the major results of the application of XCT to the study of a natural deformation gradient (**Sigüés**, Spain) and to the study of an outcrop exposing a widely studied shale-slate transition (**Lehigh Gap**, USA). The goal here is to characterize the microstructure of a fine-grained lithology for different deformation states. Some of the results presented in **Chapter *4*** have been published in *Journal of Structural Geology* (Saur et al., 2020).

- **Chapter *6*** will present a more in-depth analysis on the concept of representativeness and heterogeneity of the shape fabric measured on a 2 to 3.5 mm^3 rock volume. This work has been published in *Journal of Geophysical Research: Solid Earth* (Saur et al., 2021). **Chapter *7*** will

focus on multiple lithologies having recorded the same deformation regime. XCT will be applied with a particular focus on the same mineral phase and AMS data will complete the set.

- **Chapter *8*** will present our numerical simulation method to validate our results on the spatial distribution of grains in a clay matrix using a three-dimensional segmented XCT image or a synthetic image.

- Finally, we will present a general discussion and a conclusion in **Chapter *9***. Some perspectives to this work will be given in this chapter as well.

2 State of the art

2.1 Introduction

In this chapter, we introduce some notions of the X-ray computed tomography imaging technique. We present the main applications of this technique in shale materials. Next, we introduce the reader to the concept of rock fabric and we concisely review the techniques focusing on the grain shape characterization through image analysis. Lastly, we provide a short paragraph about the magnetic fabric measurement.

2.2 X-ray computed tomography

2.2.1 Fundamentals

X-ray CT is an imaging technique based on the attenuation of an X-ray beam passing through a material. X-rays are an electromagnetic radiation made up with photons having a wavelength comprised between 10^{-8} and 10^{-11} m. In this section, we are mainly interested in absorption (attenuation) contrast tomography but we should note that phase contrast tomography based on refraction of X-ray waves is another powerful technique. We may distinguish lab-based X-ray CT from synchrotron X-ray CT (***Figure 2.1***). In lab-based X-ray CT, the X-ray beam has a wider energy spectrum and make it polychromatic. In synchrotron facilities, the X-ray beam is higher in intensity and monochromatic typically providing a high signal to noise ratio (Cnudde and Boone, 2013). The intensity of a monochromatic beam passing through a material is expressed with the Beer-Lambert law as:

$$I = I_0 e^{-\mu x}$$

Where I and I_0 are the initial and final intensities of the X-ray beam, μ is the linear attenuation coefficient for the material being scanned, generally expressed in cm^{-1}, and x is the length of the X-ray path through the material (Kyle and Ketcham, 2015). For a heterogeneous medium composed of different phases, the equation becomes:

$$I = I_0 e^{-\sum \mu x}$$

The attenuation coefficient μ depends on the density of each material, its atomic number and is function of the X-ray beam energy, especially for polychromatic beams used in lab-based devices. In a lab-based XCT system, X-rays are generated in a tube by emitting electrons that are accelerated and directed to strike a target (anode) made of tungsten, platinum or molybdenum (Brabant, 2013; De Boever et al., 2015). The energy released generates X-rays according to two processes that are the deceleration of incident electrons (bremsstrahlung effect) and the change of energy shell position of the electrons of the anode (Wildenschild et al., 2002). The polychromatic X-ray beam produced by lab sources has thus a broad spectrum of energy. The newly created X-rays are then propagated to the material to be imaged (***Figure 2.1***). The beam interacts with the material by photoelectric absorption, Compton scattering and Rayleigh scattering. The photoelectric absorption is dominant at energies between 50 and 100 keV while Compton scattering predominates above these energies until 5-10 MeV (Ketcham and Carlson, 2001; Wildenschild and Sheppard, 2013). After passing through the material, the attenuated X-ray beam is converted in visible light by a scintillator and collected by a camera, which is usually a coupled charged device or CCD or a flat panel (***Figure 2.1***). The analyzed material or sample

is placed between the source and the detector in a predefined geometric configuration. In a typical acquisition, the sample will rotate 360° and a 2D projection is taken at each incremental angle in a constant size field of view (FOV) containing the sample. The complete set of 2D projections is used to reconstruct the 3D digital image of the sample through reconstruction algorithms (***Figure 2.1***). The final reconstruct image can be visualized and analyzed. In more advanced lab-based XCT system, geometrical magnification is coupled with optical magnification using lenses attached to the detector system. Micro CT systems can achieve images with voxels (i.e. pixels in 3D) sizes between 100 µm and 1 µm or down to 0.1 µm (Brabant, 2013; Withers et al., 2021). Nano CT permits to obtain voxel size down to 15-20 nm with a resolution of 50 nm at best. The voxel size in the reconstructed image is determined by the geometrical configuration, the focal spot size and the size of the detector pixels. Today, the most use configuration in lab-based XCT systems is the cone-beam geometry (***Figure 2.2***).

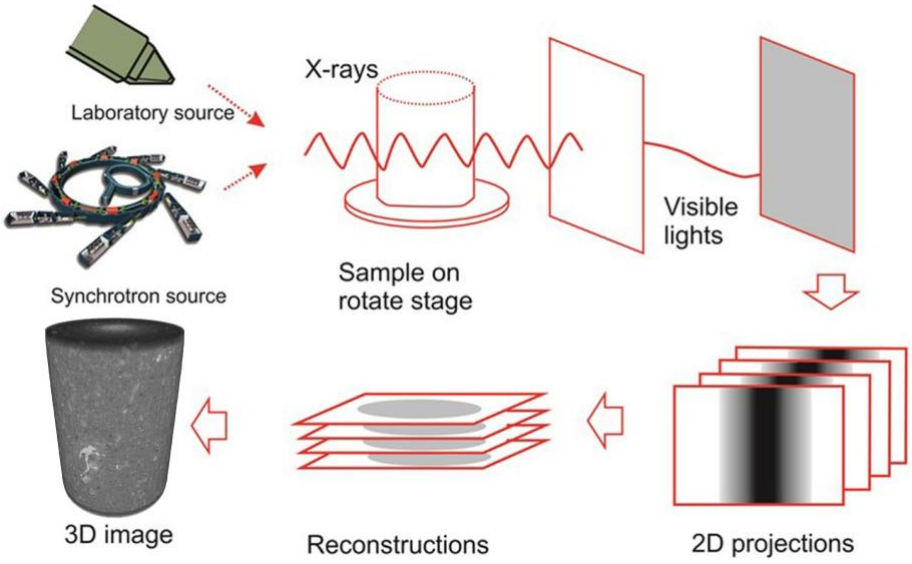

Figure 2.1: ***Schematic illustration of X-ray computed tomographical images acquisition and reconstruction that provides a final 3D image, modified from (Landis and Keane, 2010). Figure taken and modified from (Ma et al., 2017).***

Some characteristic artefacts of XCT are presented here after. Beam hardening is the most iconic artefact of the lab-based instruments due to the polychromatic nature of the X-ray spectrum. As said by Hanna and Ketcham (2017), this occurs because the lower-energy ("soft") X-rays are preferentially filtered out as they pass through an object, thereby "hardening" the beam and increasing its average energy. Indeed, the beam sees a higher effective attenuation coefficient at the beginning of its passage through an object than further in (Wildenschild and Sheppard, 2013). Due to this phenomenon, the center part of an object (e.g. a cylindrical rock sample) will appear darker than its edges. On the contrary, synchrotron facilities are free from beam hardening artefacts due to the use of a collimated monochromatic beam. Ring artefacts are also common and caused by defective or less sensitive pixels on the detector. They induce rings of abnormally high or low intensity on the reconstructed image. The size of the X-ray source or focal spot may also cause blurring in the reconstructed image. The larger the focal spot size, the more possible paths for the X-rays, which increases the blurring effect on the image (Ketcham and Carlson, 2001). There is also an inherent artefact due to the cone-beam configuration, sometimes called the cone-beam artefact (Cnudde and Boone, 2013). The upper and lower parts of the sample that are farthest from the center of the cone are not always correctly illuminated by the beam at each projection angle. Thus, the first and last slices of the reconstructed stack will appear darker than the rest of the stack because the attenuation coefficient is underestimated. In addition, heavy minerals or inclusions may cause streak artefacts due to their high

attenuating power (Hanna and Ketcham, 2017). Other possible artefacts induced by motion may arise from a poorly fixed sample, abnormally high vibrations in the surrounding laboratory area or temperature fluctuations inside the instrument.

Digital images, such as those obtained by XCT, are composed of finite structural elements called pixels in 2D and voxels in 3D. An intensity value expressed in grayscale, either in 8-bit (gray level from 0 to 255) or in 16-bit (gray level from 0 to 65,535), is attributed to each of these structural elements. Thus, these elements return a unique intensity value that averages the information of the surface or volume being analyzed. In XCT, a voxel returns the mean of the attenuation coefficient of the components being located in that volume and may average out important information. This corresponds to the so-called partial-volume effect (Ketcham and Carlson, 2001; Kyle and Ketcham, 2015). The voxel size or voxel resolution must be differentiated from the true spatial resolution, which corresponds to the smallest linear distance between two separate points that can be distinguished in the reconstructed image (Wildenschild et al., 2002; Withers et al., 2021). In general, the spatial resolution is higher than the voxel size and correspond to a certain number of voxels necessary to discriminate image features.

In this thesis, we will use the term XCT as a synonym of micro-computed tomography (µCT) or high-resolution X-ray computed tomography (HRXCT).

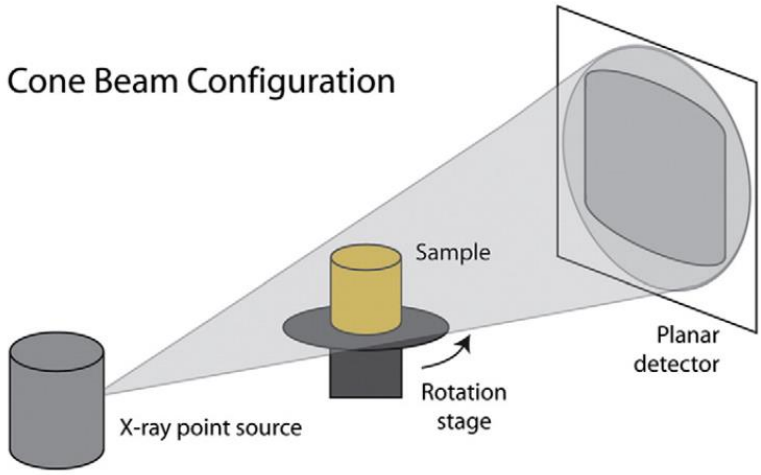

Figure 2.2: ***Schematic illustration of a cone-beam geometric configuration in an X-ray computed tomography device (Kyle and Ketcham, 2015).***

2.2.2 Short review of the major applications of XCT in geosciences and more specifically in shales

2.2.2.1 Identifying the phases of the XCT grayscale image

XCT provides a 3D image of a sample in a non-destructive way. The advantage of this imaging technique lies in its ability to provide the 3D morphology and the spatial location of each individual object such as grains or pore spaces in rocks that are distinguishable at the achieved resolution. Furthermore, if sufficient objects are identifiable, it makes the subsequent quantitative analysis statistically robust. In lab-based X-ray absorption contrast images, only spatial variations of attenuation through the rock components are reported by grayscales values assigned to each voxel. It does not provide the chemical nature of the components but rather gives information, in a relative way, on the more or less absorbing power of each of them. However, chemical identification can be performed by taking account of differences at elemental absorption edges (e.g. K-edges), with synchrotron X-rays (Gualda et al., 2010)

or by using a lab-based instrument equipped with a spectroscopic imaging detector (Egan et al., 2015; Sittner et al., 2021). Recently, phase-contrast (holo-) tomography, X-ray fluorescence tomography and X-ray diffraction were used together in order to study chemical features of zircons (Suuronen and Sayab, 2018). Otherwise, lab-based XCT can be easily combined with other techniques, such as energy dispersive X-ray spectroscopy (EDS), to determine the chemical nature of rock constituents. This 2D-3D registration method has been commonly used in studies related to the characterization of sandstone and limestone rocks (Golab et al., 2010, 2013; De Boever et al., 2015; Lai et al., 2015; Ellis and Peters, 2016) but also in metamorphic studies (Macente et al., 2017). Two-dimensional grayscale backscattered electron images (BSE) from scanning electron microscopy (SEM) can be registered with the XCT grayscale images and may help in the identification of phases (Latham et al., 2008; Sok et al., 2010). If no direct 2D-3D registration is used, combination of backscattered images and elemental maps from SEM-EDS system with XCT dataset can be applied, such as in shales (Backeberg et al., 2017; Ramos et al., 2019) or in slates (Wenk et al., 2019). Compositional data from X-ray diffraction powder (XRD) may also guide to mineral identification of the grayscale values of XCT (Hamid et al., 2018).

2.2.2.2 Literature review of the main applications

We will not provide a complete review of the application of XCT in geosciences as many excellent reviews are available (Ketcham and Carlson, 2001; Carlson, 2006; Baker et al., 2012; Cnudde and Boone, 2013) as well as more specific ones concerning ore materials (Kyle and Ketcham, 2015) and planetary materials (Hanna and Ketcham, 2017). In addition, Fusseis et al. (2014) wrote a review concerning the study of geomaterials by means of synchrotron based XCT. As we are mainly interested in the determination of shape and orientation of grains, we must take note that laboratory XCT or synchrotron XCT has proven to be valuable to study these characteristics of different mineral phases within various coarse-grained metamorphic materials (Ketcham, 2005a; Zucali et al., 2014; Sayab et al., 2015, 2017; Kahl et al., 2017), igneous rocks (Jerram and Higgins, 2007; Voltolini et al., 2011; Chatzaras et al., 2016), synthetic magmas (Arbaret et al., 2019) and sandstone (Cnudde et al., 2011b). In the following paragraphs, we will more focus on the main applications of XCT to study fine-grained rocks such as shales.

The main applications of lab-based and synchrotron XCT to study shale materials have been realized for different purposes. Firstly, the ability to image and quantify 3D structures at a fine scale has made XCT a remarkable tool for studying the pore space of shales (Kanitpanyacharoen et al., 2012, 2013; Vasin et al., 2013). An example is shown in ***Figure 2.3*****a** with a figure from Kanitpanyacharoen et al. (2012). The study of the pore space geometry and porosity has been explored through multi-scale tomography analysis using X-ray microtromography, X-ray nanotomography and FIB nanotomography/FIB-SEM tomography (Keller et al., 2011, 2013; Hemes et al., 2015; Keller, 2016; Ma et al., 2016; Goral et al., 2019, 2020). In order to better understand the influence of the fracture network and mineral fabric, Backeberg et al. (2017) have combined XCT and permeability experiments. Note that reviews concerning correlative multi-scale imaging are provided by Ma et al. (2017) and Arif et al. (2021) in which the reader will find sections about application of XCT in shale materials.

Concerning micromechanics, several studies have aimed at using 4D mechanical experiments and digital volume correlation, generally using dynamic synchrotron XCT, to investigate strain localization and fracture development (Bésuelle et al., 2006; Figueroa Pilz et al., 2017; McBeck et al., 2018). The influence of shale microstructure on the behavior of proppants for hydraulic fracturing has also been investigated using dynamic synchrotron XCT (Voltolini and Ajo-Franklin, 2020).

XCT imaging can also serve as a complementary technique to better understand anisotropic properties of shales such as their elastic anisotropy, e.g. to evaluate the impact of heterogeneity, microcracks and fractures on it (David et al., 2007; Kanitpanyacharoen et al., 2011; Allan et al., 2015; Mokhtari et al., 2016). Some studies have aimed at characterizing a specific mineral phase. Cárdenes et al. (2016) investigated heavy pyrite inclusions in slates and performed subsequent thorough statistical analysis (***Figure 2.3*b**). XCT imaging provides a unique way to investigate deformation structures in fine-grained rocks such as deformation bands in a dolomitic mudstone that have been imaged at a voxel resolution of 19 µm (Wennberg and Rennan, 2018).

The study of the rock fabric and more specifically that of mineral grains and their shape fabric by means of XCT is less extended in the literature. However, Knackstedt et al. (2005) have demonstrated its reliability to investigate grain shape fabric in core fragments of sedimentary rocks. Paris et al. (2020) have used XCT to characterize sedimentary fabric of tsunamis deposits in muddy to silty sand. In this publication, they have compared XCT data with 2D image analysis and AMS measurements proving the complementarity of XCT and AMS as powerful petrofabric techniques. Both techniques were applied by David et al. (2007) to investigate the anisotropic features of the Callovo-Oxfordian mudstone. However, the resolution of the XCT image was low and only allowed characterization of large pyrite aggregates. The authors did not suggest an influence of these aggregates on the petrophysical properties. In addition, fabric analysis of quartz and carbonates by synchrotron micro-CT have been done by Robinet et al. (2012) to study the impact of their shape anisotropy on solute diffusion of the Callovo-Oxfordian mudstone (***Figure 2.3*c**). They were particularly interested in grain shape parameters such as elongation derived from the ellipse fitting but also their orientation. However, they have performed shape determination only on 2D sections of the XCT images, parallel or perpendicular to the bedding plane (S0), and worked on a rather small volume (side length <200 µm). Other studies have looked at 3D grain shape in a high maturity shale or in a slate sample displaying a strong tectonic fabric (Kanitpanyacharoen et al., 2012; Wenk et al., 2019). Kanitpanyacharoen et al. (2012) have focused more on low and high attenuating components (i.e. pores and pyrite, ***Figure 2.3*a**). Wenk et al. (2019) have shown that in a highly deformed slate sample, quartz grains display a flattened shape and a strong preferred orientation while their crystals are rather randomly oriented (***Figure 2.3*d**).

Some authors have developed very interesting software and programs to analysis the 3D fabric of rocks or other porous materials from XCT images. However, these programs are more oriented towards the analysis of igneous or metamorphic rocks (Ketcham, 2005a, 2005b; Petri et al., 2020). Most of the applications of XCT to study the grain shape fabric have been limited to these coarse-grained rocks, nevertheless over the last decade and years the microstructure of fine-grained rocks is increasingly studied (Kanitpanyacharoen et al., 2012; Ma et al., 2016, 2021). As an example, a relatively large volume of shale has recently been imaged by means of synchrotron XCT (***Figure 2.3*e**).

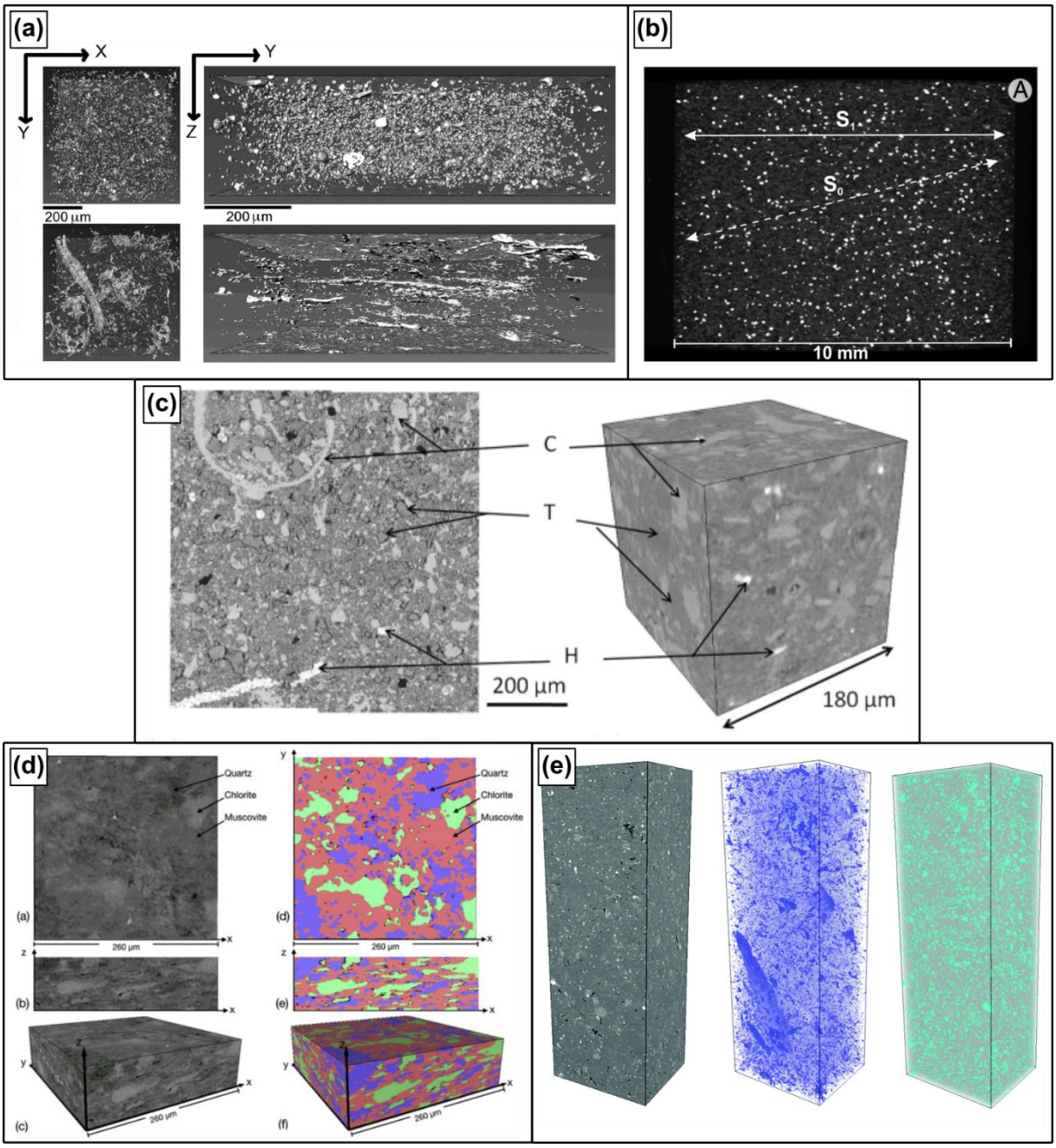

Figure 2.3: ***Compilation of selected works having applied X-ray imaging in shales and slates. (a) 3D views of pyrite, micropores, fractures and kerogen extracted from a high maturity sample of Posidonia shale (Kanitpanyacharoen et al., 2012). (b) Typical bright spots of pyrite in a reconstruct image of a slate with indication of bedding plane (S0) and cleavage plane (S1), obtained by lab-based XCT (Cárdenes et al., 2016). (c) On the left: SEM image (BSE) on a section parallel to S0 of Callovo-Oxfordian mudstone. On the right: 3D view of the grayscale synchrotron XCT image. C: carbonates, T: tectosilicates, H: heavy minerals (Robinet et al., 2012). (d) On the left: 2D grayscale slices and 3D view of a slate imaged by synchrotron XCT. On the right: 2D slices and 3D view of the segmentation of the tomographic image into minerals (Wenk et al., 2019). (d) From left to right: 3D views of a grayscale image (3 x 1 x 1 mm^3) of Bowland shale obtained by synchrotron XCT, its granular components (quartz, calcite and others) and its heavy minerals (Ma et al., 2021).***

2.3 Rock fabric characterization

2.3.1 Generalities

Rock fabric corresponds to the spatial and geometrical arrangement of rock constituents (Passchier and Trouw, 2005). Rock fabric or microfabric at small scales can be a synonym of microstructure or structural anisotropy. It encompasses the shape and shape preferred orientation (SPO) of minerals, kerogen and pores, their spatial distribution, the crystallographic preferred orientation (CPO or lattice preferred orientation LPO) of minerals and layering such as bedding for example (Hobbs, 1985; Kern et al., 2008). In this thesis, we follow the definitions of Hobbs (1985); Almqvist and Mainprice (2017). The term microfabric includes all the elements mentioned above and not only the CPO as it can be found in the literature. These characteristics lead to anisotropic mechanical and physical properties in these media. An anisotropic material is defined as material, which has different physical properties in different directions (Passchier and Trouw, 2005). For example, shales exhibit elastic anisotropy mainly due to their layered structure (bedding or sedimentary fabric), CPO of clay minerals and the SPO of non clay minerals and pore space (Kaarsberg, 1959; Vernik and Liu, 1997; Voltolini et al., 2008; Wenk et al., 2008; Kanitpanyacharoen et al., 2011; Vasin et al., 2013). In highly deformed shale or slate, planar structures form a tectonic fabric, which superimposed the original sedimentary fabric. The fabric of these fine-grained rocks is commonly studied by means of optical microscopy, electron-imaging techniques (SEM and transmission electron microscopy TEM) or X-ray diffraction techniques. These techniques have been used to determine the evolution of the phyllosilicate fabric and the main deformation mechanisms of these platy minerals along a strain gradient in the transition from mudstone to slate at Lehigh gap, Pennsylvania (Lee et al., 1986; Ho et al., 1995; van der Pluijm et al., 1998). We will provide new insights concerning the microstructure of rocks from this well-known outcrop in chapter ***5***. While imaging techniques can provide 2D shape fabrics of grains, the X-ray diffraction techniques, such as the X-ray pole figure goniometry (Oertel, 1983; van der Pluijm et al., 1994) and high-energy synchrotron X-rays (Wenk et al., 2007), aim mostly at determining the CPO of phyllosilicates in these rocks. Another powerful technique to determine the fabric of deformed fine-grained rocks is the Anisotropy of Magnetic Susceptibility or AMS (Tarling and Hrouda, 1993; Borradaile and Jackson, 2004, 2010; Parés, 2015). The AMS provides a bulk magnetic fabric, through a magnetic susceptibility tensor, retracing the preferred orientation (shape or magnetocrystalline) of both ferromagnetic (e.g. magnetite), diamagnetic (e.g. quartz, calcite) and paramagnetic (e.g. phyllosilicates, pyrite) minerals.

2.3.2 Grain shape fabric in image analysis

2.3.2.1 Overview of the different methods

The determination of the grain shape fabric can be done through image analysis techniques or petrophysical techniques. In image analysis, grain shape data were classically obtained on two-dimensional section or three mutually perpendicular two-dimensional sections (Allard and Benn, 1989; Benn and Allard, 1989; Giorgis and Tikoff, 2004). As the shape fabric characterization is intimately linked to the analysis of finite strain in deformed rocks, the flow processes in sedimentary and magmatic rocks, many brilliant techniques have been developed to combine two-dimensional information in order to get a fabric ellipsoid or a strain ellipsoid. The historical methods for the determination of a best-fit ellipsoid from two-dimensional sections are reviewed in the introduction of Robin (2002) or Mookerjee and Nickleach (2011), among others.

In digital image analysis**,** three type of measurements can be used after the images has been segmented (assigning one or more phases to the pixels of the image). The first type looks at more specifically to the data of each grain such as their size, shape and shape preferred orientation or SPO. To simplify the main features of grain morphology, the grains are often approximated by ellipses in 2D or ellipsoids in 3D (this is also useful for modeling). The ellipses or ellipsoids are generally derived from the moments of inertia of each foreground grain in the segmented image (Launeau, 2004; Mulchrone and Choudhury, 2004; Lin and Miller, 2005; Brabant et al., 2011; Cnudde et al., 2011a; Safonov et al., 2018). This region-based method corresponds to the inertia method developed in the software *SPO* (Launeau and Cruden, 1998; Launeau, 2004). This examination is sometimes referred as "texture analysis" in some works (e.g. in Knackstedt et al., 2005; Voltolini et al., 2011) but we will discard this term to avoid possible confusion with crystallographic preferred orientation (CPO) which is not the main subject of this work, except in one section in chapter ***4***. In this thesis, we rather use the term "individual grain analysis" to designate the individual shape features.

The second type of measurements focuses on the bulk data obtained from a group of grains and corresponds to the bulk fabric. This can be calculated directly from the individual data of the first type.

The third type employs the propagation of scanning lines of different orientations through the image (mean intercept length or intercept counting method), or the distribution of intercepting lines in the feature of interest (i.e. the grain) with the star length distribution and star volume distribution methods (Launeau and Robin, 1996; Ketcham, 2005b, 2005a; Launeau et al., 2010).

The second and the third type provide information on the geometrical arrangement of the grains and give the bulk fabric through the representation of a fabric tensor or a fabric ellipsoid. The shape of the ellipsoid correlates to either a linear fabric (lineation) or a planar fabric (foliation) of the grains while its anisotropy or eccentricity gives the strength of this arrangement. Note that the intercept methods are based on the boundaries of the grains and are particularly efficient when these elements are sufficiently connected, whereas the inertia method is suitable when grains are separated and distinguishable (Launeau and Robin, 1996; de Pascalis and Nacucchi, 2019; Petri et al., 2020).

Apart from these three types of measurements, additional signal processing based methods are useful to rock fabric characterization and do not necessary need image segmentation. We can cite the autocorrelation method that can be performed directly on a grayscale image (Heilbronner, 1992; Thissen and Brandon, 2015) and the wavelet transform (Gaillot et al., 1999). Yun et al. (2013) proposed an alternative method to evaluate rock fabric anisotropy in different geomaterials without the need of segmentation. They used oriented slicing plane in the grayscale image to compute statistical parameters of the attenuation values of voxels.

The above-mentioned intercept counting method works also with a limited pre-processing of a grayscale image (Launeau et al., 2010). Mainly performed in 2D with thin sections or electronic images, these methods can be used in 3D. Individual grain data and bulk grain fabric can be obtained from techniques such as the intercept counting or inertia tensor methods applied on multiple 2D sections and extended in 3D (Launeau and Robin, 1996, 2005; Launeau, 2004; Launeau et al., 2010). Such approaches have been successfully applied for minerals in igneous rocks (Grégoire et al., 1998; Launeau and Cruden, 1998; Archanjo, 2002; Archanjo and Launeau, 2004; Hastie et al., 2011, 2013; Schöpa et al., 2015) or clasts in diamictites (Archanjo et al., 2006). Similarly, 2D strain ellipses obtained by the Rf/phi or Fry methods can be combined to retrieve a 3D ellipsoid (Mookerjee and Nickleach, 2011; Sak et al., 2012).

Otherwise, these methods can be directly applied on 3D images obtained with X-ray computed tomography (XCT) in a faster and non-destructive way. While imaging techniques allow access to the individual grain data and the bulk fabric, petrophysical techniques only provide the bulk fabric. This is particularly the case for the anisotropy of magnetic susceptibility (AMS), a technique that has been widely used for 60 years and that we briefly introduce in a forthcoming section.

In this thesis, we have always processed our tomographic images in order to get segmented images. This step is performed using a dedicated image processing software. Therefore, we should present some basic notions of this image processing.

2.3.2.2 Pre-processing, segmentation and particle shape

First, during the XCT acquisition, source filters can be employed to improve the image quality of the reconstructed dataset (this is the filtering of the X-ray beam). After the acquisition, residual noise in the reconstructed XCT dataset or any kind of digital image can be reduced by applying pre-processing filters which are mathematical algorithms that act on each pixel or voxel of the image (Kaestner et al., 2008; Russ et al., 2015). The aim of the filtering process is to make the interpretation of the image easier by increasing the signal to noise ratio and the contrast between the objects (Coster and Chermant, 2001; Kaestner et al., 2008; Russ et al., 2015). This pre-processing is done in order to facilitate the next step, which is the segmentation.

The goal of segmentation is to assign each voxel of the image to a certain type of material or phase. This step is not always necessary, as methods exist to evaluate rock fabric without post-processing (see previous paragraph). The large number of different segmentation tools attest for a non-unique solution to segment any kind of image. This is particularly true in the case of rocks. Interesting reviews concerning the segmentation methods in image analysis are provided by Wirjadi (2007) and Iassonov et al. (2009). The review of Iassonov et al. (2009) focuses more on the segmentation of 3D tomographic images. There are various segmentation methods based on gray level or texture of the images (Haralick and Shapiro, 1985). Furthermore, machine learning and deep learning segmentation tools become more applied. For example, the Trainable Weka Segmentation plugin is proposed in Fiji as a machine learning program (Arganda-Carreras et al., 2017). In any case, the segmentation step should be done with some knowledge of the characteristics of the sample. Depending on the sample, segmented grains may be separated if they are too connected or blended. Separation of touching convex particles is a long lasting problem in image analysis but can be done by watershed segmentation based on distance map or gradient map (Russ et al., 2015).

Once the particles are segmented, separated and labelled, the data about their shape can be analyzed. Nevertheless, a sorting must be done to eliminate the noise, i.e. the smallest particles made of few voxels and which can be segmentation or noise artifacts. These tiny particles, whatever the voxel resolution is, may be less reliable for the quantitative analysis. Some authors have discussed what might be the appropriate threshold for having a sufficient number of voxels to describe a particle. Working on concrete materials and the spherical harmonic representation of star-shape particles, Garboczi (2002) and Garboczi and Bullard (2004) proposed that 5 to 10 voxels in each direction of the segmented object would be sufficient, corresponding to an object having a volume of 125 to 1,000 voxels in total. Later, Erdogan et al. (2006) stated that 10 voxels per unit length for this type of particle shape representation was preferable. In their study of volcanic rocks by means of synchrotron XCT, Gualda and Rivers (2006) said that crystals smaller than 5 voxels in diameter were not adequate for a proper quantification. In similar materials, Voltolini et al. (2011) set the threshold at 75 voxels to analyze the shape and SPO of crystals and vesicles. In their fabric analysis of sedimentary rocks, Paris

et al. (2020) have excluded particles having a short axis (smallest axis of the ellipsoid that fit the particle) lower than 10 voxels. This cutoff may also depend on the specific property of interest regarding the particle shape as shown by the study of Patterson et al. (2012). They have recommended at least 1,000 voxels to analyze the so-called Feret Shape 3D factor of a segmented particle. Wenk et al. (2019) retained segmented minerals with ≈73 voxels to measure the 3D aspect ratio in the tomographic image of a slate. Generally, the cutoff of 5 voxels per unit length (125 voxels in 3D) is the minimum recommendation for any kind of shape analysis.

2.3.3 Bulk magnetic fabric by AMS

Anisotropy of magnetic susceptibility is also a non-destructive technique, which use the magnetic capabilities of grains embedded in a rock matrix to respond to an applied magnetic field. This type of anisotropy is materialized by the magnetic susceptibility tensor k, a second-rank symmetric tensor relating the induced magnetization M of a sample to the applied magnetic field H (Borradaile and Jackson, 2004):

$$M = kH$$

In a matrix form, the relation becomes:

$$\begin{pmatrix} M_1 \\ M_2 \\ M_3 \end{pmatrix} = \begin{pmatrix} k_{11} & k_{12} & k_{13} \\ k_{21} & k_{22} & k_{23} \\ k_{31} & k_{32} & k_{33} \end{pmatrix} \begin{pmatrix} H_1 \\ H_2 \\ H_3 \end{pmatrix}$$

The geometric or mathematical representation of the magnetic susceptibility tensor k is an ellipsoid with principal susceptibility values k_1, k_2, and k_3 (eigenvalues of k) that correspond to the extents of the ellipsoid (magnitudes) along the principal directions $\boldsymbol{K_1}$, $\boldsymbol{K_2}$ and $\boldsymbol{K_3}$ (eigenvectors of k). The magnetic fabric provided by AMS is well-known as a powerful method to infer the bulk grain fabric of a ≈10 cm^3 rock sample in few minutes (Jelínek, 1977; Tarling and Hrouda, 1993; Borradaile and Jackson, 2004; Parés, 2015). In particular, many studies have proved the reliability of using AMS to investigate deformed sedimentary rocks because this technique can reveal subtle trends of the preferred orientation of grains. Even if no particular macroscopic fabric is observed at the outcrop scale, AMS can decipher discrete preferred orientation in very weakly deformed rocks (Aubourg et al., 1991, 1995; Parés et al., 1999; Larrasoaña et al., 2004; Cifelli et al., 2005, 2009). The anisotropy of magnetic susceptibility is due to shape preferred orientation of grains (shape anisotropy of magnetite particles), crystallographic preferred orientation (magnetocrystalline anisotropy), spatial distribution and interactions of ferromagnetic carriers (distribution anisotropy) and the intrinsic mineral susceptibility and anisotropy (Rochette et al., 1992; Stephenson, 1994; Aubourg et al., 1995; Borradaile and Jackson, 2004, 2010; Hrouda, 2007; Biedermann, 2018). Note that the magnetocrystalline anisotropy of phyllosilicates such as mica is closely related to their platy shape. In the case of fine-grained clastic rocks, the paramagnetic phyllosilicates (generally clays, chlorite and/or mica/illite) are generally the main contributors to the AMS signal and the bulk magnetic fabric often reflects the bulk clay fabric (Lüneburg et al., 1999; Parés et al., 1999; Hirt et al., 2004; Debacker et al., 2009; Pueyo-Anchuela et al., 2011; Parés, 2015; Boiron et al., 2020). Magnetic fabrics of progressively deformed/cleaved fine-grained rocks have been extensively studied in fold-and-thrust belts (Averbuch et al., 1992; Parés and Dinarès-Turell, 1993; Parés et al., 1999; Hirt et al., 2000, 2004; Robion et al., 2007; McCarthy et al., 2015). These works have shown that we can distinguish, according to main directional features of $\boldsymbol{K_1}$, $\boldsymbol{K_2}$ and $\boldsymbol{K_3}$ and their relation with the macroscopic foliations, the earliest deformation fabric, the pencil-cleavage fabric, the weak cleavage fabric and the strong cleavage fabric. Using AMS and other

magnetic analyses, Hirt et al. (2004); Housen & van der Pluijm (1991) proposed deformation mechanisms associated to slaty cleavage development in a fine-grained matrix at Lehigh gap, Pennsylvania. In his review, Parés (2015) summarized the main deformation mechanisms of clay platelets in fine-grained rocks affected by tectonic deformation (***Figure 2.4***).

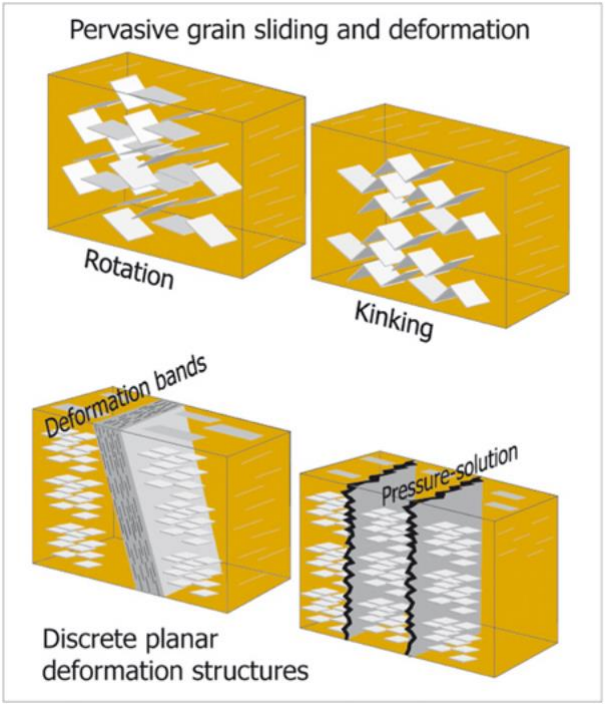

Figure 2.4: ***Summary of possible deformation mechanisms that can produce tectonic magnetic fabrics in mudrocks with a schematic illustration of clay platelets embedded in a rock volume. Some of them may be pervasive (i.e. continuous) and other may be discrete (i.e. localized). Parés (2015).***

3 Methodology

3.1 Introduction

This chapter deals with the methodology developed during this thesis. In this chapter, we present the sample preparation protocol for X-ray imaging and the details of the treatment of the tomographic dataset. We provide a section concerning the image processing of a 3D dataset and how it was implemented during this thesis. The various post-processing methodologies are presented. The post-processing concerns the study of shape based data and point distribution data after the extraction of grains in the 3D dataset. A section will present our approach to evaluate the homogeneity of the shape fabric measured in the samples. Furthermore, we present a method to combine XCT segmented images with a Finite Element Method software. Lastly, some other analytical techniques have been used to support the Sigüés case study and are explained.

3.2 Sample preparation for XCT

Before imaging a sample by XCT, we may or may not need to get an idea of its bulk petrofabric by measuring the AMS. AMS typically requires standard drill cores of 2.54 cm diameter taken in the field using a portable drilling machine. If no drilling is done in the field, an oriented bloc can be extracted with a hammer and the standard AMS core can be drilled later in the laboratory. In any case, each AMS core or oriented bloc was marked with a generatrix in the field, which corresponds to a straight arrow affixed to the top surface and is oriented in a geographic coordinate system. Because a cylindrical drill core is the optimal form to scan with a XCT instrument, the first step was to drill a millimeter-sized drill core from the AMS core or the oriented bloc (***Figure 3.1***). This drilling was achieved using a Proxxon TBH bench drill press at the DMEX laboratory. This has to be done carefully due to the degree of consolidation of the samples and/or their degree of deformation. However, we have also been able to drill a 625 µm cylindrical sample and to scan it at a voxel size of 500 nm. Some authors have used more sophisticated instruments such as laser systems to prepare small cylindrical samples of shale rocks (Backeberg et al., 2017; Bailey et al., 2017). FIB-SEM may also serve to prepare very fine samples. Prior to drilling, the generatrix of the AMS core is reported on the location of the top surface which is intended to be drilled using a fine steel pen. This permits to reorient the three-dimensional image obtained by XCT. The reference frame for each sample is indicated by the generatrix, which has azimuth and dip values related to the north. The XCT drill core is then mounted on a carbon rod that prevents artefact generation and placed into the imaging instrument (***Figure 3.1***). These small cores are not drill according to the main foliations of the sample such as bedding (S0) and cleavage (S1). They are drilled along the z-axis of the AMS cylindrical drill core or perpendicular to the oriented surface of the bloc sample for the sake of generality.

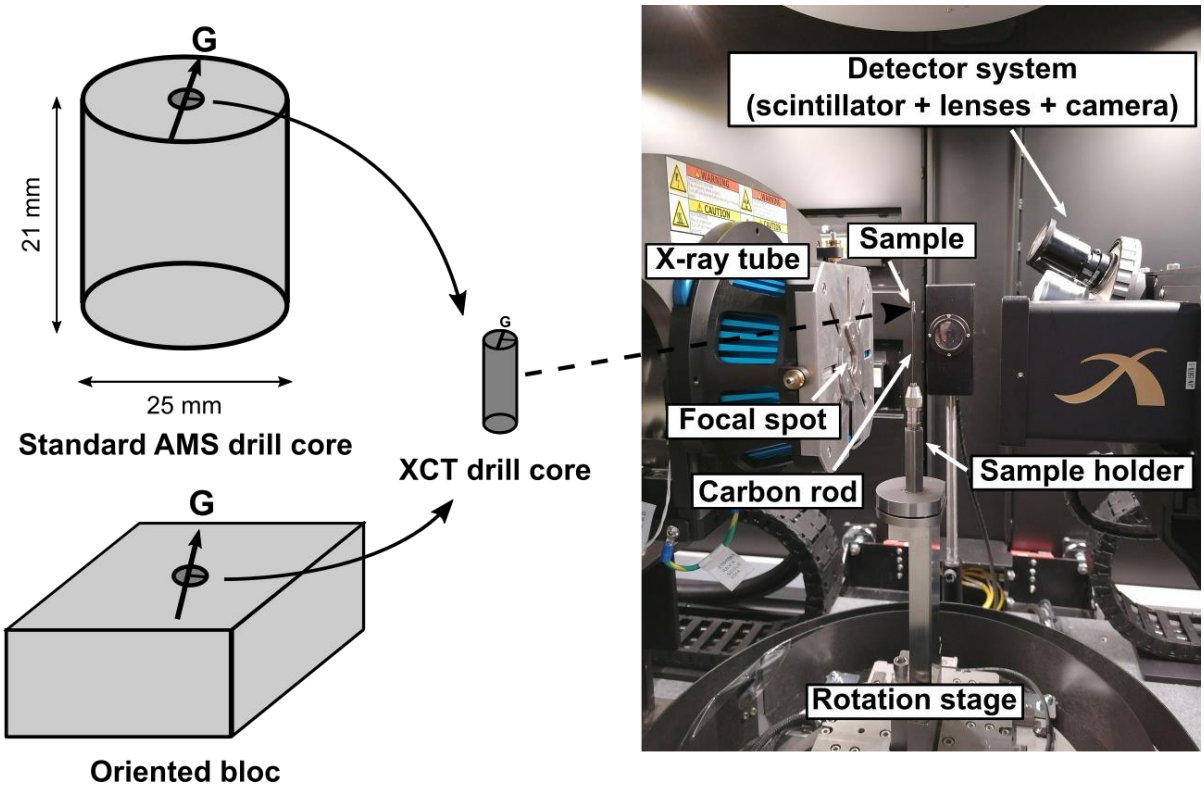

Figure 3.1: ***Preparation of the millimeter-sized drill core for XCT acquisition (left). Image of the chamber of the Zeiss Xradia 510 versa with its main elements (right).***

3.3 XCT acquisition and reconstruction of data

XCT acquisitions were performed on two instruments available at DMEX that use a polychromatic X-ray source. The main instrument is the Zeiss Xradia 510 Versa, which has a cone-beam configuration. The Zeiss tomograph can deliver energies from 30 keV to 160 keV with a theoretical spatial resolution better than 0.7 µm and a voxel resolution down to 70 nm. The instrument combines geometrical and optical magnification as well as source filters to optimize the contrast. A picture of the device used during this thesis is presented in (***Figure 3.1***). This instrument was well adapted to achieve high-resolution in fine-grained rock samples. For coarser samples such as sandstones, we have used the Bruker Skyscan 1172 instead that has only a geometrical magnification.

The complex nature of fine-grained materials with mixture of phases and small-scale features such as clays often yield poorly contrasted images. Furthermore, the weak contrast in the attenuation coefficients of the main minerals occurring in fine-grained rocks is a common issue. In ***Figure 3.2***, the attenuation coefficients of quartz, calcite and pyrite are plotted against the energy of the X-ray source. We observe that the curves of quartz and calcite merge above 120 keV, giving rise to difficulties in their distinction. Below 60 keV, a better contrast in attenuation between quartz and calcite is expected. Pyrite with Fe element is a high-density mineral, which is easily distinguished from other components in fine-grained rocks. Thus, most of the XCT acquisitions with the Zeiss tomograph reported in this thesis were performed using a source energy of 40 keV (i.e. the upper limit to the photon energy is 40 keV as we are working with a polychromatic source) for fine-grained rocks in order to maximize the contrast between mineral phases. Additionally, we applied source filters during the acquisitions to improve image quality.

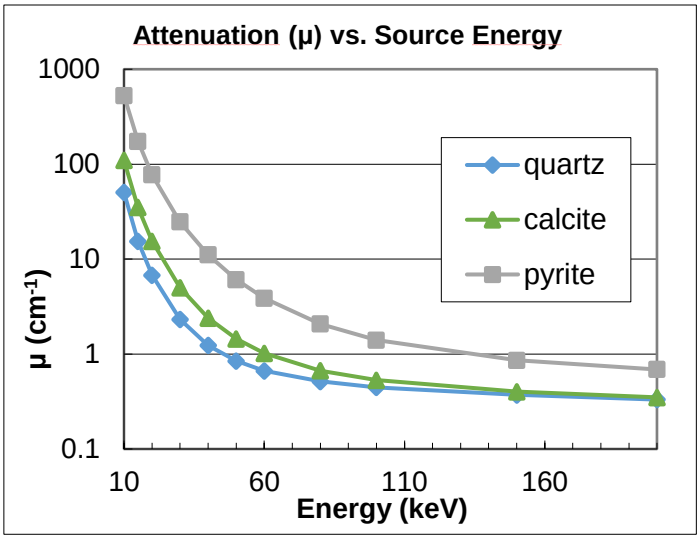

Figure 3.2: ***Attenuation coefficient of quartz, calcite and pyrite versus the energy of the X-ray source. Data and graph based on MuCalc (http://www.ctlab.geo.utexas.edu/software/mucalctool/).***

The 16-bit CCD detector of the Zeiss instrument is capable of acquiring radiographs with 2048^2 pixels. The data on the detector can also be binned, that is combining several pixels into one pixel. Some acquisitions were done using a binning by two (i.e. 1024^2 detector pixels). It increases the signal-to-noise ratio, reduces the acquisition time and the size of the dataset (Hanna and Ketcham, 2017). After the acquisition of several hours, the two-dimensional radiographs/projections are reconstructed with XRM Reconstructor® (Zeiss, version 11) based on a filtered back projection algorithm (Ramachandran and Lakshminarayanan, 1971; Feldkamp et al., 1984). Different parameters can be adjusted by the operator such as a center shift correction, a beam hardening correction and a reconstruction filter (*smooth* or *sharp* modules). The reconstructed image is converted into a stack of 2D tiff images in order to visualize and analyze the 3D image with an adapted image processing software, as dataset may be quite large.

3.4 Image processing 3D dataset

3.4.1 3D visualization and software used

A lot of free and commercial software can be used to visualize the reconstructed XCT dataset and to perform quantitative analysis such as Avizo® (Thermo Fisher Scientific, http://www.vsg3d.com), Fiji (Schindelin et al., 2012) with plugins such as 3D ImageJ Suite (Ollion et al., 2013) or Bone J (Doube et al., 2010), Dragonfly software (Object Research Systems (ORS) Inc, Montreal, Canada, http://www.theobjects.com/dragonfly), Blob3D and Qant3D (Ketcham and Ryan, 2004; Ketcham, 2005a, 2005b), YaDiv (Friese et al., 2011), Pore3D (Brun et al., 2010), Mango (https://physics.anu.edu.au/appmaths/capabilities/mango.php) and Morpho+ (Brabant et al., 2011; Cnudde et al., 2011a). The reader will find other software listed in Table 1 and Table 2 of the article of Hanna and Ketcham (2017) for example. The most used software for analyzing XCT data in the field of geosciences are probably the Blob3D and Qant3D of the University of Texas (e.g. applications in Macente et al., 2017; Arbaret et al., 2019).

In this thesis, we used Avizo software (9.0.0) to visualize and to process our 3D XCT datasets. Even though the Blob3D and Qant3D programs have been tested during the PhD, an Avizo® license was available at the X-ray laboratory and allowed efficient processing of the datasets. Chatzaras et al.

(2016) have shown that Avizo® is perfectly adapted to investigate petrofabrics. The full workflow developed in Avizo® is illustrated in ***Figure 3.3*** and ***Figure 3.6*** with an XCT image of one fine-grained sample (sample A2-2, see ***Table 3.1*** at the end of this chapter). Firstly, the entire image is visualized (***Figure 3.3*****a**). Then the cylinder-shaped image is cropped to define a hexahedral Volume of Interest (VOI, ***Figure 3.3*****b**). It is in the VOI of the whole image that the quantitative data are obtained.

In several images of fine-grained clastic rocks, we have identified microcracks appearing as low attenuating dark laminae. These structures might have been caused by the core drilling operation, stress relaxation or dehydration of the sample. When macroscopic cleavages surfaces were observed on the AMS core, these microcracks generally correspond to the location of the pressure-solution seams (these deformation structures will be shown in the next chapter).

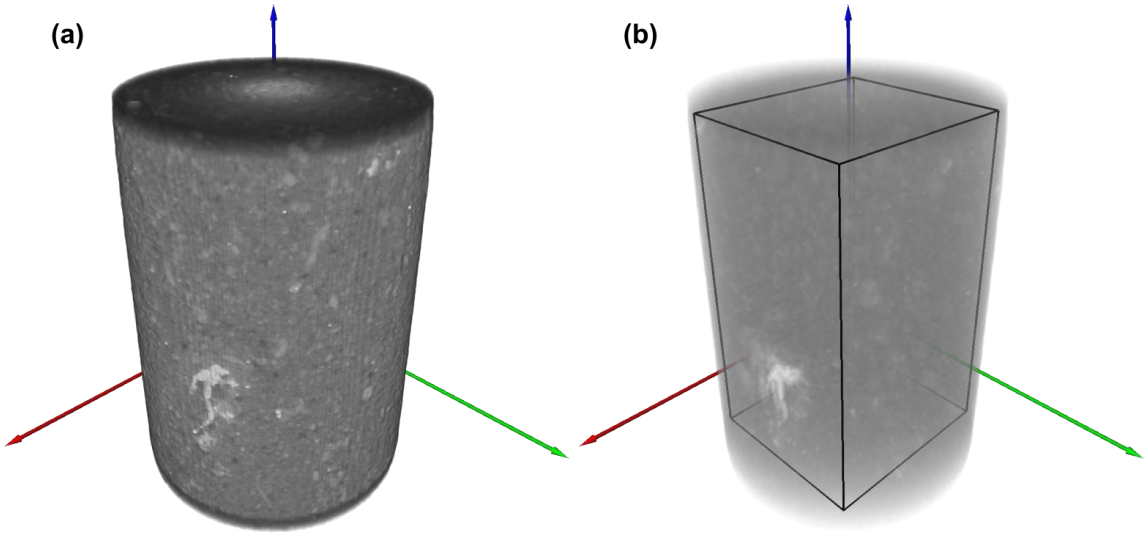

Figure 3.3: ***(a) 3D image of the scanned part of the millimeter-sized drill core of a fine-grained rock (diameter of 1.71 mm). White patch in the lower part corresponds to heavy pyrite minerals. (b) Hexahedral volume of interest (VOI) highlighted with dark edges, typical size of 2-3.5 mm³ for fine-grained rock samples.***

3.4.2 Filtering

Because of a rather unimodal histogram of gray values which does not allow to clearly distinguish the phases present in the image of a shale, we used pre-processing filter to improve the contrast. The histogram of the VOI illustrated in ***Figure 3.3*****b** is shown in ***Figure 3.4***. Therefore, an *Anisotropic Diffusion* filter proposed by Bernard et al. (2011) is applied to each XCT dataset. This filter is a modified version of the classical edge-preserving anisotropic diffusion filter (Perona and Malik, 1990). It smoothens noisy but relatively uniform regions of the image (i.e. each individual phase), while preserving the boundaries between the phases (i.e. the contours of the objects). Its efficiency has been demonstrated in a bi-phased material in Bernard et al. (2011) or in multiphase media in Porter and Wildenschild (2010) and in Schlüter et al. (2014). Two criteria are adjustable for this filter. The gradient threshold corresponds to the jump limit in gray level to the diffusion process, and the number of iterations affects the degree of smoothing. Additionally, the *Despeckle* module was applied to remove residual noise based on a mean calculation of neighborhood voxel values. ***Figure 3.4*** shows how the anisotropic diffusion filter (gray curve) smooths the original raw signal (dark curve) of gray levels. The filtered histogram, remaining mixed nevertheless, shows shoulders correlated to the different phases instead of the initial unimodal distribution. However, no distinct peaks are highlighted. In addition,

Figure 3.5 illustrates the efficiency of the filter by using a *Line Probe* module on a slice of the dataset. The output signal is more favorable to the distinction of the main features.

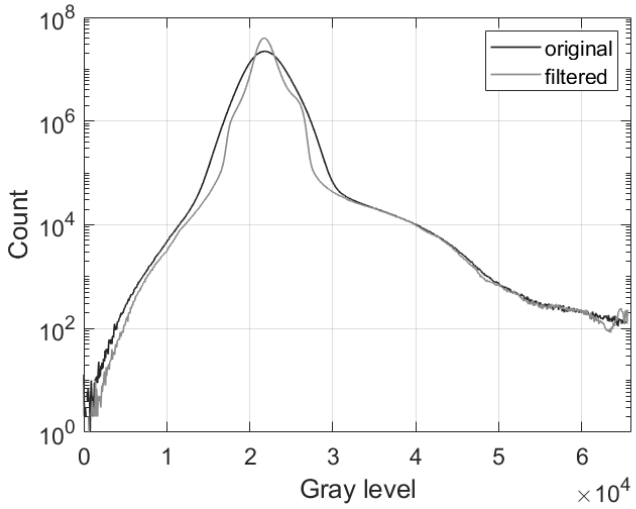

Figure 3.4: ***Histogram of gray levels of the VOI illustrated in Figure 3.3b (dark curve)and histogram after applying a filter (gray curve).***

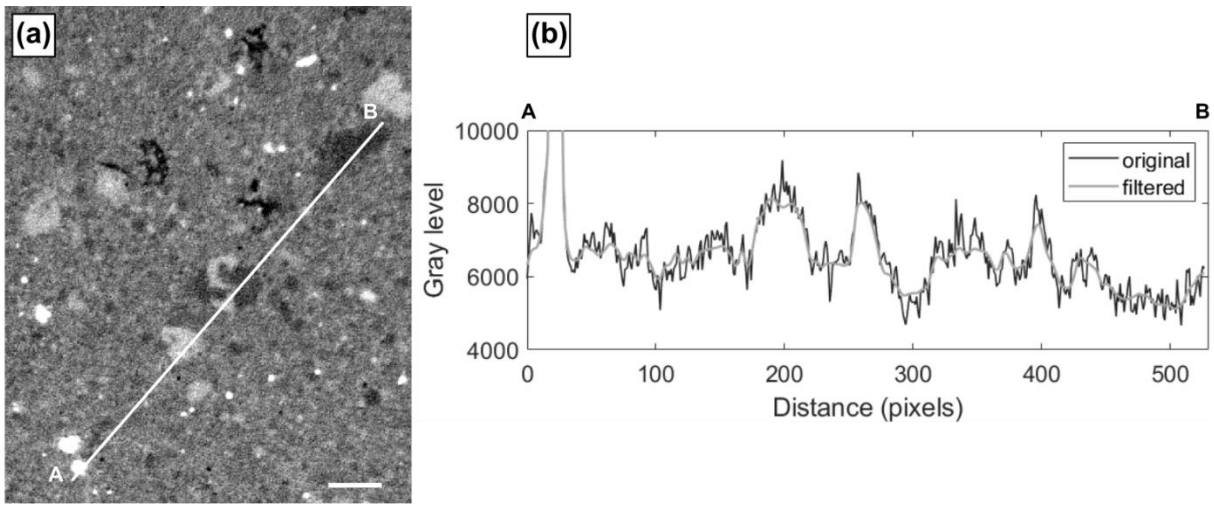

Figure 3.5: ***(a) Slice view of the raw image with a line probe between points A and B. (b) Original gray level signal (dark) and filtered signal (gray).***

The filtering process is also illustrated in the complete workflow of ***Figure 3.6***. ***Figure 3.6*****a** displays a raw slice of the VOI presented in ***Figure 3.3*****b** with all the main identifiable phases of the image. ***Figure 3.7*****a** presents the 3D view of the VOI. ***Figure 3.6*****b** displays the filtered image of ***Figure 3.6*****a** after the application of the *Anisotropic Diffusion* filter.

3.4.3 Segmentation

The main segmentation method employed in this work was the global gray level thresholding. The thresholds were selected manually or using the histogram-based Otsu method (Otsu, 1979). This last method aims at minimizing the intra-class variances, or maximizing the inter-class variances (Coster and Chermant, 2001; Iassonov et al., 2009; Schlüter et al., 2014). Alternatively, the method based on

moments by Tsai (1985) provided good results. The segmentation of one phase in the XCT image provides a segmented or binarized image (***Figure 3.6c***).

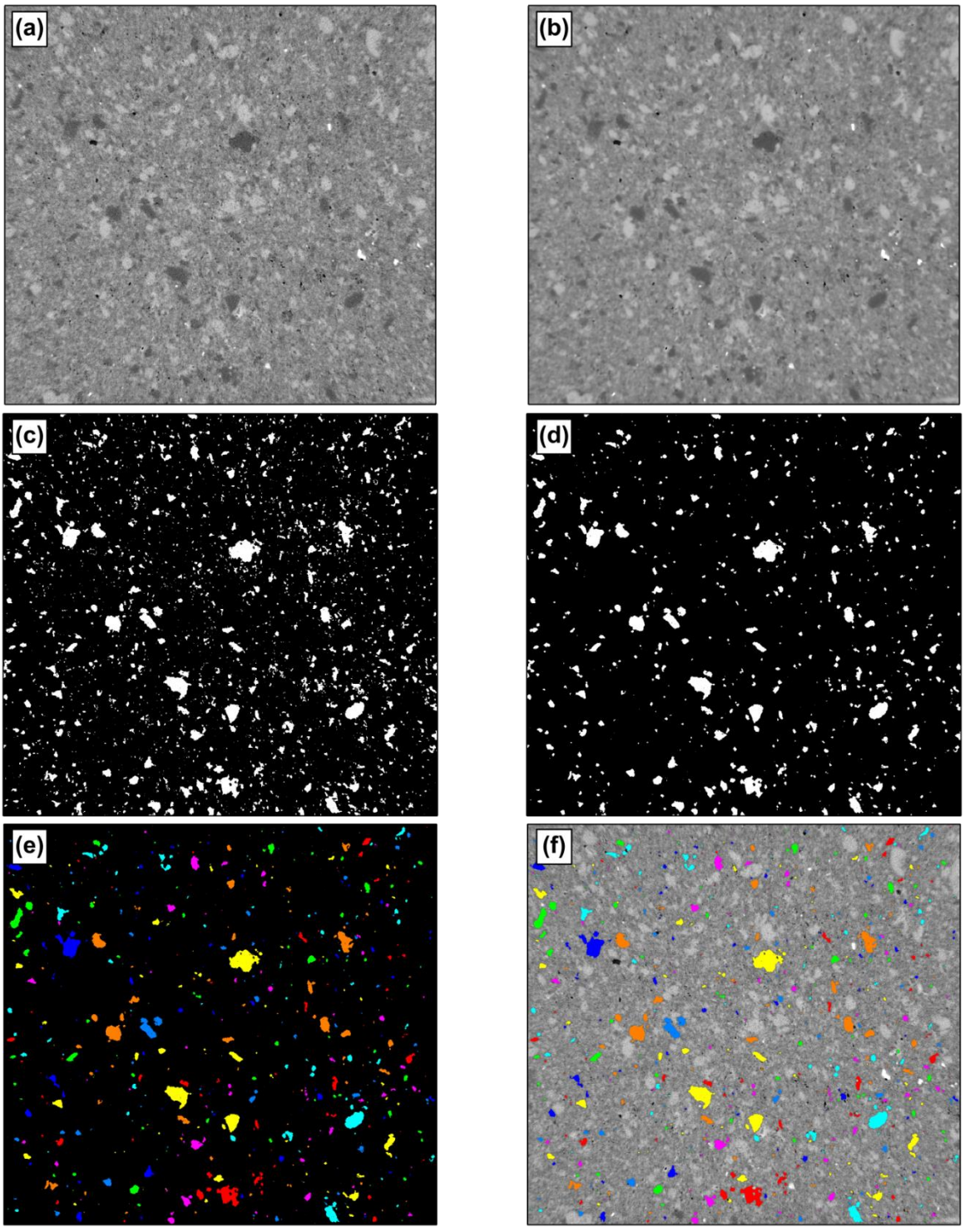

Figure 3.6: ***Image processing workflow. (a) Original slice (width: 1010 µm, height: 935 µm) of the grayscale image. (b) Filtered image. (c) Segmented image. (d) Some cleaning using morphological filters. (e) Labelled image. (f) Overlay of the resulting labelled image on the original image in (a).***

Segmentation was followed by a slight post-processing involving mathematical morphology operations (Serra and Vincent, 1992). We used the *Opening* module (operation which encompasses erosion and

dilation) to separate possible connected grains and to eliminate coating effect for some grains. The result of this cleaning is shown in ***Figure 3.6*****d**.

If the grains remained strongly connected, we had to use more sophisticated tools to separate grains. The *Separate Objects* module of Avizo® is based on the watershed principle (Beucher and Lantuejoul, 1979; Vincent et al., 1991). A marker-based watershed can also be done step by step without using the *Seperate Objects* module allowing more control to the operator. In this case, the operator computes the euclidean distance map and chooses the region minima that serve as seeds for the flooding process in the image landscape using the *Marker-Based Watershed* module of Avizo®.

As mentioned in section ***2.3.2.2***, the smaller particles were excluded as they might be artifacts related to the segmentation or image noise. Particles having at least 125 voxels (5^3 voxels) were kept for quantitative analysis. In addition, we have removed grains that were in contact with the border of the VOI using a *Border Kill* module based on mathematical morphology. Following this step, each segmented particle was labelled using the *Labeling* module in 6-connectivity (***Figure 3.6*****e**, ***Figure 3.6*****f** and ***Figure 3.7*****c**).

The result of the segmentation of one phase provides a binarized image which can be visualized in 3D with Avizo®. A multiphase segmented image may also be visualized. The software proposes an *Isosurface* module in which each segmented object can be further contoured by triangular faces providing smooth representation. Otherwise, a *Volume Rendering* module provides the raw result with cubic elements, in other terms it corresponds to the voxelized representation.

The *Label Analysis* module of Avizo® provides a standard shape description of particles, which is detailed in the next section.

3.4.4 Grain shape data and moments of inertia

3.4.4.1 Introduction

All the post-processing of grain shape, directional and spatial data were done using integrated Avizo® modules and personal scripts written in MATLAB (Mathworks®).

In this thesis, we chose to study the shape fabric of segmented and labelled grains that are composed of a least 125 voxels (side length of 5 voxels) or have a volume of at least 729 µm^3 (i.e. a cubic particle of 9 µm side length or a spherical particle of 11.17 µm in diameter). The first threshold was discussed in section ***2.3.2.2***. The volumetric threshold of 729 µm^3 is used to focus more on silt-sized (supposedly detrital) grains in shale rocks. This threshold is chosen arbitrary but aims to study silt-sized particles sufficiently resolved in the image. These are the two factors chosen for the cutoff threshold that have been applied to remove the smallest grains with the *Analysis Filter* module of Avizo®. In addition, we have discarded grains with extreme values of $Anisotropy, Flatness$ and $Elongation$ (see next section for definitions).

As presented in section ***2.3.2***, we employed a shape analysis based on the inertia tensor method, which is automatically implemented by Avizo® in its *Label Analysis* module. One of the main feature of this tool is the approximation of the grain morphology by an ellipsoid. We provide an illustration of this in ***Figure 3.7*****c**. Thus, we may distinguish morphological aspects of the grain and the shape of their equivalent ellipsoid. Throughout this thesis, we will mainly discuss grain shape in terms of the shape of the grain ellipsoid as it is well adapted to discuss grain fabric, its orientation features and anisotropy (Wildenschild and Sheppard, 2013). For disciplines that require a more precise description of the

particle shape, such as in sedimentology (Knackstedt et al., 2005; Blott and Pye, 2008) or for engineering purposes, a more in-depth analysis must be carried out, particularly by looking at factors such as sphericity and roundness (Wadell, 1932; Lin and Miller, 2005; Zhao and Wang, 2016), to name a few. The reader can find additional information in section 5.2.3 of the review of Wildenschild and Sheppard (2013). However, we will present the main 3D shape descriptors that any operator could use. We recall that an individual grain analysis and a bulk fabric can be assessed using the inertia tensor method. We present both in the following sections.

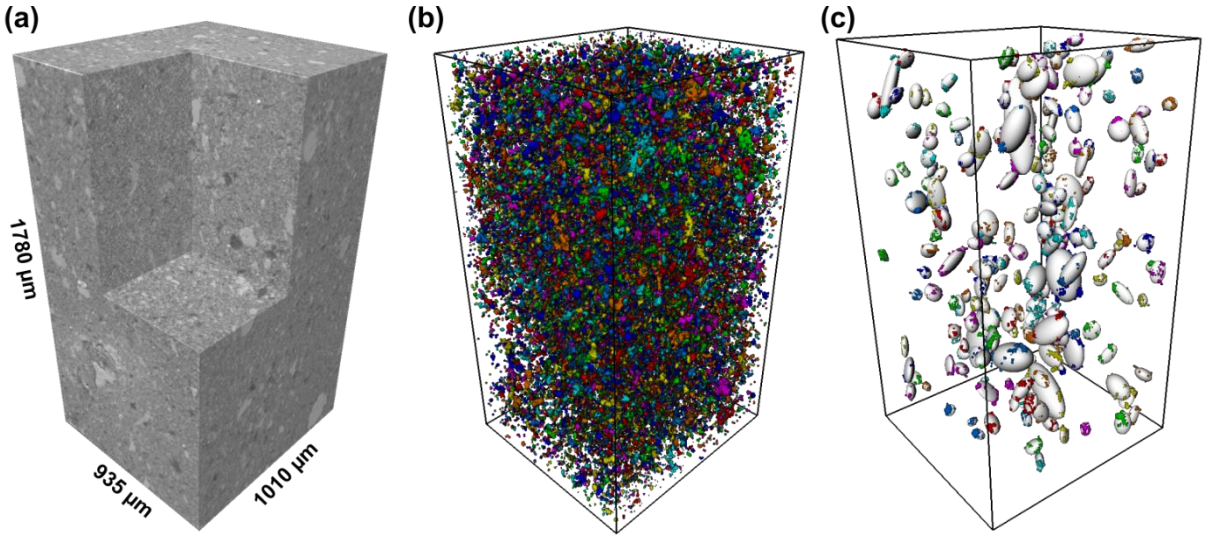

Figure 3.7: *(a) 3D view of the VOI of Figure 3.3b with corner cut option. (b) Labelled grains of Figure 3.6e. (c) Largest grains and their equivalent ellipsoid.*

3.4.4.2 Individual grain analysis

In this analysis, we tried to isolate individual grains as much as possible. However, due to the achieved spatial resolution of XCT and mixture of multi-scale features in fine-grained rocks, this task is rather complex. Thus, the resulting segmented grains may occasionally correspond to aggregates of grains. In addition, some particles may have irregular shapes that are not well represented by the equivalent ellipsoid.

Each segmented grain of the binarized 3D image can be approximated by an equivalent ellipsoid based on the theory of image moments (Hu, 1962). The details of the computation are provided here to better understand how the approximation is done and how the data are used for directional analysis but, as said before, this computation is automatically performed by Avizo® until the solution of the eigenproblem. Note that the representation of a grain by an ellipsoid remains an approximation of its true morphology by an object with orthorhombic symmetry. Firstly, we may define the global or geometric moments of order $p + q + r$ of a segmented object using:

$$m_{p,q,r} = \sum_i {x_i}^p {y_i}^q {z_i}^r$$

Where x_i, y_i and z_i are the coordinates of the voxels belonging to the grain. The zeroth order moment $m_{0,0,0}$ corresponds to the sum of the particle's voxels and gives its volume V_0 in 3D. The true volume of the particle V is then given by $V = V_0 \times (voxel\ side\ length)^3$. The first-order moments can be used to define the center of mass or centroid (x_c, y_c, z_c) of the grain according to:

$$x_c = \frac{m_{1,0,0}}{m_{0,0,0}} ; y_c = \frac{m_{0,1,0}}{m_{0,0,0}} ; z_c = \frac{m_{0,0,1}}{m_{0,0,0}}$$

Then, the general expression of the central moments of order $p+q+r$ normalized by the volume of the grain is:

$$M_{p,q,r} = \frac{1}{V}\sum_i (x_i - x_c)^p (y_i - y_c)^q (z_i - z_c)^r \quad (3.1)$$

The second-order central moments are given following equation ***3.1***:

$$M_{2,0,0} = \frac{1}{V}\sum_i (x_i - x_c)^2$$

$$M_{0,2,0} = \frac{1}{V}\sum_i (y_i - y_c)^2$$

$$M_{0,0,2} = \frac{1}{V}\sum_i (z_i - z_c)^2$$

$$M_{1,1,0} = \frac{1}{V}\sum_i (x_i - x_c)(y_i - y_c)$$

$$M_{1,0,1} = \frac{1}{V}\sum_i (x_i - x_c)(z_i - z_c)$$

$$M_{0,1,1} = \frac{1}{V}\sum_i (y_i - y_c)(z_i - z_c)$$

The six above-defined independent second-order central moments form the following covariance matrix or inertia matrix/tensor (Lin and Miller, 2005; Dong et al., 2014; Flusser et al., 2016):

$$M_2 = \begin{pmatrix} M_{2,0,0} & M_{1,1,0} & M_{1,0,1} \\ M_{1,1,0} & M_{0,2,0} & M_{0,1,1} \\ M_{1,0,1} & M_{0,1,1} & M_{0,0,2} \end{pmatrix} \quad (3.2)$$

Solving the eigenproblem of M_2 provides the principal magnitudes or eigenvalues of the equivalent ellipsoid with $L_1 \geq L_2 \geq L_3$ and the three principal orthogonal directions or eigenvectors $\vec{\boldsymbol{L}}_{\boldsymbol{1}}(v_{1x}, v_{1y}, v_{1z})$; $\vec{\boldsymbol{L}}_{\boldsymbol{2}}(v_{2x}, v_{2y}, v_{2z})$; $\vec{\boldsymbol{L}}_{\boldsymbol{3}}(v_{3x}, v_{3y}, v_{3z})$:

$$\begin{pmatrix} M_{2,0,0} & M_{1,1,0} & M_{1,0,1} \\ M_{1,1,0} & M_{0,2,0} & M_{0,1,1} \\ M_{1,0,1} & M_{0,1,1} & M_{0,0,2} \end{pmatrix} = \begin{pmatrix} v_{1x} & v_{2x} & v_{3x} \\ v_{1y} & v_{2y} & v_{3y} \\ v_{1z} & v_{2z} & v_{3z} \end{pmatrix} \begin{pmatrix} L_1 & 0 & 0 \\ 0 & L_2 & 0 \\ 0 & 0 & L_3 \end{pmatrix} \begin{pmatrix} v_{1x} & v_{1y} & v_{1z} \\ v_{2x} & v_{2y} & v_{2z} \\ v_{3x} & v_{3y} & v_{3z} \end{pmatrix}$$

The matrix M_2 is similar to the inertia tensor method implemented in *SPO2003* (Launeau, 2004) or presented for 2D ellipses in Mulchrone and Choudhury (2004). We will keep the inertia tensor designation in this manuscript. However, we should note that second-order central moments can be used to express a moment of inertia tensor inspired from mechanics. This type of inertia tensor is also used to retrieve an equivalent ellipsoid of a particle and is presented in many studies (Ikeda et al., 2000; Al-Raoush, 2007; Wang et al., 2007). With the terms of equation ***3.2***, this inertia tensor can be defined according to equation 7 of Safonov et al. (2018) or equation 4.26 of Flusser et al. (2016). In our case, this method gives the same results as those of the eigen solution of the covariance matrix M_2. The covariance matrix or inertia tensor must be considered as a measurement of mass (here voxels) distribution around a gravity center.

The morphology of each individual ellipsoid can be described using the shape parameter $\boldsymbol{T_G}$ and the corrected degree of anisotropy $\boldsymbol{P_j}$ proposed by Jelinek for susceptibility tensors (Jelínek, 1981):

$$T_G = 2\frac{\ln(L_2/L_3)}{\ln(L_1/L_3)} - 1$$

$$P_j = \exp\sqrt{2[(\ln L_1 - \ln L_m)^2 + (\ln L_2 - \ln L_m)^2 + (\ln L_3 - \ln L_m)^2]}$$

where L_m is the mean magnitude: $L_m = (L_1 + L_2 + L_3)/3$

Jelinek's fabric parameters are well suited to describe an ellipsoid and have been extensively used to quantify the magnetic fabric (Tarling and Hrouda, 1993; Borradaile and Jackson, 2004, 2010) but also to study the grain fabric from photomicrographs or digital images (Launeau and Cruden, 1998; Archanjo, 2002; Chatzaras et al., 2016). The shape parameter $\boldsymbol{T_G}$ corresponds to the shape of the considered ellipsoid and ranges from prolate ($\boldsymbol{T_G} = -1$) to oblate ($\boldsymbol{T_G} = +1$) via triaxial ($\boldsymbol{T_G} = 0$). It characterizes the symmetry of the ellipsoid. The symmetry of an oblate (disc-shaped) ellipsoid is done with respect to its minor axis ($\boldsymbol{L_3}$) while the symmetry of a prolate (rod-shaped) ellipsoid is done with respect to its major axis ($\boldsymbol{L_1}$). A wide range of ellipsoidal morphologies is possible between these two end-members. The parameter $\boldsymbol{P_j}$ corresponds to its degree of anisotropy (eccentricity).

Avizo® also proposed three dimensionless parameters based on the eigenvalues to describe the shape of the ellipsoid, which are the *Anisotropy*, *Flatness* and *Elongation*:

$$Anisotropy = 1 - L_3/L_1$$

$$Flatness = L_3/L_2$$

$$Elongation = L_2/L_1$$

The three semi-axes or radii a, b and c of the equivalent ellipsoid can be obtained using the eigenvalues as demonstrated by Dong et al. (2014):

$$a = \sqrt{(5L_1)}$$

$$b = \sqrt{(5L_2)}$$

$$c = \sqrt{(5L_3)}$$

The semi-axes can be plotted in a Flinn type diagram for example instead of using an eigenvalue-based Jelinek diagram. We can define here the aspect ratio of each grain, which corresponds to the ratio a/c of its equivalent ellipsoid.

The *Shape Factor* parameter of Avizo® corresponds to the inverse of the so-called *Compactness* (Safonov et al., 2018). We can find a similar notion in the form factor called *Sphericity* (Wadell, 1932; Bernard et al., 2011; Zhao and Wang, 2016). The *Sphericity* permits to quantify how close to a spherical shape the particle of interest is. It indicates the degree of irregularity of the particle shape and it is expressed as (Bernard et al., 2011):

$$Sphericity = \left(\frac{1}{Shape\ Factor}\right)^{\frac{1}{3}} = \frac{\pi^{\frac{1}{3}}(6V)^{\frac{2}{3}}}{A}$$

A is the particle surface area, V its volume. Another useful parameter can be computed as the ratio between the volume of the particle V and the volume of its corresponding ellipsoid. We call this parameter *Ellipsoid Filling*. It indicates how filled is the ellipsoid by the voxels belonging to the particle. In addition, an *Equivalent Diameter* of each grain can be determined using the following relation:

$$EqD = (6V/\pi)^{\frac{1}{3}}$$

The equivalent diameter corresponds to the diameter of a sphere having the same volume as the particle of interest.

3.4.4.3 Bulk fabric

Bulk fabric is evaluated by computing the mean inertia tensor (or fabric ellipsoid) of an ensemble of grain ellipsoids obtained in the individual grain analysis. We use a Python program developed by Montoya-Araque & Suarez-Burgoa (2018) for the processing of anisotropy of magnetic susceptibility (AMS) data. Instead of using the components of the susceptibility tensors as input of the program, we take the central moments that form the inertia tensor of each grain (see equation ***3.2***). In the program, each term of an individual tensor M_2 (grain ellipsoid) is first normalized by the trace of the tensor following the procedure proposed by Jelinek for susceptibility tensors (Jelínek and Kropáček, 1978). The normalized tensor $\overline{M_2}$ of the grain is given by:

$$\overline{M_2} = \frac{1}{M_a}\begin{pmatrix} M_{2,0,0} & M_{1,1,0} & M_{1,0,1} \\ M_{1,1,0} & M_{0,2,0} & M_{0,1,1} \\ M_{1,0,1} & M_{0,1,1} & M_{0,0,2} \end{pmatrix} = \begin{pmatrix} \overline{M_{2,0,0}} & \overline{M_{1,1,0}} & \overline{M_{1,0,1}} \\ \overline{M_{1,1,0}} & \overline{M_{0,2,0}} & \overline{M_{0,1,1}} \\ \overline{M_{1,0,1}} & \overline{M_{0,1,1}} & \overline{M_{0,0,2}} \end{pmatrix}$$

Where M_a is the mean moment of the considered grain: $M_a = \left(M_{2,0,0} + M_{0,2,0} + M_{0,0,2}\right)/3$ and $\overline{M_{m,n,p}} = M_{m,n,p}/M_a$

The mean tensor M of a group of K grains is then given by:

$$M = \frac{1}{K}\begin{pmatrix} \sum \overline{M_{2,0,0}} & \sum \overline{M_{1,1,0}} & \sum \overline{M_{1,0,1}} \\ \sum \overline{M_{1,1,0}} & \sum \overline{M_{0,2,0}} & \sum \overline{M_{0,1,1}} \\ \sum \overline{M_{1,0,1}} & \sum \overline{M_{0,1,1}} & \sum \overline{M_{0,0,2}} \end{pmatrix} \tag{3.3}$$

where the summation sign runs over the grains. Alternatively the mean tensor M could also be computed by using the three orientation tensors of the axes $\boldsymbol{L_1}$, $\boldsymbol{L_2}$ and $\boldsymbol{L_3}$ and the characteristic length of these axes for each grain as explained by Petri et al. (2020). The morphological parameters $\boldsymbol{T_B}$ and $\boldsymbol{P_j}$ are calculated as before after solving the eigenproblem of M. The use of normalization implies that every grain contributes equally to the mean tensor calculation and it avoids the excessive contribution of large and anisotropic (high P_j values) grains which can be responsible of subsidiary subfabrics (Borradaile, 2001; Petri et al., 2020). Therefore, the shape of the most common grains contribute more to the mean tensor, and thus the bulk fabric. The reader will take note that such normalization is not mandatory (Borradaile, 2001, 2003a). If $\boldsymbol{T_B} = +1$, the bulk fabric ellipsoid is oblate and grains parallel a common planar structure (foliation, S-fabric). If $\boldsymbol{T_B} = -1$, the bulk fabric ellipsoid is prolate and grains parallel a common linear structure (lineation, L-fabric). The shape parameter $\boldsymbol{T_B}$ characterizes the shape of the fabric ellipsoid, i.e. it illustrates the average orientation of the ensemble of individual ellipsoids and the symmetry of this orientation distribution. It is important to distinguish $\boldsymbol{T_B}$ from the shape parameter $\boldsymbol{T_G}$ of individual ellipsoid (Borradaile, 2001; Giorgis and Tikoff, 2004; Chatzaras et al., 2016). $\boldsymbol{P_j}$ is the degree of anisotropy of the fabric ellipsoid and gives the strength of the fabric[1]. The

[1] Avizo® also offers the possibility to compute a structural degree of anisotropy using the boundary-based Mean Intercept Length method (see section ***2.3.2.1***).

principal directions of a fabric ellipsoid are given by the eigenvectors $\vec{L}_{1m}$, $\vec{L}_{2m}$ and $\vec{L}_{3m}$ throughout the manuscript.

The main grain and ellipsoid shape descriptors of the individual grain analysis and of the bulk fabric are summarized in ***Figure 3.8***.

3.4.5 Directional data, reorientation and representation

Two type of directional data are then available. The axial data from eigenvectors and the tensorial data from the second-order central moments. The longest eigenvectors $\boldsymbol{L_1}$ corresponds to the lineation of the grain while the shortest eigenvector $\boldsymbol{L_3}$ corresponds to its pole of foliation (they are axes strictly speaking due to the orthorhombic symmetry). These two axes are the most useful for identifying the principal directions. Axial and tensorial data are obtained in the software's coordinate system. Both type of data can be reoriented in another coordinate system. If R denotes the rotation matrix, both can be reoriented into the geographic coordinate system by the following relations:

$$\begin{pmatrix} v'_{1x} \\ v'_{1y} \\ v'_{1z} \end{pmatrix} = \begin{pmatrix} R_{11} & R_{12} & R_{13} \\ R_{21} & R_{22} & R_{23} \\ R_{31} & R_{32} & R_{33} \end{pmatrix} \begin{pmatrix} v_{1x} \\ v_{1y} \\ v_{1z} \end{pmatrix}$$

$$\begin{pmatrix} M'_{2,0,0} & M'_{1,1,0} & M'_{1,0,1} \\ M'_{1,1,0} & M'_{0,2,0} & M'_{0,1,1} \\ M'_{1,0,1} & M'_{0,1,1} & M'_{0,0,2} \end{pmatrix} = \begin{pmatrix} R_{11} & R_{12} & R_{13} \\ R_{21} & R_{22} & R_{23} \\ R_{31} & R_{32} & R_{33} \end{pmatrix} \begin{pmatrix} M_{2,0,0} & M_{1,1,0} & M_{1,0,1} \\ M_{1,1,0} & M_{0,2,0} & M_{0,1,1} \\ M_{1,0,1} & M_{0,1,1} & M_{0,0,2} \end{pmatrix} \begin{pmatrix} R_{11} & R_{12} & R_{31} \\ R_{12} & R_{22} & R_{32} \\ R_{13} & R_{23} & R_{33} \end{pmatrix}$$

v'_1 corresponds to the eigenvector components in the new coordinate system. $M'_{m,n,p}$ corresponds to the second-order central moments in the new coordinate system. In this thesis, we are dealing with axial data (AMS, shape fabric, crystallographic fabric) which do not have a sense as opposed to vector or polar data. The directions of axial data are thus classically represented in hemisphere stereographic projections or Schmidt net (Schmidt, 1925). We use the equal area and lower-hemisphere projection. All the results concerning shape fabric will be plot using contouring method available in the OpenStereo software (Grohmann and Campanha, 2010). For contouring purposes, a grid of equally spaced nodes is used. The software employs an exponential weighting function based on a Fisher distribution (Fisher, 1953) with a node spacing of 2.5° and a K parameter of 100 which approximate a 1% counting area and is recommended for large datasets (Robin and Jowett, 1986; Jowett and Robin, 1988). In this case and as explained by the software's user manual, the angular distance between a point and every node of the grid is exponentially smoothed using a Fisher distribution. The result gives smooth density contours to the stereographic representation that are well-suited to the interpretation of the main directional features of a dataset (***Figure 3.8***). The obtained density values correspond to the percentage of points occurring per percentage area of the stereonet.

The directional data of a mean tensor (fabric ellipsoid) are also represented in equal area and lower-hemisphere projection. The three principal directions and their confidence ellipses are obtained according to the method of Jelínek and Kropáček (1978) and are classically represented as in ***Figure 3.8***.

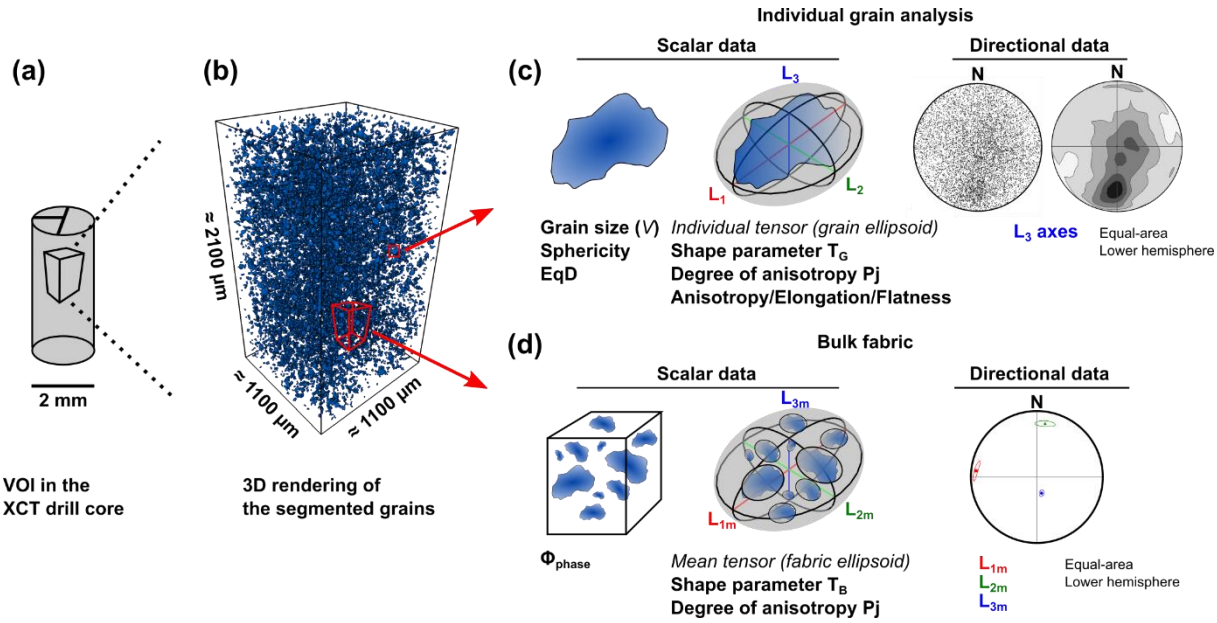

Figure 3.8: ***Illustration of the two strategies to determine the shape fabric. (a) Selection of the volume of interest (VOI) inside the XCT dataset. (b) 3D rendering of the segmented grains. (c) Individual grain analysis. The size of the grain corresponds to the total number of its voxels times the voxel volume, the individual tensor is the equivalent ellipsoid of the grain and can be described with parameters*** T_G ***and*** P_j***. The directional data correspond to the representation of the axes direction of each grain (here the*** L_3 ***axis) in equal area and lower hemisphere projection. It can be simplified by a density contouring diagram with a Fisher distribution counting method. (d) Bulk fabric analysis. The volume fraction of the phase of interest in a given box corresponds to the cumulative volume of the quartz grains in the box divided by the volume of the box (*** Φ_{phase}***). The mean tensor is calculated based on all the individual tensors embedded in the box. The mean tensor is an ellipsoid that can be described with parameters*** T_B ***and*** P_j***. The directional data are the three principal orthogonal directions of the mean tensor and their 95 % confidence ellipses.***

3.5 Estimation of a representative volume

The Representative Elementary Volume (REV) is defined as the minimum volume over which the property of interest no longer varies and that is large enough to capture a representative amount of the heterogeneity (Bear, 1988). Several methods exist to estimate the size of a representative surface or volume and have been reviewed by Cosenza et al. (2019). In this thesis, we applied the box-counting method (Kameda et al., 2006; Klaver et al., 2012; Houben et al., 2013) to monitor the evolution of different fabric parameters throughout the VOI. This method is applied in chapters ***6*** and ***7***. The aim is to evaluate the property of interest in one or several increasing boxes through the whole image. The representative size is reached when fluctuations become negligible and the property remains constant. Eight starting boxes placed at the corners of the VOI were chosen and the dimensions of these boxes were increased to ultimately reach the size of the VOI (***Figure 3.9***). At each given box size, the property of interest is calculated for the eight boxes. Only grains having their centroid inside the box were selected. Two types of parameters were studied (***Figure 3.9***). First, we analyzed morphological features of grains in the individual grain analysis. Secondly, we analyzed bulk fabric parameters such as the phase volume fraction and the $\boldsymbol{T_B}$ and $\boldsymbol{P_j}$ parameters of the mean tensor. Note that in the first boxes sizes, there is no overlap between the eight boxes and they are totally disconnected. After reaching 1/8 of the VOI's size, boxes start to overlap and they are no longer independent. This method allows to determine the representative size for a given property and to assess its variability in the image. In the individual grain analysis, a box size is said representative when the mean of the fraction

does not deviate more than 10% from the value obtained for the whole VOI. In the bulk analysis, we consider that the phase volume fraction is representative when the mean of the eight boxes does not deviate more than 10% from the value of the whole VOI. This threshold is also used for the degree of anisotropy of the fabric ellipsoids. For the shape parameter of the fabric ellipsoids, the mean of the eight boxes should be lower than 10% of the maximum value (i.e. ±0.1) to determine a representative size.

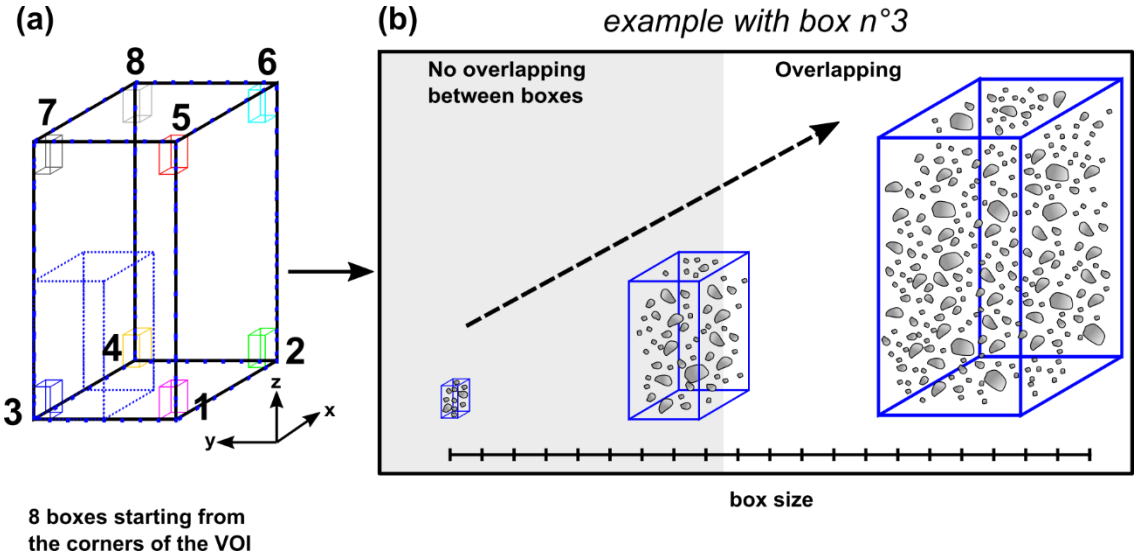

Figure 3.9: ***Box-counting method principle to evaluate a representative size. (a) Schematic representation of the Volume of Interest (VOI) with the initial positions of the 8 boxes. (b) The dimensions of the eight boxes are increased until they reach the VOI size. Here an example with the third box. At each given box size, the fabric parameters are calculated for the eight boxes.***

3.6 Identifying localized subfabrics by subvolume analysis

In addition, we can evaluate and quantify microfabric heterogeneities of a specific phase by looking at smaller volume inside the VOI. We chose to split the volume of interest into eight subvolumes or twenty-seven subvolumes (***Figure 3.10***). We applied the bulk fabric analysis (using mean tensor calculation of section ***3.4.4.3***, equation ***3.3***) to each subvolume of the VOI. The mean tensor is computed by using the centroids of all the grains embedded in the considered subvolume. Then, scalar data and directional data of the mean tensor are analyzed. This permits to split the volume of interest into different and independent "fabric windows" and to gain insight in localized subfabrics of grains in the sample.

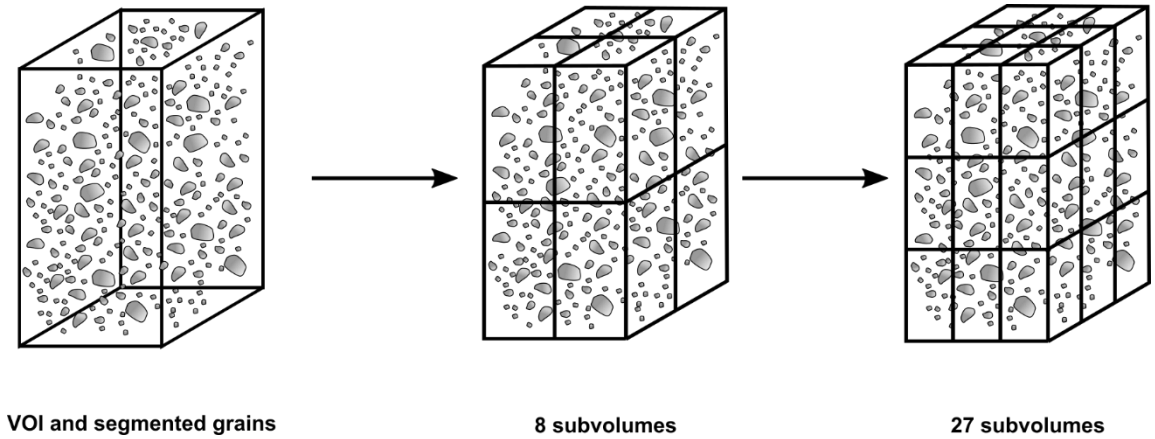

Figure 3.10: ***Schematic representation of the VOI subdivision into 8 and 27 independent subvolumes for subfabric analysis.***

3.7 Spatial distribution of grains and finite strain estimation in shales

3.7.1 Generalities

Several method have been used to estimate finite strain is shales or siltstones. Examples include the analysis of pressure shadows around rigid grains of pyrite (Beutner and Diegel, 1985; Gray, 1997; Hirt et al., 2000) or the analysis of deformed fossils such as brachiopods, crinoid ossicles and graptolites (Engelder and Engelder, 1977; Wright and Platt, 1982; Goldstein et al., 1998; Sak et al., 2012). A well-known method of strain determination in rocks using the spatial distribution of rigid elements embedded in a rock matrix has been developed by Fry (1979). This method can be applied in shales or in slates (Hirt et al., 2000) and is well suited if the spatial distribution of grains before deformation was isotropic and anti-clustered. The goal is to use the pairwise distances and locations for each pair of grain to obtain an ellipsoid that is similar to the strain ellipsoid. Generally, it yields an elliptical vacancy in the center of the so-called Fry diagram. Ailleres and Champenois (1994); Ailleres et al. (1995) have used the covariance matrix to fit the pixels located in the vacancy of a two-dimensional Fry diagram. In our three-dimensional case, we tried to fit the general distribution of the neighbors of grains by an ellipsoid, not the central vacancy. The centroids of each grain are used. Two methods to fit the spatial distribution of points were tested on MATLAB after the computation of the pairwise distance of a dataset. The first one uses the *Ellipsoid fit* function of **Yury** (**https://www.mathworks.com/matlabcentral/fileexchange/24693-ellipsoid-fit**) and the second one employs the covariance matrix of the distribution to build an inertia ellipsoid. After several tests on simulated point distributions, the first method appears to overestimate the strain ratio calculated from the length of the axes of the "pseudo" strain ellipsoid. This first method (i.e. *Ellipsoid fit* function) approximates a 3D set of points by an ellipsoid if their distribution is close to such as surface, this can be an alternative way to define a best-fit ellipsoid for each segmented grain using the surface voxels of the particle for example. For our distribution analysis, we employed the covariance matrix to get the ellipsoid (denoted as the distribution ellipsoid) of the spatial distribution. The 3D covariance matrix of a set of neighboring centroids relative to each centroid in the same coordinate system (similar to a 2D Fry diagram) is expressed as:

$$\begin{pmatrix} \sum x^2 & \sum xy & \sum xz \\ \sum xy & \sum y^2 & \sum yz \\ \sum xz & \sum yz & \sum z^2 \end{pmatrix}$$

Where x, y and z denote the direction cosines of the axis between the centroids of two grains and the summation sign runs over the pair of grains. Here again, the eigen solution of this covariance matrix can be represented as an ellipsoid with eigenvalues and eigenvectors. The scalar data (eigenvalues $E_1 \geq E_2 \geq E_3$) can be used in a Jelinek plot ($\boldsymbol{T_S}$ and $\boldsymbol{P_j}$) and the directional data (eigenvectors $\boldsymbol{E_1}$, $\boldsymbol{E_2}$ and $\boldsymbol{E_3}$) can be plotted in a stereonet. If the shape parameter $\boldsymbol{T_S} = +1$, the grains are disposed in planar structures. If the shape parameter $\boldsymbol{T_S} = -1$, the grains are disposed along lines. The degree of anisotropy $\boldsymbol{P_j}$ provides a quantification of the intensity of this spatial distribution. The semi-axes $a \geq b \geq c$ of the distribution ellipsoid are given by the square roots of the eigenvalues.

The use of the covariance matrix with an isotropic and anti-clustered distribution in pure shear and simple shear is provided in ***Figure 3.11***. In this figure, we show the spatial distribution in a plane strain case (i.e. no volume change). The obtained axial ratios (a/c) of the ellipsoids are equal in a non-plane strain case.

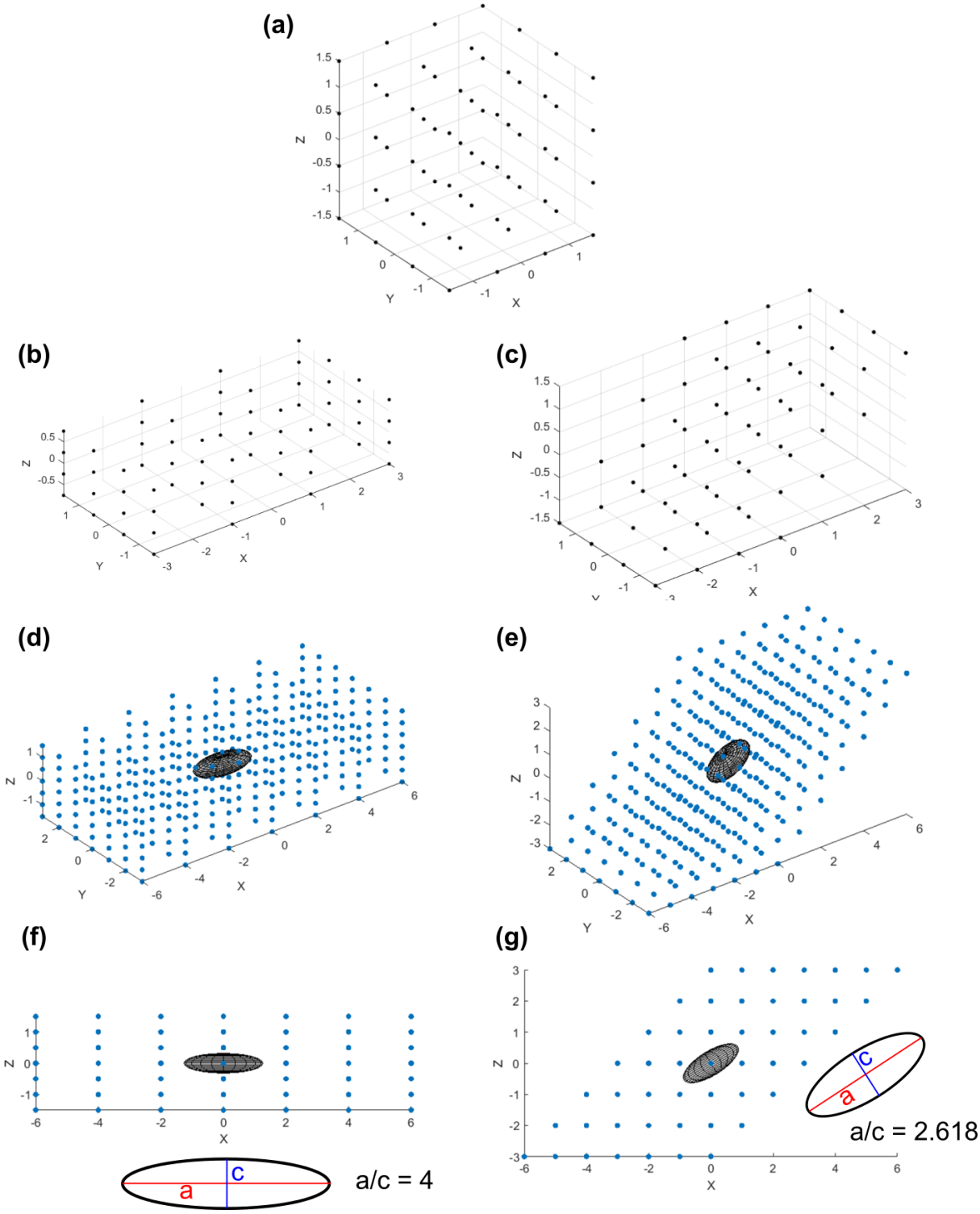

Figure 3.11: ***Simulated pure and simple shear, in plane strain (i.e. no volume change) of an isotropic and anti-clustered 3D point pattern (the points simulate the centroids of grains). The ellipsoid determined by the covariance matrix transcripts the distribution of the centroids. (a) Initial centroids distribution. (b) Pure shear of 50% along z-axis. (c) Simple shear:*** $\gamma = 1$***. (d) Resulting diagram of the location of the neighboring centroids relative to each***

centroid for pure shear with the associated distribution ellipsoid. (e) Resulting diagram of the location of the neighboring centroids relative to each centroid for simple shear with the associated distribution ellipsoid. (f) xz view of the diagram in (d). (g) xz view of the diagram in (e).

3.7.2 Spatial distribution of grains in natural samples

The 3D distribution anisotropy of magnetite grains extracted from XCT in natural samples has been studied by Schöpa et al. (2015) as interactions between magnetites are known to contribute to the anisotropy of magnetic susceptibility (AMS) signal (Stephenson, 1994; Grégoire et al., 1998). In our case, we focus more on dispersed rigid grains of quartz, as they can be a good strain indicator in shales or siltstones (Sak et al., 2012; Morley et al., 2017). First, we had to take into account the edge effect and the slightly elongated shape of the VOI (hexahedral shape) which could disturb the result of the spatial distribution analysis. Thus, we have developed a MATLAB routine[2] in which the nearest neighbors of each grain are those which are in the largest sphere which is not in contact with the edges of the VOI and which is centered on the grain centroid of interest. The *rangesearch* function of MATLAB is well suited to define a finite radius for searching neighbors but we have used a combination of *pdist2* and *find* functions to reduce the computation time. In addition, the largest grains tend to be more anticlustered compared to the smallest ones so they are of greater interest. Small grains are mainly influenced by the location of the largest grains and they could be artefacts of the image processing. Therefore, a loop was also implemented to run over different size classes of grains to take into account that small grains may be less reliable and may influence the result. We tried to keep at least 500 to 1000 grains for the robustness of the analysis, especially for the last size class (composed of the largest grains). A representation of how this method works is given in ***Figure 3.12*** for a natural turbiditic sample. Because for each of the size classes there is always variability in grain size, we have normalized the distances. We normalized the distance for each pair of grains by a sphere having an equivalent volume as the grain's ellipsoid in a similar manner as proposed by Erslev (1988) for 2D images. This method takes into account the size homogeneity of grains (the sorting) in the nearest neighbor analysis. In 3D, this normalized distance is expressed as:

$$D'_{1-2} = \frac{D_{1-2}}{\sqrt[3]{a_1 b_1 c_1} + \sqrt[3]{a_2 b_2 c_2}}$$

D_{1-2} and D'_{1-2} are the Euclidean and normalized distances (between a centroid 1 and centroid 2), respectively. The parameters a, b and c are the semi-axes of the grain ellipsoid, which have been defined in section ***3.4.4.2***.

[2] Other scripts have been implemented using the Delaunay triangulation or the largest sphere inscribed in the VOI for the nearest neighbor analysis. However, we present only the methodology that was used to obtain our results in this manuscript.

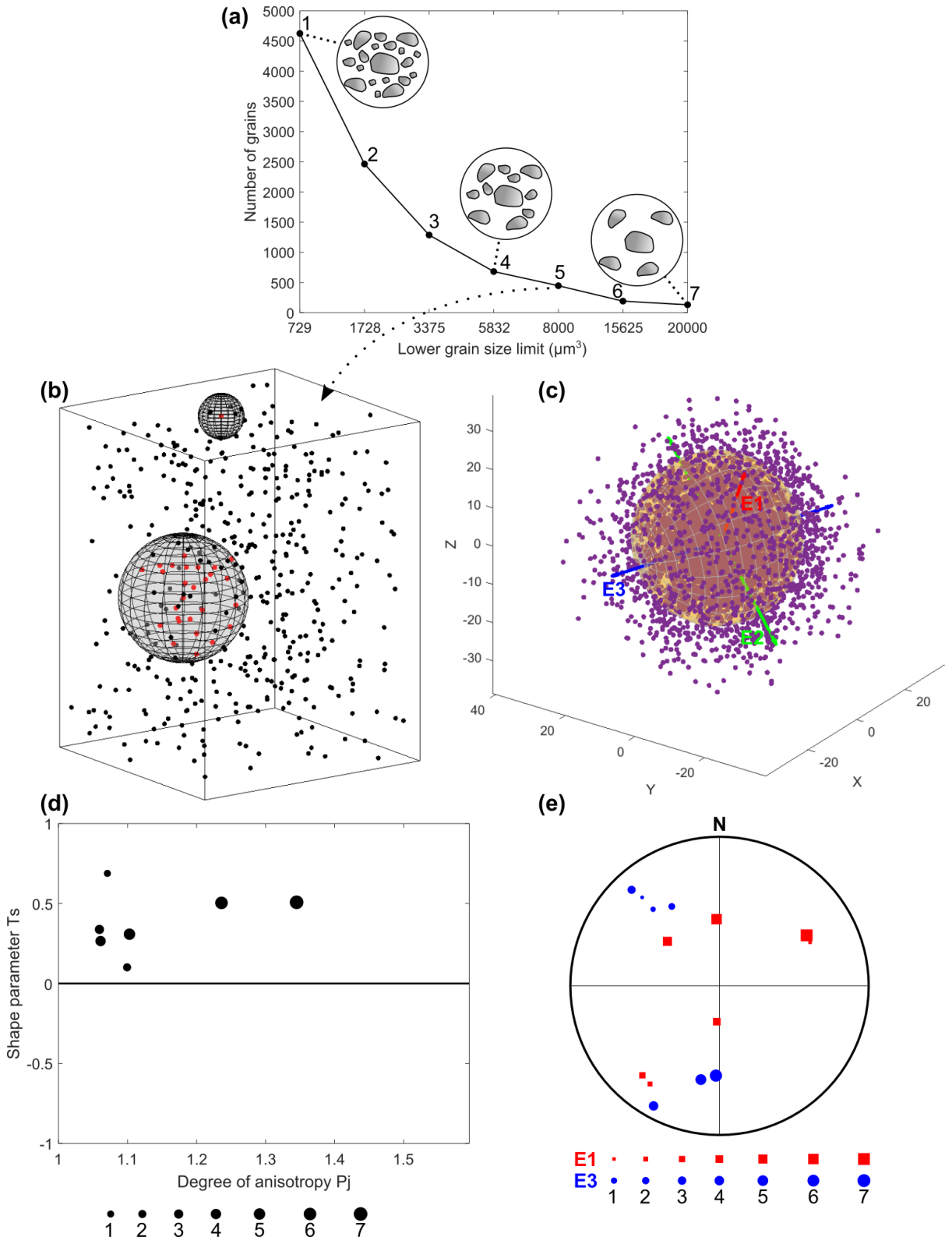

Figure 3.12: *Spatial distribution method. (a) The spatial distribution is evaluated for each grain size class, here there are seven classes and the corresponding number of grains. The number of grains corresponds to the grains which have at least one neighbor. (b) 3D view of the centroids corresponding to the class 5 of the graph in (a). Illustration of the use of the rangesearch function to take into account the edges of the VOI. (c) 3D view of the location of the neighboring centroids relative to each centroid and the corresponding distribution ellipsoid with its three perpendicular axes and eigenvalues ($E_1 \geq E_2 \geq E_3$). (d) Scalar parameters of the seven distribution ellipsoids in a Jelinek diagram. (e) Directional data (principal directions E_1 and E_3) of the seven distribution ellipsoids.*

3.8 Voxelized image and simulation

3.8.1 Introduction

We employ the Cast3M software developed by the CEA to simulate mechanically the 3D deformation of grains in a ductile matrix. The goal is to simulate the elastic response of a system with grains embedded in a weaker matrix using true elastic parameters a plastic deformation of rigid grains in a ductile matrix. With an elasticity problem, we desire to evaluate the change in the spatial distribution of grain and their shape fabric. The mesh is built as a 3D XCT image so the elements are hexahedral (cubes) that are comparable to each unit voxel[3]. Then a voxel can belong to the clay matrix phase ("soft" phase) or to a particle/grain ("hard" phase such as quartz or pyrite). We assume an isotropic elastic behavior for both phases. We use Cast3M to get the displacement field of all rigid particles. The software resolves the linear elasticity problem according to Hook's law that relates the strain tensor to the stress tensor (both second-order symmetric tensors) by the fourth-order stiffness tensor. Then, using a MATLAB script, we import the displacements and we analyze the results. I built the MATLAB script based on the *regionprops3* function with additional personal implementations.

3.8.2 Description of the methodology

The methodology presented therein can work by starting from either the real 3D segmented image or a synthetic 3D image by simplification of the main features of the real image. The main steps are summarized in ***Figure 3.13***.

Here, the methodology starting from a synthetic image is presented. The first step is to build a synthetic binary image with two phases using MATLAB. Voxels labelled as 0 correspond to the clay matrix and voxels labelled as 1 correspond to the rigid grains (quartz or pyrite). The shape of the silt-sized grains is derived from the data of the three orthogonal semi-axes (a, b and c) of their equivalent ellipsoid. Thus, the grains are represented as pseudo ellipsoids made of cubic elements according to the voxel resolution of the real image. The initial parameters correspond to the geometry of the constituents: size, shape and orientation. Their spatial distribution along the z-axis is also derived from the data of the real image. As we wish to carry out the simulations within a reasonable amount of time, we cannot study the entire VOI (≈3 mm^3 with around 1200^3 or 725^3 voxels). However, the population of silt grains in this mesh is intended to be representative of the one at the scale of the VOI. Note that we present the methodology for a two-phase mesh but the methodology can easily work for a multi-phase microstructure.

After exporting the binary text file from MATLAB, we input this file in Cast3M. The mechanical parameters of the constituents are Young's modulus, Poisson's ratio and density to each phase. After having given the boundary conditions, we apply a given deformation to the mesh. The voxel displacement field is obtained by the difference between the position of the deformed centroids of each voxel and that of the respective initial centroids. All the displacements values along x, y and z are exported as .inp file to reintroduce the displacement values in the binary image in MATLAB.

[3] Initial attempt has been done using a tetrahedral mesh after the building of a triangular isosurface on the segmented grains in Avizo®, however this resulted in too large data.

In MATLAB, the displacement field is used to deform the initial synthetic image. We use the *scatteredInterpolant* function of MATLAB to perform this step. Both the initial and deformed image can be exported as a tiff stack in order to read it in another software such as Avizo or Fiji.

Post-processing of the results is done by using our own script based on the *regionprops3* function. In case of connected grains, a *watershed* transform or a *bwconncomp* (6-connectivity separation) module from the MATLAB image processing toolbox can be applied to separate the grains before using the function. The post-processing includes plotting of scalar and directional data as well as other shape parameters of the deformed ellipsoids. In addition, the mean neighbor distance and an ellipsoid that fit the spatial distribution can be computed.

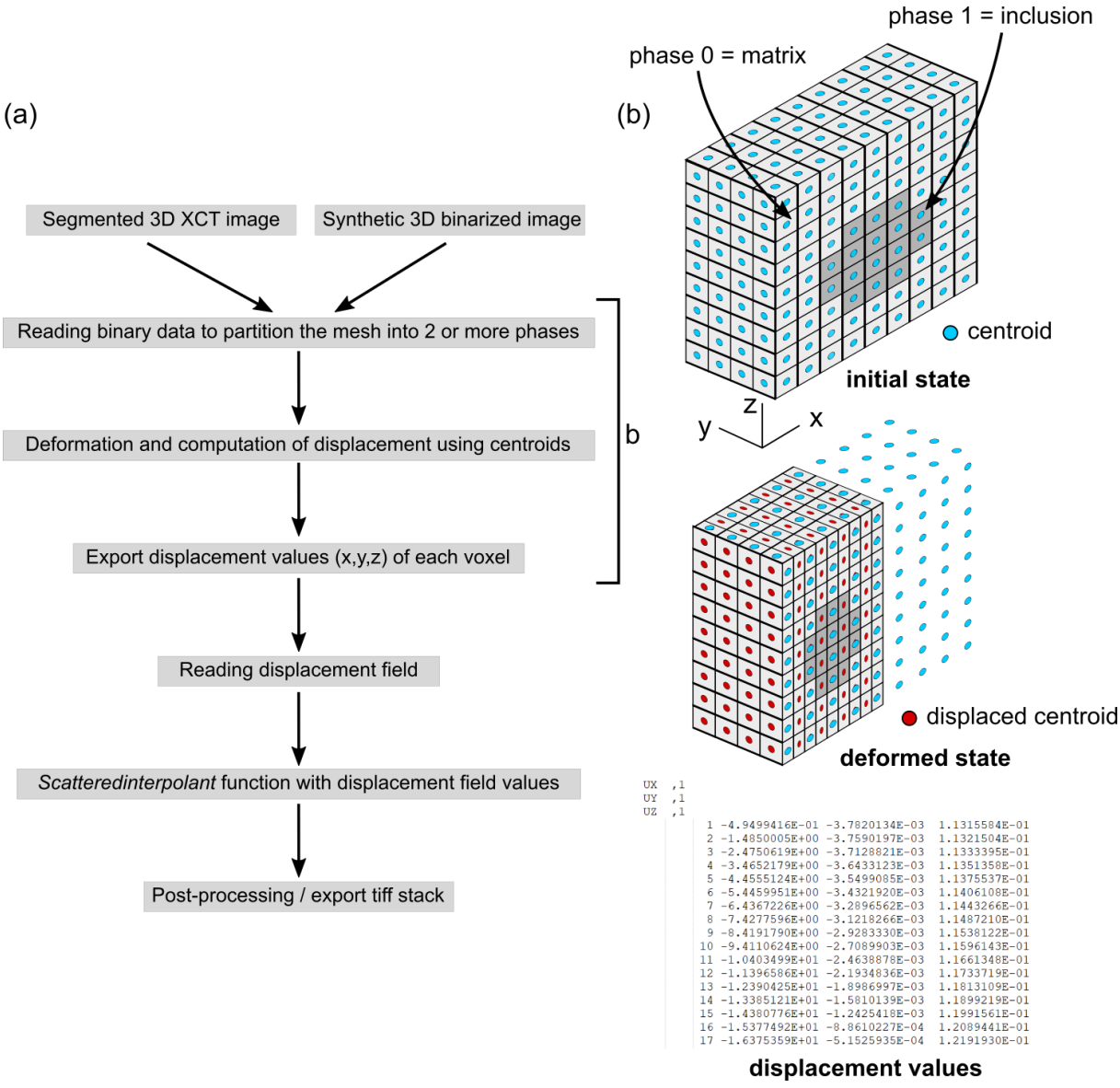

Figure 3.13: *(a) Workflow of the simulation combining MATLAB and Cast3M. (b) Schematic representation of the deformation of cubic elements in Cast3M.*

3.9 EDS – XCT combination

Energy dispersive X-ray spectroscopy (EDS) enables acquiring a chemical or elemental map at nanometer resolution of the elements from Li to U situated on the analyzed surface. Associated with

SEM devices, an EDS detector uses X-rays generated by the interaction of an electron beam with a sample to characterize the elemental composition (Goldstein et al., 2018). Because of its accessibility and simplicity, we chose to use EDS to supplement information from lab-based X-ray absorption-contrast images. However, we should note that this approach is destructive.

In this thesis, we have used EDS in a qualitative approach to identify the major constituents of the calcareous shale samples of Sigüés. A grid of scanning electron microscopy (SEM) and energy-dispersive X-ray spectroscopy (EDS) images is acquired to compose a chemical map of a plane surface obtained after the core has been polished in the longitudinal direction (***Figure 3.14***). SEM-EDS data acquisition is performed at the Raimond Castaing Microanalysis Centre (Toulouse, France). SEM images are collected as backscattered electrons (BSE) with a JEOL JSM-7800F Prime equipped with a Silicon Drift Detector from Oxford Instruments to generate the EDS images. The acceleration voltage used for our study is 10 kV. One EDS map is obtained for each detected chemical element. Two samples (A1 and A2) have been characterized to identify major constituents of the rock. SEM images are not used in this work because they are redundant with the X-ray dataset.

Registration of the EDS images and the XCT volume is done in order to propagate chemical identification given by EDS images into the whole XCT volume. First, the registration of the initial XCT image with the final XCT image after polishing is performed. This operation is essential to precisely locate the surface analyzed by EDS inside the initial XCT volume. The Mutual Information method from Avizo® is used to register these XCT datasets and the plane that corresponds to the polished surface is extracted from the initial XCT volume. This plane and the EDS image are not strictly superimposable because they are not exactly parallel, nor do they have the same resolution. Furthermore, the EDS image integrates information over a thickness of several microns. Therefore, we fine-tune the registration based on landmarks (i.e. characteristic features in the image).

Four out of five grayscale XCT phases can be directly associated to a mineral, namely quartz, clayey matrix, calcite and pyrite for phases two to five, respectively. Light elements cannot be detected by EDS, and therefore phase 1 (lowest X-ray attenuation) can be associated with the air-filled pores of the material. This procedure enables propagating the chemical information from 2D EDS maps to the entire XCT volume and to subsequently perform a shape fabric analysis of each phase.

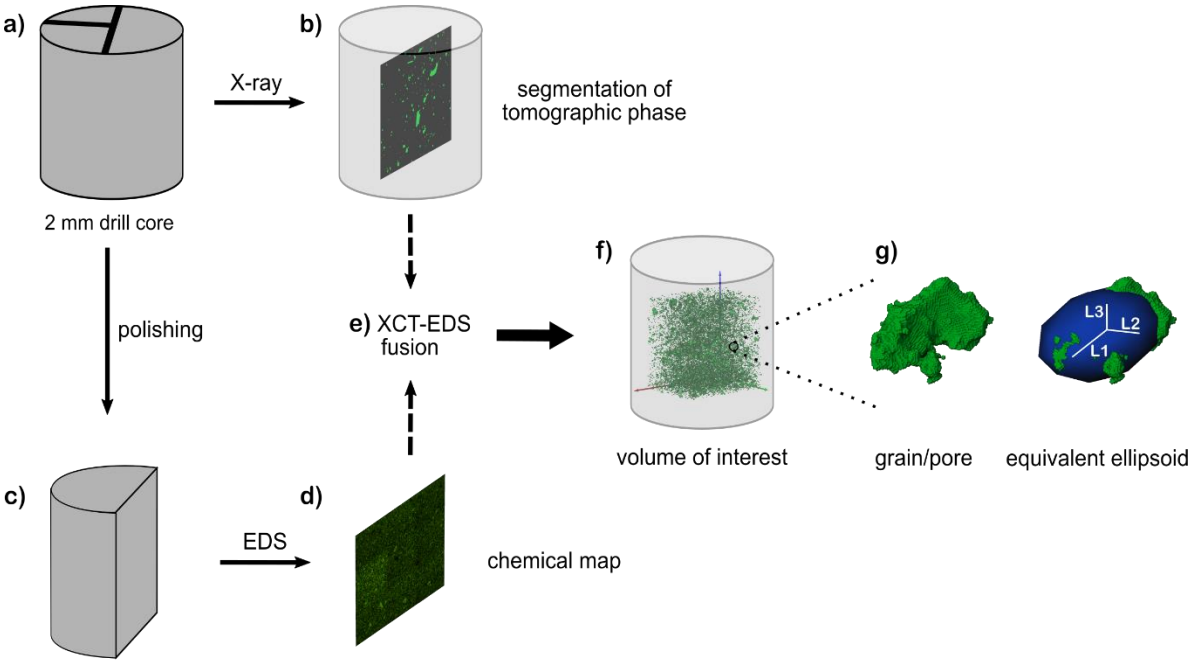

Figure 3.14: ***Workflow of XCT-EDS combination method used in this study. (a) Drill core extracted from field sample with indication of the generatrix ('T' shaped marker on the top) measured in the field. (b) XCT acquisition followed by image processing to isolate phases of interest. (c) Drill core polishing for EDS analysis. (d) Chemical map obtained on the polished surface. (e) Data fusion corresponds to the registration of the XCT volume and the EDS map. (f) Selection of a VOI inside the XCT volume, each segmented tomographic phase is chemically identified. (g) Each grain or pore space in the VOI is approximated by an equivalent ellipsoid for shape fabric analysis (see Figure 3.8).***

3.10 Texture information from EBSD

Electron backscattered diffraction (EBSD) is a diffraction technique used to obtain elemental maps and the crystallographic preferred orientation of minerals (Adams et al., 1993; Prior et al., 1999, 2009). This technique, which is also destructive, permits to obtain the complete CPO data as opposed to bulk X-ray diffraction techniques from all minerals with a micron or sub-micron spatial resolution (Prior et al., 2009; Peternell et al., 2010; Wenk et al., 2020). The EBSD acquisition for two samples was done by T. Boiron and P. Sénéchal. I did the post-processing of the raw data and the analysis with the HKL Channel 5 software.

Samples A2 and A5 were studied by the EBSD technique. First, they were polished along the generatrix plane marked on the XCT drill core. Data were acquired at the Raimond Castaing Microanalysis Centre. We used a FEG-SEM JSM-7100TTLS LV SEM equipped with an EBSD AZtec HKL detector. The main limitation of EBSD with fine-grained rocks is due to the poor indexation of clays because of their low crystallinity (Valcke et al., 2006; Prior et al., 2009). Other minerals such as quartz and calcite are rather well indexed. The total area mapped were 1112 x 275 μm^2 for A2 and 688.5 x 294.5 μm^2 for A5 with a step of 0.5 µm (***Figure supp 1***). The data were then processed using HKL Channel 5 software. We performed a noise reduction to remove non-indexed or badly indexed pixels. The resulting indexation rate was about 45%.

3.11 Magnetic fabric from AMS

Low-field AMS measurements (976 Hz with an applied field of 200 A/m) were done at room temperature using a MFK1-FA Kappabridge (Pokorný et al., 2011) coupled with the *Safyr6* software (Studýnka et al., 2014) and performed on standard cylindrical samples (2.54 cm diameter and ≈10-11 cm^3). The magnetic susceptibly tensor was obtained from 15 directional susceptibility measurements towards the rock sample according to Jelínek (1977) because the 3D rotator (Studýnka et al., 2014) was not available at the time of the measurements. Post-processing was done using the *Anisoft5* software (Chadima and Jelínek, 2008) that provides the principal directions of the magnetic susceptibility ellipsoid $\boldsymbol{K_1}$, $\boldsymbol{K_2}$, $\boldsymbol{K_3}$ and their confidence regions in geographic coordinate system as well as the mean susceptibility, the shape parameter $\boldsymbol{T}$ and the corrected degree of anisotropy $\boldsymbol{P_j}$. For each sampling site or a given group of AMS specimen, a mean tensor can be computed by the method of Jelínek and Kropáček (1978). The mean tensor and its confidence ellipses are determined by summing the normalized tensors and computing the variance-covariance matrix (Jelínek and Kropáček, 1978; Hrouda, 2007).

3.12 Overview of samples used in this thesis

A brief summary of the samples used in this thesis as well as the main techniques employed is provided in the tables below.

***Table 3.1:** Samples taken in the Sigüés area (Jaca basin, Roncal Valley, southern Pyrenees, Spain).*

	A1	A2	A3	A4	A5	A1-2	A2-2	A3-2	A4-2	A5-2	A4-HR
Rock type	Calcareous shale (marl)										
XCT drill core diameter (mm)	2.80	1.90	1.75	1.84	1.90	1.85	1.71	1.85	1.71	1.88	0.62
XCT image	☑	☑	☑	☑	☑	☑	☑	☑	☑	☑	☑
XCT voxel resolution (µm)	1.5	1.3	1	1.2	1.2	1.2	1.2	1.2	1.2	1.2	0.5
SEM-EDS	☑	☑									
EBSD		☑			☑						
Published magnetic data	☑	☑	☑	☑	☑	☑	☑	☑	☑	☑	☑
Involved in chapter(s)	4	4	4	4 and 6	4	4	4	4	4 and 6	4	4

***Table 3.2:** Samples taken in the Lehigh Gap area (Lehigh County, Pennsylvania, United States).*

	LH3	LH4	LH6	LH7
Rock type	Siltstone	Siltstone	Siltstone	Coarse siltstone
XCT drill core diameter (mm)	1.78	1.76	1.75	1.82
XCT image	☑	☑	☑	☑

XCT voxel resolution (µm)	2	2	2	2
Published magnetic data	☑	☑	☑	☑
Involved in chapter(s)	5			

Table 3.3: ***Samples taken in the West Burgui site 2T (Jaca basin, Roncal Valley, southern Pyrenees, Spain).***

	2T7A	**2T8B**	**2T8B-HR**	**2T12B**	**2T14B**	**2T16B**	**2T18B**
Rock type	Carbonate turbidites						
XCT drill core diameter (mm)	1.69	1.62	1.14	1.92	1.86	1.72	1.71
XCT image	☑	☑	☑	☑	☑	☑	☑
XCT voxel resolution (µm)	2	2	1.5	2	2	2	2
AMS measurements	☑	☑	☑	☑	☑	☑	☑
Involved in chapter(s)	7						

Table 3.4: ***Samples taken in the North Roncal site 1T (Jaca basin, Roncal Valley, southern Pyrenees, Spain).***

	1T1A	**1T4C**	**1T5A**	**1T7B**	**1T17**	**1T11B**	**1T13**	**1T15A**
Rock type	Carbonate turbidites/siltstones					Fine to medium sandstones		
XCT drill core diameter (mm)	1.75	1.61	1.66	1.73	1.63	4.66	4.88	4.86
XCT image	☑	☑	☑	☑	☑	☑	☑	☑
XCT voxel resolution (µm)	2	1.7	1.75	1.2	1.8	3.95	3	3.95
AMS measurements	☑	☑	☑	☑	☑	☑	☑	☑
Involved in chapter(s)	7							

4 Sigüés: characterization of calcite and quartz fabrics in calcareous shales along a natural strain gradient

4.1 Aims

Here we propose a novel methodology to study the shape fabric of common shale-bearing minerals (calcite, pyrite and quartz), but also pore space, in three dimensions by combining of XCT and EDS (see methodology presented in section ***3.9***). The proposed method is than applied to study deformed shales from the South Pyrenean foreland. Results demonstrate that the shape fabric of quartz and calcite exhibit a contrasting evolution along a km-long strain gradient. The results obtained from the millimeter-sized samples is consistent with the macroscopic observations. The measurement is repeated on a set of 5 new samples to evaluate the robustness of our data. The purpose of this work is however not to go through details about the geological setting but more to emphasize the usefulness of the method that can be applied on fine-grained rocks in various geological contexts.

4.2 Geological setting and samples

The Jaca basin is a piggyback basin of the South Pyrenean foreland, incorporated in the Pyrenean Orogeny from the Eocene to the Early Miocene (Labaume et al., 1985; Hogan and Burbank, 1996; Izquierdo-Llavall et al., 2013; Crognier et al., 2018). The Jaca basin is filled with tertiary deposits localized between the south Pyrenean front and the axial zone (***Figure 4.1*****a**). The Northern part of the Jaca Basin is made up of the Hecho turbiditic group (***Figure 4.1*****b**). The Sierra de Leyre (***Figure 4.1*****b**) bounds the southern part of the Hecho group. We focus on the Hecho Marls or Arro-Fiscal Formation (Eocene), which outcrop near the Sigüés locality (***Figure 4.1*****c** and ***Figure 4.1*****d**), and more precisely on the footwall of a steep thrust, which delineates the southern anticline of the Sierra de Leyre. The bedding (S0) of Hecho marls is sub-horizontal (***Figure 4.2*****a**), except at few meters from the emerged thrust, where footwall syncline developed, marked by overturned bedding dipping to the North (***Figure 4.2*****e**).

In this study, we observed a strain gradient associated to cleavage development (S1) north of Sigüés, correlated to the distance from the thrust. Cleavage develops as axial planes parallel to the major folds axes (mostly oriented N100) but damage is induced by thrust propagation. At ~2 km south from the emerged thrust, there is no cleavage, and shales are only affected by a fracture network (Crognier et al., 2018). We refer to this type of petrofabric, corresponding to a low strain area, as “cleavage-free” throughout the text. In this domain, bedding has a dip of 15° towards the South (***Figure 4.2*****a**). In the range ~1 km-0.5 km from the thrust, a pencil cleavage develops, dipping to the North and oblique to the bedding. The spacing between cleavage planes is metric at ~1 km and evolves gradually to millimetric at ~0.5 km. We refer to this petrofabric, corresponding to an intermediate strain area, as “pencil-cleavage”. In this study, the bedding is still well observed in the pencil-cleavage domain (***Figure 4.2*****b** and ***Figure 4.2*****c**). The dip of the bedding is 10° towards the South. At a distance below 0.5 km from the thrust, the cleavage intensity increases and the cleavage spacing becomes infra millimetric. We refer to this petrofabric, corresponding to a high strain area, as “slaty-cleavage”. Here cleavage is strongly oblique to a horizontal bedding (***Figure 4.2*****d**). Continuing towards the North, the bedding is now barely detectable and the change between sub-horizontal to overturned beds is difficult to observe near the thrust. The slaty cleavage, strongly dipping to the North, superimposes the bedding

that has a dip of 60° towards the North forming a transposition structure (***Figure 4.2e***). This is the slaty-cleavage domain where cleavage and bedding are nearly parallel due to high strain. The Sigüés site exhibits therefore an exceptional exposure where it is possible to monitor, meter by meter, the evolution of a fine-grained sedimentary matrix in response to cleavage development.

In this study, five AMS drill cores of calcareous shale (A1, A2, A3, A4, A5) have been collected from the South to the North, with respectively a cleavage-free petrofabric (A1, 1.95 km from thrust), an incipient pencil-cleavage petrofabric (A2, 0.95 km), a pencil-cleavage petrofabric (A3, 480 m) and two slaty cleavage petrofabrics (150 and 15 m for A4 and A5 respectively). For the A4 sample, the bedding is sub-horizontal, superimposed by a steep cleavage. For the A5 sample, located near the thrust in the footwall syncline, overturned bedding and cleavage are nearly parallel due to the transposition of the two structures.

The chapter is presented as follows. Firstly, a set of 5 XCT dill cores (A1 to A5) were extracted from the 5 AMS drill cores to perform an individual grain analysis on the XCT images. The results have led to the publication of a paper in the Journal of Structural Geology review. After this work, a second set of five XCT dill cores (A1-2 to A5-2) were extracted from the same AMS drill cores but in another location of the core. Thus, we present in this chapter the results obtained in the individual grain analysis on the XCT images of this second set of samples. After what, we present bulk shape fabric results of the two sets in regards of the bulk magnetic measurements obtained by Boiron et al. (2020). Then, the results of the spatial distribution of quartz grains are provided. Lastly, a comparison between the SPO of calcite and quartz and their CPO measured by means of EBSD technique is proposed for two samples of the first set.

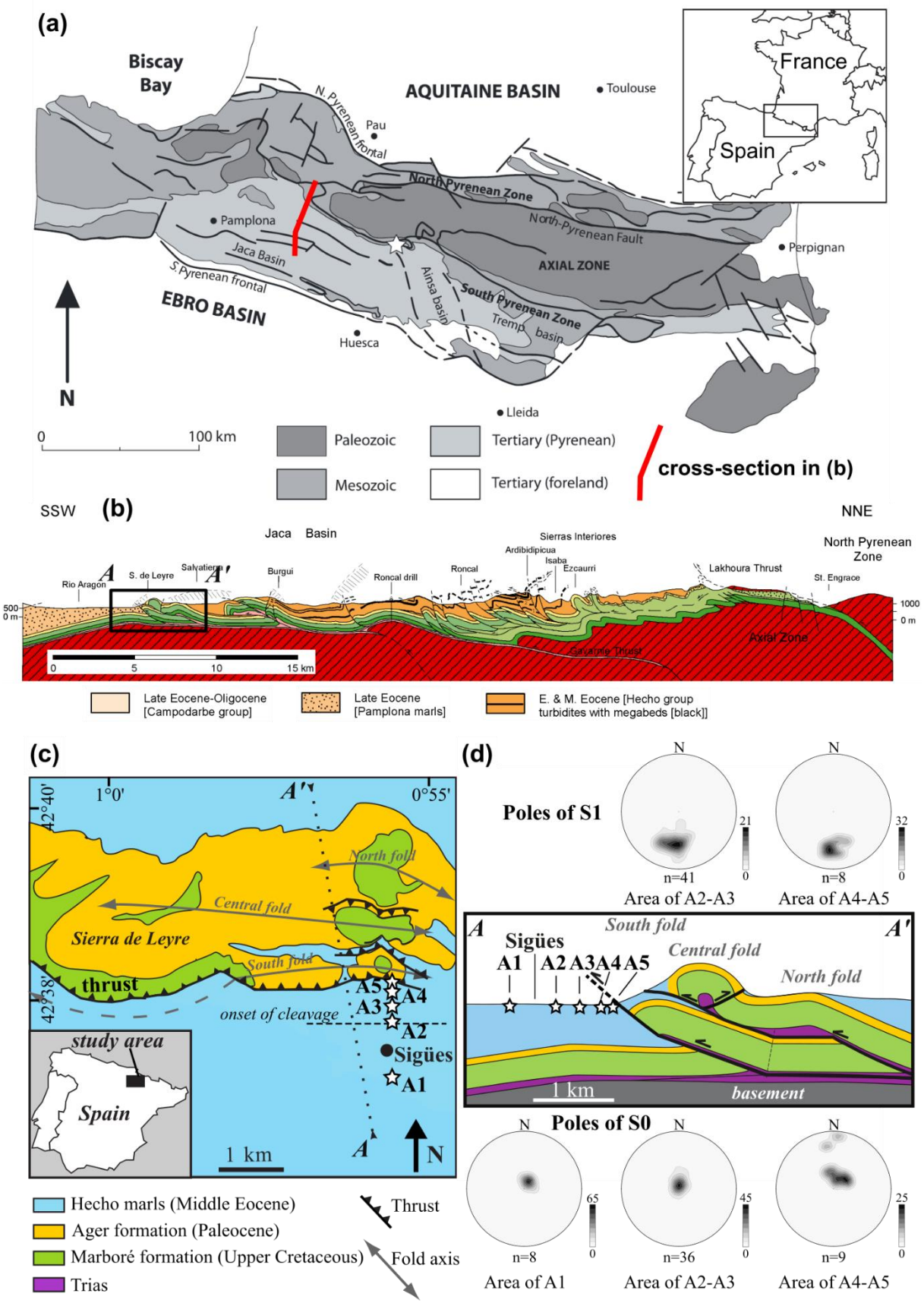

Figure 4.1: *(a) Structural map of the Pyrenees with the location of the cross-section in the Jaca basin, modified from Lacroix et al. (2014, 2015). (b) Cross-section running through the Belagua valley and the Roncal valley. Redrawn by Schellart (2002) after Labaume et al. (1985). The black insert is enlarged in (d). (c) Simplified geological*

map between Sigüés and Salvatierra in the Southern Pyrenees, Spain (adapted from Puigdefábregas (1975)). Sampling locations are indicated on the map. (c) North-south cross-section corresponding to the box in the above cross-section and to the A-A' profile on the geological map (adapted from Labaume et al. (1985)). Projected positions of the samples with respect to the cross-section are indicated. Poles of bedding (S0) and cleavage (S1) measured in the field are reported onto equal area lower hemisphere steroplots using density contouring.

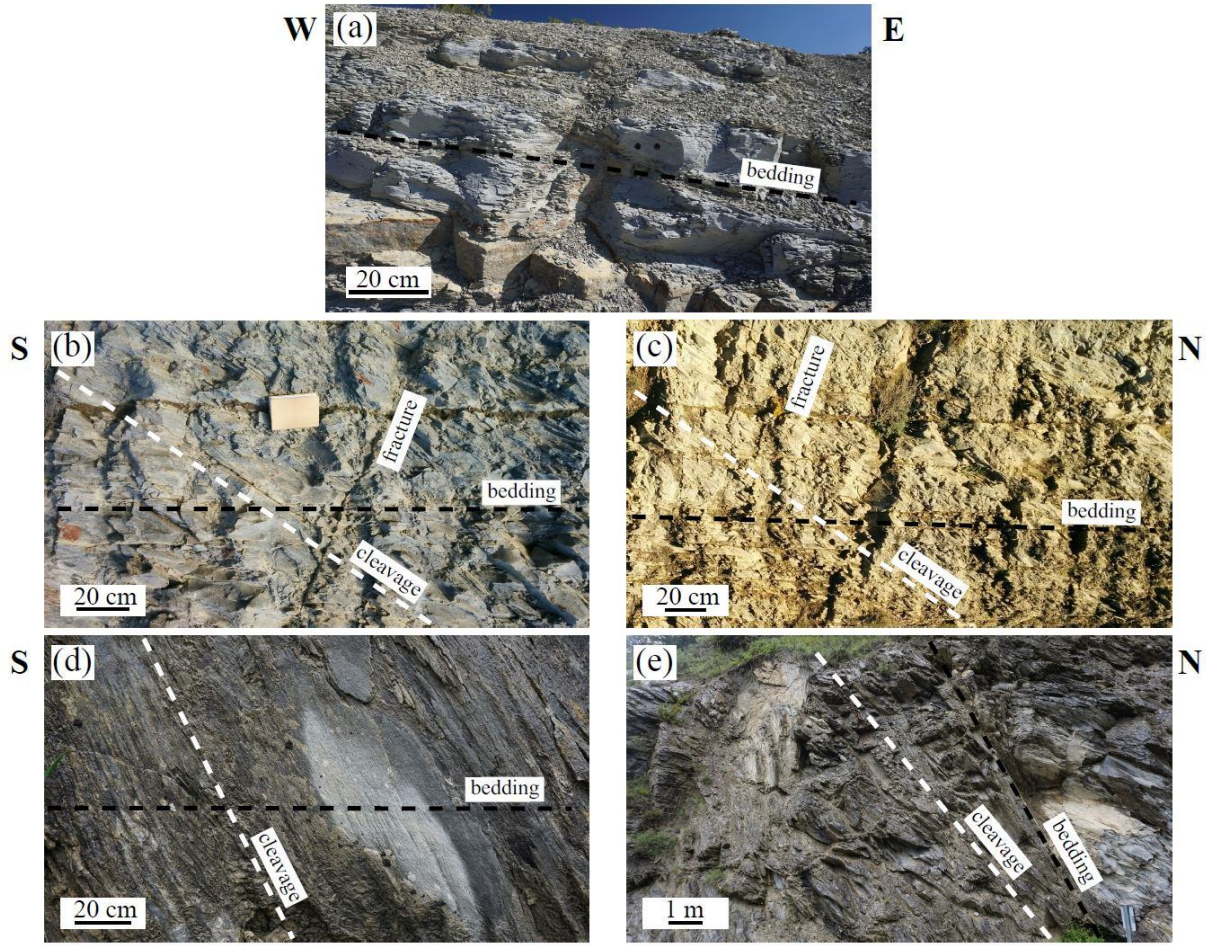

***Figure 4.2:** Outcrop pictures of (a) cleavage-free domain (A1), (b) onset of cleavage (A2), (c) pencil-cleavage domain (A3), (d) slaty-cleavage domain with cleavage oblique to bedding (A4), (e) slaty-cleavage domain with superimposition of cleavage on bedding. Distance from the thrust decreases from (a) to (e).*

4.3 Results

4.3.1 Individual grain analysis: first set of 5 samples (A1 to A5)

4.3.1.1 Distribution of phases

The results concerning quartz, calcite and pores phases are provided in the following lines. The study of the phyllosilicate matrix is discarded because of insufficient XCT resolution and attenuation contrast. The number of objects belonging to each phase (calcite, quartz and pore spaces) and their relative abundance in the volume of interest of the samples are reported in ***Table 4.1***. In this study, objects under 729 µm^3 (corresponding to 216 voxels in A1, 332 voxels in A2, 729 voxels in A3, 422 voxels in A4 and A5) are considered as noise and are discarded. Thus, the volumetric contribution of each phase obtained with XCT underestimates the real quantity present in the samples to some extent. All together, the three phases represent 3.5 to 7.6% of the volume of interest. In comparison, the rock

matrix represents around 92.4 to 96.5%. We thus focus on a small fraction of the rock volume (***Table 4.1***). An example of the results of the segmented phases is provided in ***Figure 4.3*** for the sample A4. The volume distribution of the objects ranges from 729 to about 2 x 10^6 µm^3 for the biggest calcite grains. Nevertheless, among each mineralogical phase (quartz and calcite), around 95% of the studied particles have a size ranging from 729 to 20729 µm^3. The respective distributions, in the five samples, of quartz and calcite ranging from 729 to 20729 µm^3, are represented in ***Figure 4.4*** and show a remarkable similarity.

Table 4.1: ***Volume of interest for each sample. Number and volume fraction of quartz, calcite and pores particles in this volume, obtained after segmentation, cleaning and removal of boundary grains.***

Sample	A1	A2	A3	A4	A5
Volume of interest (mm^3)	6.12	2.10	1.76	2.34	2.15
Number of quartz grains	13,451	5,282	13,109	8,311	7,371
Volume fraction of quartz (1)	1.63 %	1.48 %	2.92 %	2.07 %	1.74 %
Number of calcite grains	15,932	9,950	15,610	13,324	12,938
Volume fraction of calcite (2)	1.82 %	4.27 %	3.17 %	5.35 %	5.04 %
Number of pores	435	277	104	1,500	713
Volume fraction of pores (3)	0.065 %	0.023 %	0.009 %	0.134 %	0.372 %
(1)+(2)+(3)	3.52 %	5.77 %	6.10 %	7.55 %	7.15 %

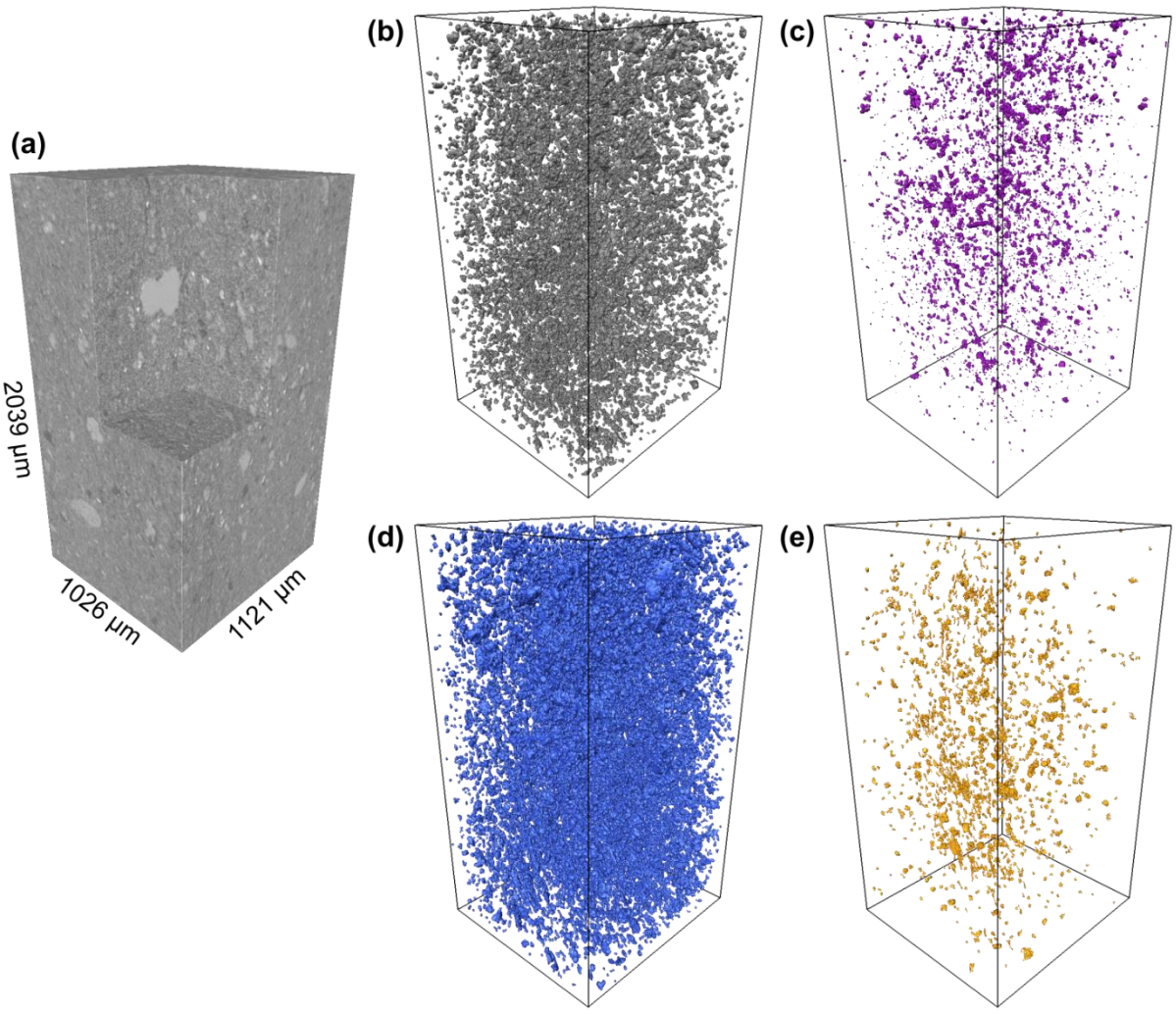

Figure 4.3: *(a) 3D grayscale image of the VOI of sample A4. Note the large calcite made foraminifera in the upper center. (b) Isosurface rendering of the segmented quartz grains. (c) Isosurface rendering of the segmented pyrite grains. (d) Isosurface rendering of the segmented calcite grains. (e) Isosurface rendering of the segmented pore space.*

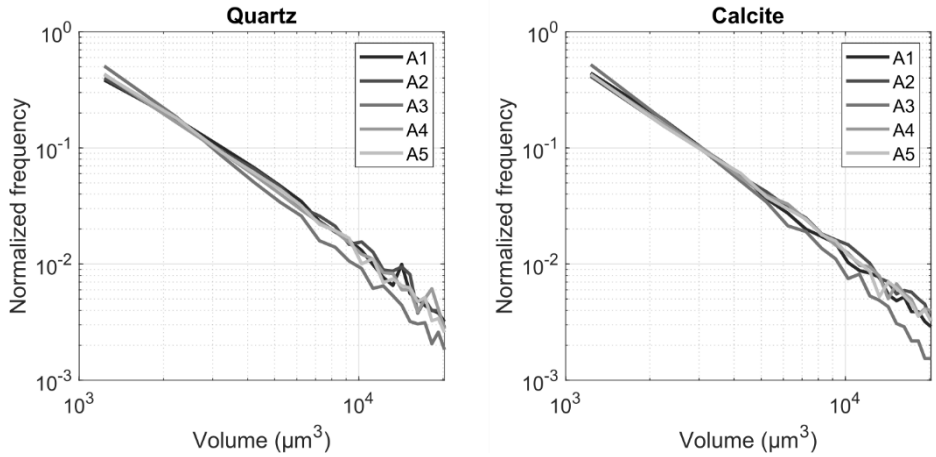

Figure 4.4: *Size distributions of quartz and calcite in the five samples (A1 to A5).*

4.3.1.2 Description of the XCT images

Figure 4.5 presents a vertical north-south cross section through each sample, illustrating the horizontal bedding orientation from A1 to A4, the appearance of a cleavage plane from A3 onwards, as well as the rotation of this plane from A3 to A5. As the depicted cross-section intersects each cylindrical sample in an oblique fashion, the shapes of the cross-sections differ from one sample to the next.

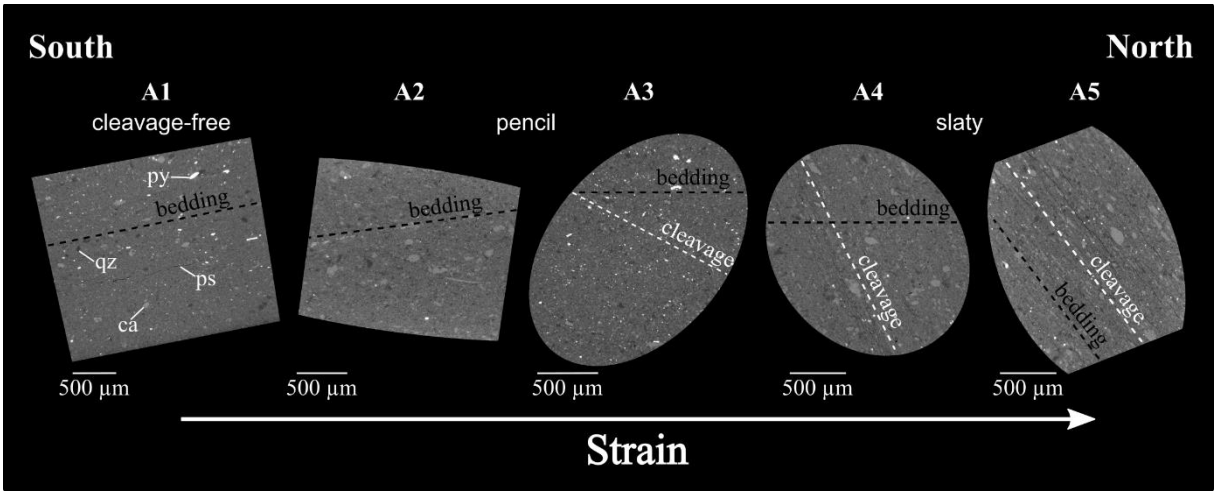

Figure 4.5: *XCT cross sections through the five samples (A1 to A5) in a common geographic coordinate system. The odd shape of the contours reflects that the presented north-south oriented plane intersects each cylindrical sample in a different way. Ca: calcite, ps: pore space, py: pyrite, qz: quartz. Strain intensity increases from A1 to A5. Cleavage and bedding planes in A5 are subparallel but cannot be differentiated.*

Figure 4.5 shows that most of the calcite grains have a rounded shape and correspond to microfossils and shell fragments. On the contrary, quartz grains are more angular. At this micron scale, we observe a preferred alignment of grains in the least deformed samples (A1 and A2). This fabric is attributed to bedding as this planar structure is sub-horizontal, which is in accordance with field observations. In sample A3, a secondary planar fabric becomes slightly visible, it corresponds to the pencil-cleavage that cross-cut bedding structures at low angle. Cleavage domains are subtle in this XCT image, sometimes marked by preferred alignment of calcite bioclasts and spaced by more than 1 mm in this

sample. In samples A4 and A5, the traces of cleavage domains are deduced from high porosity surfaces, which appear as microcracks in the XCT images. Because clay minerals are known to concentrate in cleavage domains (seams), clays may have dehydrated during storage of the samples and formed microcracks. From these structures, we can infer the presence of pressure solution seams. Furthermore, the calcite bioclasts are often truncated by the seams (***Figure 4.6*****a** and ***Figure 4.6*****b**) and confirm that pressure solution has been responsible of the growth of these surfaces (Engelder and Marshak, 1985; Passchier and Trouw, 2005). The truncation of calcite by pressure solution seams is supported by optical microscopy observation (***Figure 4.6*****c**). The cleavage domains are more penetrative in A5 than in A4. Average spacing between cleavage domains is of 212 µm ± 65 µm in A4 and of 116 ± 16 µm in A5. However, the measure of the spacing of cleavage depends on the scale of observation and the true spacing is certainly less than these values. In our case, spatial resolution depends on the voxel size of the XCT images. In A4, the seams are discontinuous, subparallel to slightly anastomose around grains and rather rough. In A5, the seams appear discontinuous, subparallel and smoother. In both samples A4 and A5, grains within or close to the cleavage domains are strongly aligned, parallel to the seams. In between the cleavage domains of A4, grains are either subparallel, orthogonal (related to the bedding fabric) or randomly oriented. In between the cleavage domains of A5, calcite grains are mostly aligned parallel to seams giving a strong planar fabric to the rock. Quartz grains are rather randomly oriented in A5. We remark that cleavage domains are heterogeneously spaced in A4 compared to cleavage domains in A5, which are equally spaced throughout the rock volume.

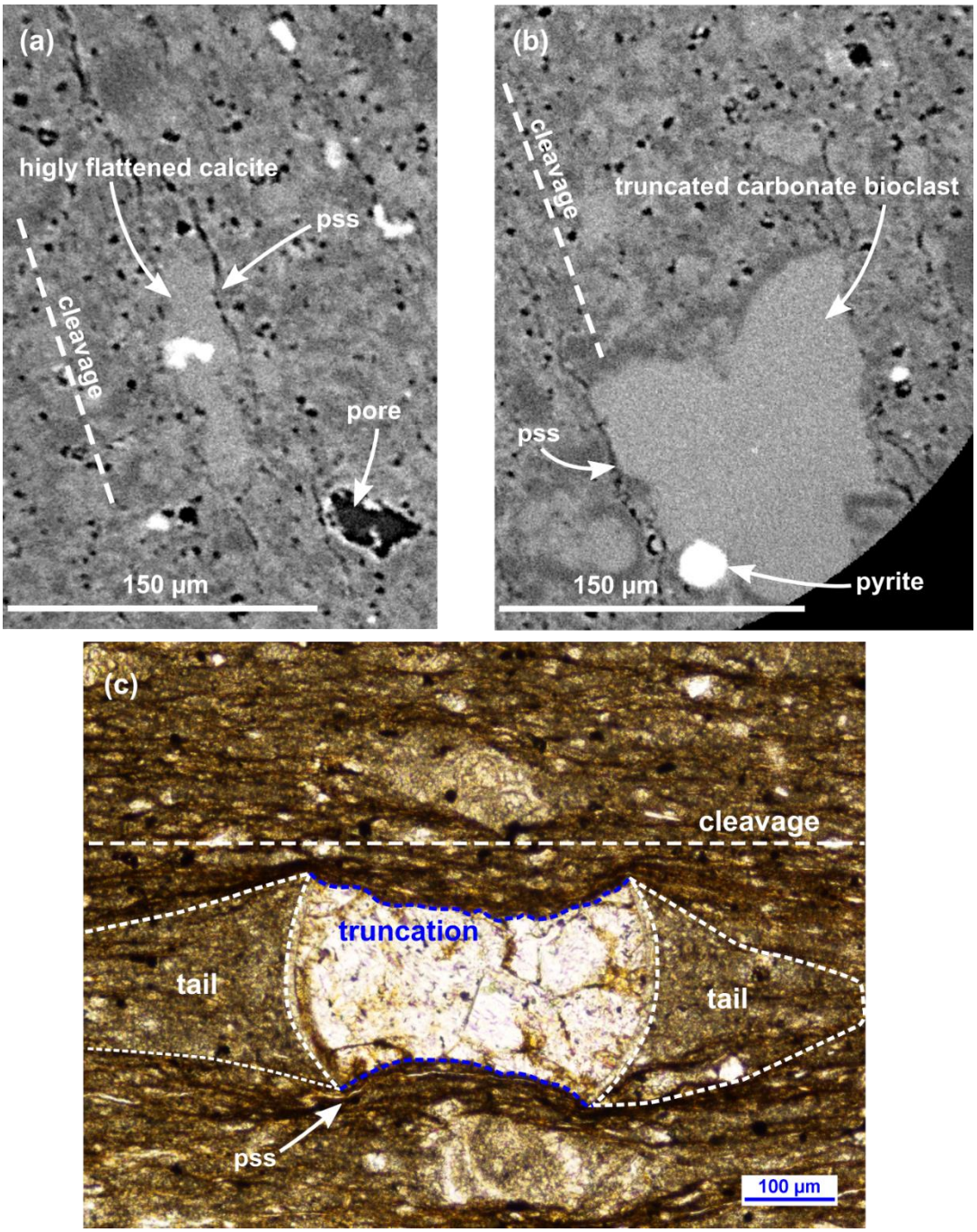

Figure 4.6: *(a) Highly flattened calcite and pressure solution seams (PSS) observed in XCT image. The large pore is partially filled by pyrite. (b) Evidence of truncated bioclast in XCT image (c) Truncated calcite grain with pressure-shadows (tails) formed in the cleavage plane, observation by optical microscopy using in-plane-polarized transmitted light. Tails seem to be composed of the original rock matrix.*

4.3.1.3 Grain and pore space shape

Here we discuss the shape features of the equivalent ellipsoid (see section ***3.4.4.2***) of the grain of calcite and quartz as well as the pore space.

At first glance, the distribution of the shape parameters of quartz, calcite and pores highlights a global transition towards more anisotropic, more elongated and flatter objects from the cleavage-free domain (A1) to the slaty-cleavage domain (A5) (***Figure 4.7***). However, the evolution of the shape parameters is not the same for each phase.

Concerning the quartz (***Figure 4.7***), the major shift in distributions of both anisotropy, elongation and flatness takes place between A1 and A2. After that, the distribution of these parameters is not really distinguishable between samples A2, A3, A4, A5. However, we should note that distributions in A3 feature the most anisotropic, elongated and flattened quartz grains.
Concerning the calcite (***Figure 4.7***), there is a regular shift of the distribution of the three parameters from A1 to A5. As strain increases, calcite grains gradually become more deformed. This is particularly well illustrated by the evolution of anisotropy and flatness. However, we should note that distributions of anisotropy and elongation in A3 are close to those in A5. The distribution of flatness in A3 is similar to that in A4. We should note that quartz and calcite have similar distributions of anisotropy, elongation and flatness in A1 and A2.
Concerning the pore spaces (***Figure 4.7***), the distribution of anisotropy and flatness are delicate to interpret due to a high proportion of very anisotropic and flattened pores in A1 and A5. These pores may in fact correspond to microcracks present in A1 and A5. Elongation of the pore spaces is similar for the five samples.

As significant results, we thus retain common shape features of quartz and calcite grains in samples A1 and A2, the change of quartz shape between A1 and A2 solely, contrasting with the continuous and regular evolution of calcite shape across the five samples. We also note that quartz grains seem to be more deformed in sample A3. It has been verified that the specific segmentation thresholds for each phase have no influence on the evolution of the reported shape parameters.

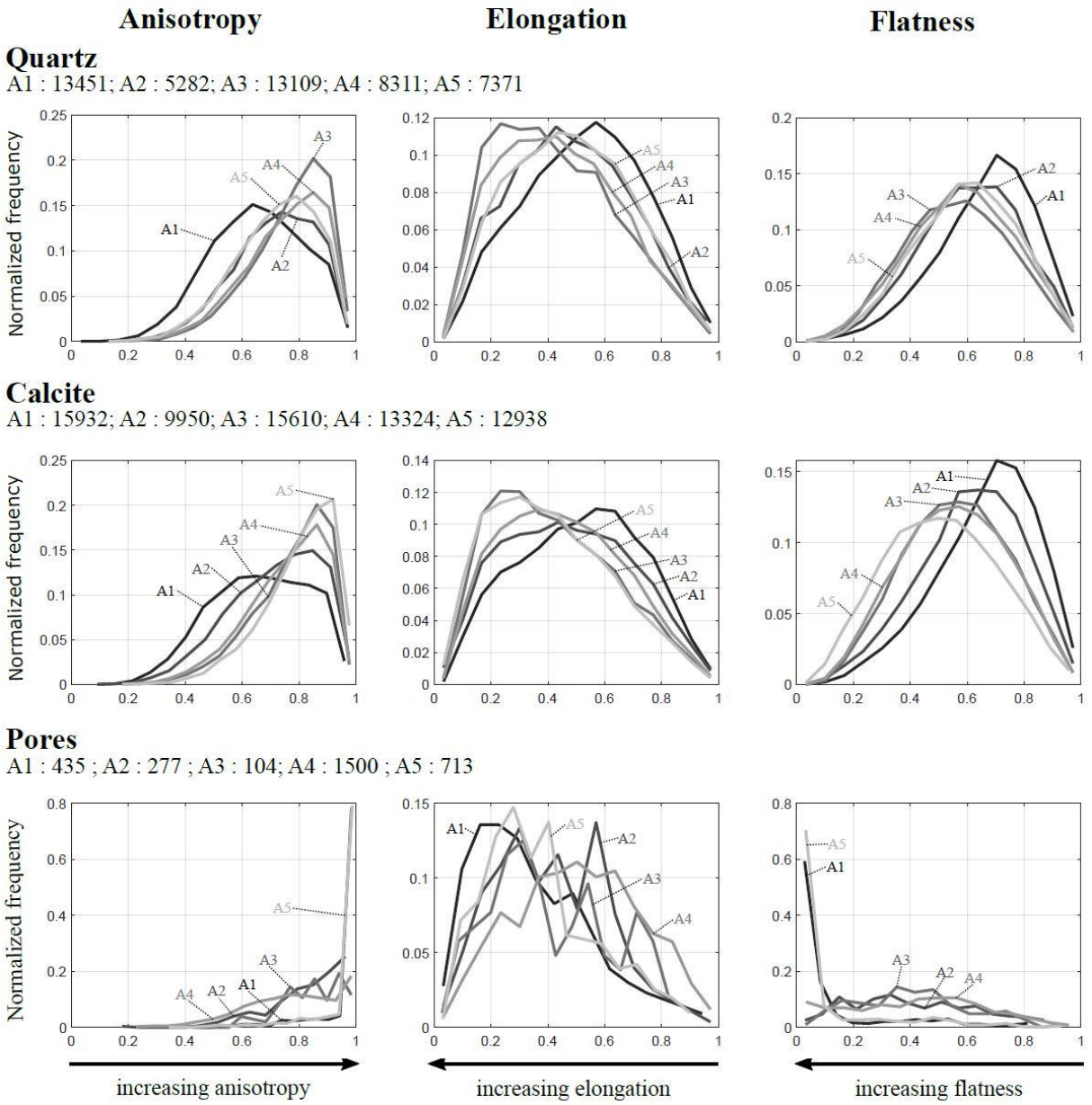

Figure 4.7: ***Normalized histograms of anisotropy, elongation and flatness measured for quartz, calcite and pores in the five samples. Number of bins: 15. The number of considered objects in the samples is indicated below each subtitle.***

4.3.1.4 SPO of quartz, calcite and pores

We plot density contours of the short ($\boldsymbol{L_3}$) and long ($\boldsymbol{L_1}$) axes corresponding to thousands of objects (grains, pore spaces) in lower hemisphere equal area stereographic plots representing a geographic coordinate system (North-East-Down) (***Figure 4.8*** and ***Figure 4.9***). In fabric analysis, it is generally common to assign $\boldsymbol{L_3}$ as the pole of foliation (***Figure 4.8***) and $\boldsymbol{L_1}$ as the lineation (***Figure 4.9***). Poles of the bedding and cleavage planes measured on the XCT images from the alignment of grains (***Figure 4.5***) are also reported onto these stereographic plots in a common geographic coordinate system (North-East-Down).

In the cleavage-free domain (sample A1), all objects display foliation parallel to the bedding plane (***Figure 4.8***). Pore spaces are well-organized with a maximum density near 30% around the pole of bedding. Quartz and calcite display almost the same degree of dispersion and have maximum densities

coinciding with the pole of bedding (3.5% and 3.8% respectively). Lineation of individual ellipsoid long axes ($\boldsymbol{L_1}$) spread sub-horizontally in the bedding plane with a slight NW-SE trend (***Figure 4.9***). At the onset of the pencil-cleavage domain (sample A2), all poles of foliation spread near the bedding pole. Here again, quartz and calcite have similar maximum densities (3.3% and 3.7% respectively). Poles of the pores are more disorganized. No evident lineation is observed but we can notice a slight preference towards NW-SE for quartz and calcite (***Figure 4.9***). Lineation is related to bedding. In the pencil-cleavage domain, where cleavage is oblique to bedding (sample A3), we observe notable differences. Quartz displays a scattered foliation related to the bedding pole with a maximum density of 2.2% (***Figure 4.8***). Calcite shows a NNE-SSW directed girdle of the pole of foliation between the pole of cleavage and the pole of bedding. However, calcite foliation mostly indicates a cleavage related fabric with a maximum density of 3.0% around the pole of cleavage. The pole of foliation of pore spaces seems to be scattered between the pole of cleavage and the pole of bedding. The lineation is sub-horizontal and related to bedding for quartz grains but still displays a preference towards NW-SE as in A1 and A2 (***Figure 4.9***). As of now, the lineation tends ESE-WNW for calcite grains and correspond to an intersection lineation of bedding and cleavage planes. Calcite lineation also displays incipient contours in the cleavage plane. The lineation of pore spaces cannot be assessed. In the slaty cleavage domain, where cleavage is strongly oblique to bedding (sample A4), we also observe notable differences. Quartz displays a N-S directed girdle of the pole of foliation between the pole of cleavage and the pole of bedding (***Figure 4.8***). Quartz grains are thus influenced by these two planes. In contrast, calcite grains and pore spaces have a well concentrated foliation near the pole of cleavage. At this strain state, quartz and calcite show different maximum densities around the pole of cleavage, 2.3% for quartz compared to 6.6% for calcite. The lineation tends slightly E-W for quartz, close to an intersection lineation (***Figure 4.9***). For calcite and pore spaces, the intersection lineation mostly lies E-W sub-horizontally but is also depicting the cleavage great circle with some steep lineations within the cleavage plane. In the slaty-cleavage domain, where bedding and cleavage are parallel to each other (sample A5), all foliation poles are grouped parallel to the bedding/cleavage pole (***Figure 4.8***). However, quartz foliation is still quite disorganized and shows a weaker maximum density of 2.9%. Maximum density at the pole of cleavage reaches 11.4% for calcite foliation. The dispersion of the quartz foliation may indicate that bedding and cleavage planes are not exactly parallel. The pole of foliation of pores is well defined and displays a maximum density of 38.2%. The lineation is relatively scattered, sub-horizontal in trend for quartz but also with a girdle around the dip of the cleavage plane (***Figure 4.9***). Calcite and pore spaces display a down-dip stretching lineation with a maximum density of 4.0% and 7.0% respectively. We should note as a general trend that foliation of grains and pore spaces is better defined than their lineation.

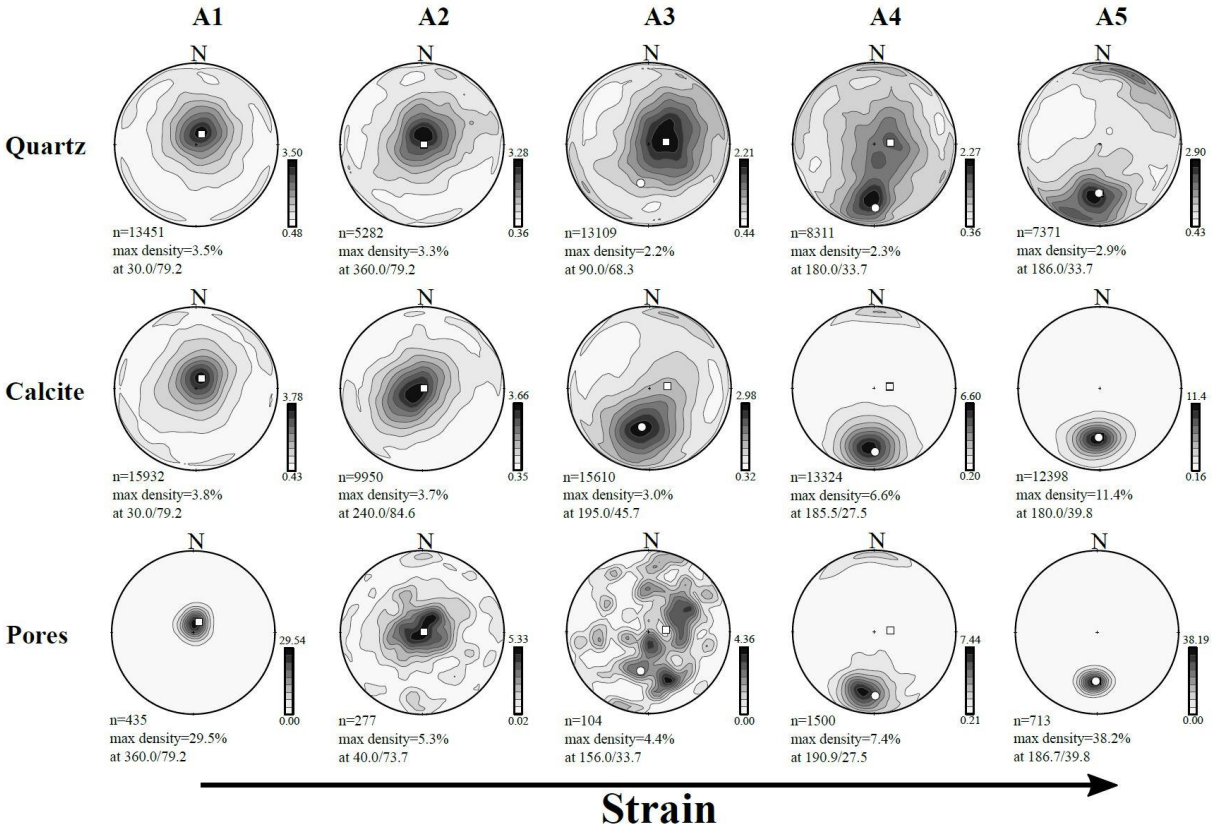

Figure 4.8: ***Stereoplot of equivalent ellipsoids' short axes (L_3) for quartz, calcite and pores in the five samples. White squares: pole of bedding; white circles: pole of cleavage. Note that in A5 the two poles are superimposed due to the transposition structure. The poles are deduced from the preferred alignment of grains in the XCT images. n: number of considered objects.***

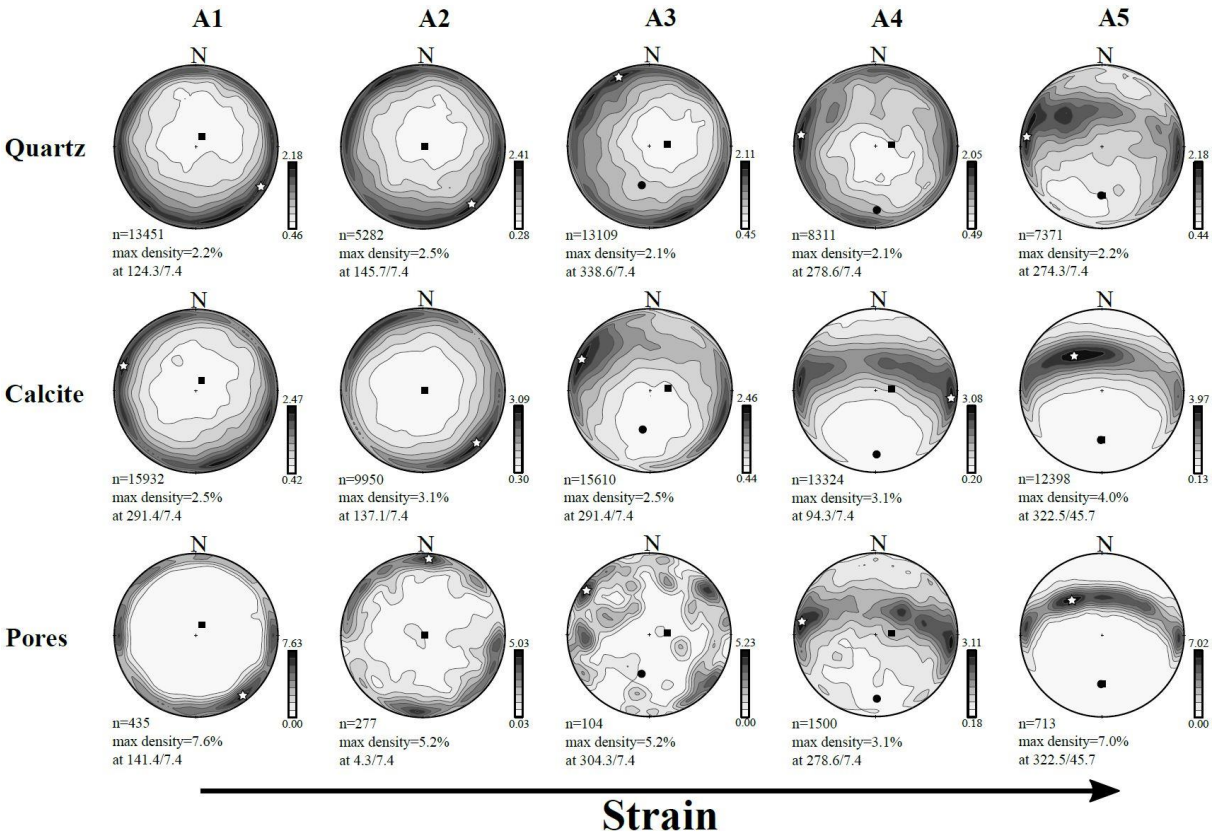

Figure 4.9: ***Stereoplot of equivalent ellipsoids' long axes (L_1) for quartz, calcite and pores in the five samples. Dark squares: pole of bedding; dark circles: pole of cleavage; white stars: maximum density. Note that in A5 the two poles are superimposed due to the transposition structure. The poles are deduced from the preferred alignment of grains in the XCT images. n: number of considered objects.***

4.3.1.5 SPO of heavy minerals: pyrite inclusions

In addition to the above-presented results that have been published, we have added the SPO results of pyrite grains. Anisotropy distribution of the equivalent ellipsoids of pyrite across the five samples are shown in ***Figure 4.10*****a**. Pyrite from sample A1 are more distributed in terms of their anisotropy while pyrite extracted from the other samples are mostly anisotropic. Sample A1 is particularly rich in pyrite and sample A2 is almost depleted in pyrite.

The individual directional data of $\boldsymbol{L_3}$ and $\boldsymbol{L_1}$ axes are shown in stereonets with density contours in ***Figure 4.10*****b**. Overall, pyrite show similar trends as the SPO of quartz along the strain gradient. Pyrite shows a significant bedding fabric in samples A1 and A2 with foliations reaching more than 5%. The most striking observation is the asymmetric girdle of $\boldsymbol{L_3}$ axes in samples A4 that indicates, according to the subvertical bedding pole, a top to the south shearing. However, the greater difference between pyrite SPO and quartz SPO is observed in the most deformed sample A5. The rather strong foliation of pyrite is contrasting with the weak one previously observed for quartz. The down-dip lineation of pyrite, parallel to thrust movement, is well expressed in this sample.

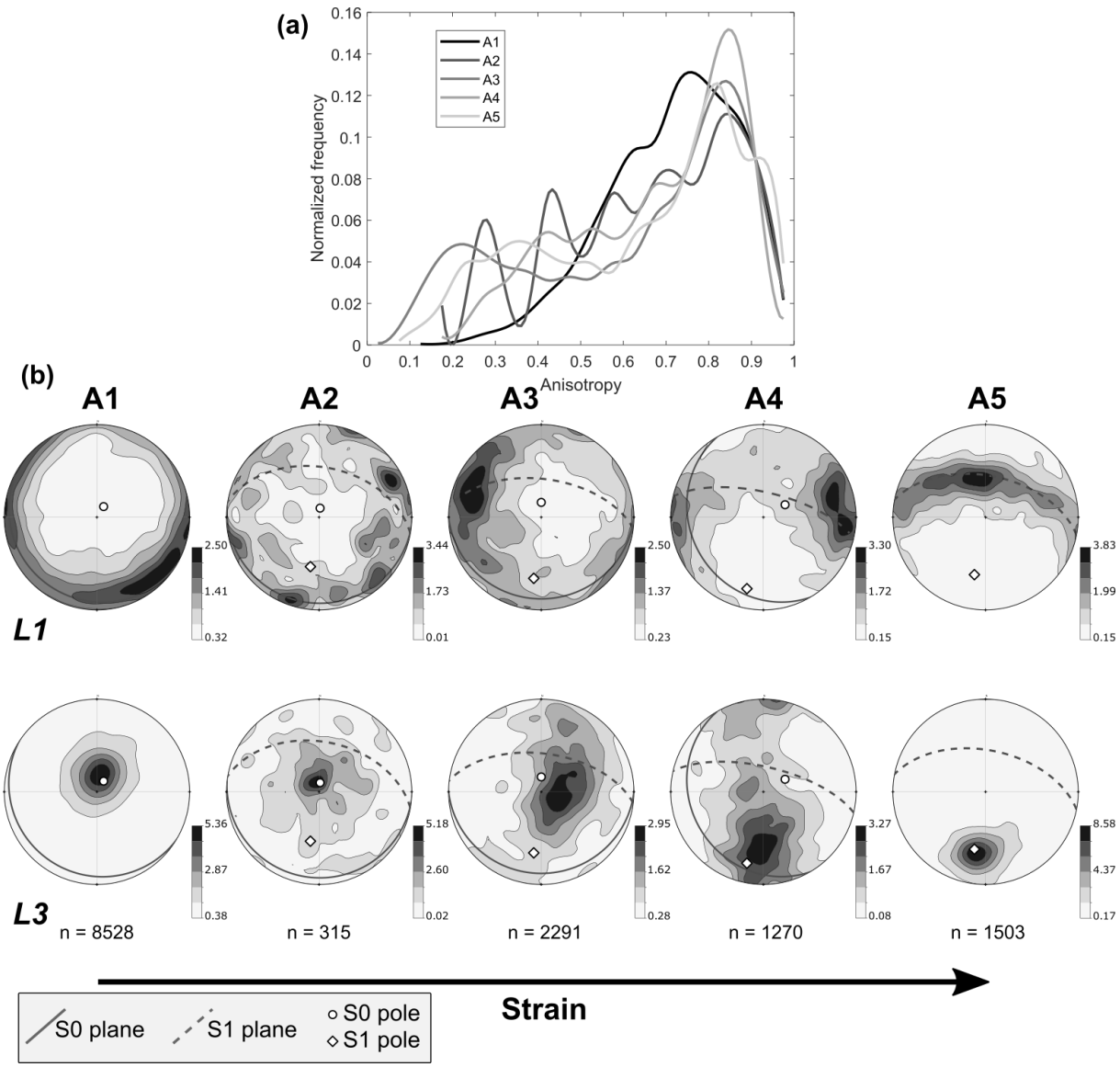

Figure 4.10: *(a) Normalized histograms of anisotropy measured for pyrite in the five samples. (b) Stereoplots of* L_1 *and* L_3 *axes of pyrite grains in the samples.*

4.3.1.6 Discussion

Results of this microscale study are fully consistent with field data. Cleavage development along the strain gradient is well recorded in XCT images and is demonstrated by our microstructural approach on quartz, calcite and pores. Although we have worked on a small rock volume (volume of interest between 1 to 6 mm^3), results are well correlated to field observations and show clear trends, indicating that the samples are representative. The representativeness of sample is also illustrated by the volume distribution remarkably similar for calcite and quartz, independently of strain. Moreover, the amount of investigated objects from XCT data of each sample (≈10000 for quartz and calcite, more than 100 for pores) makes the study statistically robust.

In the cleavage-free domain (A1), quartz and calcite have similar shape features (***Figure 4.7***) and SPO (***Figure 4.8***, ***Figure 4.9*** and ***Figure 4.11***). In these shales, quartz grains may mostly be provided by detrital inputs whereas calcite grains may be provided by carbonates pelagic particles. Grain shape may result from compaction both during burial/diagenesis and tectonic compression. SPO of quartz and calcite is governed by a typical bedding-parallel fabric with short axis $\boldsymbol{L_3}$ normal to the bedding

plane and no specific orientation of the long axis $\boldsymbol{L_1}$ (***Figure 4.9***). SPO of pores is also governed by the bedding.

At the onset of pencil-cleavage domain (A2), we observe similar shape features (***Figure 4.7***) and SPO (***Figure 4.8***, ***Figure 4.9*** and ***Figure 4.11***) for quartz and calcite but they have evolved with respect to the undeformed sample A1. Particles are more deformed (***Figure 4.7***) but their foliation remains close to the pole of bedding, lineation is almost the same as in A1. No specific change in SPO is recorded in this low strain intensity area. Grain shape may change due to microfracturing, as illustrated in ***Figure 4.12***. Evolution of grain shape and SPO is reported in a sketch presented in ***Figure 4.12*** that follows this discussion.

In the pencil-cleavage domain (A3), where cleavage is oblique to the bedding orientation, shape features and SPO differ between quartz and calcite. Quartz and calcite grains are more deformed in this sample as shown by the distribution of shape parameters (***Figure 4.7***). Quartz SPO is still related to bedding but disturbed (***Figure 4.8***, ***Figure 4.9*** and ***Figure 4.11***). Calcite SPO is developing a cleavage foliation and is depicting an intersection lineation. Some calcite grains might still be related to the bedding as described by the girdle of $\boldsymbol{L_3}$. The pore fabric in this sample is more difficult to interpret because of the weak number of pore spaces. Mechanical rotation, pressure-solution and new crystallization of phyllosilicates grains have been commonly proposed as the major processes acting during cleavage development associated to the transition from mudstones to shales and slates (Engelder and Marshak, 1985; Lee et al., 1986; Ho et al., 1995, 1996; Passchier and Trouw, 2005). van der Pluijm et al. (1998) discussed the possible roles of thermal and strain energy in determining which process dominates. Generally, mechanical rotation is said to be the dominant process affecting detrital grains in early stages of cleavage development, as proposed by works on phyllosilicates grains (Ho et al., 1995, 1996; Hirt et al., 2004) and on magnetite grains (Housen and van der Pluijm, 1991). This would be consistent with our observations on the quartz and calcite grains in the pencil-cleavage domain. Changes in shape features and SPO of quartz and calcite may result from mechanical processes such as grain rotation. Alternatively, one could assume that grain rotation does not take place during deformation (***Figure 4.12***), especially for grains located in between the cleavage domains. Both scenarios are end-members. In between we can find intermediate models that may explain the dispersion of the poles of foliation and low maximum densities. Brittle fracturing of grains may also erode grain contours and affect their shape. At this intermediate strain intensity, we cannot detect evidences for pressure-solution in the XCT image so we propose that grain rotation and grain fracturing are the dominant deformation processes to accommodate shortening. However, we do not exclude the play of pressure-solution. It is important to note that this strain state shows the weakest maximum densities of foliation and lineation which attest for the most disturbed shape fabrics of grains and pores.

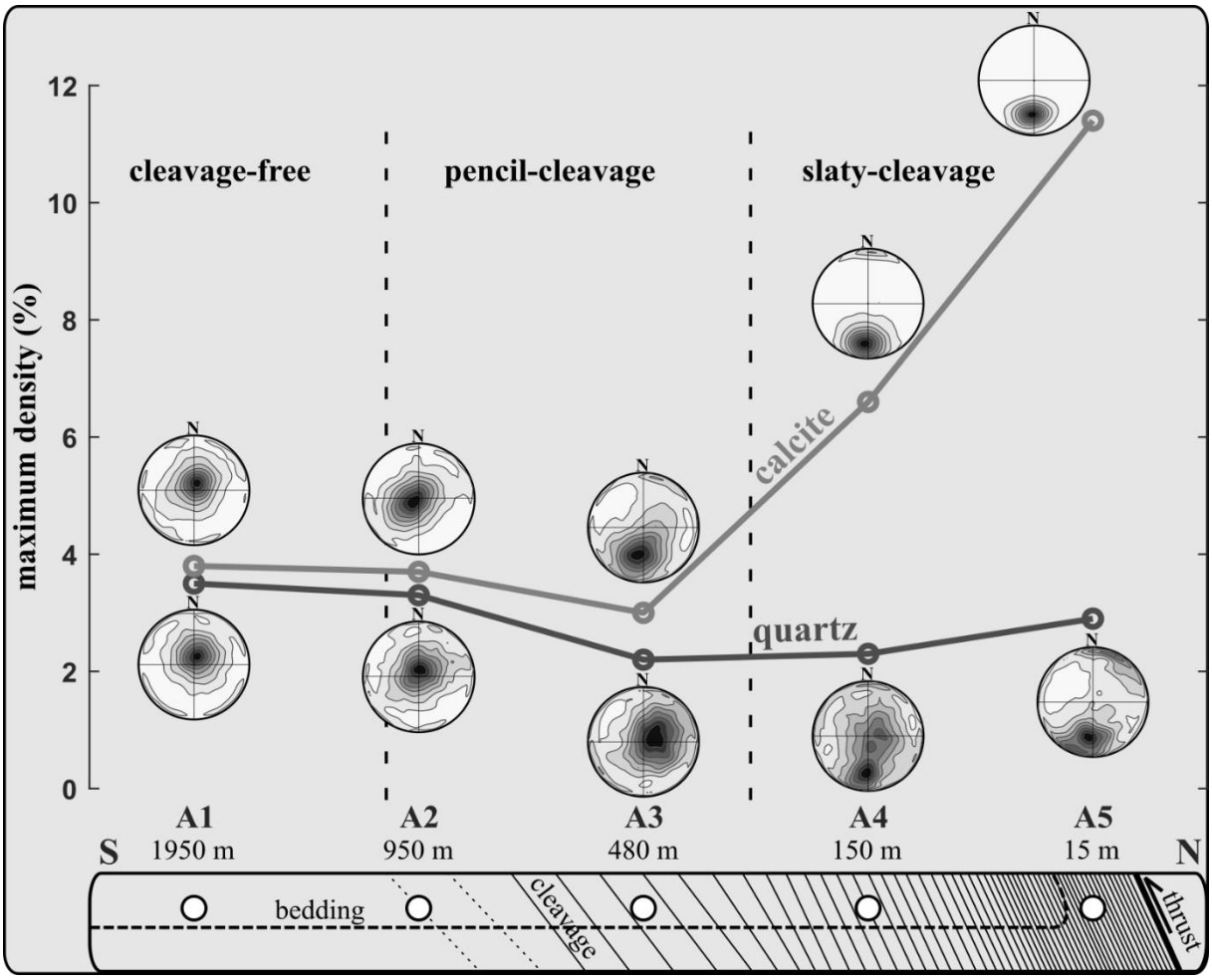

Figure 4.11: ***Evolution of the maximum density of the pole of foliation*** L_3 ***showing contrasting SPO patterns of quartz and calcite across each sample. At the bottom, the sample's distance from the thrust with indication of the orientation of bedding and cleavage planes is schematically represented.***

In the slaty-cleavage domain (A4), where cleavage is strongly oblique to the bedding orientation, shape features and SPO differ between quartz and calcite. The shape of the quartz grains remains the same as in A2, while the calcite grains continue to deform (***Figure 4.7***). The major step in the SPO evolution of grains is apparent in this sample and well demonstrated by differences in the maximum density of quartz and calcite foliations (***Figure 4.11***). Quartz foliation is now related to poles of both bedding and cleavage (***Figure 4.8***). More precisely, one third of the total quartz grains keep a bedding influenced fabric in this sample, compared to calcite and pores particles which are strictly governed by cleavage. We have compared the shape of the quartz grain population related to both the pole of cleavage and the pole of bedding, by selecting particles having a dip above or under 45°, but no differences have been observed in their respective size distribution. At first glance, these different orientations are not related to the size of the quartz grains. In this sample, we have seen some evidence for pressure-solution such as truncated calcite grains (***Figure 4.6***). Pressure-solution is also supported by thin section observations in which truncated calcite grains show pressure shadows (***Figure 4.6c***, aspect ratio of the grain is 4:1). It should be noticed that in XCT data, a truncated grain and its pressure shadows (tails) can be assimilated as one grain because of similar densities, as opposed to what can be seen in optical microscopy. Furthermore, fine grains present in pressure shadows are beyond conventional XCT image resolution. It explains the high degree of anisotropy of calcite grains obtained by XCT data processing which encompass many sub-micrometric grains to define one grain. In this sample, the increasing deformation of calcite grains and changes in their SPO could be explained by

pressure-solution. We suppose that this process may be the reason of the divergent evolution of the shape features and SPO between quartz and calcite in A3 (***Figure 4.12***). Pressure-solution may proceed on calcite grains but may be less effective or may not happen for quartz grains. It is well-known that pressure solution is a function of the thermodynamics conditions, especially temperature (Houseknecht, 1984; Bjorkum, 1996; Tournier, 2010), of the size and the composition of grains as well as of the stress conditions (Gratier et al., 2013). Another paramount parameter is the role of phyllosilicate in enhancing dissolution process of grains such as calcite and quartz (Dewers and Ortoleva, 1991; Renard et al., 1997; Meyer et al., 2006). More precisely, illite and mica are known to favor quartz dissolution in sandstones (Weyl, 1959; Houseknecht, 1988; Bjorkum, 1996; Tournier, 2010; Kristiansen et al., 2011). Even though both types of these phyllosilicates are present in our shales, the results of this study is not conclusive on their role in quartz dissolution. These shales have only experienced a peak temperature near 180°C (Izquierdo-Llavall et al., 2013) and we can propose that the thermodynamic conditions were prone to pressure-solution of calcite while they were not for quartz grains, or at least to a lesser extent. In particular, temperature may be the limiting parameter for quartz dissolution. It should be noticed that the distribution of the size of quartz and calcite remains similar in the five samples, which is particularly stunning considering the amount of strain recorded by the samples in the slaty-cleavage domain. It seems that even though calcite grains are affected by pressure-solution processes, all grain size classes are equally sensitive to them. The grain shape evolves due to the processes mentioned above but the removed material is probably only redistributed and grain size remains stable.

In the slaty-cleavage domain (A5), where cleavage and bedding are parallel, shape features and SPO of quartz and calcite are still displaying differences. Quartz shows the same shape as in A2 and A3 while calcite becomes more strained (***Figure 4.7***). Quartz SPO is mostly related to cleavage but still scattered both in terms of foliation and lineation (***Figure 4.8*** and ***Figure 4.9***). Calcite and pores' foliation are governed by cleavage and are well defined. Calcite lineation, which is close to the dip of cleavage, may correspond to a stretching lineation. Evidences for pressure-solution on calcite grains are also highlighted in this sample A5 (***Figure 4.6***). Thus, evolution of calcite shape and enhancement of its SPO at this strain state could be explained by pressure-solution (***Figure 4.12***). Here also, quartz grains might not be or at least less be affected by this process.

The SPO from the individual grain analysis of pyrite is similar to the SPO of quartz from sample A1 to A4. In the slaty-cleavage sample A5, the SPO of pyrite is more pronounced and rather comparable to the calcite one.

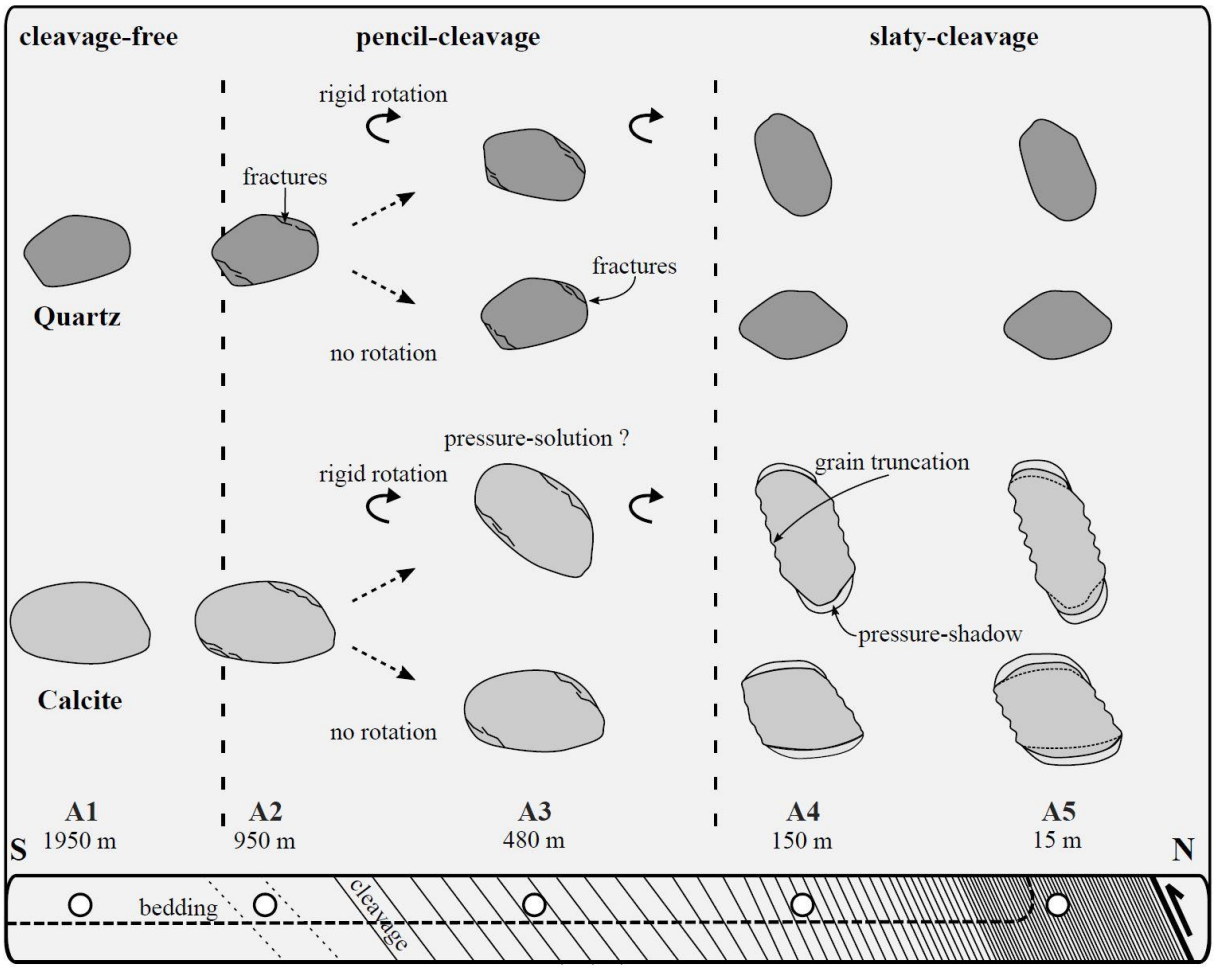

Figure 4.12: ***Interpretative sketch of the dominant processes that affect the shape fabric of quartz and calcite in the matrix from the cleavage-free domain to the slaty-cleavage domain. Note that this sketch accounts for changes in grain SPO as changes in terms of their foliation. The sample's distance from the thrust is schematically represented at the bottom, with indication of the orientation of bedding and cleavage planes. For each type of grain (quartz or calcite), two scenarios are envisaged from A3 onwards, a first one featuring grain rotation and a second one without grain rotation. A1: no deformed grain; A2: grain fracturing; A3: grain fracturing, pressure-solution may occur; A4: no further deformation of quartz grains, pressure-solution of calcite grains; A5: no further deformation of quartz grains, enhanced pressure-solution of calcite grains.***

4.3.1.7 Conclusion

The combination of XCT and EDS data is a reliable way to produce a three-dimensional chemical and structural characterization of a representative volume of a fine-grained rock sample at a micrometric scale. It is possible to identify the major rock constituents, to extract shape parameters and to gain insight in shape-preferred orientation of thousands of mineral grains and hundreds of pores. Therefore, investigating fine-grained rock fabric by means of XCT appears as a promising tool. According to this approach, we document for the first time the 3D shape fabrics of quartz and calcite and their evolution across a km-long strain gradient in the South Pyrenean foreland:

In five gradually more deformed calcareous shale samples (A1 to A5), we demonstrate that:

- quartz and calcite grains embedded in the matrix have analogous shape and SPO in the cleavage-free and at onset of pencil-cleavage domain (A1 and A2);
- quartz and calcite have distinct shape and SPO in the pencil-cleavage domain (A3) and in the slaty-cleavage domain (A4 and A5);
- pore fabric mimics calcite fabric along the strain gradient.

We envisage grain fracturing, grain rotation and pressure-solution as dominant processes acting in the matrix but affecting differently quartz and calcite. Quartz deformation may be mostly induced by grain fracturing and rigid rotation of grains and occurs preferentially in the first stages of cleavage development (onset of pencil-cleavage domain and pencil-cleavage domain). Detrital quartz grains could appear as rigid markers of strain. Calcite deformation may be favored by pressure-solution in the slaty-cleavage domain whereas it is not the case for quartz. Calcite could be a useful strain gauge as shown by its regular shape fabric evolution according to strain intensity.

4.3.2 Individual grain analysis: second set of 5 samples (A1-2 to A5-2)

4.3.2.1 Introduction

The first five samples (A1 to A5) studied by XCT thus show a convincing pattern to characterize a strain gradient. However, we must tackle the question of the representativeness of these results. One way to do this is to repeat the analysis. Another way to achieve this is to practice a more in depth analysis about representativeness. The latter method will be performed in chapter ***6***. The former method is treated in the following lines.

A second set of five drill cores (A1-2, A2-2, A3-2, A4-2 and A5-2) of 2 mm each, taken from the same AMS cores as the first set employed for the article were extracted to investigate possible heterogeneity of the shape fabric of the main phases. The goal is to discuss if our approach on small rock volume of shales is repeatable and representative. We attempted to drill these new cores in a way to maximize differences that could be due to the small investigated rock volume. This means that according to the position of the initial samples A1 to A5 and according to the macroscopic elements of the fabric visible on the centimeter-sized AMS cores, the new samples were drilled near the fabric elements (e.g. cleavage plane) or far from them when practically possible.

The number of segmented objects belonging to each phase (calcite, pore space, pyrite and quartz) and their relative abundance in the VOI of the samples are reported in ***Table 4.2***.

Table 4.2: ***Volume of interest for each sample. Number and volume fraction of quartz, calcite, pyrite and pores particles in this VOI, obtained after segmentation, cleaning and removal of boundary grains.***

Sample	A1-2	A2-2	A3-2	A4-2	A5-2
Volume of interest (mm^3)	3.14	2.90	3.24	2.80	3.35
Number of quartz grains	14,771	19,446	19,575	10,384	17,419
Volume fraction of quartz (1)	1.89 %	3.23 %	2.51 %	1.93 %	2.18 %
Number of calcite grains	17,660	18,114	24,803	20,400	19,934
Volume fraction of calcite (2)	2.56 %	3.89 %	2.64 %	4.34 %	3.87 %
Number of pyrite grains	5,433	355	4,730	1,571	2,338
Volume fraction of pyrite (3)	0.53 %	0.045 %	0.38 %	0.14 %	0.15 %
Number of pores	315	198	80	640	471
Volume fraction of pores (4)	0.065 %	0.016 %	0.0057 %	0.043 %	0.47 %
(1)+(2)+(3)+(4)	5.05 %	7.18 %	5.54 %	6.45 %	6.67 %

4.3.2.2 Microstructures

The main microstructures in the new samples are comparable to those observed for the first set of five samples and which are described in section ***4.3.1.2***. We show in ***Figure 4.13*** a 3D view of the sample A5-2 in which we can see a well-defined planar fabric and a major microcrack correlated to pressure-

solution seam going through the entire VOI. Additional images are available in ***Figure supp 2***, ***Figure supp 3***, ***Figure supp 4***, ***Figure supp 5*** and ***Figure supp 6***.

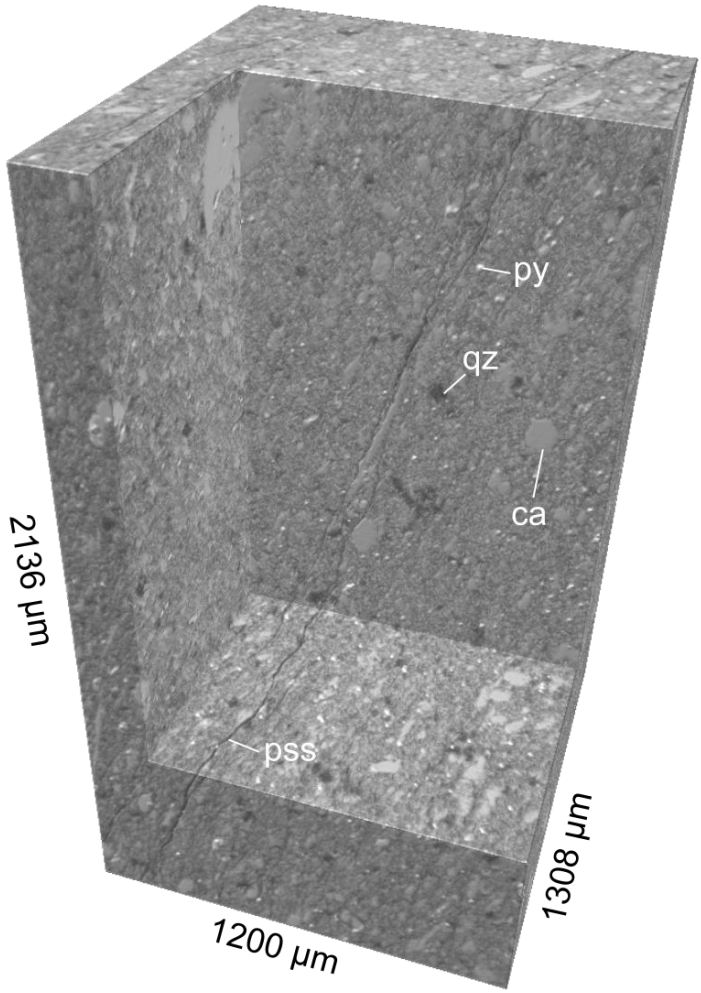

Figure 4.13: *3D grayscale image of sample A5-2 displaying a cleavage fabric. Ca: calcite, pss: pressure-solution seam, py: pyrite, qz: quartz.*

4.3.2.3 Grain shape data

The distribution of the individual data of all phases across the five new samples are shown in ***Figure 4.14***. In this figure, grain size and ellipsoid parameters distributions ($\boldsymbol{T_G}$ and $\boldsymbol{P_j}$) are plotted. The size distribution of quartz are comparable in all samples. We may note that the sample A1-2 has more small grains. The distribution of the shape parameter $\boldsymbol{T_G}$ of the ellipsoids is similar and prolate type ellipsoids dominate. The distribution of the parameter $\boldsymbol{P_j}$ is shifted towards more anisotropic values for sample A5-2 and is distinguishable from the other samples. Pyrite inclusions are smaller compared to quartz. The distribution of $\boldsymbol{T_G}$ is more homogeneous for pyrite and sample A1-2 appears to have the most anisotropic pyrite. Size distribution are almost identical for calcite but the grains are slightly smaller in sample A1-2 and are slightly larger in sample A2-2. $\boldsymbol{T_G}$ distributions for calcite are similar to those obtained for quartz with a higher representation of prolate forms. There is a slight shift towards the oblate domain for sample A5-2. This shift is even more pronounced for the distribution of $\boldsymbol{P_j}$ parameter. As expected and seen in ***Figure 4.13***, calcite are more anisotropic in sample A5-2. The most remarkable observations concerning the pores are the highly represented oblate ellipsoids in sample A1-2 and A5-2. This over representation is due to the presence of microcracks in these samples, which

is highlighted in ***Figure 4.13*** for example. The large microcracks are also deduced in the distribution of the degree of anisotropy.

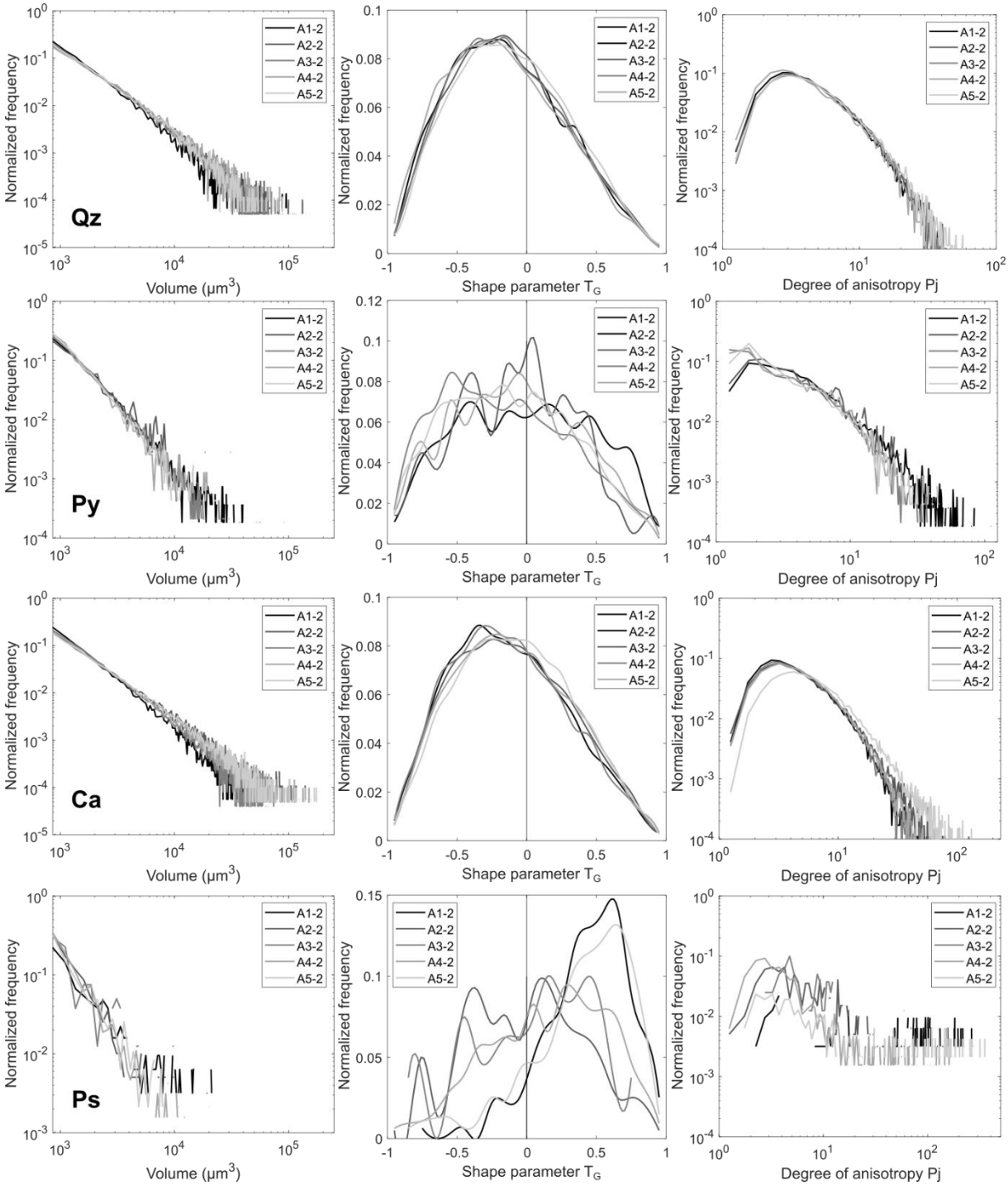

Figure 4.14: ***Normalized distributions of grain volume, shape parameter*** T_G ***and degree of anisotropy*** P_j ***of the grain ellipsoid for the four main phases across the five samples. Qz: quartz, Py: pyrite, Ca: calcite, Ps: pore space.***

4.3.2.4 SPO of the different components

The directional data of all phases are shown in ***Figure 4.15*** and ***Figure 4.16***. All results are rather consistent with the first set of samples. SPO evolution of quartz and pyrite are quite similar while the SPO of pore space mimics that of calcite. Differences appear in the transition zone, i.e. the pencil-cleavage domain and most importantly the slaty-cleavage domain where intensity of bedding and

cleavage may be comparable. In sample A4-2 (***Figure 4.15***), quartz foliation shows a symmetric girdle centered near the bedding pole while we observed an asymmetric girdle in sample A4 with a greater influence of cleavage. An asymmetric girdle of L3 axes is again observed for pyrite in sample A4-2 and comparable to quartz in the sample A4. The foliation of calcite and pores are strongly related to a cleavage fabric in sample A4-2 (***Figure 4.15***). All foliations are comparable in the slaty-cleavage sample A5-2 with higher intensities for calcite and pores.

Concerning lineation (***Figure 4.16***), an intersection lineation is expressed by all phases in sample A3-2 as we have seen for sample A3 (except for quartz). In sample A4-2, the intersection lineation is still observed for quartz and pyrite while there is a transition between this type of lineation and a girdle type in the cleavage plane for calcite and pores. In sample A5-2, all phases display a down-dip lineation with higher intensities for calcite and pores.

We will later on perform a more detailed analysis of the representativeness of these results by taking the two samples A4-1 and A4-2 of the slaty-cleavage domain that display different shape fabrics of quartz.

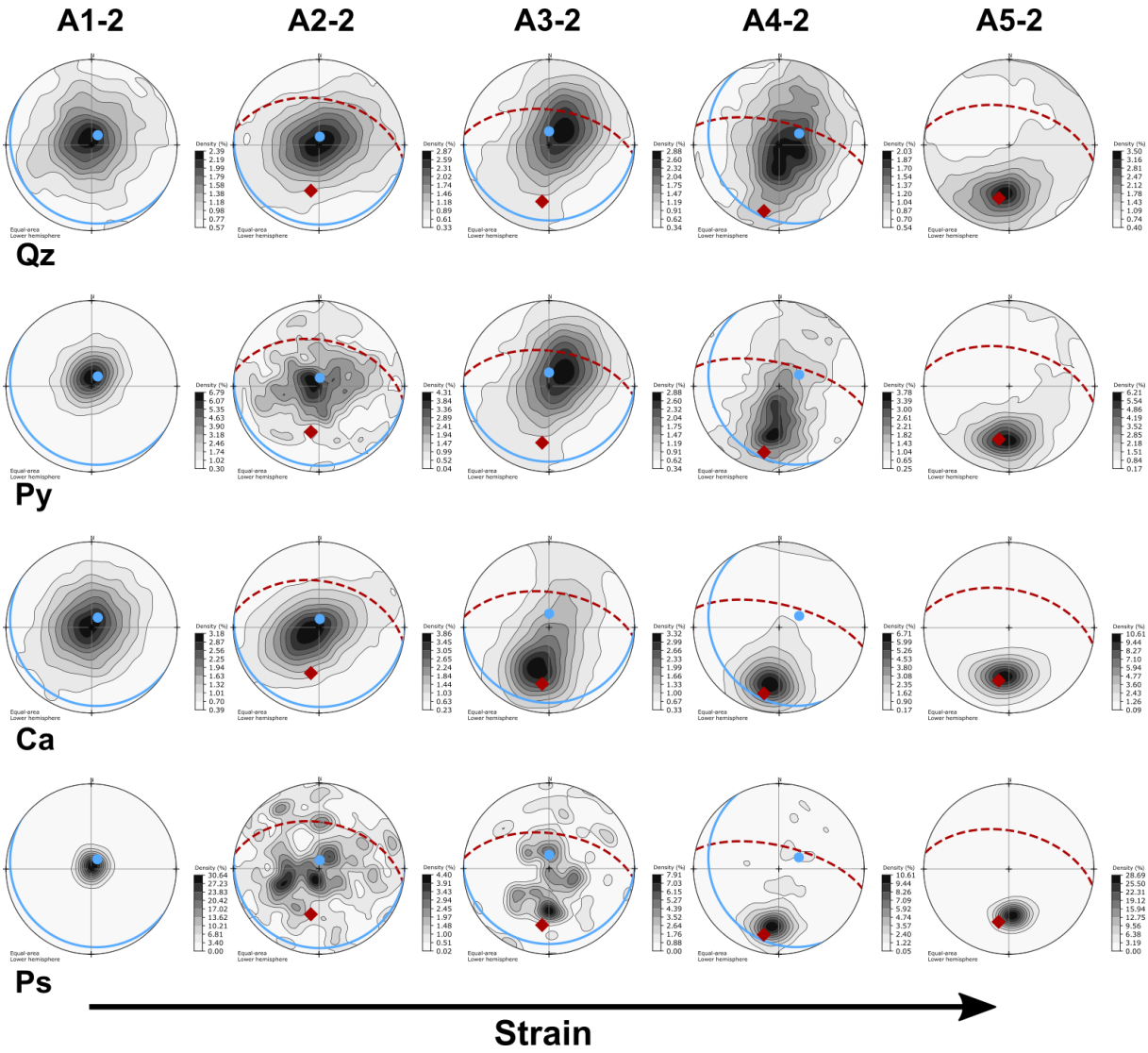

Figure 4.15: ***Stereoplot of ellipsoids' short axes (L_3) for quartz, pyrite, calcite and pores in the five samples (A1-2 to A5-2). Here the pole of bedding (blue) and cleavage (red) are the mean poles measured in the field.***

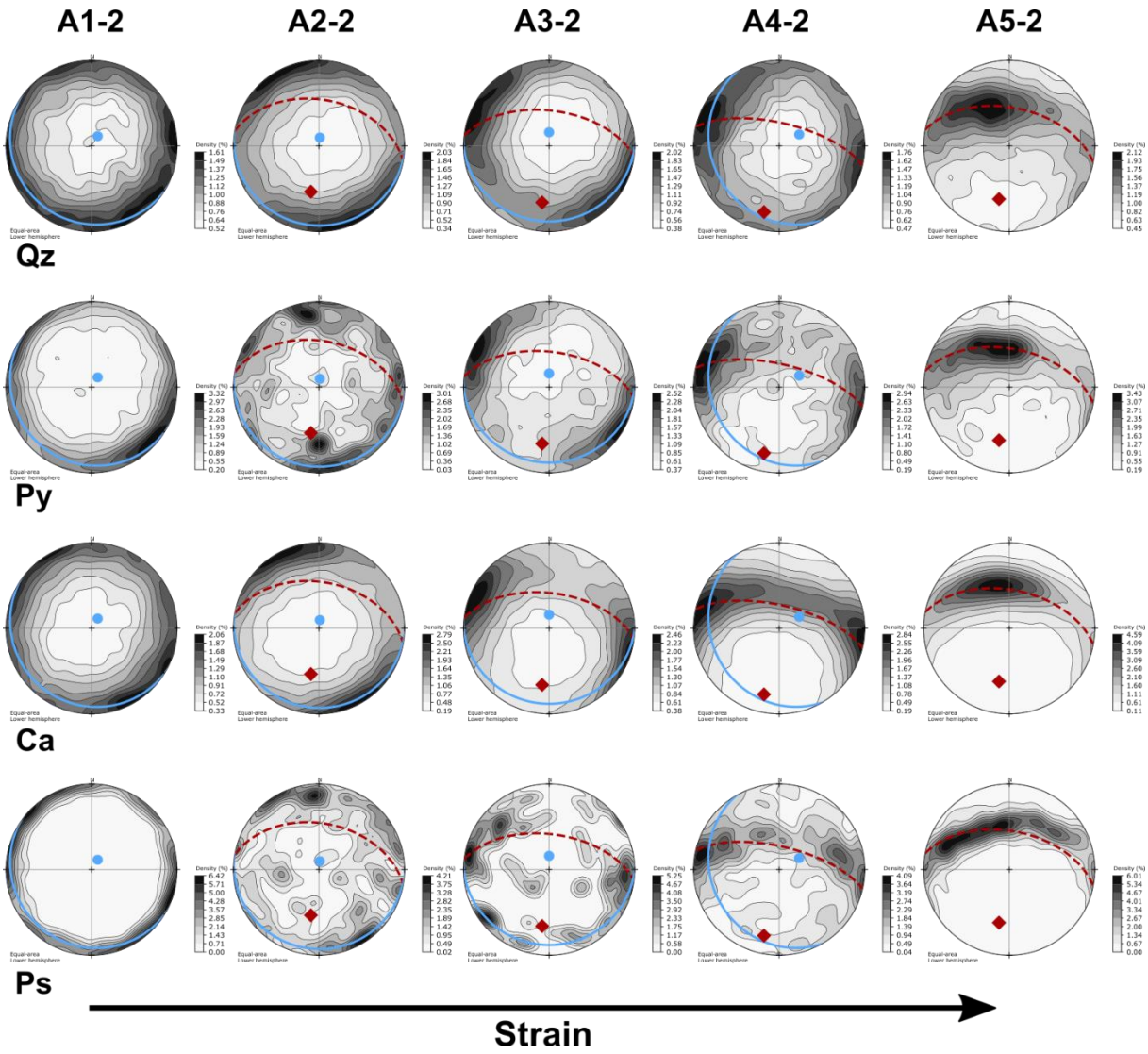

Figure 4.16: ***Stereoplot of ellipsoids' long axes (L_1) for quartz, pyrite, calcite and pores in the five samples (A1-2 to A5-2). Here the pole of bedding (blue) and cleavage (red) are the mean poles measured in the field.***

4.3.3 Bulk shape fabric vs bulk magnetic fabric

4.3.3.1 Introduction

Here we present the scalar and directional data of the bulk analysis of the data of the 10 samples. The mean shape tensors of all studied phases (calcite, quartz, pyrite and pore space) are compared to the susceptibility tensors retrieved from AMS. Magnetic data are taken from the paper of Boiron et al. (2020). In this paper, the authors have shown that paramagnetic clays dominate the susceptibility signal and more specifically illite grains. Thus, the AMS results give us the preferred orientation of the minerals of the fine-grained matrix that was not resolvable at the resolution of the XCT image. All these data taken together provide a complete view of the preferred orientation of the main phases in calcareous shale rocks. Note that the volume investigated by the XCT is small compared to the volume investigated by means of AMS (≈ 10 cm^3). The directional results for the two sets of samples (A1 to A5 and A1-2 to A5-2) are presented in ***Figure 4.17***. The principal directions of the tensors represent the main fabric directions while preserving orthorhombic symmetry. Therefore, these data gather and average the information previously seen for the individual analysis (with the stereoplots of $\boldsymbol{L_1}$ and $\boldsymbol{L_3}$

axes). The size extent of the confidence regions associated to each principal direction is correlated to the dispersion of the individual axes. Note that in the case of the shape fabric tensor, the large number of data is prone to reduce the size of the confidence regions. In addition, the scalar data (shape parameter and degree of anisotropy of the fabric and susceptibility ellipsoids) are reported in ***Figure 4.18*.**

4.3.3.2 Results

In the samples from the **cleavage free domain (A1 and A1-2)** the directional data of the shape fabrics are consistent with those of the magnetic fabric. $\boldsymbol{L_{3m}}$ axes are parallel to bedding pole. $\boldsymbol{L_{1m}}$ direction of all type of data is mostly parallel to bedding strike and it attests for a NE-SW compression axis, which may characterize a Layer Parallel Shortening (LPS) fabric (Pueyo-Anchuela et al., 2012), even if the absence of cleavage is reported for A1 and A1-2. The susceptibility tensor (AMS) is highly oblate in the two samples. This oblate feature is equally reported for the fabric ellipsoids of all phases, to a lesser extent concerning calcite (***Figure 4.17***). All these data are in agreement with a sedimentary to LPS fabric but with variable intensities. The lowest $\boldsymbol{P_j}$ values are obtained for quartz, $\boldsymbol{P_j}$ is slightly higher for calcite and more pronounced for pyrite ($\boldsymbol{P_j} > 1.5$). The intensity of the sedimentary fabric is strong for pore space in samples A1 and A1-2. The microcracks are responsible for extreme pancake morphologies of the fabric ellipsoids of pores in samples A1 and A1-2.

The principal directions of the magnetic fabric, with a K2 axis parallel to bedding-cleavage intersection, depicts an LPS fabric in **samples A2 and A2-2** (Pueyo-Anchuela et al., 2012). This feature is less observed in the directions of $\boldsymbol{L_{2m}}$ in the fabric ellipsoids (***Figure 4.17***). There is a drastic decrease of $\boldsymbol{P_j}$ for pore space in sample A2 and A2-2 but it remains quite high ($\boldsymbol{P_j} \approx 2$) compared to the other phases. The oblateness of the susceptibility ellipsoid is similar to the previous samples. The oblateness decreases in all shape fabrics of the two sets (***Figure 4.18***). The degree of anisotropy increases for calcite and quartz while this parameter decreases for pyrite and strongly for pore space.

In the **pencil-cleavage domain (A3 and A3-2)**, the directions of quartz and pyrite shape fabric are in accordance with the magnetic fabric (***Figure 4.17***). They show an intersection lineation fabric with foliation parallel to S0. Calcite and pores show an intersection lineation fabric too but with intermediate foliation between the bedding and cleavage poles. The oblateness of the fabric and susceptibility ellipsoids decreases significantly and approaches the triaxial type ellipsoid (***Figure 4.18***). The reduction of oblateness is not very pronounced for the fabric ellipsoid of quartz. The degree of anisotropy $\boldsymbol{P_j}$ of the fabric ellipsoid does not change significantly or show a slight reduction.

In the **slaty-cleavage domain (A4 and A4-2)**, quartz, pyrite and AMS show an intersection lineation fabric with intermediate position of $\boldsymbol{L_{3m}}$ and $\boldsymbol{K_3}$ axes (***Figure 4.17***). Calcite and pores display also an intersection lineation with a cleavage foliation. The shape parameter of AMS remains the same and its degree of anisotropy decreases (***Figure 4.18***). The shape parameter $\boldsymbol{T_B}$ decreases for quartz and pyrite. This parameter increases towards oblate shape for calcite and pore space. An interesting feature is the almost perfectly triaxial fabric ellipsoid of pyrite in both samples similar to the AMS. Weak $\boldsymbol{P_j}$ values are reported for quartz and AMS. On the contrary, calcite shows a noticeable increase in $\boldsymbol{P_j}$ and its shape fabric is getting stronger.

All directional data illustrate a strong cleavage fabric in the **most deformed samples A5 and A5-2**. AMS and shape fabric show a down-dip lineation more or less parallel to thrust movement indicating a shearing component (***Figure 4.17***). The susceptibility ellipsoid is oblate in these two samples (***Figure 4.18***). The fabric ellipsoids of calcite, pyrite and quartz are triaxial-oblate to oblate. The fabric ellipsoid

of pores is strongly oblate with high P_j values caused by the alignment of microcracks. The degree of anisotropy increases if we take the phases in the following order: quartz, pyrite, calcite and pore space. This attests for stronger fabric anisotropy of calcite and pore space in these cleaved samples.

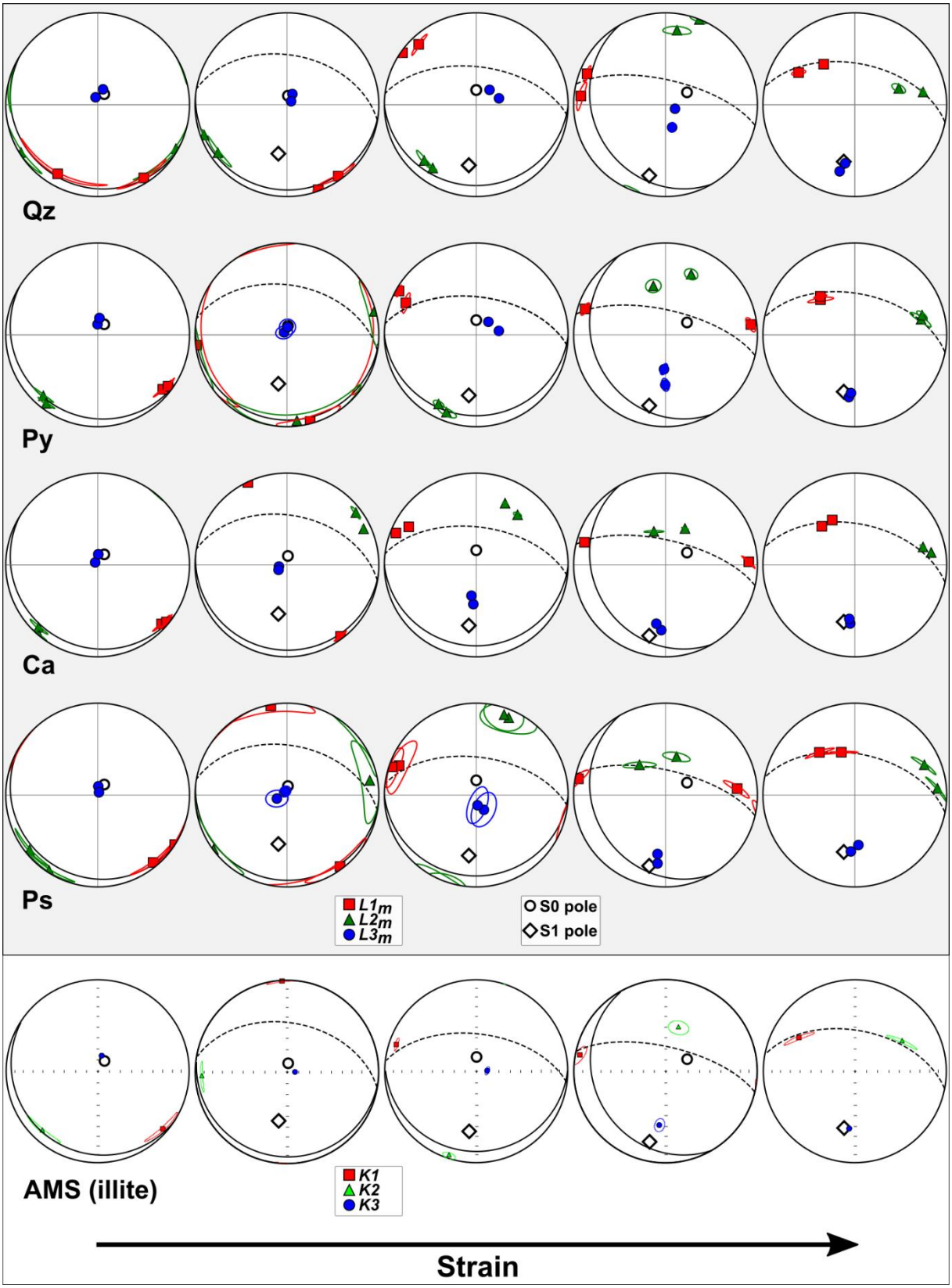

Figure 4.17: ***Comparison of the directional data of the bulk shape fabric of the four identified phases by means of XCT (first and second set of samples) to the directional data of the bulk magnetic fabric measured by AMS (on a single standard AMS drill core). The principal directions are plotted with their respective confidence regions. The number of grains used for the bulk shape fabric are given in Table 4.1 and Table 4.2.***

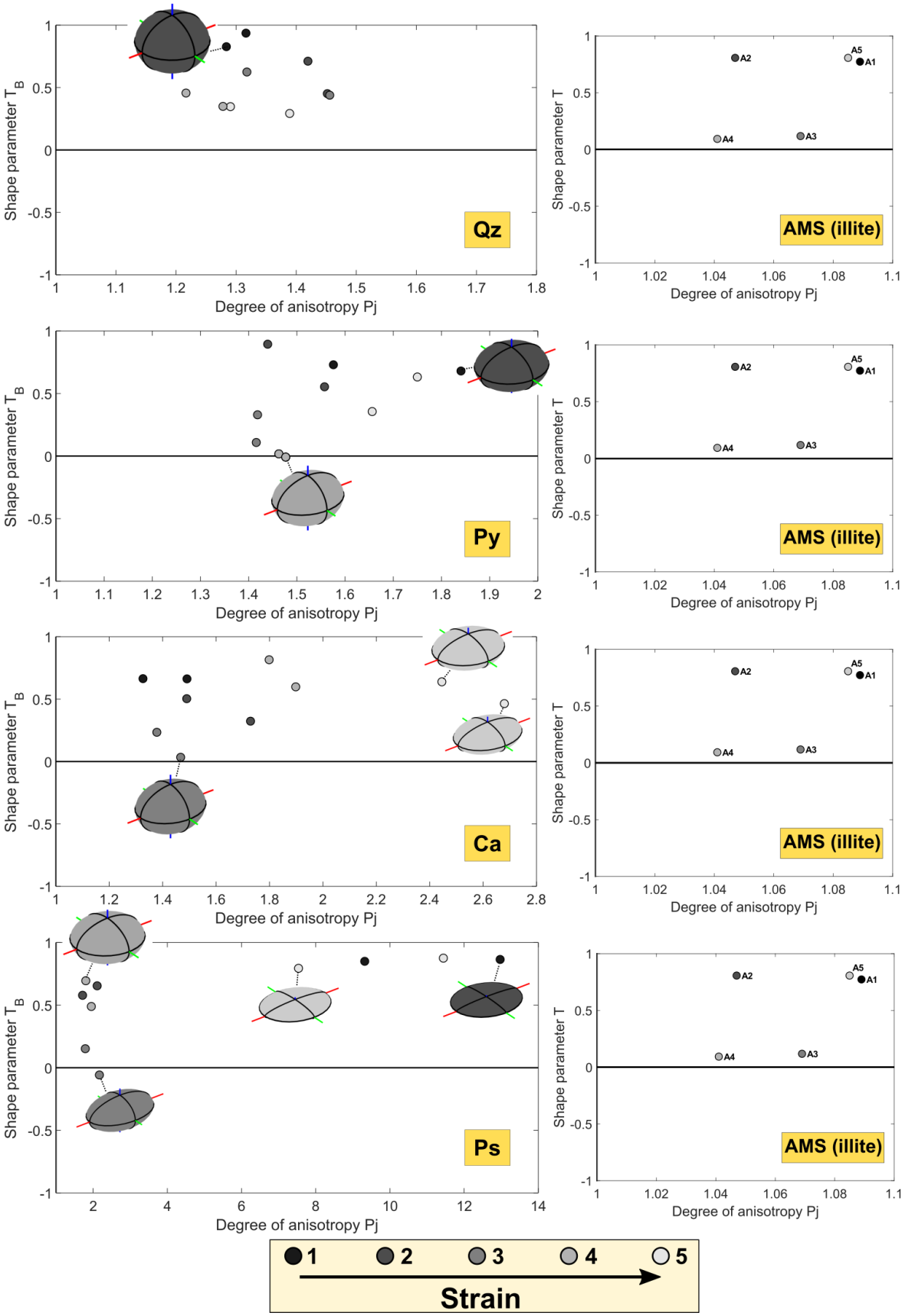

Figure 4.18: ***Jelinek diagrams of magnetic fabrics and shape fabrics in samples from the two sets. Qz: quartz, Py: pyrite, Ps: pore space, Ca: calcite. Some illustration of fabric ellipsoids corresponding to data points are provided. Note the difference in the scale of the degree of anisotropy in the diagrams.***

4.3.4 Spatial distribution of quartz grains

4.3.4.1 Introduction

In this section, we present the results of the spatial distribution analysis of quartz grains in the 10 samples. The results were obtained according to the methodology explained in section ***3.7.2***. We chose eight size classes of grain to perform this analysis. From size 1 to size 8, the influence of the numerous smallest grains of quartz decrease, leaving more room for the spatial distribution information of the coarsest particles. The results for the first set (A1 to A5) are presented in ***Figure 4.19***. The results of the second set (A1-2 to A5-2) are presented in ***Figure 4.20***. In these figures, each row with three graphs corresponds to one sample. In addition, some visualization of the arrangement of grain ellipsoids is provided for the size class 7 for samples A1, A5, A1-2 and A5-2 in ***Figure 4.21***. The purpose of this analysis is to characterize the anisotropy of the quartz grain distribution and possibly detect deformation patterns from the particular distribution. Because (detrital) quartz grains are rigid clasts embedded in a ductile clay rich matrix they may have deformed in a non-passive deformation. Similarly, pyrite may also serve in this analysis.

4.3.4.2 Results

In sample A1, the spatial distribution of quartz is independent of the grain size. Results across the eight size classes are rather homogeneous. The $\boldsymbol{E_3}$ axes of the distribution ellipsoids are parallel to the pole of bedding and it implies that the distance between grains is shorter in this direction. This would suggest that the dominant stress component is parallel to this direction. The morphology of the distribution ellipsoids remains in the oblate field and it attests for quartz grains that are spatially located in planes rather than along lines. This is quite noticeable in ***Figure 4.21*****a** for grains with a volume above 15625 µm^3 but this arrangement is far from a perfect disposition of grains along planes as the value of $\boldsymbol{T_S}$ is around 0.5 and the anisotropy is only of 1.2. In sample A2, directional data of the distribution ellipsoids are comparable but with more variability in the $\boldsymbol{E_3}$ direction. The $\boldsymbol{E_1}$ direction is correlated to the lineation of quartz grains. The shape of the ellipsoids changes with the classes and quartz grains may be distributed along lines or along planes. By decreasing the influence of the small grains, it seems that the distribution ellipsoid changes from prolate to triaxial with a noticeable anisotropy. This sample A2 is the most depleted in quartz gains compared to the others. The results of the sample A3 are hardly interpretable, as much variability exists. This is probably due to the lack of a specific distribution of quartz grains in the rock matrix. This is confirmed by the weak values of $\boldsymbol{P_j}$ (generally $\boldsymbol{P_j} < 1.1$). Taking all the grain sizes, the ellipsoid is oblate. The spatial distribution of the largest grains is rather along lines. In the slaty-cleavage sample A4, directional data are less variable than in the previous sample. $\boldsymbol{E_3}$ axes point towards western directions with a dip of about 25° for the eight classes. $\boldsymbol{E_1}$ axes are parallel or oblique to the bedding pole. The shape of the distribution ellipsoids 1 to 8 are mostly in the oblate field but the weak $\boldsymbol{P_j}$ values indicate that grains are more randomly distributed than organized. In the sample A5, $\boldsymbol{E_3}$ axes are directed southerly, not so far from a similar trend as the cleavage pole. $\boldsymbol{E_1}$ axes are clustered in west, north-west direction. These directional results indicate that distances between grains are smaller in a North-South direction while they are greater in the west direction. Maximum compression axis may be oriented in the north-south direction. The greater distances in the west may be correlated to the stretching lineation of grains. While expecting a distribution of grains along planes due to the pronounced cleavage planes in this

sample, the prolate shape of the ellipsoids indicates that grains are very slightly distributed in lines. The arrangement of individual ellipsoids of grains for the class 7 in this sample is illustrated in ***Figure 4.21*b**.

In the second set of samples (***Figure 4.20***), the number of grains in the analysis is higher because the investigated volume by XCT is larger. The sample A1-2 shows a result in accordance with the sample A1. The principal directions $\boldsymbol{E_1}$ and $\boldsymbol{E_3}$ of the distribution ellipsoids are the same as in A1. Shorter distances between grains are found perpendicularly to the bedding planes. There is more variability in the morphologies of the distribution ellipsoids than in sample A1. The ellipsoids 7 and 8 have an oblate shape with a more intense anisotropy. Thus, larger grains are not randomly distributed. An illustration of the distribution of grains belonging to the class 7 in sample A1-2 is provided in ***Figure 4.21*c**. In the other samples (A2-2 to A5-2), the very weak values of $\boldsymbol{P_j}$ indicate that quartz grains are rather randomly distributed. This is also confirmed by the variability in the shape attributes of the distribution ellipsoids and the variability of their principal directions. As for the sample A5, a view of the distribution of quartz belonging to the class 7 in sample A5-2 is proposed in ***Figure 4.21*d**.

4.3.4.3 Conclusion

The main conclusion from this spatial distribution analysis is that this approach seems to well record the strain related to the sedimentation and compaction while the tectonic strain is hardly seen. We have seen that in sample A1 and A1-2, a distribution of quartz grains in planar structures, parallel to bedding, may exist. The directional and scalar data obtained in these two samples provide the maximum stress direction. It is certainly the different deformation processes and the superposition of a tectonic fabric on a primary sedimentary fabric that affects the spatial position of the quartz grains in the other samples (2 - 5) and that disturbs this analysis. Moreover, if pressure-solution creep was a main deformation mechanism, this may altered the analysis (Dunne et al., 1990).

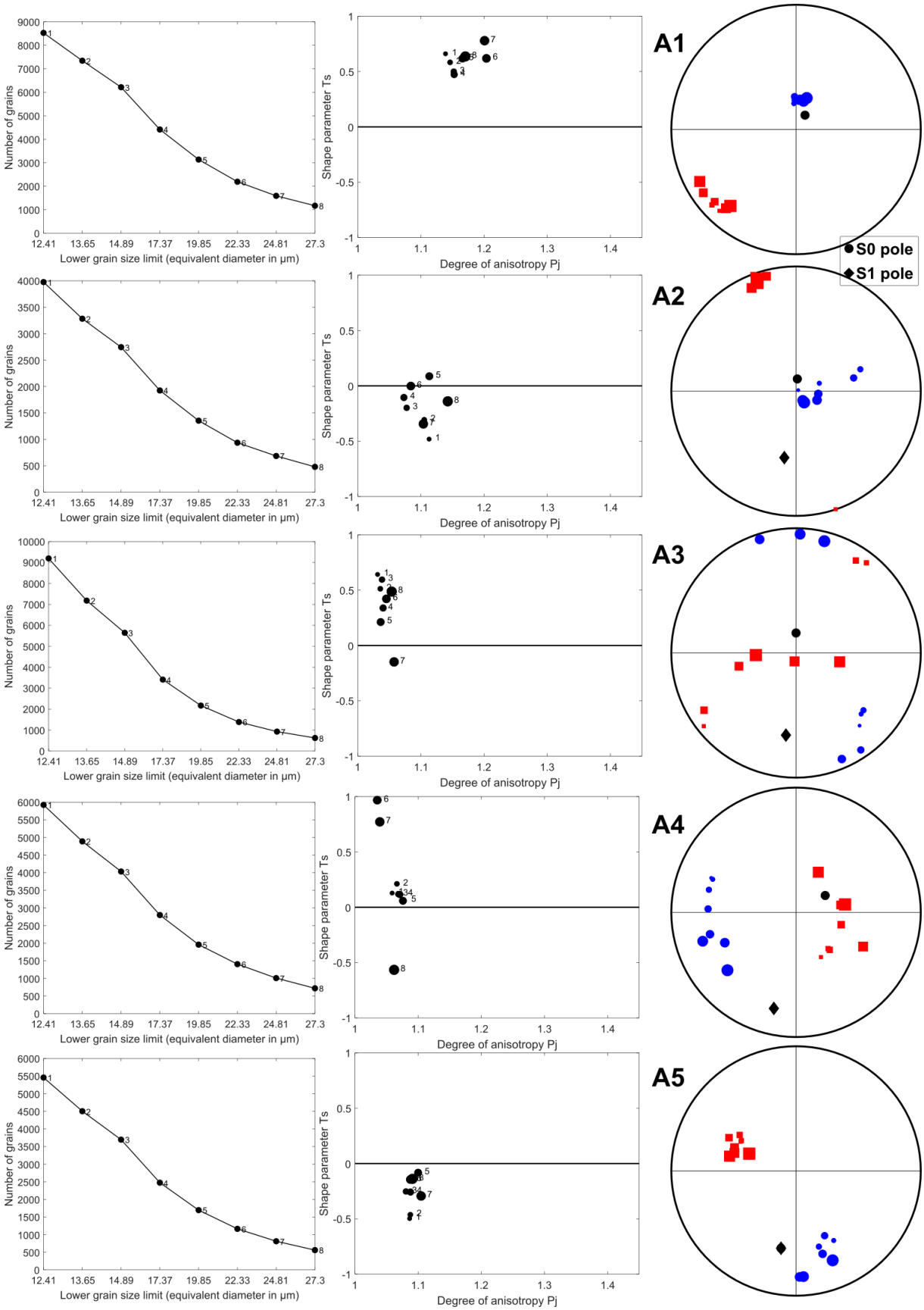

Figure 4.19: *Spatial distribution analysis of quartz in samples A1 to A5. Each row is dedicated to one sample. From left to right: number of grains in the eight classes with the lower threshold size limit, Jelinek diagram with*

the eight distribution ellipsoids data points, stereoplot of the principal directions E_1 ***and*** E_3 ***of the eight distribution ellipsoids in geographic coordinate system.***

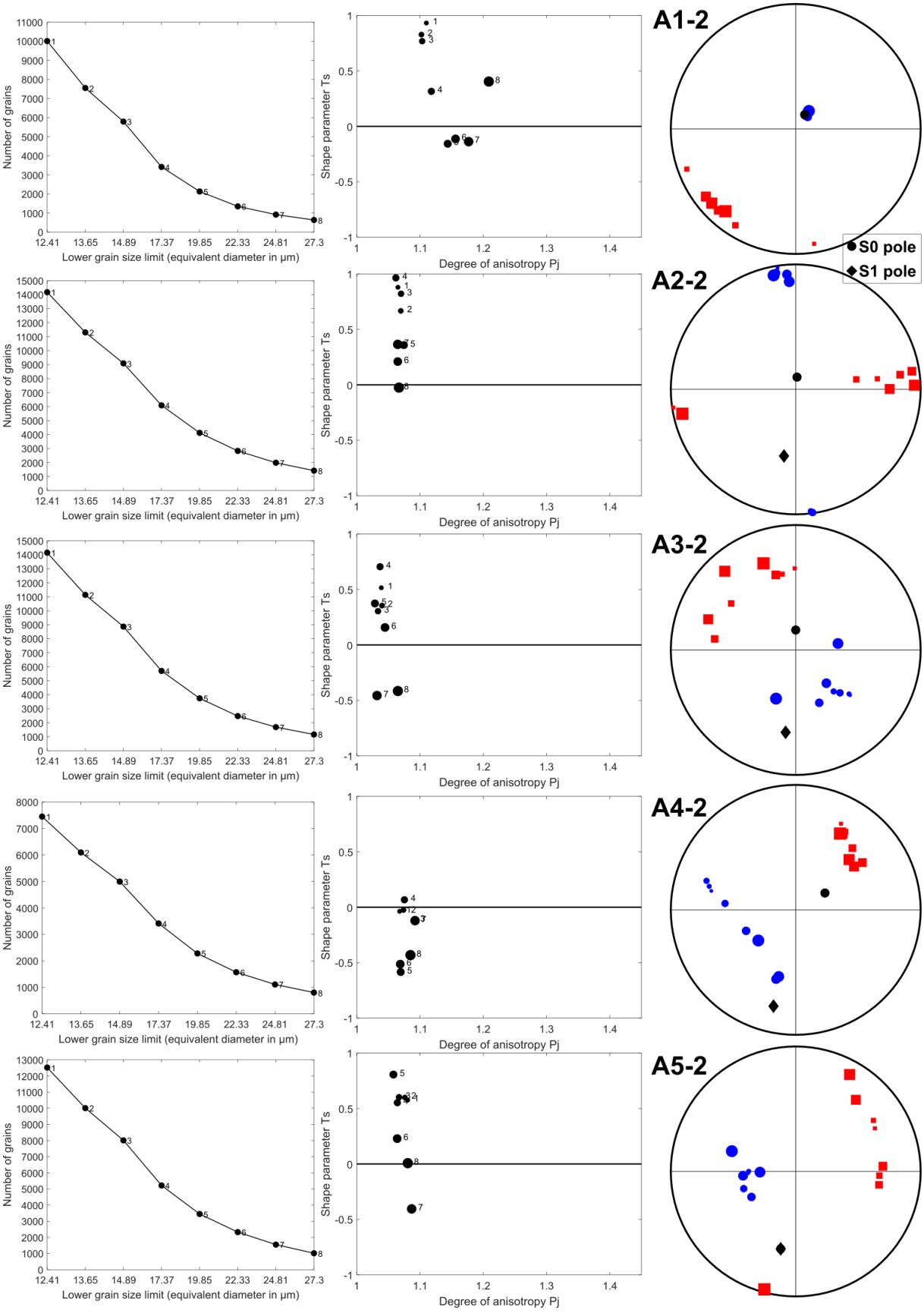

Figure 4.20: *Spatial distribution analysis of quartz in samples A1-2 to A5-2. Each row is dedicated to one sample. From left to right: number of grains in the eight classes with the lower threshold size limit, Jelinek diagram with the eight distribution ellipsoids data points, stereoplot of the principal directions* E_1 *and* E_3 *of the eight distribution ellipsoids in geographic coordinate system.*

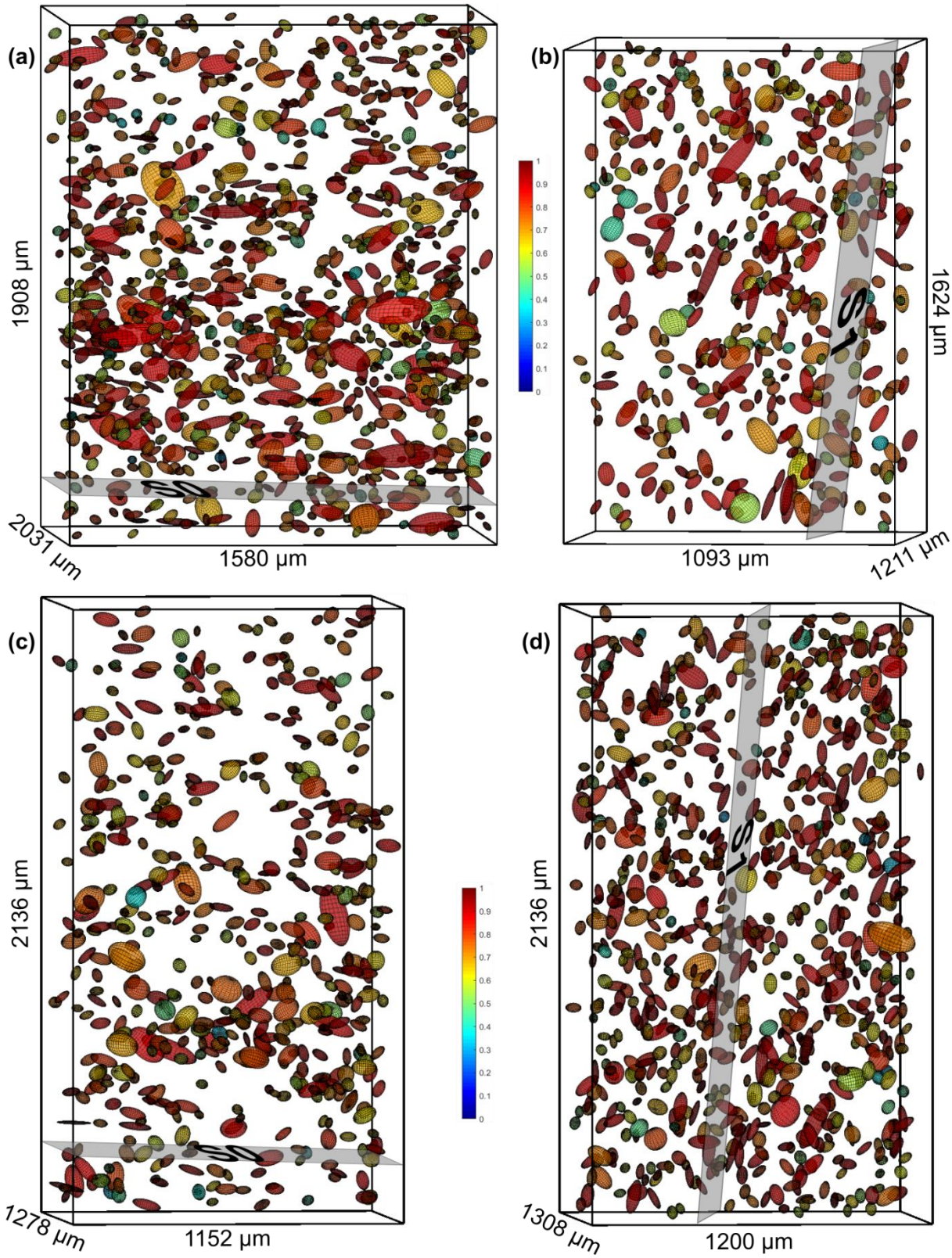

Figure 4.21: *3D visualization of spatial disposition of the individual ellipsoids of quartz grains in A1 (a), A5 (b), A1-2 (c) and A5-2 (d). All grains associated with these ellipsoids have at least a volume of 15625 µm³. The color of*

the ellipsoid is indicative of its shape anisotropy (0 = isotropic and blue, 1 = anisotropic and red). S0 plane direction is indicated for (a) and (c). S1 plane is indicated for (b) and (d).

4.3.5 SPO and CPO: contrasting patterns between quartz and calcite

4.3.5.1 Introduction

This section is devoted to the presentation of the results obtained by EBSD measurements on the samples A2 and A5. The EBSD acquisition was done on a section plane parallel to the generatrix of the XCT drill core (***Figure 4.22*****a**). We will present crystallographic data for calcite and quartz phases. The crystallographic directional data of grains belonging to these two phases will be compared to the morphologic directional data retrieved from XCT imaging. Quartz and calcite have trigonal symmetry (Borradaile and Jackson, 2010; Biedermann, 2018). The crystal forms are represented in ***Figure 4.22*****b**.

4.3.5.2 Results

In sample A2, the calcite phase represents 73.5 % of the total number of detected grains and quartz represents 22.9 %. In sample A5, calcite represents 65.8 % and quartz represents 30.1 %. A detected grain comprises a more or less important number of pixels. For both samples, the pixel size is 0.5 µm. When misorientation between neighboring data points is comprised between 1° and 10°, subgrains boundaries are defined. If this misorientation is superior to 10°, a grain boundary is defined.

We report size distribution, aspect ratio and grain orientation spread values (GOS) for calcite and quartz in ***Figure 4.23***. Note that the grain size is expressed as an area because the measurement is done in 2D. The aspect ratio corresponds to the ratio of the major axis to the minor axis of the best-fit ellipse of a grain. GOS corresponds to the average deviation in orientation between each point in a grain (i.e. each pixel) and the average orientation of the grain (Wright et al., 2011). Size distributions are similar for calcite and quartz in the samples A2 (***Figure 4.23*****a**)**.** The curves do not change significantly in the deformed sample A5 (***Figure 4.23*****d**). The mean grain size is around 10 μm^2 for calcite and quartz (***Table 4.3***). The distributions of the aspect ratio are remarkably similar for both phases and in the two samples (***Figure 4.23*****b** and ***Figure 4.23*****e**). The mean aspect ratio oscillates between 1.65 and 1.75 (***Table 4.3***).The distribution of GOS values indicates a greater dispersion of orientation within the quartz grains in sample A2 (***Figure 4.23*****c**) and in sample A5 (***Figure 4.23*****f**) compared to the values obtained for calcite grains. This is also reported by the calculation of the mean values (***Table 4.3***). However, the overall values remain low for both phases, generally under 3°. The size and aspect ratio obtained by EBSD may be irrelevant due to the specific sectioning in the sample preparation (***Figure 4.22*****a**). Hence, we provide the 3D data of the XCT in ***Table 4.4***. An increase in the aspect ratio (shape anisotropy) of calcite grains is noticeable while that of quartz remains stable.

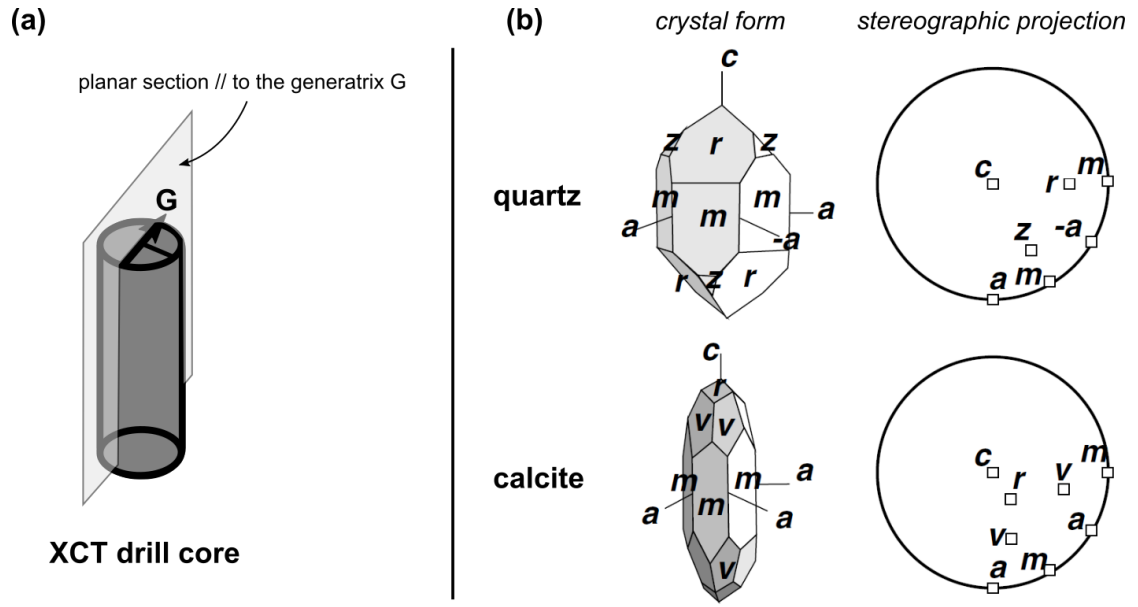

Figure 4.22: *(a) Planar section used for EBSD analysis. This section was prepared parallel to the generatrix of the XCT drill core and not to the bedding or cleavage. (b) Quartz and calcite crystal form (modified from Lloyd et al., 2011).*

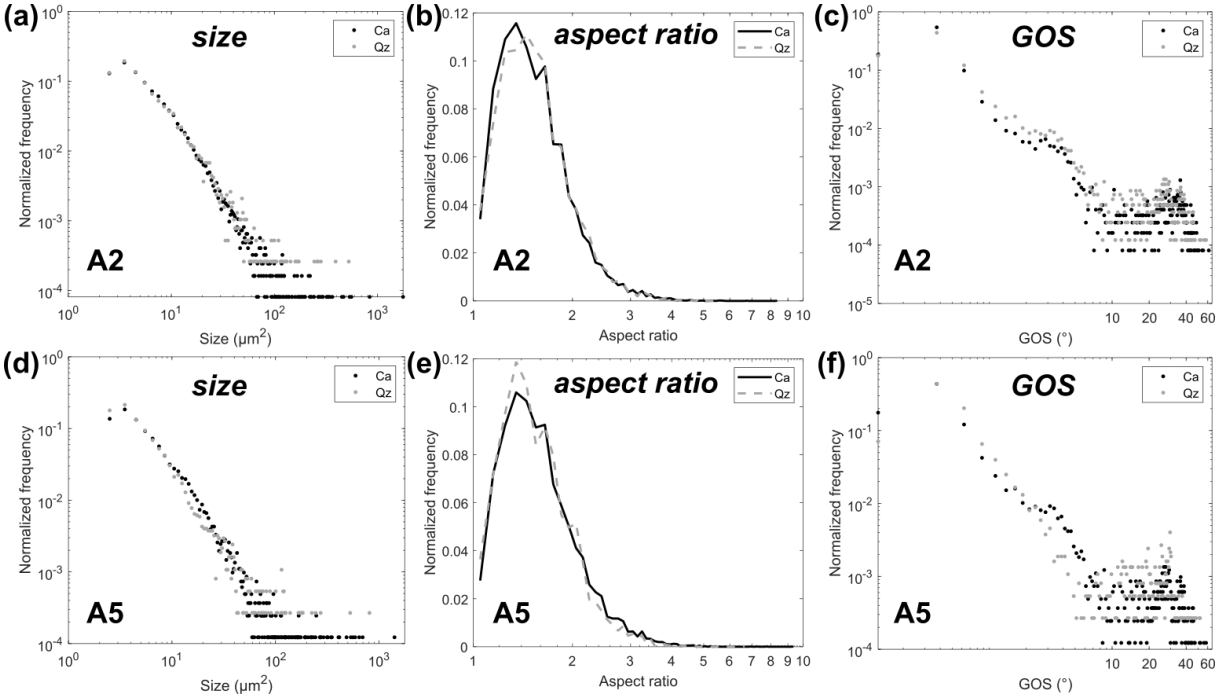

Figure 4.23: *Size (a), aspect ratio (b) and GOS (c) distributions of calcite (dark) and quartz (light gray) grains in sample A2. Size (d), aspect ratio (e) and GOS (f) distributions of calcite (dark) and quartz (light gray) grains in sample A5.*

Table 4.3: *Mean values of size, aspect ratio and GOS obtained from EBSD.*

	Mean size (μm²)		Mean aspect ratio		Mean GOS (°)	
	Calcite	Quartz	Calcite	Quartz	Calcite	Quartz
Sample A2	9.88	9.73	1.66	1.67	1.99	3.13
Sample A5	10.61	8.90	1.75	1.69	2.40	2.51

Table 4.4: ***Mean values and standard deviation of size (i.e. volume), aspect ratio (a/c of the grain ellipsoid) obtained from XCT.***

	Mean size (µm³)		Mean aspect ratio	
	Calcite	Quartz	Calcite	Quartz
Sample A2	9,006 ± 47,115	5,889 ± 16,223	2.20 ± 0.98	2.11 ± 0.70
Sample A5	8,730 ± 41,602	5,080 ± 11,883	2.66 ± 1.13	2.12 ± 0.70

The CPO results are provided in ***Figure 4.24*** and ***Figure 4.25***. In these figures, poles figures of *c*-axis {0001}, *a*-axis {11-20} and axis {10-10} (i.e. axis orthogonal to *m* face, ***Figure 4.22*****b**) obtained for the whole set of calcite and quartz grains are represented using density contours in equal area and lower hemisphere projections. The density values are expressed as multiple of uniform distribution (MUD). Note that a value of one MUD would signify a complete random distribution of axes orientation. In a pole figure, the CPO of grains are represented in the sample coordinate system. In our study, it corresponds to the plane parallel to the generatrix of the AMS drill core. Therefore, the 2D SPO data of grains identified by EBSD are not used, as the reference generatrix plane is not of particular interest. However, the 3D SPO results obtained by means of XCT are presented in regards to the CPO results in the same coordinate system.

In sample A2, the *c*-axis (i.e. the longest crystal habit) of calcite is parallel to (aligned in) the bedding plane with a MUD value of 3.34. This *c*-axis direction is roughly parallel to the lineation of calcite grains identified by XCT. The *c*-axis of quartz is more randomly distributed with a slight girdle. A maximum MUD of 2.87 is found in an oblique direction to the bedding pole. SPO results show that lineation of calcite and even more quartz display a girdle in the bedding plane. Their pole of foliation coincide with the pole of bedding. The intensity values of their SPO are comparable in this sample.

In sample A5, the *c*-axis of calcite is more scattered but a cluster close to the pole of cleavage is visible. The *c*-axis direction is thus quite similar to the $\boldsymbol{L_3}$ axis direction. The MUD value of CPO is rather weak (≈ 2 %). On the contrary, the foliation of calcite SPO (normal to the $\boldsymbol{L_3}$ axis) is strongly defined and parallel to the cleavage plane (maximum density ≈ 12 %). The results show that there is a discrete CPO of calcite grains with *c*-axis perpendicular to the cleavage plane and that there is a pronounced SPO of calcite aggregates with their short axis $\boldsymbol{L_3}$ perpendicular to the cleavage plane. The CPO of quartz is more pronounced (MUD = 4.31) with few dispersion of *c*-axis. This crystallographic axis is mostly oriented in an oblique position (≈ 45°) to the cleavage pole.

Further investigation of calcite and quartz CPO in sample A5 is done by defining subsets of the whole dataset. The first subset of calcite grains corresponds to the smallest grains that have an area between 0 µm² and 10 µm² (***Figure 4.26*****a**). These small grains may correspond to the recrystallized fraction of calcite. This subset represents 35 % of the data points belonging to calcite. For this subset, the *c*-axis is clearly perpendicular to the cleavage plane with a MUD of 2.80 and *a*-axis is parallel to the cleavage plane. The second subset corresponds to the most deformed calcite grains that have a local misorientation above 2° and below 5°. Local misorientation is a Kernel Average Misorientation (KAM). It calculates the average misorientation between every pixel and its surrounding pixels, and assigns the mean value to that pixel. We used a square grid of five pixels (2.5 µm side length) to calculate this component. To account for the grain boundary effect, a tolerance angle of 5° was employed to study small subgrain deformations in the grains. This subset represents 2.90 % of the data points belonging to calcite and thus it is a more selective criterion. However, it includes only small grains. For this subset,

the *c*-axis is again perpendicular to the S1 plane with a higher intensity (MUD = 6.5) and it attests for a CPO of calcite grains (***Figure 4.26*b**).

The first subset of quartz grains corresponds to the smallest grains that have an area comprised between 0 µm^2 and 10 µm^2 (***Figure 4.27*a**). This subset represents 34 % of the data points of quartz. The pole figure indicates that *c*-axes are almost randomly distributed (MUD = 1.82) and no CPO of small quartz is found. The second subset encompasses quartz grains that have a GOS above 20° (***Figure 4.27*b**). GOS values indicate the density of internal misorientations in the grains. This subset represents 7.64 % of the data points of quartz. The pole figure of *c*-axis give a strong and clear CPO with a MUD value that reaches 43. This *c*-axis orientation coincides with the main pattern observed for the entire set of quartz in ***Figure 4.25***. Interestingly, this *c*-axis orientation is approximately 45° oblique to the pole of cleavage but this direction is included in the asymmetric girdle of the L_3 axis of quartz. This asymmetric girdle attests for some shearing concerning quartz grains.

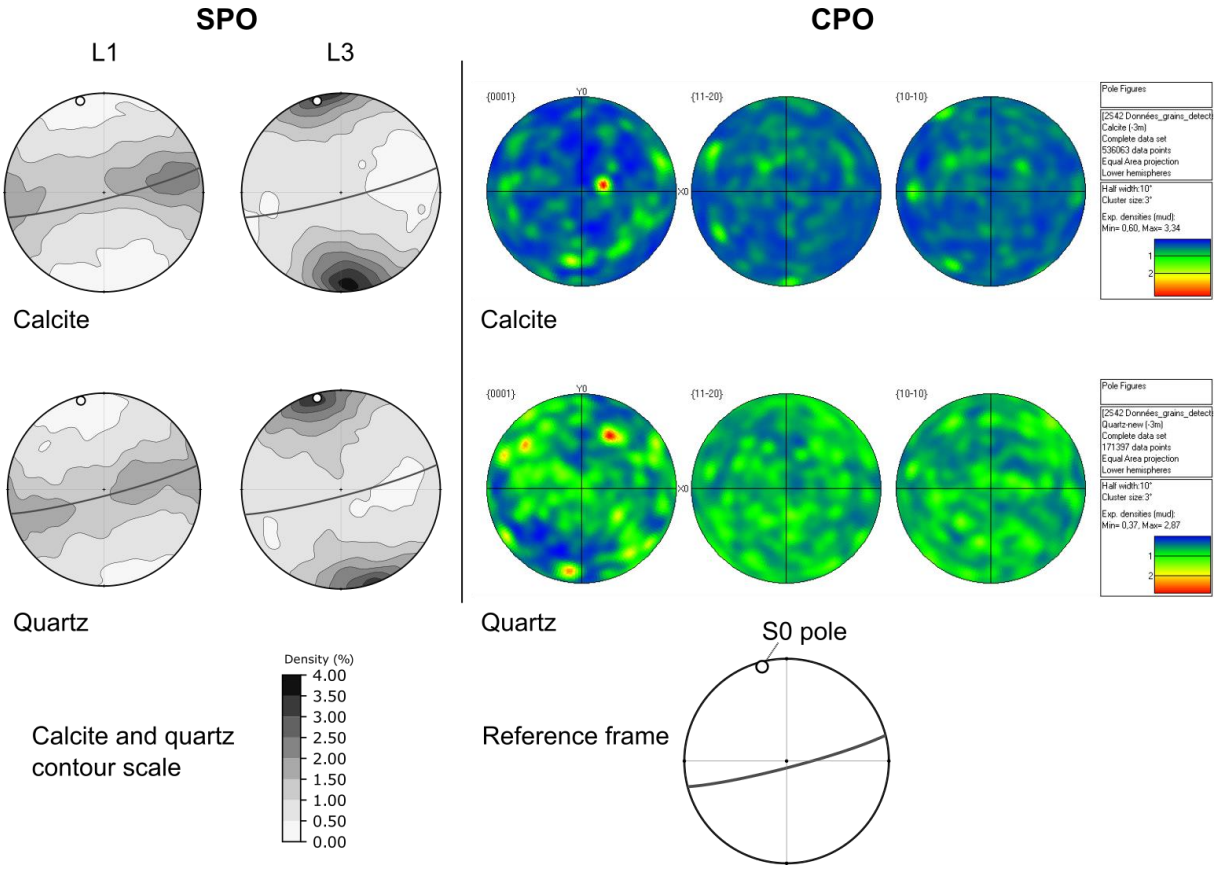

Figure 4.24: ***Sample A2. On the left: SPO data of calcite and quartz obtained by means of XCT. Common contour scale for both phases. On the right: EBSD pole figures of calcite and quartz. Mud: multiple of uniform distribution. The coordinate system is identical for all data.***

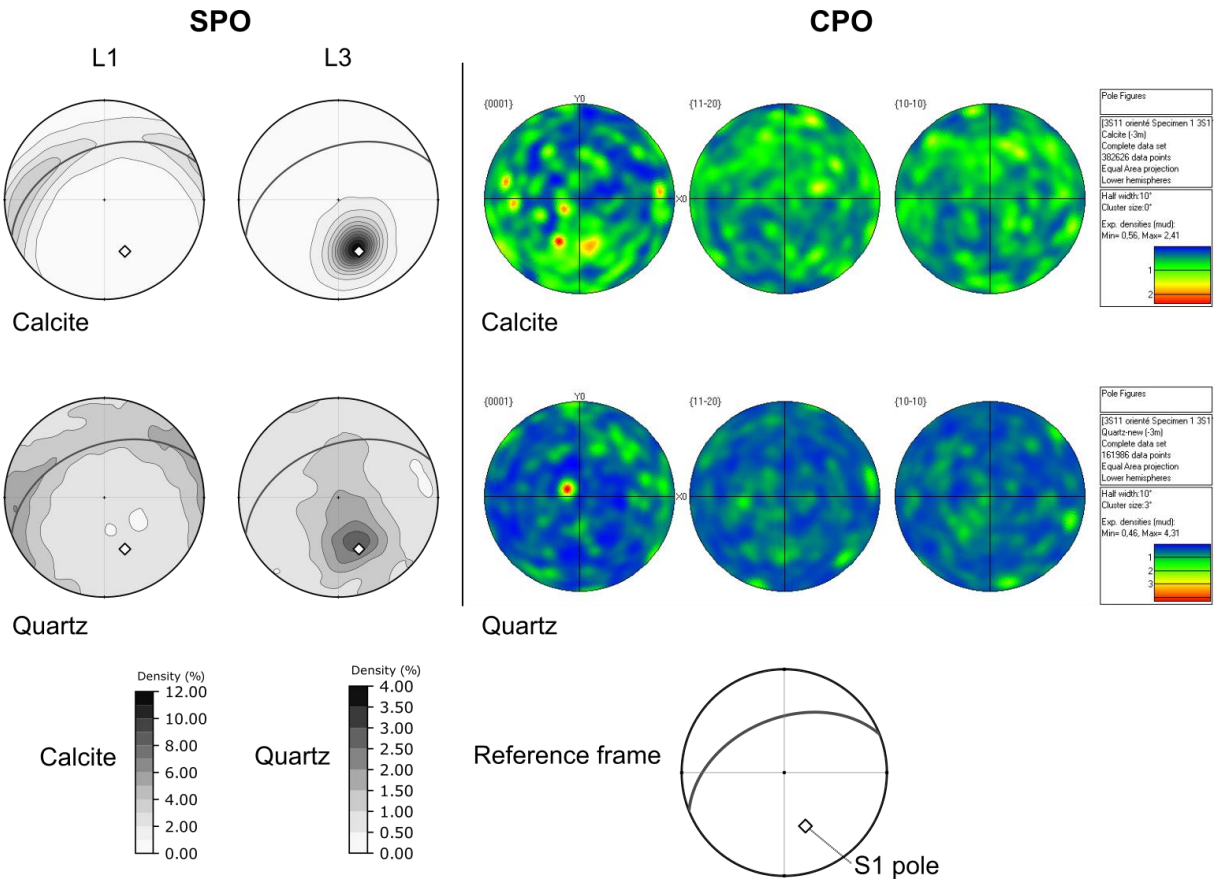

Figure 4.25: ***Sample A5. On the left: SPO data of calcite and quartz obtained by means of XCT. Different contour scale for calcite and quartz. On the right: EBSD pole figures of calcite and quartz. Mud: multiple of uniform distribution. The coordinate system is identical for all data.***

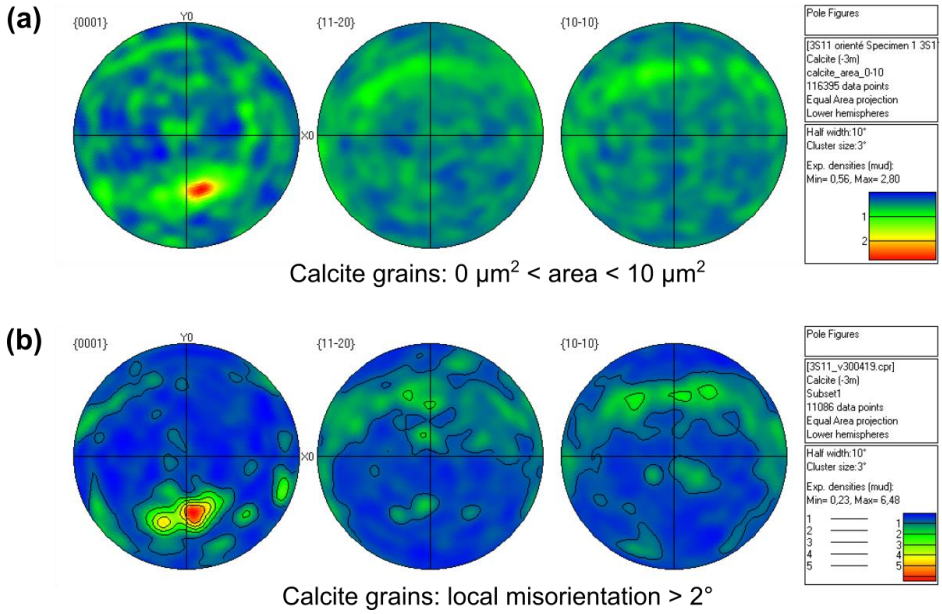

Figure 4.26: ***Subset analysis for calcite in sample A5.***

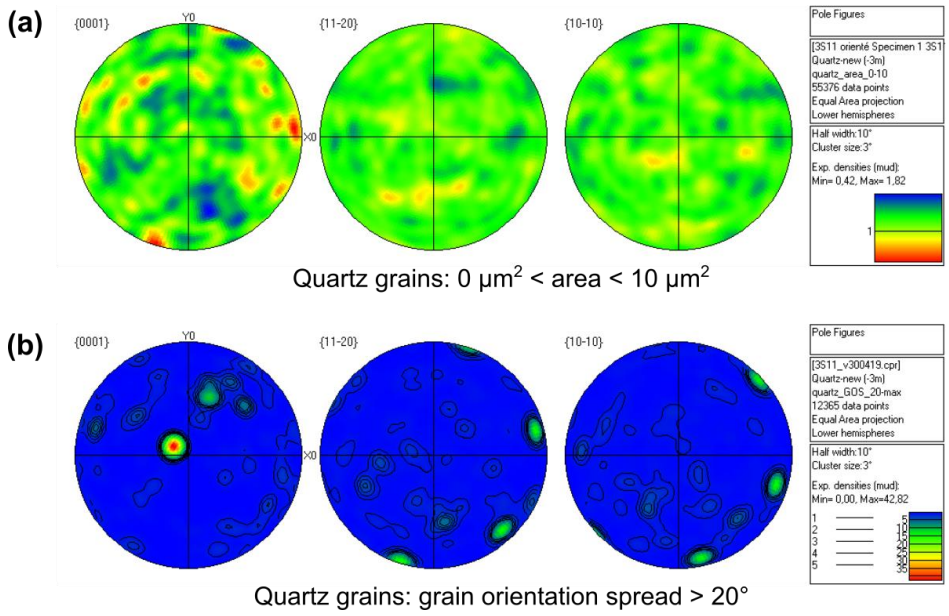

Figure 4.27: ***Subset analysis for quartz in sample A5.***

4.3.5.3 Discussion

The scalar grain shape data (size, aspect ratio) of calcite and quartz are quite similar in the two samples. GOS values are slightly higher for quartz grains.

In sample A2, calcite and quartz have similar SPO but calcite shows a better CPO than quartz. In sample A5, calcite has a strong SPO related to cleavage while it has a slight CPO. In this sample, quartz has also a SPO related to cleavage but this one is significantly weaker. Quartz displays a more pronounced CPO.

In both samples, we report a CPO of quartz grains. Near random quartz CPO measured by EBSD in shales and siltstones (displaying only a sedimentary fabric) have been observed by Valcke et al. (2006). These authors have reported a slight CPO for the siltstone sample but poor indexation obtained for shale was not prone to the investigation of quartz CPO. The virtual absence of quartz CPO have been demonstrated in many studies focused on fine-grained materials using different analytical techniques. No CPO has been observed for quartz in black shales from the Appalachian Plateau (Kuehn et al., 2019). Other crystallographic data obtained by means of X-ray diffraction in shales have shown no specific CPO of quartz (Wenk et al., 2008; Kanitpanyacharoen et al., 2011, 2012). In experimentally deformed clay-quartz aggregates measured by synchrotron hard X-rays, Voltolini et al. (2008) have also reported the absence of CPO of quartz. If we compare these data to our data of sample A2 that has a sedimentary fabric and may slightly record the tectonic shortening, the MUD value of quartz *c*-axis is more noticeable. Weak CPO for quartz with *c*-axes aligned in the bedding plane have been reported by Wenk et al. (2010) in Kimmeridge shale. We do not have this pattern for quartz but rather for calcite grains. The *c*-axis is roughly parallel to $\boldsymbol{L_1}$ and aligned in the bedding plane for calcite. This might have to do with carbonate cementation effects. In any case, this *c*-axis direction is not in accordance with that observed for calcite in high maturity sample (gas window) of Posidonia shale by Kanitpanyacharoen et al. (2012), which was oriented perpendicular to bedding plane.

The weak or random CPO of quartz has also been observed in tectonically deformed fine-grained rocks such as slates (Wenk et al., 2019, 2020; Cárdenes et al., 2021). Thus, we would have expected a more random scheme for quartz CPO in our sample A5 but there is a noticeable quartz CPO in this sample. Wenk et al. (2019) have investigated the quartz CPO and SPO by means of synchrotron hard X-rays and

synchrotron XCT in a slate sample from the Ardennes. This slate falls in the greenschist facies as temperature in this area was at least 300°C (Fielitz and Mansy, 1999). This is significantly higher than the temperature experienced during the tectonic deformation of sample A5 collected near Sigüés. Even in this highly deformed slate, Wenk et al. (2019) have found no particular CPO of quartz. On the contrary, the SPO of quartz grains was strong in this study, possibly much more important than our measurement of quartz SPO. They measured an average 3D aspect ratio of 2.70 for quartz grains but in a rather small VOI (260 x 260 x 80 μm^3). We report an average 3D aspect ratio of 2.12 for quartz in sample A5 (***Table 4.4***). Even in other metamorphosed (high pressure-low temperature) clastic sedimentary rocks, some studies did not find evidence for dislocation creep of quartz (Schwarz and Stöckhert, 1996; Trepmann and Stöckhert, 2009). Clastic quartz grains showed a marked SPO and flattened form (2D aspect ratio of 3-4 for clastic quartz in a metagreywacke highlighted by Trepmann and Stöckhert, 2009). The bulk CPO inferred by X-ray diffraction (Schwarz and Stöckhert, 1996) and EBSD (Trepmann and Stöckhert, 2009) were weak. These studies have suggested and demonstrated that dissolution-precipitation creep is the dominant deformation process over the dislocation creep to account for this absence of quartz CPO. The existence of a CPO is generally linked to dislocation creep mechanism, although some authors have demonstrated that a pressure-solution driven CPO may develop in some cases (Stallard and Shelley, 1995; Bons and Den Brok, 2000). Concerning calcite, this phase may show a slight CPO with *c*-axis perpendicular to the cleavage plane in slates (Wenk et al., 2020). This is in accordance with our results in the most deformed sample A5. Therefore, we have shown that calcite *c*-axis is parallel to calcite $\boldsymbol{L_3}$ axis and, if we extrapolate, to the $\boldsymbol{K_3}$ axis measured by AMS. Calcite exhibits an inverse fabric (Rochette, 1988; Borradaile and Jackson, 2010) with its longest crystal habit parallel to $\boldsymbol{K_3}$ and thus normal to the cleavage plane.

Reported strain data from local misorientation (KAM) and grain orientation spread (GOS) are quite low ($\leq 3°$) for both calcite and quartz and independent of the sample deformation state. These low values indicate that no intracrystalline or plastic deformation may have occurred in sample A5. Generally, low strain values are associated to recrystallized grains (Cross et al., 2017). In this sample the smallest grains of calcite and quartz (***Figure 4.26*****a** and ***Figure 4.27*****a**), which include the recrystallized fraction of the grains, show different pole figures. Recrystallization of calcite may occur in the S1 plane while crystal axes of recrystallized quartz are randomly distributed. There is possibly a cleavage-controlled recrystallization of the calcite. The pressure-solution mechanism may explained the random CPO of small quartz grains as it has been suggested in slates (Wenk et al., 2019). The investigation of quartz CPO to determine the shear movement in mylonitic rocks has been an important research topic but here we are dealing with rocks affected by very-low grade metamorphic conditions ($Temperature \leq 200°C$). Dislocation creep of quartz is known to take place at temperature of at least 300°C in deformed rocks (Passchier and Trouw, 2005). Therefore, the quite strong CPO of quartz grains observed in sample A5 (***Figure 4.25***) and in the second subset (***Figure 4.27*****b**) of this sample are probably due to inherited deformation state of detrital grains. It may be delicate to associate this strong CPO to rocks deformed in the local tectonic conditions. Furthermore, we have observed slightly higher GOS values for quartz. Higher GOS value may indicate higher internal strain of quartz grains and it is typical of relict grains (Cross et al., 2017). Quartz grains with significant values of GOS may correspond to relict detrital grains with inherited strain and CPO. If these detrital grains have a large area (see ***Figure supp 1c***), they integrate more data points and this can explain the intensity of the quartz CPO in sample A5. This hypothesis of relict detrital grains implies that high GOS quartz grains should not be affected by dissolution-precipitation creep.

4.4 Conclusion

In this multi-technique study, we have seen that the combination of XCT and EDS are relevant to characterize fine-grained rocks. We have shown that, by working at low X-ray energy with a lab-based XCT instrument, the major phases in marly rocks or calcareous shales are quite identifiable and can be extracted through an image processing analysis. From low X-ray attenuation to high X-ray attenuation, these phases are respectively the pore space, quartz, calcite and pyrite. The very fine-grained matrix composed of a mixture of clays, microquartz and microcalcite is not resolvable at the spatial resolution obtained by conventional X-ray imaging. We have worked with X-ray images having a voxel resolution ranging from 1 µm to 1.5 µm. From these images, we have demonstrated that the segmentation of pore space and individual silt-sized grains of the main phases is valuable. The subsequent three-dimensional shape fabric analysis of pore space and silt grains has shown that the evolution of pores and calcite are similar while quartz and pyrite have more features in common.

We have shown that the first set of samples (A1 to A5) analyzed was representative of the macroscopic evolution of the rock fabric observed in the outcrop. In order to test the repeatability of the measurement performed on rock volume of about 3 mm^3, we have analyzed a second set of samples (A1-2 to A5-2). Inter-sample results were in accordance but subtle differences have been noted. The major differences have been observed when the intensity of the tectonic fabric increases.

The spatial distributions of rigid grains such as quartz in these rocks is more delicate to interpret. However, a possible strain quantification by means of this approach can be done in the uncleaved samples.

Actually, the Sigüés site appears to be an excellent natural laboratory to study the microstructures in fine-grained rocks. The main advantage of this outcrop is the opportunity to study the same rock unit showing different deformation states. In addition, other analytical techniques and geophysical techniques could be experimented.

Overall, this work offers new perspectives of investigations for the study of fine-grained rock fabric in 3D and in various geological contexts. The interesting results obtained on the site of Sigüés generate the temptation to experiment this shape fabric analysis elsewhere. Fine-grained rocks coming from a site presenting similarities with Sigüés could be studied by means of XCT to evaluate the reliability of the method presented. In addition, it would provide new insight into the characterization of microstructures at the silt-sized grain scale and perhaps answers to remaining questions. Lehigh Gap in Pennsylvania (USA) is one of those very well studied sites where many works have been carried out to characterize the microstructure evolution in a progressive transition from mudstone to slate. Recently, Boiron et al. (2020) have compared the magnetic fabric evolution in the two sites but the quantification of shape anisotropy and SPO of silt-sized grains in 3D has never been evaluated. This is the object of the next chapter.

5 Unraveling microstructure of Lehigh gap's Martinsburg shale by means of X-ray imaging

5.1 Aims

The Lehigh Gap outcrop has been intensively studied since the sixties. It has been described as a natural laboratory to study a strain gradient in mudrocks and many publications have improved our knowledge of the processes involved in cleavage development (Holeywell and Tullis, 1975; Wintsch, 1978; Woodland, 1982; Lee et al., 1984, 1986; Housen and van der Pluijm, 1990, 1991; Wintsch et al., 1991, 1996; Housen et al., 1993b; Ho et al., 1995; van der Pluijm et al., 1998; Hirt et al., 2004). The transition, from shale with a sedimentary fabric to slate with a tectonic (cleavage) fabric, takes place on approximately 130 m and has been characterized by many analytical and imaging techniques. However, 3D X-ray imaging has never been applied and may provide complementary insights. In this chapter, we will discuss the "strain gradient" appellation of this well-known geological site. A synthesis comparing the results of this chapter to those of Sigüés will be proposed in the general discussion of the thesis (section ***9.2.1***). Here we want to highlight the usefulness of XCT as a complementary technique to describe rock fabric and to propose new insights on the deformed rocks of Lehigh Gap. A difference should be noted about the geometry of the outcrop. Contrary to Sigüés, the transition takes place down the stratigraphic series (or oblique to the bedding) due to the dip of bedding exposed at the outcrop. Thus, the monitoring of the shape fabric cannot be made for the same bed as opposed to the Sigüés case.

5.2 Geological setting, previous works and new samples

5.2.1 Review

The Lehigh Gap outcrop is located at the junction of the Great Valley and the Valley and Ridge sections of the central Appalachian fold and thrust belt in Eastern Pennsylvania, USA (***Figure 5.1***). The central Appalachian fold and thrust belt results from the late Paleozoic Alleghanian orogeny involving the collision between Laurentia and Gondwana continents (Stamatakos et al., 1996). At Lehigh Gap locality, a deformation gradient can be studied over a hundred meters in the shale/siltstone and greywacke beds of the Martinsburg Formation (Upper Ordovician) (***Figure 5.2*****a**). The gradient is illustrated by the development of a cleavage that affects the Pen Argyl Member turbiditic series of the Martinsburg Formation (Housen et al., 1993b). Photographs of the outcrop are provided in ***Figure 5.2*****b**. Furthermore, the reader can virtually visit the outcrop of Lehigh Gap thanks to a wonderful job by Martha Villegas Soto, Dave Anastasio, Claudio Berti and Al Bodzin from Lehigh University (https://gisweb.cc.lehigh.edu/lehighgapvirtualtour/#).

All the studies agree in identifying a zone relatively free of cleavage to the north of the outcrop, with however some others pencil-like and slickensides structures. The north part of the outcrop coincides also with the contact between the Ordovician Martinsburg Fm with the conglomerates of the Silurian Shawangunk Fm (***Figure 5.2*****a**). This contact corresponds to an unconformity and the Blue Mountain décollement (Epstein et al., 1974; Epstein and Lyttle, 1993). Then, moving south, cleavage gradually develops from pencil cleavage to slaty cleavage. This cleavage, perpendicular to the bedding beyond 60 m from the contact, results from a regional layer parallel shortening (LPS) acquired at the end of

the Paleozoic during the Alleghanian orogeny (Housen et al., 1993b; Wintsch et al., 1996). Engelder and Engelder (1977) estimated as much as 15% shortening due to this north-northwest LPS in the Appalachian Plateau (***Figure 5.1*****b**). More recently, using previously published data (including those of Engelder and Engelder, 1977) and new strain data from distorted fossils and distribution of quartz grains, Sak et al. (2012) suggested 13% LPS in the Appalachian Plateau and 20% LPS in the Valley and Ridge province. Peak burial temperature of the Martinsburg Fm is estimated at approximately 270-320°C by Conodont colour alteration indices (Epstein et al., 1977; Gray, 1997). Lee et al. (1986) have suggested a peak temperature of ≈ 230°C. The origin of the gradient is not discussed much by the authors, who repeat the initial suggestion of Epstein and Epstein (1969). They proposed that the massive sandstone unit of the Shawangunk Fm uncomfortably overlying the Martinsburg Fm, acts as a strain/pressure shadow for cleavage (Epstein and Epstein, 1969; Epstein, 2006).

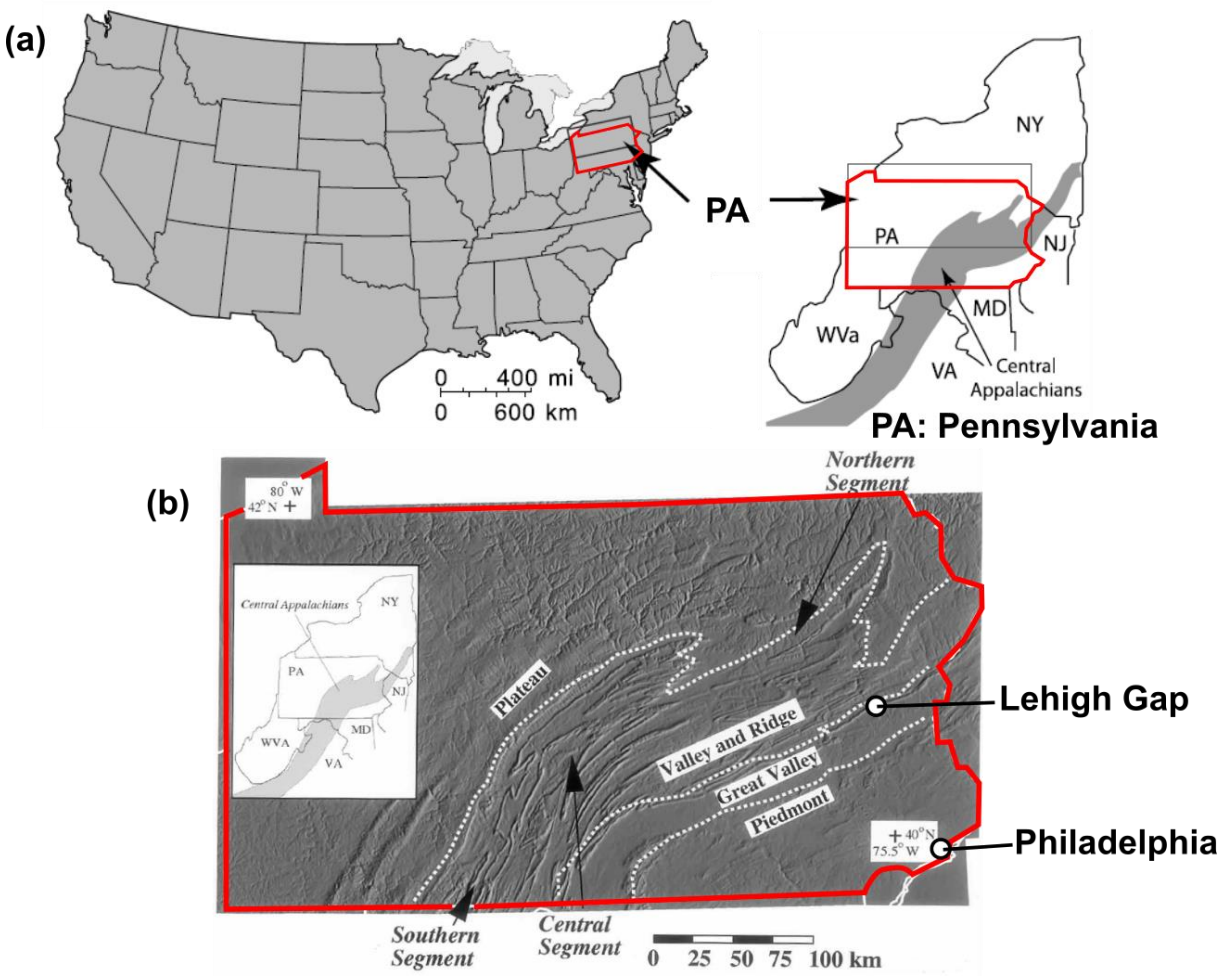

Figure 5.1: ***(a) Map of the United States of America and zoom in the Pennsylvania state and the Central Appalachians (modified from Milliken et al. 2013). Digital elevation model of Pennsylvania and location of Lehigh Gap (modified from Gray and Stamatakos, 1997).***

The Martinsburg formation consists of quartz (≈45%), illite (≈35%), chlorite (≈10%) and feldspar (≈10%) (Lee et al., 1986). This bulk chemical composition remains globally constant along the outcrop (Lee et al., 1986; Ho et al., 1995). The clay fraction has been intensively studied by physical, geochemical, and electron microscopy methods (Beutner, 1978; Wintsch, 1978; Lee et al., 1984, 1985, 1986). The magnetic mineral fraction, including clays and magnetite, has also been the subject of several publications (Housen et al., 1993b; Ho et al., 1995). If we restrict ourselves to the studies dealing specifically with the fabric of clays and magnetites, we can see that major trends are emerging (***Figure***

5.2c). For the sake of simplicity, we focus only on the bulk foliation and we separate the outcrop into three zones. In zone 1 only pencil structures are identified (0 - 60 m). In zone 2 a pencil cleavage fabric is dominant (60 - 100 m), corresponding to the transition zone of Ho et al. (1995). Ultimately, in zone 3, a slaty cleavage affects both the fine siltstones and the more sandy beds.

The analysis of the bulk fabric provided by the anisotropy of magnetic susceptibility technique (AMS) attests to a foliation largely governed by clays, and more specifically by chlorite (Housen and van der Pluijm, 1990, 1991). In zone 1, the bulk magnetic foliation is oblique to the bedding. The foliation is distributed between bedding and orientation of cleavage that develop in zones 2 and 3. This pattern is also found in zone 2, however, with some poles of the magnetic foliation that are parallel to the cleavage pole. It was initially noted that the transition from bedding-controlled to cleavage-controlled foliation was abrupt at ≈ 80 m (Housen and van der Pluijm, 1990), but this observation has been reviewed by a more recent sampling study that better averages the trends (Hirt et al., 2004). In zone 3, the magnetic foliation is parallel to the slaty cleavage. Similarly, the X-ray pole figure data of Holeywell and Tullis (1975) were in favor of an abrupt change of chlorite and mica from bedding fabric to cleavage fabric but Ho et al. (1995) later showed that the shift was gradual.

This evolution portrayed by AMS studies is quite consistent with that of the clay fabric detected by X-ray texture goniometry. This is especially true for chlorite, less for illite that is controlled by bedding in zone 1. This difference between illite and chlorite has been the subject of several interpretations. Indeed, it was detected early on that the chlorite foliation was at an angle of about 20°-30° to the bedding (Holeywell and Tullis, 1975; Wintsch, 1978). Ho et al. (1995) also reported this observation but they noticed that this angular difference decreases from the contact to about 60 m. To account for this obliquity, several explanations have been proposed, ranging from diagenetic origin (Wintsch, 1978) or from a precursor detrital mineral (Lee et al., 1984) but this initial difference between illite and chlorite remains an unresolved issue (Ho et al., 1995). The bulk magnetic foliation of magnetites has been studied by with the anisotropy of anhysteretic magnetization technique (AARM). In Zone 1 and Zone 3, this foliation is controlled by bedding and cleavage respectively. In zone 2, a transition appears to occur with magnetic foliation poles distributed between the bedding pole and the cleavage pole.

Perhaps one of the most discussed issues in the Martinsburg Formation shales concerns the mechanisms of clay reorientation, either by mechanical reorientation in an unconsolidated fine-grained sediment (Maxwell, 1962) or by pressure solution creep (Holeywell and Tullis, 1975; Beutner, 1978; Wintsch et al., 1991). Lee et al. (1986) were favorable in syntectonic crystallization over pressure solution. This concept of recrystallization under stress has been demonstrated by van der Pluijm et al. (1998), based precisely on Lehigh Gap samples and other slates from the study of Ho et al. (1996). van der Pluijm et al. (1998) stated that mechanical processes (grain kinking and rotation) of phyllosilicates are favoured in relatively low-energy environments (i.e. low thermal and strain energy), whereas chemical processes (grain dissolution and neocrystallization) of phyllosilicates are favoured in relatively high-energy environments.

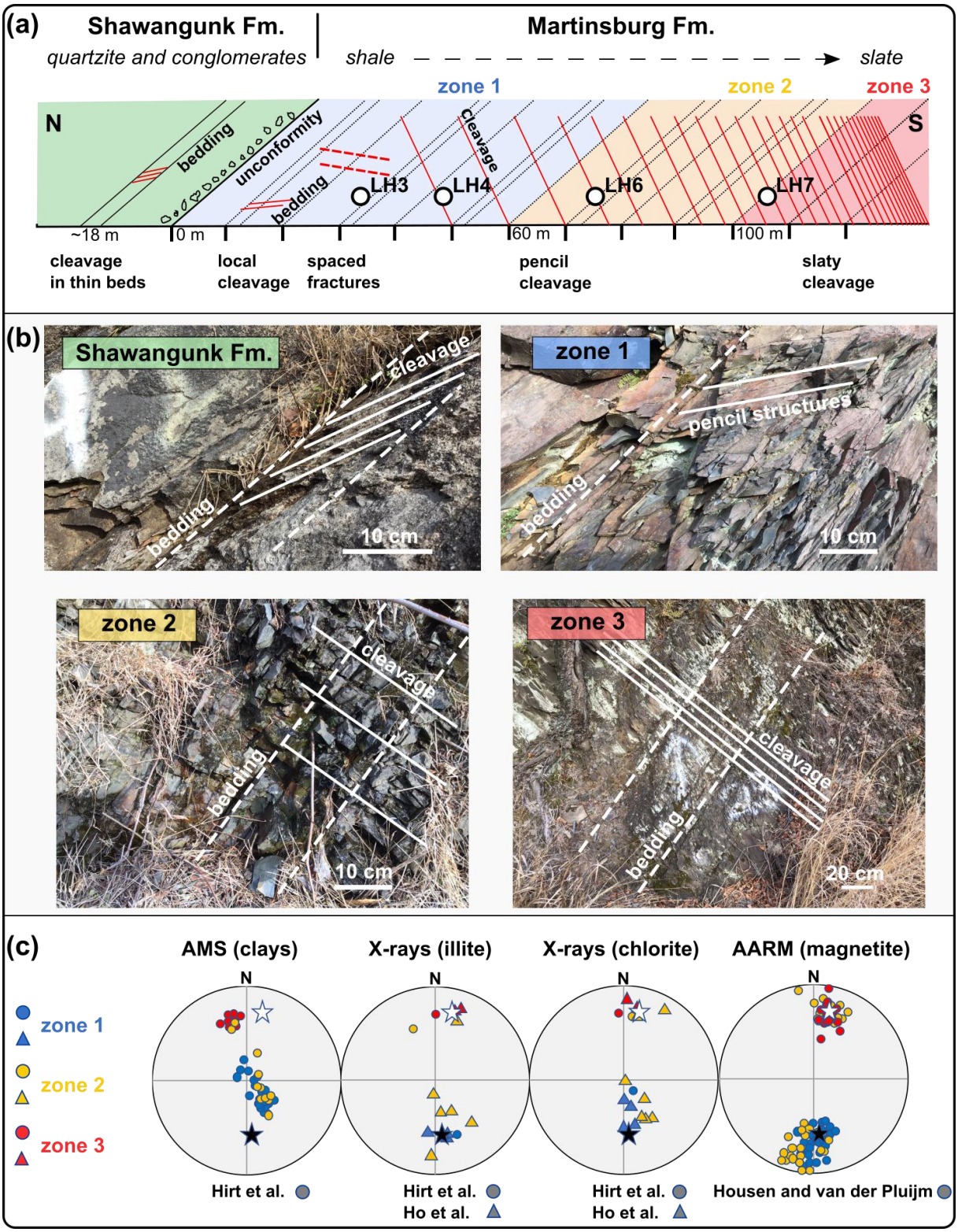

Figure 5.2: *(a) Schematic illustration of the main macroscopic structures at Lehigh Gap. The location of the newly collected samples (LH3, LH4, LH6 and LH7) are indicated. (b) Representative photographs of the different zones of the outcrop. (c) Compilation of the orientation data of the pole of foliation obtained in previous studies (Housen and van der Pluijm, 1991; Ho et al., 1995; Hirt et al., 2004).*

5.2.2 Introduction to our study

The structural observations of the Martinsburg shales are very similar to those described in previous studies. From the first few meters of Zone 1, we observed metric fracture planes dipping slightly to the south (***Figure 5.2*b**). A very weak cleavage zone is suggested 2 m from the contact, dipping slightly to the north. More clearly, we observed a millimeter-spaced cleavage in the thin beds of the Shawangunk Formation, dipping ≈ 20° to the south (***Figure 5.2*b**). This observation was briefly described by Epstein et al. (1974) and reported by Gray and Mitra (1993), but this observation has not been further explored. The angular relationship between bedding and cleavage is that of an overturned fold system.

In this study, we took oriented bloc specimens along the outcrop to cover the entire transition. Four samples (LH3, LH4, LH6 and LH7) of about 2 mm in diameter have been scanned by X-ray computed tomography (XCT) to provide 3D grain shape fabric of silt-sized grains and pore space. LH3 and LH4 samples were taken, in the almost non-cleaved area (zone 1), at 32 m and 49 m respectively from the contact between Martinsburg formation and Shawangunk formation. LH6 in the pencil-cleavage area (zone 2) at 75 m from the contact and LH7 in the slaty-cleavage area (zone 3) at 107 m from the contact. Therefore, we will provide new data on the fabric of other mineral phases across the three main zones using XCT.

5.3 Results

5.3.1 Microstructures from XCT

The VOI extracted from the XCT images of the four samples can be visualized in ***Figure 5.3***. Samples LH3 and LH4 were taken with their z-axis (longest dimension) perpendicular to the S0 plane. Samples LH6 and LH7 were extracted with their z-axis perpendicular to the S1 plane. All the XCT images were obtained with a voxel resolution of 2 µm. We can see that the lower part of sample LH3 appears clearer in the 3D view, attesting for an enrichment in high X-ray absorption components. Samples LH4 and LH6 appear more homogeneous in this global view. The sample LH7 stands out from the others due to its coarser composition. There is also an anastomosing network of relatively attenuating laminae that wrap the gray clasts in this sample.

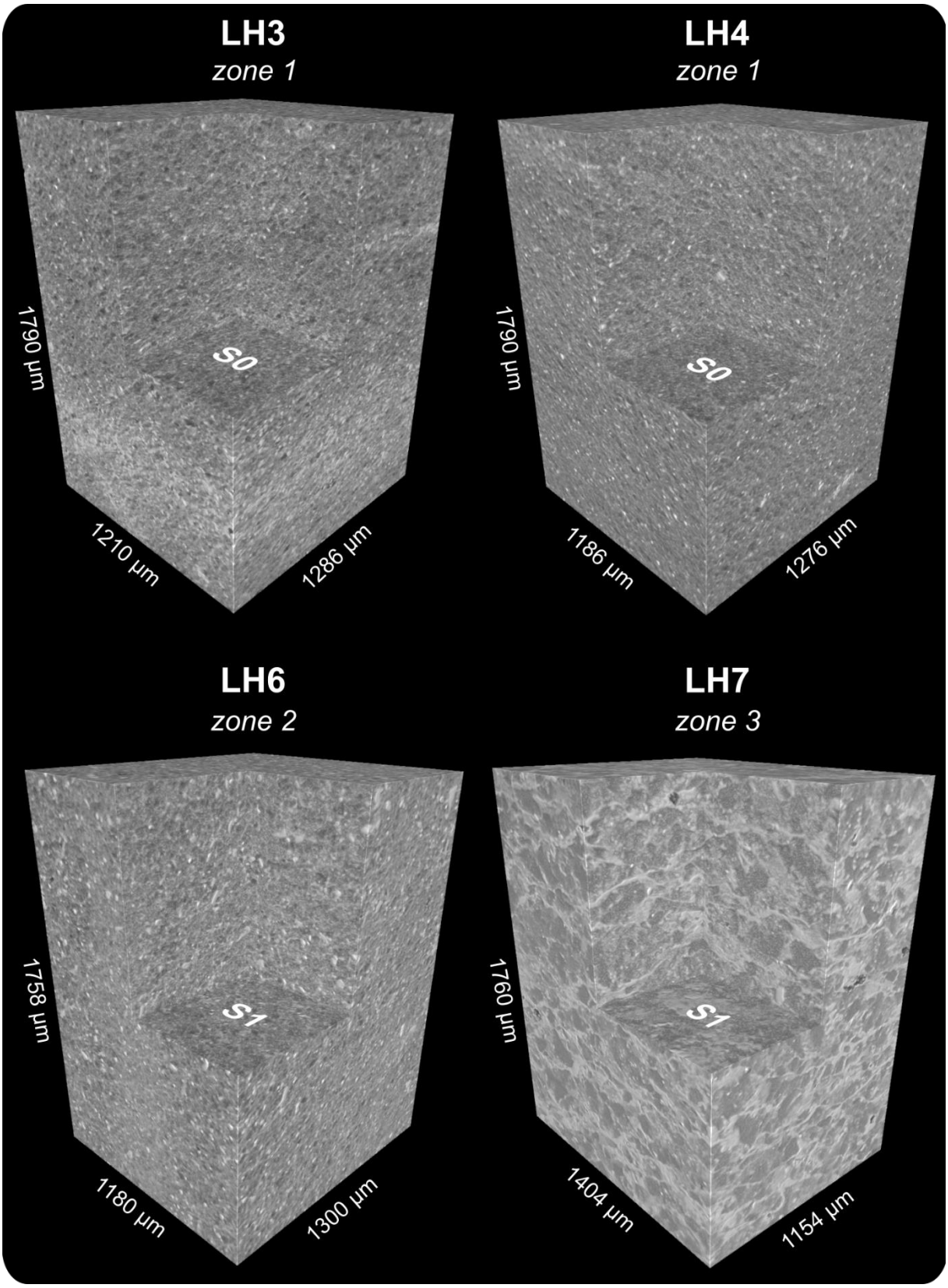

Figure 5.3: ***3D view of the VOI of each sample obtained by XCT. The VOI size oscillates between 2.7 and 2.85 mm³. Note the coarser sample LH7 displaying an anastomosing laminae network.***

The major phases were identified by similar gray tones as in the samples of Sigüés. The main difference here is the depletion in carbonate content of the rock samples. In addition, we have been able to

compare the different gray levels of XCT to SEM images obtained in a previous study and that help in the identification of the different components (***Figure 5.4*a**). Silt-sized grains of quartz appear as individual elongated or rounded polygons all embedded in a fine-grained matrix in the 2D images (***Figure 5.4*b** and ***Figure 5.4*c**). Light gray rods correspond to detrital mica and bright spots may correspond to pyrite and iron oxide. This last phase will be labelled as pyrite throughout this chapter. We will focus our interest on three main phases, which are quartz, pyrite and pore space.

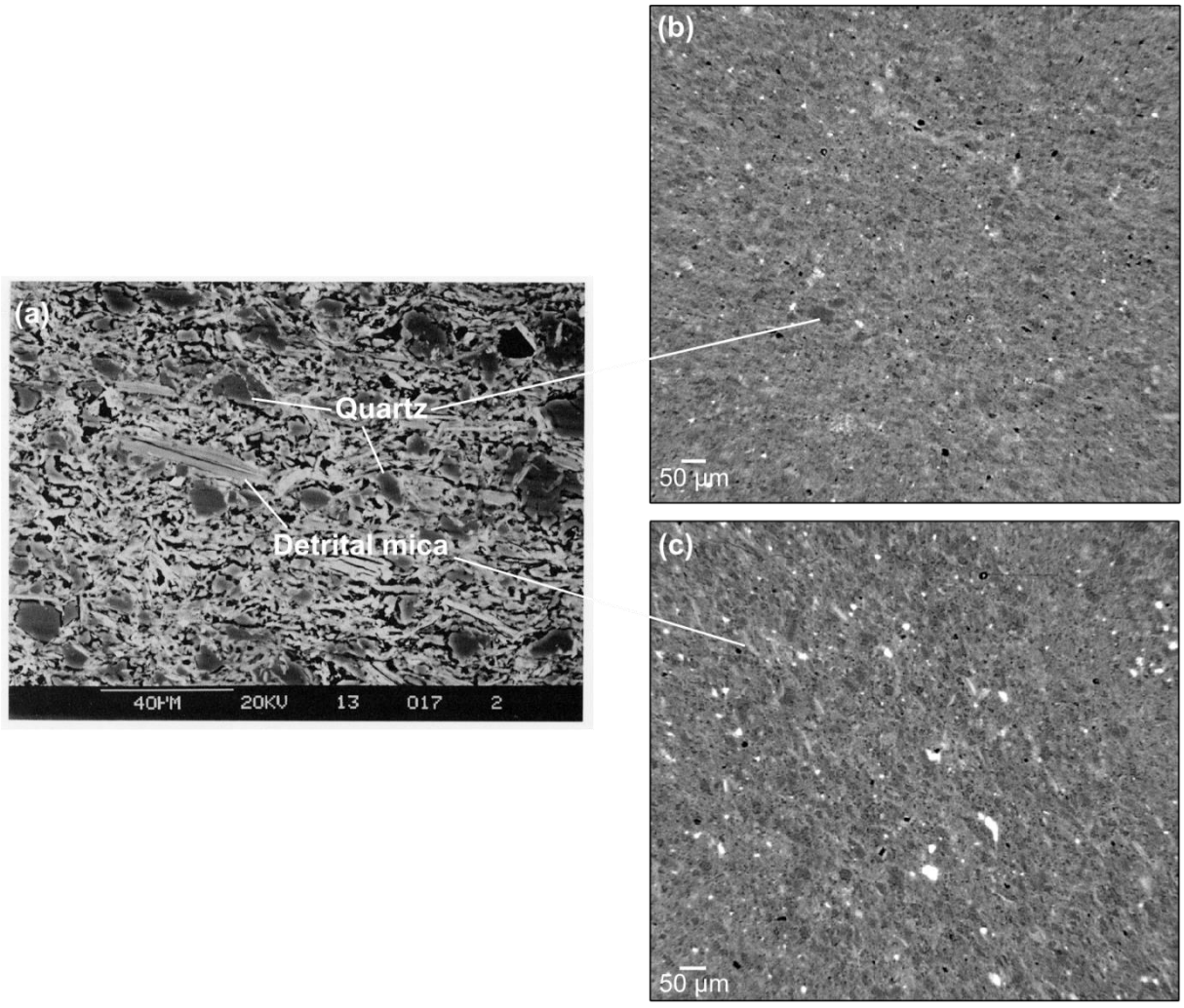

***Figure 5.4:** (a) Photomicrograph (Backscattered Electrons from Scanning Electron Microscope) of an uncleaved mudstone (zone 1) taken from Wintsch et al. (1996). No feldspar has been reported by the author in this photomicrograph. (b) XCT image of sample LH3. (c) XCT image of sample LH6. Silt-sized quartz appear as dark gray in the BSE image and can be identified in the XCT images (b) and (c). Large detrital mica/phyllosilicates appear in light gray in the BSE images and can be seen as well in the XCT image in (c). Bright spots correspond to pyrite and iron oxide in (b) and (c).*

We propose four oriented slices of the XCT images in a geographic coordinate system, in the same perspective as the outcrop is seen in the field, in ***Figure 5.5***. This allows for comparison with macroscopic fabric observed in the outcrop. S-C like structures are observed in sample LH3 with C-planes corresponding to S0 and S-planes to S1. Some bright hairy phyllosilicates are aligned with the S-planes. In LH4, the bedding is hardly visible. However, a secondary plane, illustrated by the alignment of a few quartz grains, plunges to the North at a lower angle compared to S0. In sample LH6, cleavage is marked by small planes of pressure solution. A thinner relict bedding layer can be seen in the top part of the image. However, the general arrangement remains difficult to see due to the similar

intensity of the bedding and the cleavage fabric. For LH7, the pressure-solution seams (PSS) are well marked, with a spacing of about 100 µm. They correspond to the network of bright laminae observed in ***Figure 5.3***.

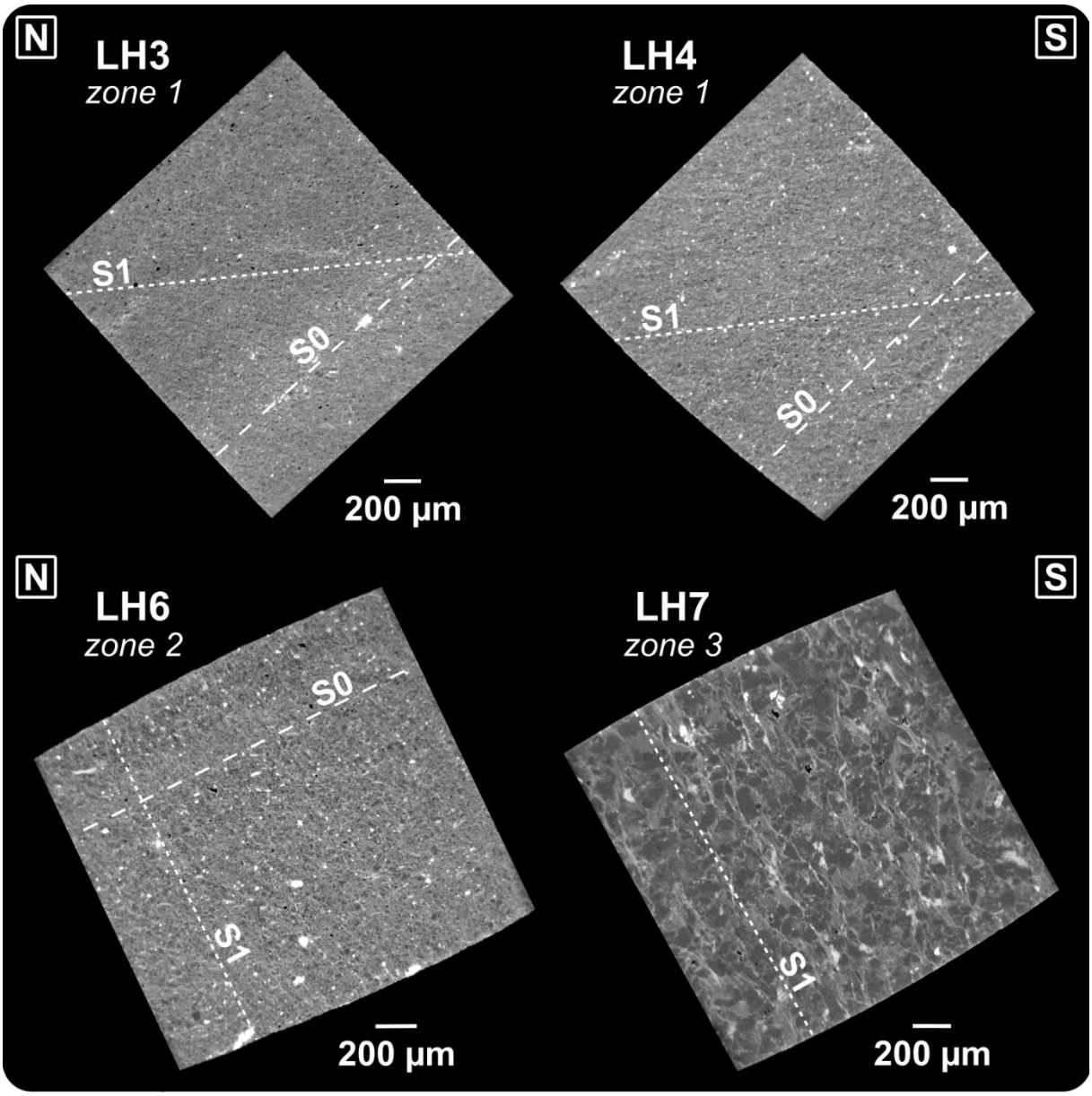

Figure 5.5: ***XCT cross sections through the four samples in a common geographic coordinate system with the north on the left side and the south on the right side. Strain intensity is supposed to increase from LH3 to LH7. Note the preservation of a begging layer in the pencil-cleavage sample LH6.***

5.3.2 Grain shape data

Quartz and pyrite grains as well as pore space have been segmented in the XCT images. The cut-off threshold size for all phases is 1000 µm^3, which corresponds to a particle of 125 voxels (5 voxels side length). The number of particles and their corresponding volume fractions are reported in ***Table 5.1***. The distribution of the particle size, the shape parameter $\boldsymbol{T_G}$ and the degree of anisotropy $\boldsymbol{P_j}$ of their equivalent ellipsoid measured in the four samples are given in ***Figure 5.6***.

Table 5.1: ***Volume of interest for each sample. Number and volume fraction of quartz, pyrite and pores particles in this VOI, obtained after segmentation, cleaning and removal of boundary grains.***

Sample	LH3	LH4	LH6	LH7
Volume of interest (mm^3)	2.785	2.709	2.697	2.852
Number of quartz grains	7,287	17,035	12,966	5,344
Volume fraction of quartz (1)	0.71 %	2.40 %	1.83 %	21.51 %
Number of pyrite grains	764	2,758	1,836	436
Volume fraction of pyrite (2)	0.08 %	0.32 %	0.22 %	0.12 %
Number of pores	1,284	149	839	512
Volume fraction of pores (3)	0.09 %	0.01 %	0.07 %	0.12 %
(1)+(2)+(3)	0.88 %	2.73 %	2.12 %	21.75 %

Sample LH3 shows the smallest grains of quartz (***Figure 5.6***). Similar size distributions are observed in LH4 and LH6. The coarser composition of LH7 is confirmed by the size distriubtion of quartz grains. No specific discrimation can be made concerning the shape of the ellipsoids ($\boldsymbol{T_G}$) associated to quartz grains. The distribution of the degree of anisotropy shows that LH4 and LH6 do have the most anisotropic populations. Quartz grains are less anisotropic in LH3 and even less in the slaty cleaved sample LH7.

Pyrite particles are smaller than quartz (***Figure 5.6***). The size distribution diagram does not show significant differences in the four samples but the samples are provided in different ways in pyrite (see ***Table 5.1***). As it was the case in the Sigüés case study, the shape of pyrite ellipsoids is more homogeneously distributed with approximately equal number of prolate and oblate forms. A slight enrichment in oblate ellipsoid is seen for sample LH7. Sample LH6 and LH7 contain more anisotropic pyrite compared to LH3 and LH4.

Pore particles are smaller than quartz and pyrite (***Figure 5.6***). Larger pores are present in sample LH7. Oblate ellipsoids are more represented in samples LH3 and LH4. In terms of the degree of anisotropy ($\boldsymbol{P_j}$), there is no significant difference in its distribution across the four samples.

In addition we provide in ***Figure 5.7*** the distributions of the equivalent diameter, ellipsoid filling parameter and sphericity. The sphericity of quartz grains decreases along the outcrop. A similar trend is observed for pore space. The distribution of the ellipsoid filling of pore space indicates that these particles are not well constrained from the segmentation of our XCT images.

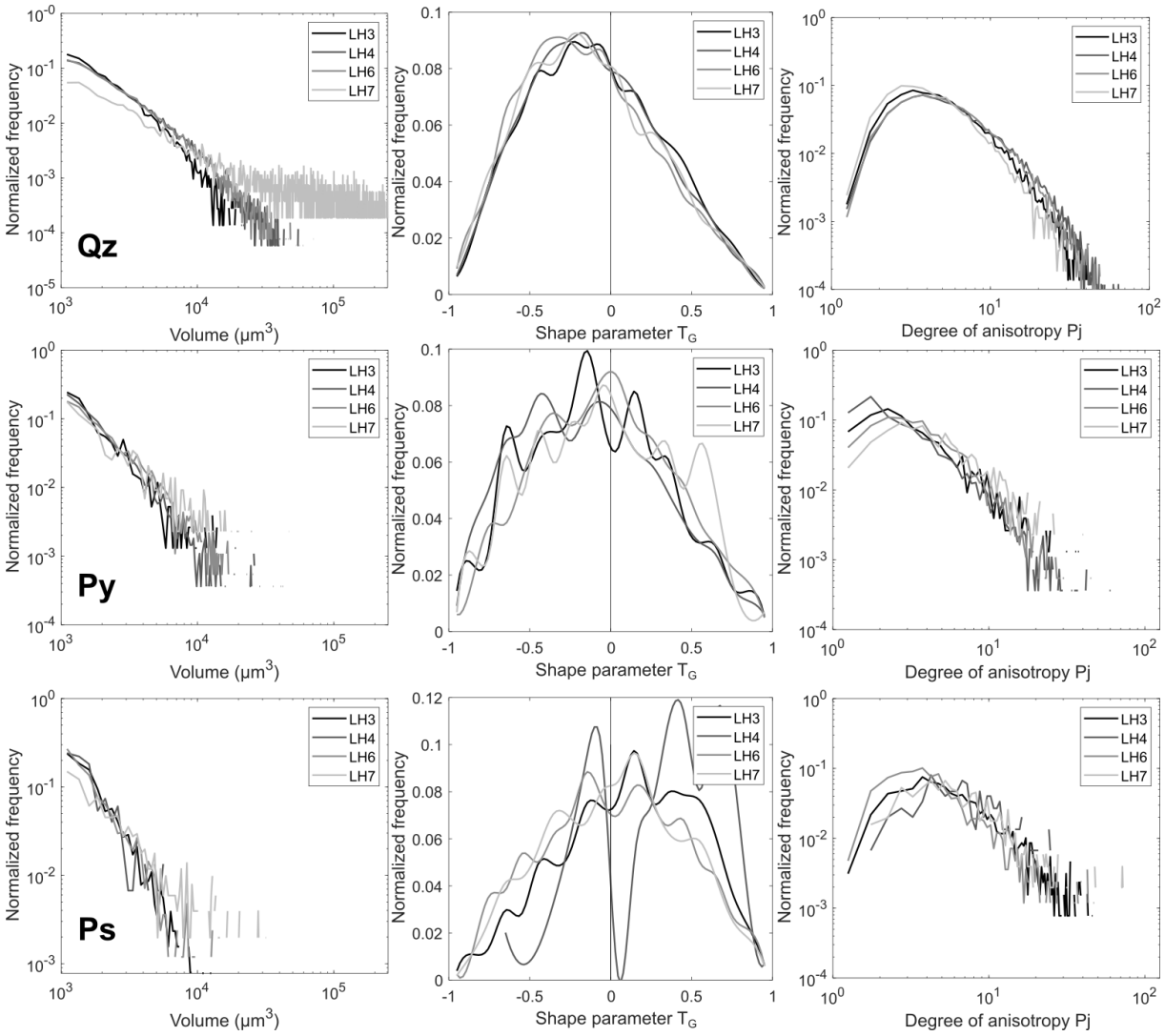

Figure 5.6: ***Normalized distributions of grain volume, shape parameter*** T_G ***and degree of anisotropy*** P_j ***of the grain ellipsoid for the three main phases across the four samples (LH3, LH4, LH6 and LH7). Qz: quartz, Py: pyrite, Ps: pore space.***

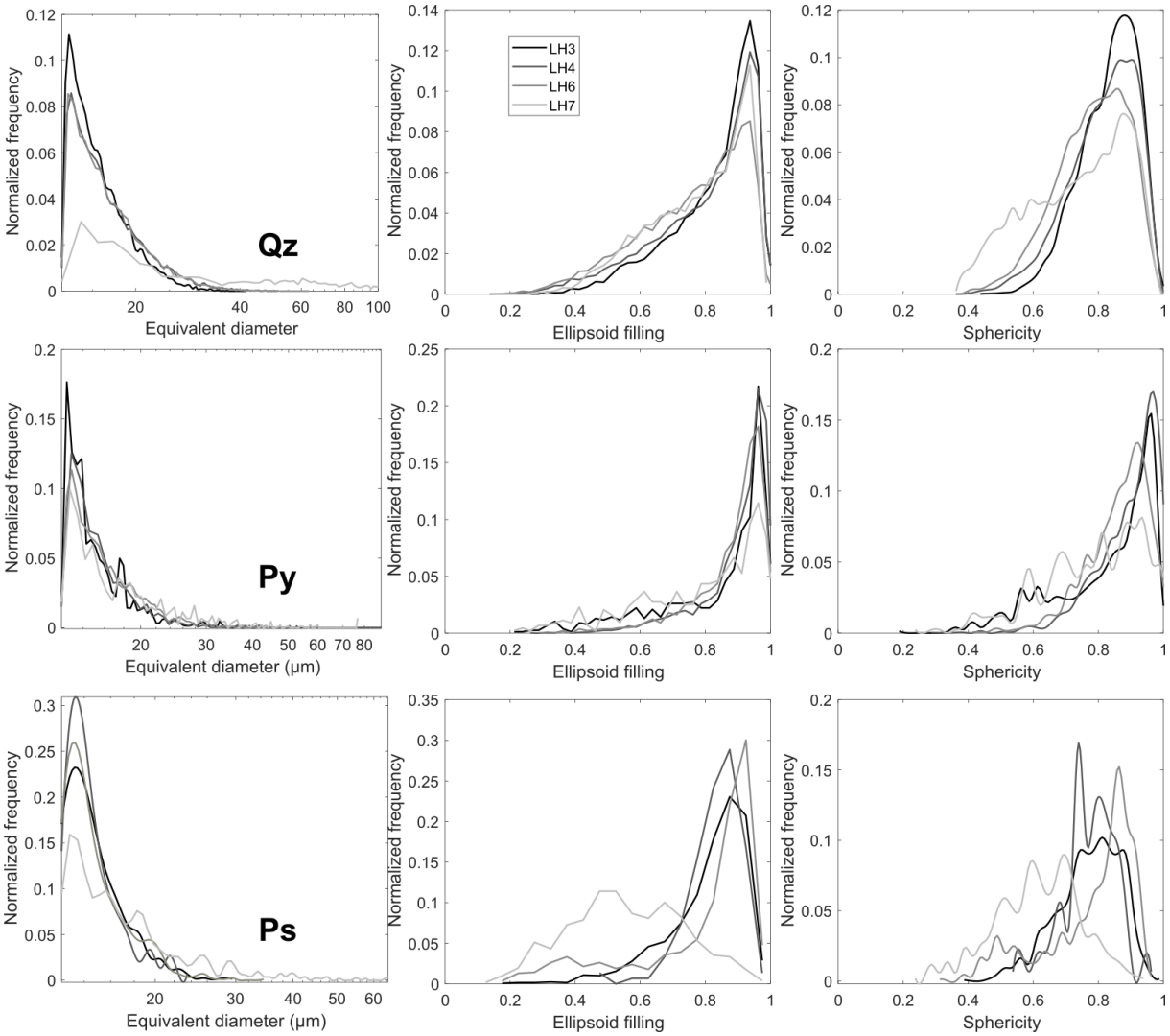

Figure 5.7: ***Normalized histogram of equivalent diameter, ellipsoid filling and sphericity of the three main phases across the four samples. Qz: quartz, Py: pyrite, Ps: pore space.***

5.3.3 SPO analysis

The directions of $\boldsymbol{L_3}$ axes of quartz, pyrite and pores extracted from the four samples are shown in ***Figure 5.8*** as well as the principal directions ($\boldsymbol{L_{1m}}$, $\boldsymbol{L_{2m}}$ and $\boldsymbol{L_{3m}}$) of their corresponding bulk shape fabric ellipsoid which are superimposed on the same stereoplot. The 3D isosurface rendering of the three above-mentioned phases located in the VOI is illustrated in the same figure. The scalar data ($\boldsymbol{T_B}, \boldsymbol{P_j}$) associated to the bulk fabric ellipsoids are provided in ***Figure 5.9***.

As previously seen in ***Figure 5.3***, we can notice the enriched layer of high-density mica/illite and pyrite grains at the bottom of sample LH3 and the depletion in quartz grains in this part. The sample LH4 is more homogeneous but some layers appear enriched in pyrite and other in quartz. In the left part of sample LH6, we can see a depleted band that corresponds to the bedding layer seen in ***Figure 5.5***.

A striking observation from the directional data of $\boldsymbol{L_3}$ axes is the obliquity of foliation of quartz and pores regarding bedding plane S0 in samples LH3 and LH4. These two samples belong to the zone 1, which is supposed to be uncleaved. On the contrary, pyrite shows a foliation subparallel to bedding in these two samples. Most importantly, the intensities of SPO of quartz and pore space are strong with

maximum densities of up to 7% and up to 11% in sample LH3. The maximum densities are even more pronounced for these two phases in sample LH4 with 9% for quartz and 14% for pore particles. The SPO of pyrite is more intense in sample LH3 than LH4 (up to 5% in LH3). The bulk directional data confirm the differences in SPO. The northwest gentle dipping foliation plane of quartz and pore particles (i.e. the plane containing $\boldsymbol{L_{1m}}$ and $\boldsymbol{L_{2m}}$ axes) is obliquely oriented compared to S0. The foliation plane of pyrite is subparallel to S0. In ***Figure 5.9***, the fabric ellipsoid obtained by mean tensor computation is not perfectly oblate but rather triaxial oblate in sample LH3 and LH4 ($\boldsymbol{T_G} < 0.5$). The strength of the quartz shape fabric is confirmed by the high values of the degree of anisotropy ($P_j > 2.3$). On the same diagram, the data points of pyrite indicate an oblate fabric ellipsoid ($\boldsymbol{T_G} > 0.75$) with more anisotropy for sample LH3. The shape of the fabric ellipsoids of pore space is more oblate than quartz but less oblate than pyrite. The main difference is the stronger fabric of pores with $\boldsymbol{P_j} \geq 3$. To summarize, in the two samples coming from the non-cleaved area (i.e. zone 1), we have pyrite grains that have a bedding fabric while quartz and pores have a 15°-20° off fabric to bedding with stronger anisotropy. It is also important to note that the fabric anisotropy of quartz has an intensity (i.e. $\boldsymbol{P_j}$ value) comparable to that observed for calcite in the most deformed samples of Sigüés (see ***Figure 4.18***).

In sample LH6 from the pencil-cleavage area (zone 2), all phases display girdle development of $\boldsymbol{L_3}$ axes between S0 and S1 poles (***Figure 5.8***). $\boldsymbol{L_3}$ axes of quartz tend to parallelize cleavage pole with a significantly weaker SPO as compared to the previous samples. Its maximum density reaches 4% at its best. Foliation of pores is poorly defined with weak intensity. Pyrite shows an intermediate foliation with no dip. These elements confirm that pencil cleavage fabric dominates here. However, it appears that there is an obliquity of our S0 pole measure taken in the field compared to the obtained stereplots for this sample. The principal directions of the fabric ellipsoids indicate an intersection lineation fabric with $\boldsymbol{L_{1m}}$ parallel to S0-S1 intersection and intermediate positions of the $\boldsymbol{L_{3m}}$ axes. These elements characterize a pencil-cleavage fabric, which is demonstrated by the shape parameter $\boldsymbol{T_G}$ for quartz and pore space (***Figure 5.9***). These elements are also in agreement with field observations. The fabric ellipsoid of pyrite is triaxial here. All phases show a decrease in the degree of anisotropy.

In sample LH7 from the slaty cleavage area (zone 3), all phases have a cleavage-controlled fabric with $\boldsymbol{L_3}$ axes parallel to the S1 pole. As seen from the density values, the preferred orientation are the weakest in this sample. The bulk directional data allow us to classify the quartz and pore space fabric as intersection lineation fabric with cleavage-controlled foliation. The shape fabric of pyrite can be defined as a cleavage fabric with $\boldsymbol{L_{1m}}$ axis suggesting shear in the S1 plane. The Jelinek diagrams confirm the weak SPO in this sample (***Figure 5.9***). Only quartz does have a moderate fabric anisotropy with $\boldsymbol{P_j} = 1.5$. The shape of its fabric ellipsoid is triaxial. More oblateness is seen for pore space ($\boldsymbol{T_G} \approx 0.35$) and significantly more for pyrite ($\boldsymbol{T_G} \approx 0.7$). Note that this sample has coarser quartz grains as shown by the surface rendering of the segmented grains compared to the first three samples (***Figure 5.8***).

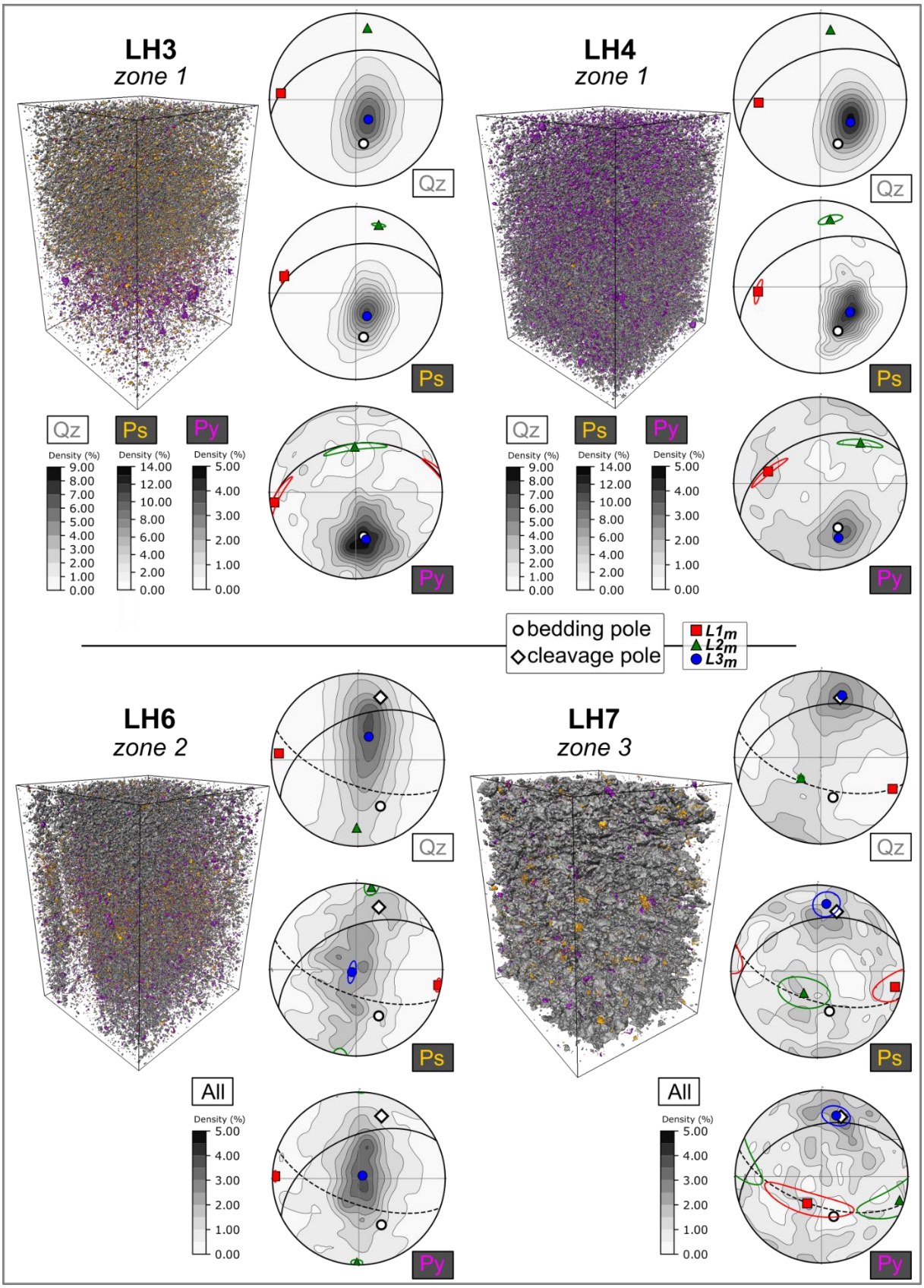

Figure 5.8: *Directional data of the SPO analysis. The 3D segmentation of quartz (gray), pore space (yellow) and pyrite (magenta) is provided by an isosurface rendering. Dimensions of the VOI are equal to those mentioned in Figure 5.3.*

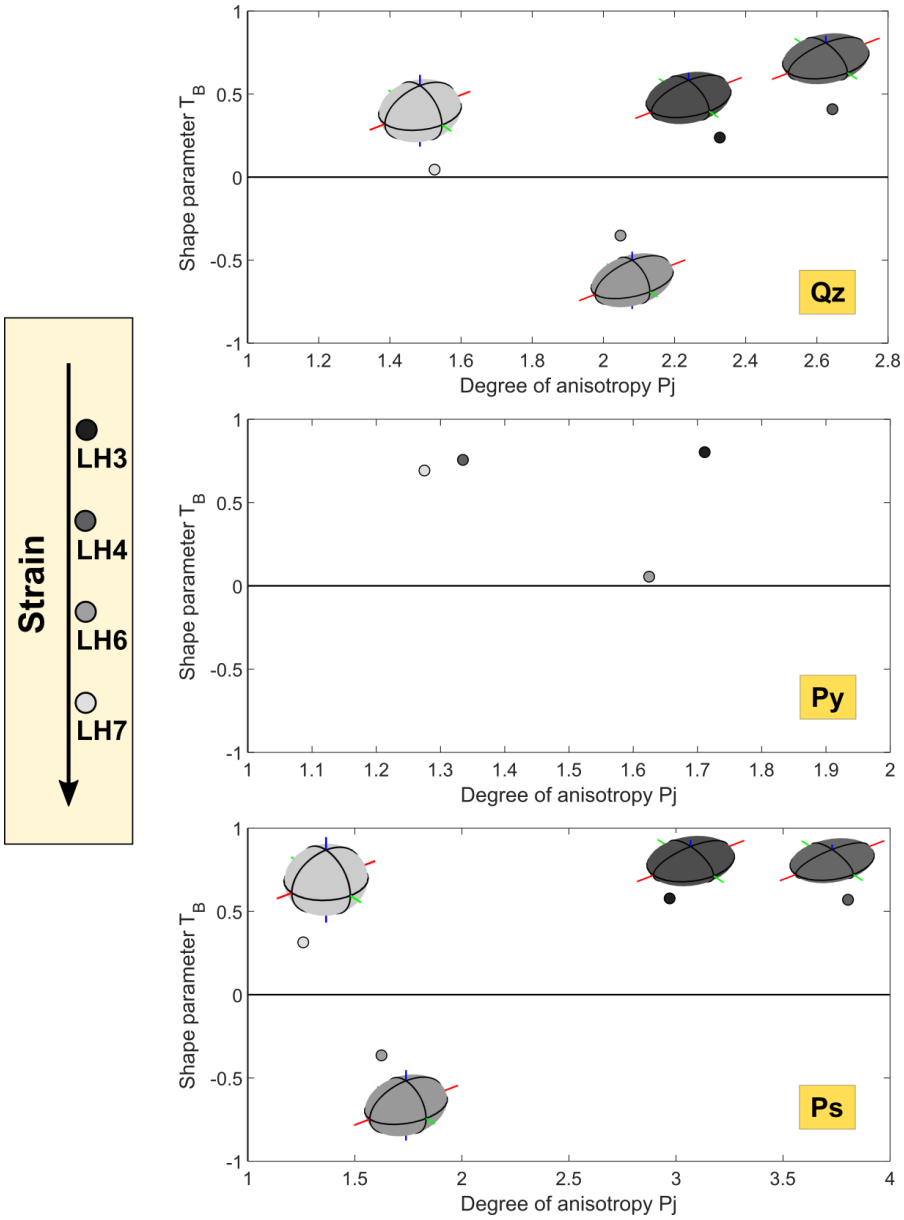

Figure 5.9: ***Jelinek diagrams of the scalar parameters of the bulk shape fabric. Qz: quartz, Py: pyrite, Ps: pore space. Some illustration of fabric ellipsoids corresponding to data points are provided. Note the difference in the scale of the degree of anisotropy in the diagrams. Strain should increase from LH3 to LH7, but note that the LH7 sample is very different from the previous one and may skew the picture.***

5.3.4 Spatial distribution of quartz and pyrite particles

In this section, we present the results of the spatial distribution analysis of quartz grains in the four samples. The results were obtained according to the methodology explained in section ***3.7.2***. In addition, spatial distribution analysis of pyrite inclusions is also proposed. We first present the results concerning quartz, which are summarized in ***Figure 5.10***.

5.3.4.1 Quartz

In sample LH3, from the first to the fifth grain class we have at least 1000 grains involved in the analysis. The analysis is performed on more than 500 grains but less than 1000 in classes 6 to 8. We have seen in ***Figure 5.6*** that this sample does not contain a lot of “large” grains. In this respect, results obtained

for classes 6, 7 and 8 must be taken with caution. The results for the first five classes show that distribution ellipsoids are oblate and have a noticeable anisotropy ($\boldsymbol{P_j} > 1.2$). Thus, quartz grains may not be randomly disposed in the rock matrix. More precisely, the oblate morphology ($\boldsymbol{T_S} \approx 0.75$) informs that grains are distributed along planar structures. The directional data show that $\boldsymbol{E_3}$ axes are distributed nearly parallel to the S0 pole but with a slight upward shift on the sterepolot for these first five classes. This is possibly due to the presence of the secondary foliation observed in the shape fabric analysis. Their $\boldsymbol{E_1}$ axes are oriented in this intermediate plane. For classes 6 to 8, the influence of the small grains is reduced, the shape parameter $\boldsymbol{T_S}$ decreases while the degree of anisotropy increases progressively. As a general trend, the compression axis is parallel to the bedding and may indicate the strain related to the vertical compaction recorded during the acquisition of the sedimentary fabric. When we remove the small grains, the signature of the $\boldsymbol{E_1}$ axes that are parallel to bedding strike, is more that of an LPS fabric.

In sample LH4, much more grains are considered in the analysis. The eight distribution ellipsoids are highly oblate ($\boldsymbol{T_S} > 0.75$ in most cases) and grains are distributed in planes. The anisotropy of the distribution ellipsoids increases when smaller grains are progressively removed in the computation. For the first six classes, the noticeable values of $\boldsymbol{P_j}$ attest for a slight to moderate spatial organization of the grains in planar structures. Larger grains do have a clear spatial distribution as shown by the $\boldsymbol{P_j}$ values ($\boldsymbol{P_j} > 1.65$) of data points 7 and 8. For these classes, the grains are rigorously distributed in the rock matrix. The directional data illustrate a sharp distribution related to the vertical compaction of the sedimentary fabric with $\boldsymbol{E_3}$ axes parallel to the S0 pole. The class 8 (with ≈ 500 grains) provides an interesting 3D view of how larger grains are disposed in the bedding layers (***Figure 5.11*a**). This figure complements well the scalar and directional data obtained in our nearest neighbor analysis. The spacing of the bedding lenses, at least those made up of the coarser materials, can be estimated of nearly 500 µm. This figure shows how the fine turbiditic inputs can be seen in the fabric. The reader will furthermore notice that the secondary foliation highlighted by the SPO analysis is here confirmed by the 20° dip of the particle off the bedding layer (***Figure 5.11*a**).

In sample LH6, the distribution ellipsoids have similar morphologies (triaxial prolate) indicating that grains are distributed along lines. The ellipsoids have similar degrees of anisotropy. This parameter oscillates between 1.15 and 1.2 and may indicate a slight arrangement of the particles. The scalar data are thus quite stable throughout the distribution analysis. A similar observation is made with the directional data. $\boldsymbol{E_3}$ axes are clustered not so far from the bedding pole. The deletion of small grains does not affect the principal directions of the mean distribution ellipsoids. The direction of $\boldsymbol{E_3}$ axis is the shortest dimension of the distribution ellipsoid and possibly to the strain ellipsoid. This direction coincides with the maximum compression direction. Here again the results attest for a vertical compaction which can be attributed to the sedimentary fabric. This relict/preserved sedimentary fabric has been highlighted in ***Figure 5.5***. Interestingly, the $\boldsymbol{E_1}$ axes are well grouped horizontally, in an east-west direction indicating a possible lateral compaction oriented north south. The offset of the bedding pole is probably due to a slight directional measurement error in the field as we have seen for the SPO analysis.

In the slaty-cleavage sample LH7, the weak degrees of anisotropy ($\boldsymbol{P_j} \approx 1.05$) suggest that there is no specific arrangement of the quartz grains and they tend to have a random distribution. Directional data show lot of variability with mixture of vertical and lateral compaction that are more delicate to interpret. The results in this sample are poorly reliable.

As a general trend, we can notice that from sample LH3 to LH7, the strength of the spatial distribution decreases. As seen previously for the SPO, the distribution anisotropy of quartz is more important in zone 1 (samples LH3 and LH4). In these samples, the distribution anisotropy is mainly caused by the vertical compaction of sediments but a horizontal compaction related to LPS can be seen by the orientation of $\boldsymbol{E_1}$ axes parallel to the bedding strike. The hierarchized structure of sample LH4 with bedding lenses and various grain sorting may explain the significant increase in the distribution anisotropy when small grains have less weight in the analysis. The arrangement of grains along linear structures in sample LH6 is in accordance with the macroscopic pencil cleavage fabric and the microscopic SPO results. The sample LH7 is different compared to the other samples and the quartz may be randomly disposed in this sample and strongly affected by pressure solution seams.

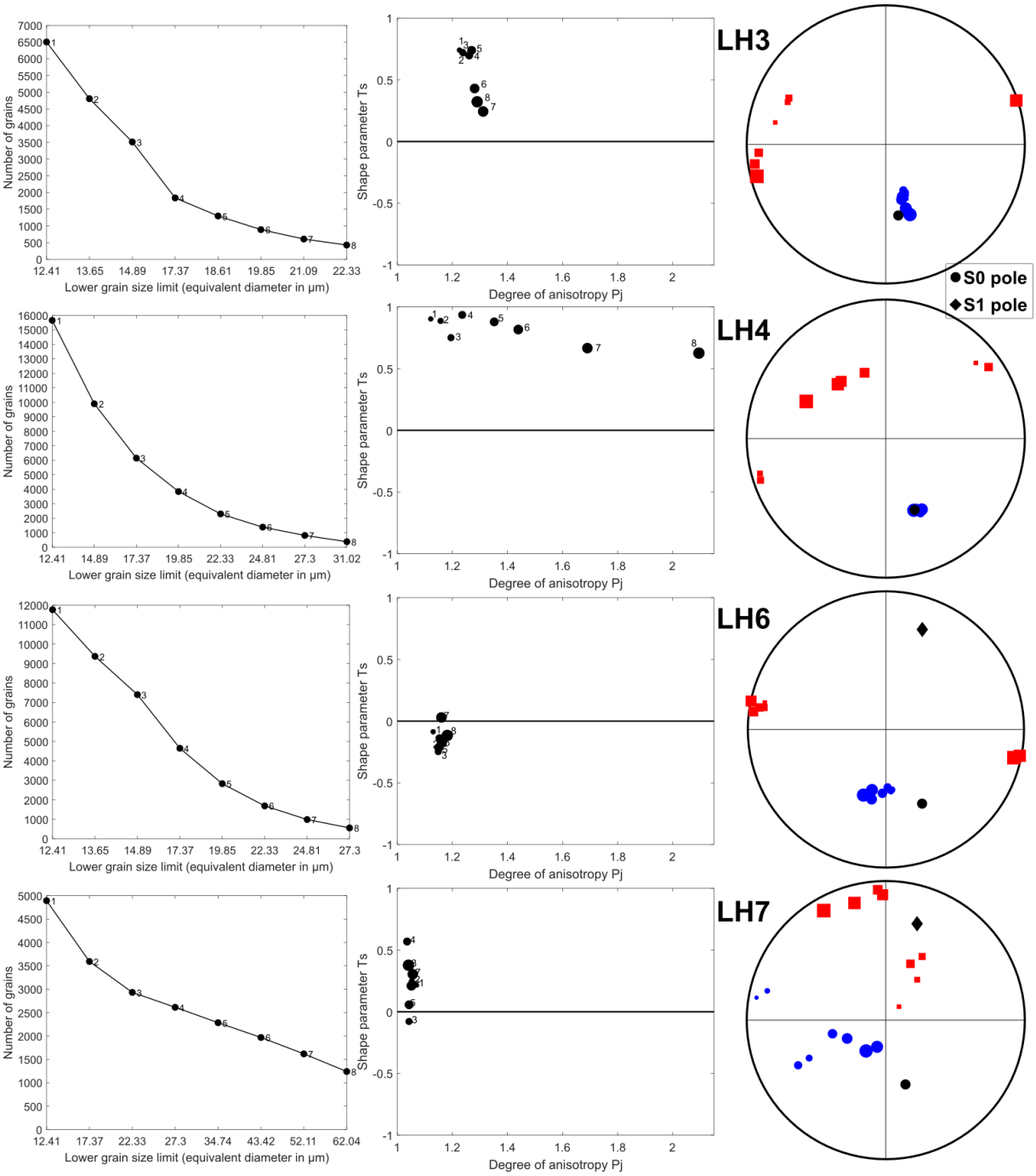

Figure 5.10: ***Spatial distribution analysis of quartz in samples LH3 to LH7. Each row is dedicated to one sample. From left to right: number of grains in the eight classes with the threshold size limit, Jelinek diagram with the eight distribution ellipsoids data points, stereoplot of the principal directions*** E_1 ***and*** E_3 ***of the eight distribution ellipsoids in geographic coordinate system.***

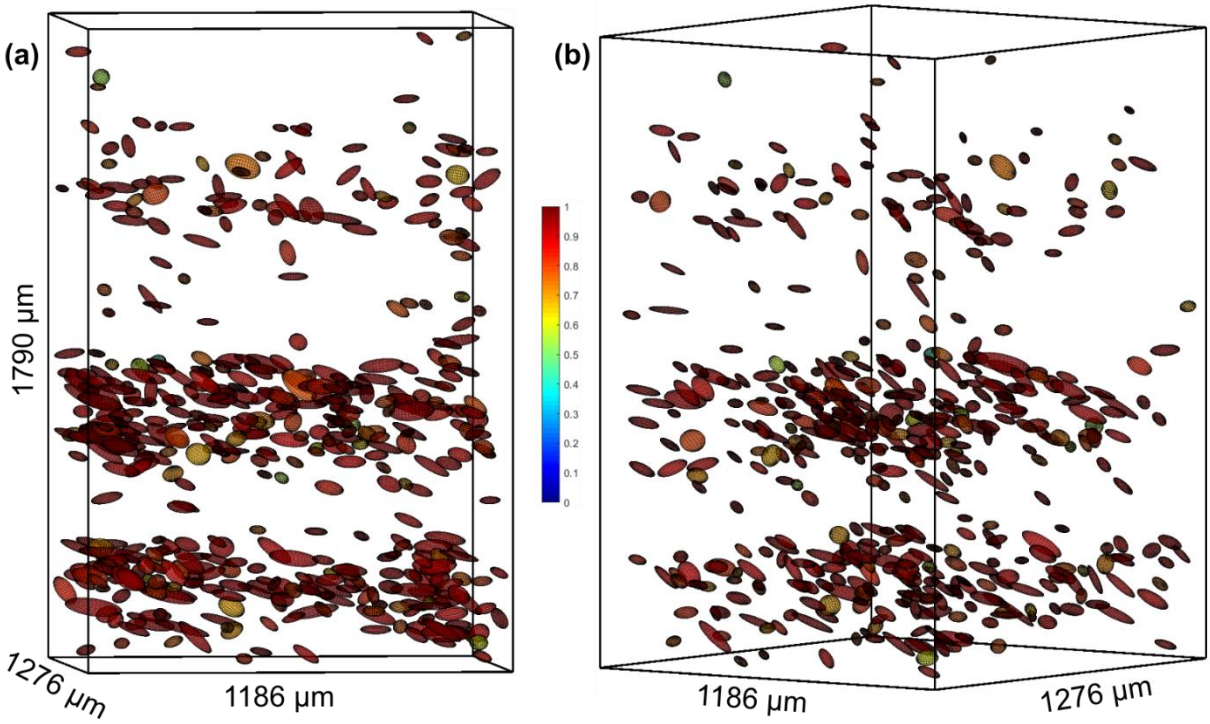

Figure 5.11: ***3D visualization of spatial arrangement of the individual ellipsoids of quartz grains in LH4 sample. Grains have at least a volume of 15625 µm³ (i.e. an equivalent diameter of 31.02 µm). (a) Note the sedimentary lenses with a spacing of about 500 µm. (b) A different view from which the bedding lenses can be seen as well as a secondary foliation that crosscut the sedimentary lenses. The color of the ellipsoid is indicative of its anisotropy (0 = isotropic, 1 = anisotropic).***

5.3.4.2 Pyrite

The results concerning pyrite are shown in ***Figure 5.12***. The sample LH3 is poorly provided in pyrite grains. Therefore, we have taken all the grains in one time for the analysis. The corresponding distribution ellipsoid is oblate ($\boldsymbol{T_S} \approx 0.55$) with a moderate $\boldsymbol{P_j}$ value of about 1.33. The scalar data indicate that pyrite particles are distributed in planar structures. The $\boldsymbol{E_3}$ axis of the distribution ellipsoid is close to the direction of the bedding pole. Pyrite inclusions are thus distributed along north dipping planes and these planes correspond to the bedding layers.

In sample LH4, which contains more pyrite, we have divided the spatial distribution analysis into 5 classes. The shapes of the associated five distribution ellipsoids vary between triaxial oblate and triaxial prolate with weak anisotropy ($\boldsymbol{P_j} \approx 1.1$). Grains may not be well distributed. $\boldsymbol{E_3}$ axes are dipping to the northeast in a rather close direction to the virtual S1 pole. This observation would indicate that there is a northeast – southwest axis of compression recorded by the spatial distribution of pyrite.

In sample LH6, we have divided the spatial distribution analysis into 4 classes. The distribution ellipsoids of these classes mostly fall in the oblate field of the Jelinek diagram, except for class 3. $\boldsymbol{P_j}$ ranges from 1.08 (class 1) to 1.13 (class 3). The scalar data show that pyrite are distributed in planar structures in a weak configuration. The directional data show that $\boldsymbol{E_3}$ axes are dipping southwest at 80° while the $\boldsymbol{E_1}$ axes are oriented to the northwest and almost horizontal. The cluster of the $\boldsymbol{E_3}$ axes is possibly linked to the bedding foliation but there is a significant obliquity with the S0 pole.

Unfortunately, sample LH7 does not contain a sufficient number of pyrite grains and was not suitable to perform the distribution analysis.

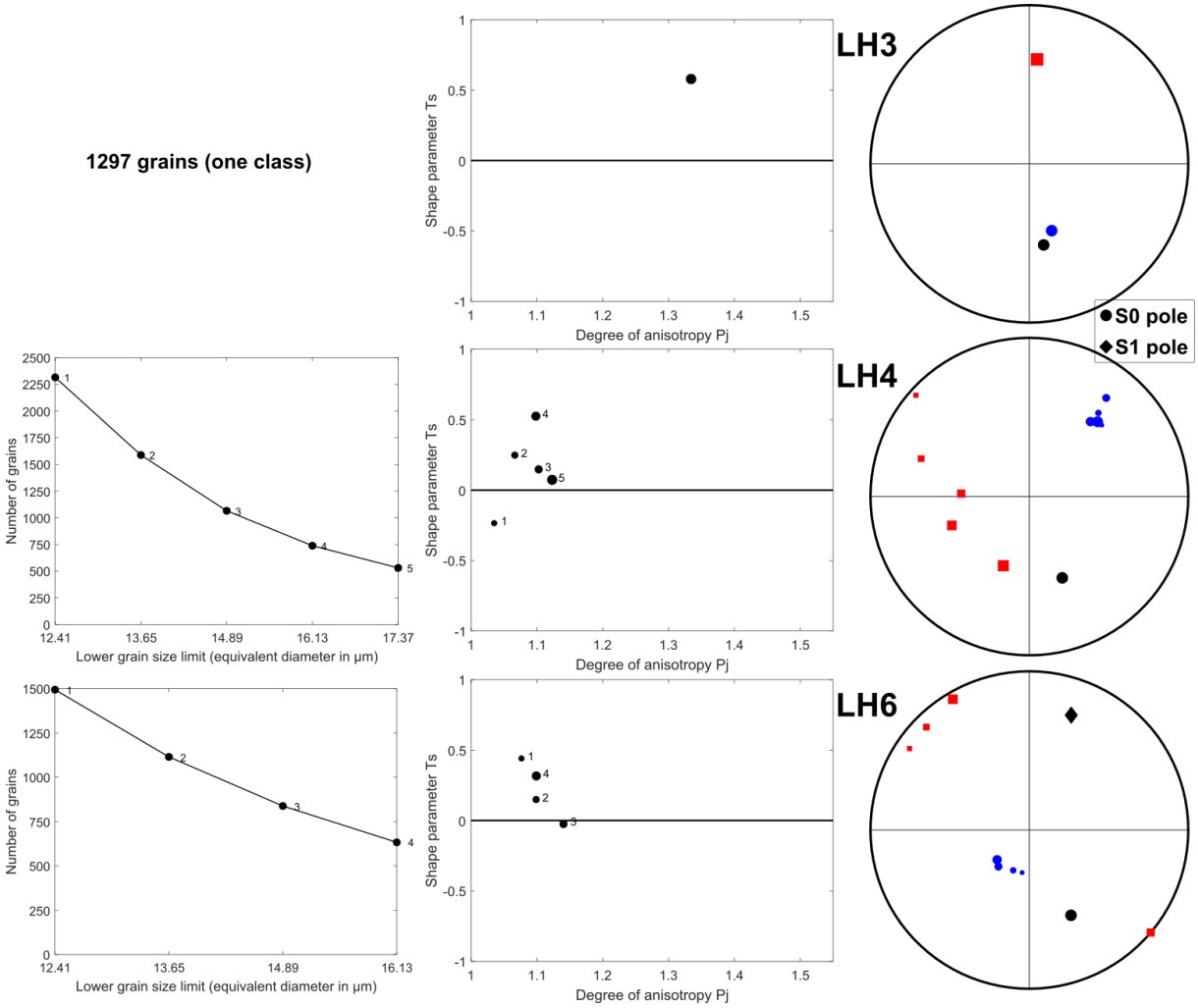

Figure 5.12: ***Spatial distribution analysis of pyrite in samples LH3 to LH6. Each row is dedicated to one sample. From left to right: number of grains in the eight classes with the threshold size limit, Jelinek diagram with the eight distribution ellipsoids data points, stereoplot of the principal directions*** E_1 ***and*** E_3 ***of the eight distribution ellipsoids in geographic coordinate system.***

5.4 Discussion

The four samples of this study correspond to three well-sorted shaly siltstones (LH3, LH4, and LH6) and one fine sandstone (LH7) displaying different macroscopic fabrics along the transition from shale to slate. At the microscale, the results show that quartz and pores have strong shape fabrics not related to bedding in samples LH3 and LH4. These fabrics might be due to a secondary planar fabric or cleavage, which may form the S-C structures observed in the grayscale XCT images (***Figure 5.5***). However, XCT images and spatial distribution results indicate that bedding lenses (structures) are well preserved. This structural layering was highlighted for sample LH4. Thus, distribution analysis of quartz and pyrite suggests that the dominant stress is associated to the sedimentary compaction while the SPO is linked to the secondary foliation. This illustrates the contrast between fabric anisotropy on the one hand and distribution anisotropy on the other. Only one case concerning pyrite (sample LH4) suggests a lateral compaction that could be attributed to LPS.

The secondary foliation or cleavage in samples LH3 and LH4 appears to be very penetrative as it was captured in two millimeter-sized samples and well materialized by the SPO results. However, the cleavage surfaces are not clearly distinguishable at the image resolution and crosscut the bedding foliation at low angle. This cleavage is intended to correspond to the same cleavage that is expressed further along the outcrop. However, the cleavage is rotated in the first 60 m of the outcrop. From a larger point of view, Epstein (2006) has called this the arching of cleavage caused by the contrast in rock competency at the hinge of an overturned syncline fold. The concept behind this is similar to a pressure shadow around a rigid grain at small scale. According to Epstein and Epstein (1969) and Epstein (2006), Lehigh Gap outcrop is supposed to be located in a strain shadow due to this structure and it may explain the lack of cleavage close to the contact. In his optical microscope study, Woodland (1982) has reported cleavage 8 m from the contact but then no cleavage from 8 m to 60 m. Our results from XCT imaging demonstrate that this "rotated" cleavage is present at 32 m and 49 m. Even if the pencil cleavage structures in zone 1 are visible macroscopically, the results of this study show that it is a pervasive fabric at microscale. This north-dipping cleavage is also present in the fine-grained beds of the Silurian Shawangunk Formation with a comparable dip, which is less steep than the bedding and may indicate a common shear deformation. A perspective to this work would be to sample these thin beds of the Shawangunk Formation to verify and compare the intensity of the SPO of quartz grains and to confirm or infirm the relationship between the two planar fabrics.

The intensity of the SPO provided by density contour stereoplots and by the degree of anisotropy of the mean fabric ellipsoid is quite high for quartz. The shape fabric of quartz is considerably stronger than that of the Sigüés samples. Interestingly, the intensity of the quartz fabric in the LH3 and LH4 samples is comparable to the intensity of the calcite fabric in the most deformed samples of Sigüés. We have shown that dissolution-precipitation mechanism was responsible of this intense fabric of calcite in the previous chapter. Therefore, the shape fabric of quartz in Lehigh Gap samples LH3 and LH4 may be due to dissolution-precipitation or recrystallization processes. This idea of quartz shape fabric induced by pressure solution was also supported by Lee et al. (1986) but at 60 m at least from the contact. We propose that the shape of quartz is influenced by dissolution-precipitation creep in Zone 1 and that this mechanism orients quartz more readily than pyrite. In Zone 2, corresponding to the pencil state deformation, both pyrites and quartz are reorganized in the matrix but quartz still be more reactive to the ductile deformation. All phases are strongly affected by pressure solution in Zone 3.

The central Appalachian fold-and-thrust belt remains a complex area due to multiple orogenic events and subsequent deformation and cleavage generation with more or less resolvable overprinting relations (Epstein et al., 1974; Lash, 1978; Epstein, 1980; Epstein and Lyttle, 1993; Gray and Mitra, 1993). Hence, it is difficult to state clearly the mechanism behind the shale microstructure in zone 1. While cleavage in zone 2 and 3 is typical of an LPS mechanism, cleavage surfaces in zone 1 are more intriguing. At the scale of the XCT images, we have reported S-C structures with bedding forming the C planes. This could be attributed to the top to the northwest layer-parallel shear activity of the Blue Mountain decollement (Epstein et al., 1974; Lash, 1978) or the regional top-the-foreland layer-parallel shear (Gray and Mitra, 1993). The movement on the decollement is supposed to have been synchronously active to the regional cleavage development (Epstein et al., 1974). Such deformation may have formed a differentiated LPS and the competence contrast between the two formations (Martinsburg - Shawangunk) has played a significant role. It seems reasonable to assume that the cleavage reflects a single event and not the expression of two or more events, although the latter cannot be completely ruled out. In particular, the competence contrast between the two formations was favorable to later flexural slip and fexural flow mechanisms that may have generated other types

of cleavage. Flexural slip features near the Martinsburg - Shawangunk contact has been reported by Epstein (1980) in surroundings areas of Eastern Pennsylvania. Additional microstructural elements would help to understand the relation between cleavage in fine-grained Shawangunk rocks, in the shale of zone 1 and beyond 60 m from the contact.

The quartz and pores fabric are in accordance with the results obtained by AMS that attest for a bulk clay fabric without bedding foliation in zone 1. This absence of bedding foliation was also reported for chlorite with X-ray pole figure goniometry measurements (Holeywell and Tullis, 1975; Ho et al., 1995). Thus quartz, pore space and chlorite show this 20° oblique foliation. On the other hand, pyrite fabric is similar to the illite/mica fabric and to the magnetite fabric mentioned in previous studies (***Figure 5.2c***). The fabric of pyrite, illite and magnetite corresponds to a compaction fabric in zone 1.

5.5 Conclusion

3D shape fabric analysis by means of XCT images of four rock samples of the Lehigh Gap transect we have shown that rocks close to the contact (distance <60 m) are deformed while many studies said they were not. Two samples have shown that a pervasive sheared cleavage is present before the pencil-cleavage domain of the outcrop and the fabric anisotropy of quartz grains in these samples is strong. The characterization of grain shape fabric by means of XCT appears as a complementary tool to other well-known methods in geosciences to provide additional microstructure data.

In these first two chapters of the application axis of the thesis, we have seen that the information captured in small samples appears to be rather representative of macroscopic observations. Moreover, the measurements of the shape fabric bring essential elements to understand the internal organization of fine-grained rocks and how it evolves with deformation.

In the case of Sigüés we have repeated the measurement on small samples to highlight contrasting information. In the case study presented in this chapter, we did not have the necessary time to perform supplementary analysis. However, from the results concerning Sigüés, it appears that when the deformation structures intensify, differences are recorded in the shape fabric of the most rigid grains such as those belonging to quartz or pyrite phases.

6 Representativeness of grain shape fabric in strained shales

6.1 Aims

We have seen that a few numbers of millimeter-sized rock samples can provide grain shape fabrics, which are representative of the deformation fabric along a km-long (chapter ***4***) strain gradient and a 130 m-long transition (chapter ***5***). In the following chapter, we want to investigate more precisely the representativeness of such data and the variability that may exist in the shape fabric of these deformed fine-grained rocks. We use the sample A4 (hereafter referred to as sample A4-1 to distinguish it from the AMS drill core A4) and the sample A4-2 from the Sigüés case study of chapter ***4***, which have shown differences in the SPO of quartz grains. This work has been published in *Journal of Geophysical Research: Solid Earth* (Saur et al., 2021).

The aim of this study is to evaluate the homogeneity of the fabric of two millimetric samples of deformed shales in which two planar fabrics interfere, a sedimentary fabric (bedding) and a tectonic fabric (cleavage). The samples come from the Sigüés section initially studied by Boiron et al. (2020) and in chapter ***4***. Boiron et al. (2020) analyzed the magnetic fabric of clays to study a deformation gradient. In chapter ***4***, we have proposed the extraction of calcites, quartz and pores to study their SPO using XCT images. Neither of these two studies involved a thorough analysis of the REV concept. In this chapter, we carry out XCT images to analyze the grain shape fabric of quartz particles in a highly deformed rock matrix of the Sigüés section (***Figure 4.1*c** and ***Figure 4.1*d**). While exploring the fabric in different subvolumes and for different classes of grains, we will compare individual grain data to the bulk fabric computed from mean tensor analysis and to the magnetic fabric results of Boiron et al. (2020) obtained at the outcrop scale. The study shows that heterogeneities in the fabric anisotropy (bedding dominated and cleavage dominated) easily lead to a biased interpretation of the bulk fabric.

6.2 Samples

This study is based on a field sample, here referred to as A4, which corresponds to an oriented drill core of 2.5 cm in diameter, and on two sub-samples taken from it to investigate the fabric by means of XCT. The rock type is a calcareous shale composed of about 30-50 % calcite, 29-37 % quartz and 15-33 % phyllosilicates (Boiron et al., 2020). The calcareous shale comes from the Eocene Arro-Fiscal marls formation, which outcrop in the piggyback Jaca basin (Spain). Field observations in this high-strain area, show that a slaty-cleavage is developed throughout the rock unit (***Figure 6.1*a**). The cleavage (S1) is materialized by closely spaced planes according to which the rock breaks down preferentially. These deformation planes which constitute the tectonic planar fabric are dipping steeply to the north and crosscut the sedimentary fabric (or bedding, S0) which is gently dipping to the southwest. The mean measured angle between bedding and cleavage planes is 84°. In the field, cleavage spacing is millimetric to sub-millimetric and gives a continuous deformation fabric to the rock. Under an optical microscope, the fabric also appears continuous with closely spaced pressure solution seams (***Figure 6.1*b**). The drill core A4 appears homogeneous and exhibits discrete subvertical cleavage surfaces (***Figure 6.1*c**). The clay fabric of 72 samples taken over an area of 50 m^2 show an oblique average magnetic foliation between the bedding plane and the cleavage plane (Boiron et al., 2020) (***Figure 6.1*d**). The two mm-sized drill cores for XCT were extracted approximately 4 mm apart on the top face

of the bigger oriented drill core A4 (***Figure 6.1c***). The two small drill cores are labelled A4-1 and A4-2 (***Figure 6.1d***). Sample A4-1 has already been used in the study presented in chapter ***4*** (under the label A4) to provide the SPO of quartz grains in a 2.5 mm^3 rock volume (***Figure 6.1e***). Note that these samples were not drilled parallel nor orthogonal to the bedding or cleavage planes for the sake of generality. However, A4-1 was drilled to capture a cleavage domain and A4-2 was drilled in a more homogeneous zone where cleavage surfaces are not observable to maximize the potential to observe inter-sample differences (***Figure 6.1c***). A4-1 and A4-2 were oriented respecting the orientation of the generatrix (G) affixed on the A4 drill core.

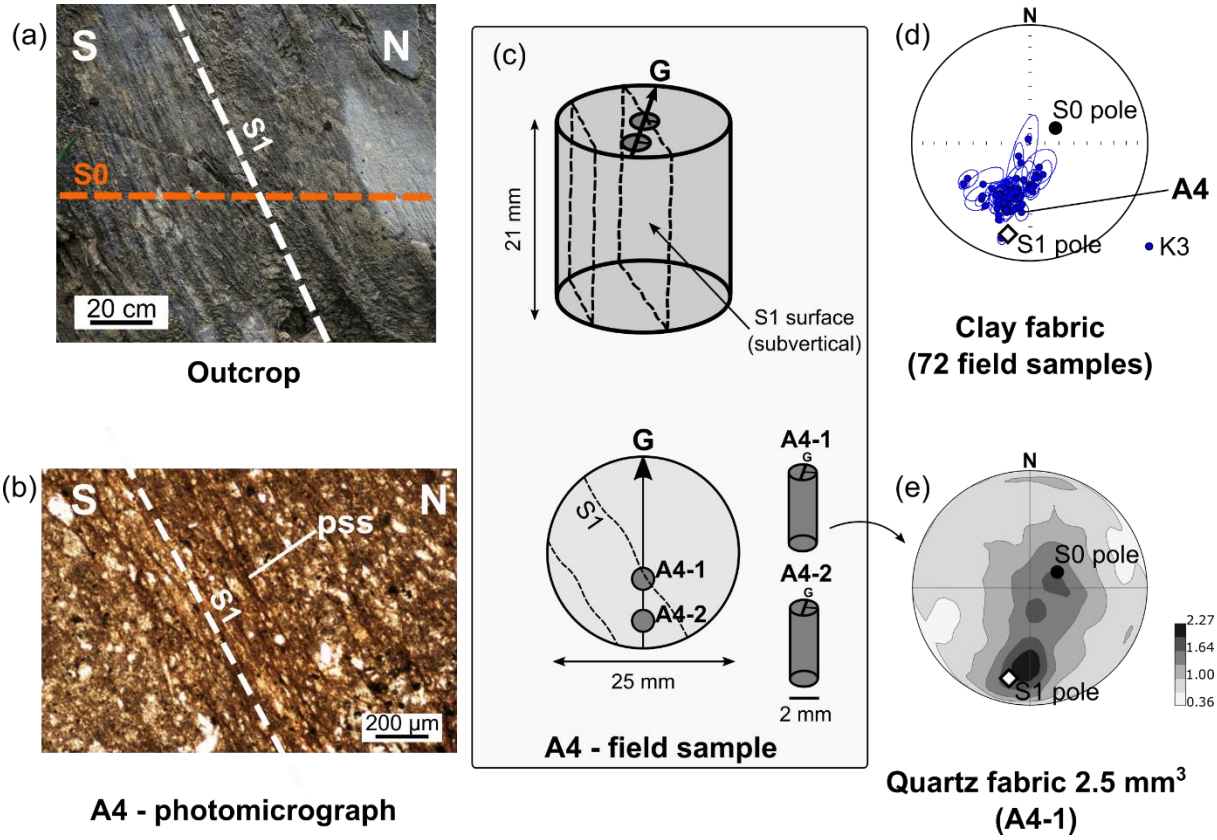

Figure 6.1: ***(a) Outcrop photograph showing the intense cleavage where A4 sample was collected. (b) Photomicrograph of sample A4. Dark laminae correspond to pressure solution seams (pss). (c) Schematic representation of the A4 field sample and the two mm-sized drill cores A4-1 and A4-2 which have been extracted for XCT analysis. G stands for generatrix (d) Magnetic foliation poles (Minimum axes K_3) of the magnetic fabric data of 72 specimens (A4 included) in equal area and lower hemisphere projection (data from Boiron et al., 2020). (e) Density contour (Fisher distribution) of small axes (L_3) of quartz grains extracted from the image processing of XCT data (Saur et al., 2020). S0 and S1 correspond to bedding and cleavage respectively.***

6.3 Results

6.3.1 Image processing

The raw XCT images of samples A4-1 and A4-2 are presented in ***Figure 6.2a*** and ***Figure 6.2b***. The identified quartz grains are colored blue and superimposed onto the raw images in ***Figure 6.2c*** and ***Figure 6.2d***. The other phases visible on the images correspond to pores (black), fine-grained matrix (dark gray), calcite (light gray) and pyrite (white). Multiple morphological parameters were subsequently obtained for each segmented quartz grain, based on image moments (see section ***3.4.4***).

Truncated objects situated at the edges of the VOI were excluded, as they would bias the fabric analysis. In addition, we removed objects smaller than 729 µm^3 so that a sufficient number of voxels (422) define a grain. It also permits to focus mainly on detrital quartz grains, avoiding the possible selection of microquartz in the fine-grained matrix. The cut-off threshold was arbitrarily selected, yet it was verified that a larger or smaller value did not influence the presented results.

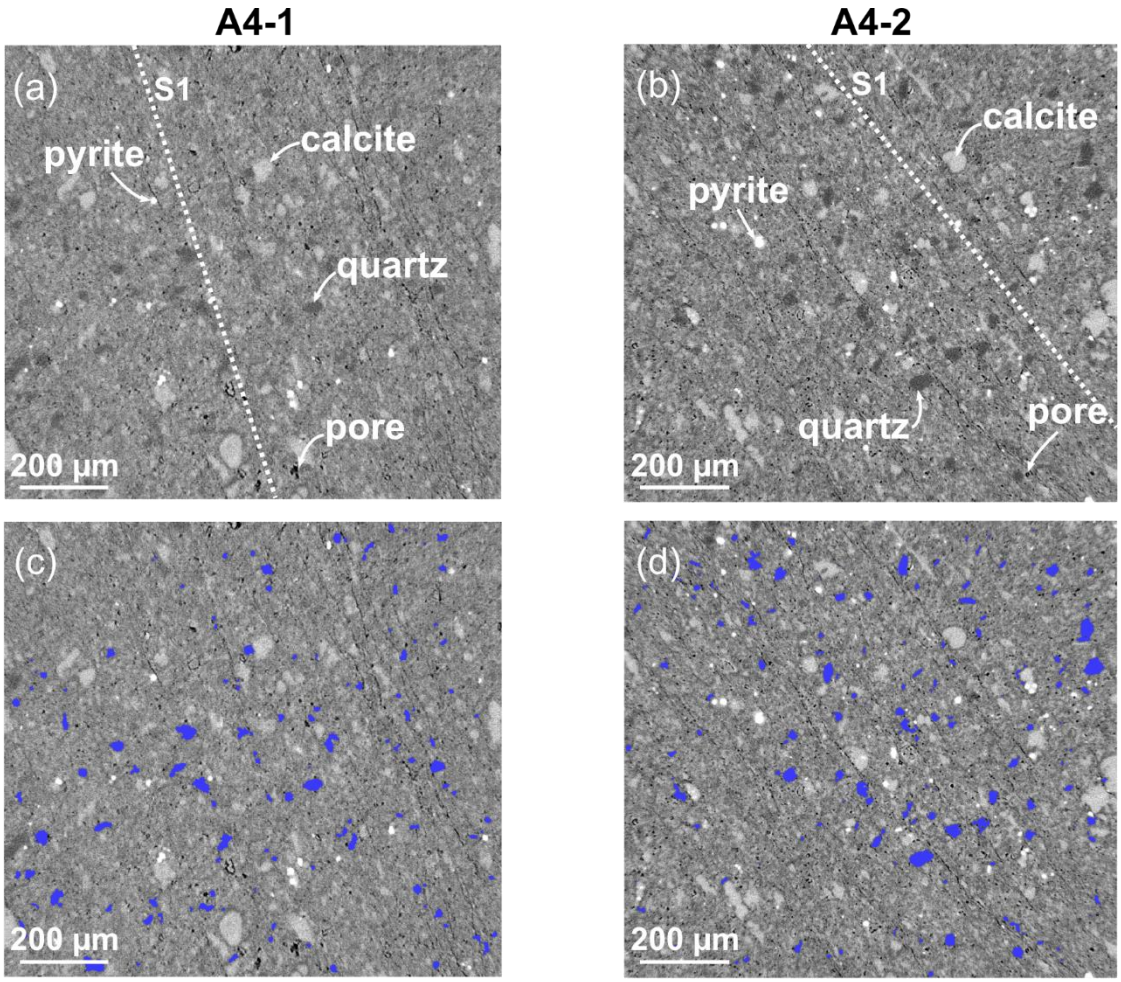

***Figure 6.2:** XCT grayscale image of a slice through sample A4-1 (a) and A4-2 (b). Overlay of quartz segmentation on the grayscale images of A4-1 (c) and A4-2 (d).*

6.3.2 Microstructures

At first glance, microstructures displayed in the images of the two samples are quite comparable (***Figure 6.3***). Slices through A4-1 and A4-2 mostly display silt-sized grains of quartz and calcite, embedded in a clayey matrix. Quartz grains have sub-angular shapes while calcite grains are more rounded and often correspond to microfossils or bioclasts. The length of quartz grains, not that of their equivalent ellipsoid, is in the range 10-100 µm. Quartz grains are generally independent and dispersed in the clay matrix. We can see the subtle sedimentary fabric marked by the alignment of some microfossils but a strong cleavage fabric predominates in these samples. The cleavage fabric is materialized by cleavage domains where pressure-solution seams appearing as dark laminae are developed. The pressure-solution seams are closely spaced in A4-1 but localized and form a high strain zone in the right part of the image (***Figure 6.3***). Thus, the cleavage fabric appears less continuous at this scale compared to what we can see in the outcrop (***Figure 6.1a***). In A4-2, the pressure-solution

seams are more homogeneously distributed in the XCT image and give a continuous cleavage fabric at this scale (***Figure 6.3***). Calcite grains are often wrapped or truncated by the pressure-solution seams such as we have seen in the photomicrograph (***Figure 6.1*****b**).

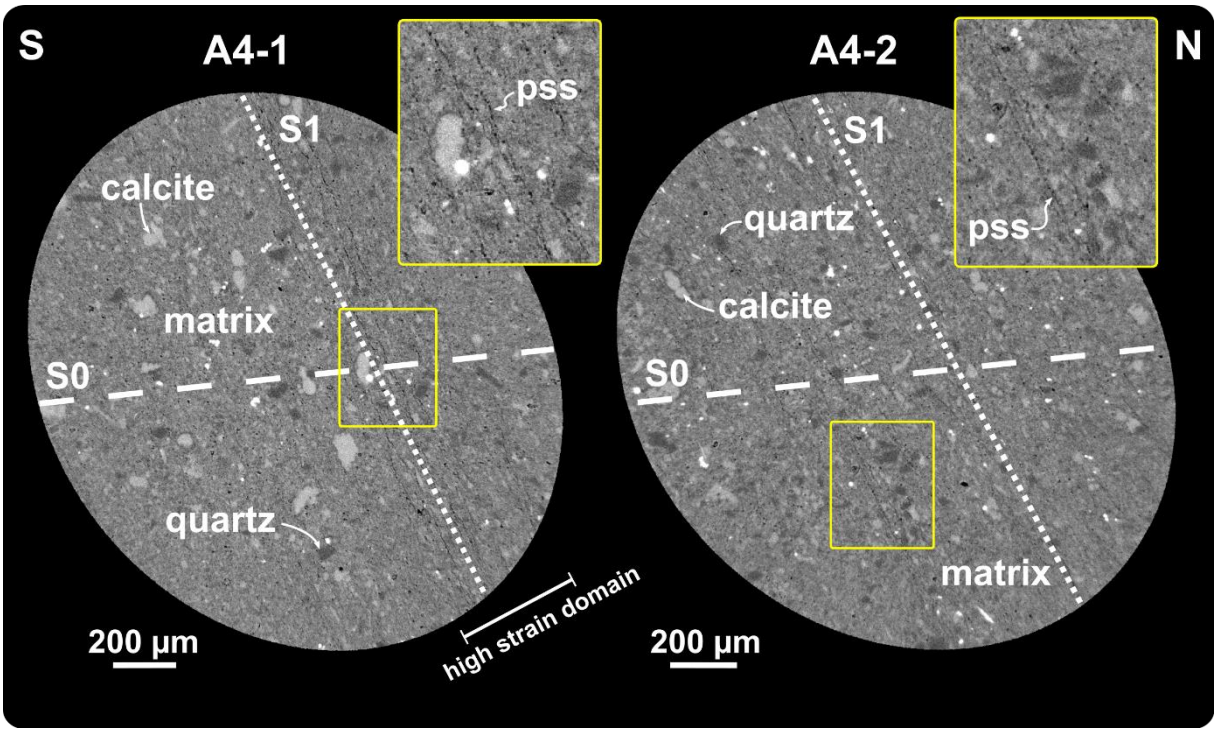

Figure 6.3: *2D slices of XCT images of A4-1 and A4-2 in geographic coordinate system. PSS = pressure solution seam. Note the difference in the PSS distribution for the two samples. S0: bedding; S1: cleavage.*

6.3.3 Grain size distribution and ellipsoids shape parameters

Quartz grain size distributions are provided in ***Figure 6.4*****a** for the two samples. We observe similar curves, even though A4-2 has a greater quantity of small grains and its distribution is a bit steeper. In total, 8311 and 10384 quartz grains have been extracted from the VOIs of A4-1 and A4-2, respectively. As we have selected grains with a minimum volume of 729 µm^3 we implicitly direct the analysis to detrital silt grains.

The distribution of the degree of anisotropy $\boldsymbol{P_j}$ is shown on ***Figure 6.4*****b** and the one of the shape parameter $\boldsymbol{T_G}$ on ***Figure 6.4*****c**. We observe a maximum frequency for $\boldsymbol{P_j}$ between 2 and 5 for both samples. A4-1 has slightly more anisotropic grains compared to A4-2. The grains are mainly triaxial prolate ($-0.5 < \boldsymbol{T_G} < 0$) to prolate ($\boldsymbol{T_G} < -0.5$) for the two samples as shown by the distribution of the shape parameter $\boldsymbol{T_G}$. Overall, the two samples do not show significant differences in the distribution of these scalar parameters.

For the individual grain analysis, we subdivided each distribution in ***Figure 6.4*** into three sub-categories. The size categories are: $729 \leq \mathrm{V1} < 1728\ \mu\mathrm{m}^3$, $1728 \leq \mathrm{V2} < 5832\ \mu\mathrm{m}^3$ and $\mathrm{V3} \geq 5832\ \mu\mathrm{m}^3$. The 729 µm^3, 1728 µm^3 and 5832 µm^3 correspond to a cubic volume of 9 µm, 12 µm and 18 µm side length, respectively. The anisotropy categories are: $1 \leq \mathrm{P1} < 4$, $4 \leq \mathrm{P2} < 8$ and $\mathrm{P3} \geq 8$. The shape categories are: $\mathrm{T1} < (-1/3)$, $(-1/3) \leq \mathrm{T2} < (1/3)$ and $\mathrm{T3} \geq (1/3)$. In a simplified manner, T1 corresponds to prolate ellipsoids, T2 to triaxial ellipsoids and T3 to oblate ellipsoids.

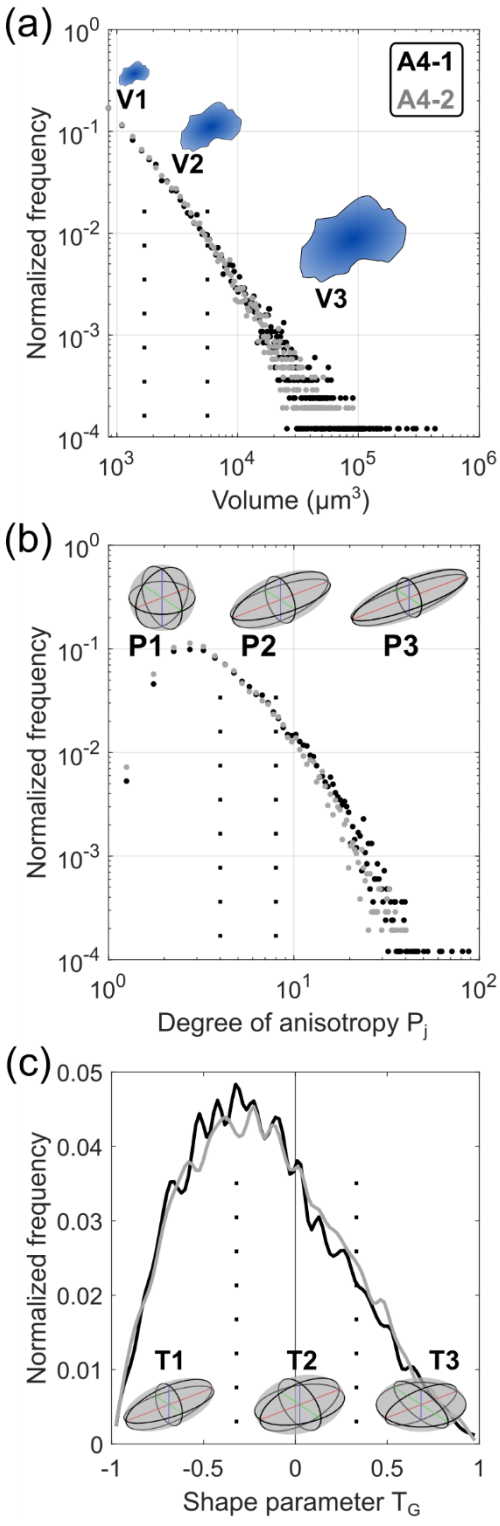

Figure 6.4: *(a) Quartz size distribution for A4-1 and A4-2. Schematic representation of the three size categories (b) Distribution of the degree of anisotropy (P_j) of quartz's equivalent ellipsoid. Schematic representation of the three anisotropy categories (for a prolate ellipsoid, i.e. T_G = -1) (c) Distribution of the shape parameter (TG) of quartz's equivalent ellipsoid. Schematic representation of the three shape categories.*

6.3.4 Representative volume for quartz shape fabric

6.3.4.1 Individual grain analysis

Figure 6.5 shows all results for this analysis. Each row of graphs corresponds to a specific parameter (size, anisotropy, shape), and the columns correspond respectively to samples A4-1 and A4-2. Each graph tracks the evolution of a single parameter, such as the grain size, for each sub-category ("small", "medium" and "large" grains) as a function of the size of the box containing the grains. Both the mean over the eight boxes and the standard deviation between the results obtained for the individual boxes are plotted. The results are normalized. The first data point of the top-left plot shows for example that the smallest box contains on average 50% small grains, 30% medium-sized grains and 20% large grains, with a ±10% variation on these quantities depending on the specific box location. For each sub-category, the density contour of $\boldsymbol{L_3}$ axes of the ellipsoids embedded in the ultimate box size (i.e. the VOI) is plotted as well (***Figure 6.5***). It indicates the foliation of the grains. Please note that the box sizes are not identical for the A4-1 and A4-2 samples, as the total VOI differs.

In both samples, the proportion of quartz belonging to the three categories of size is oscillating in the smallest boxes (***Figure 6.5*****a** and ***Figure 6.5*****b**). The mean value is within 10% of the equilibrium value from the fourth box onward (296 x 281 x 561 µm^3) for A4-1 and from the third box (247 x 238 x 474 µm^3) for A4-2. Note that the reduction of the standard deviation from the 10th box onward is mainly due to the increasing overlap between the boxes. The three categories of grain size show different patterns of $\boldsymbol{L_3}$ axes directions for the two samples. In A4-1 (***Figure 6.5*****a**), the foliation of the small grains (V1) is mainly controlled by the cleavage plane. The $\boldsymbol{L_3}$ axis is scattered along a girdle for the medium-sized grains (V2). The foliation of the large grains (V3) is sub-parallel to the bedding. As opposed to A4-1, small grains and medium-sized grains in A4-2 have their $\boldsymbol{L_3}$ dispersed but mainly controlled by the S0 pole. The large grains have their $\boldsymbol{L_3}$ slightly oblique to the S0 pole.

The greater standard deviations suggest more variability in the anisotropy categories of A4-1 than A4-2 (***Figure 6.5*****c**). However, the mean values stabilize at the third box size for A4-1 (247 x 238 x 474 µm^3). We remark that isotropic grains (P1) have no preferred orientation of the $\boldsymbol{L_3}$ axis. Slightly anisotropic grains (P2) display a girdle pattern with a greater influence of the S0 pole while anisotropic grains (P3) are strongly controlled by cleavage. In A4-2 (***Figure 6.5*****d**), the proportion of the anisotropy categories stabilize at the fifth box size (358 x 341 x 667 µm^3). Similarly, P1 grains in A4-2 have no $\boldsymbol{L_3}$ preferred orientation. P2 grains show a cluster of $\boldsymbol{L_3}$ around the S0 pole while P3 grains have their $\boldsymbol{L_3}$ slightly oblique to the S0 pole, comparable to the large grains.

Less variation is observed in the shape categories (***Figure 6.5*****e** and ***Figure 6.5*****f**). Stable values are reached around the third box size (247 x 238 x 474 µm^3 for A4-1 and 254 x 246 x 484 µm^3 for A4-2). The directional data of A4-1 (***Figure 6.5*****e**) show a marked girdle distribution of $\boldsymbol{L_3}$ for prolate grains (T1) and to a lesser extent for triaxial prolate to triaxial oblate grains (T2). The distribution of $\boldsymbol{L_3}$ is more bimodal for oblate grains (T3), $\boldsymbol{L_3}$ is controlled by either the S0 pole or the S1 pole. We should note that the symmetry of prolate grains makes it easier to depict a girdle distribution of $\boldsymbol{L_3}$ while this is not the case for oblate grains. For the A4-2 sample (***Figure 6.5*****f**), all shape categories have their $\boldsymbol{L_3}$ controlled by the S0 pole or slightly oblique to it and the influence of cleavage is almost absent.

To summarize, inter-box variability of quartz morphology is greater in A4-1 than in A4-2, especially in terms of grain size and ellipsoid shape. As the box size increases the variability decreases, yet some parameters converge faster then others. This implies that different parameters have a different associated REV. As a whole, a representative size emerges for volumes of ≈0.07-0.08 mm^3 that include

an average of nearly 300 grains. It gives a good insight on the heterogeneity of grains. The directional data of $\boldsymbol{L_3}$ axes in A4-1 show that small grains are more anisotropic and have their foliation governed by the cleavage. The large grains in A4-1 have their foliation subparallel to the bedding. In A4-2, the directional data of $\boldsymbol{L_3}$ are particularly stable indicating a foliation subparallel to the bedding plane. Note that A4-1 and A4-2 are only 4 mm apart, which attests to heterogeneity at this scale.

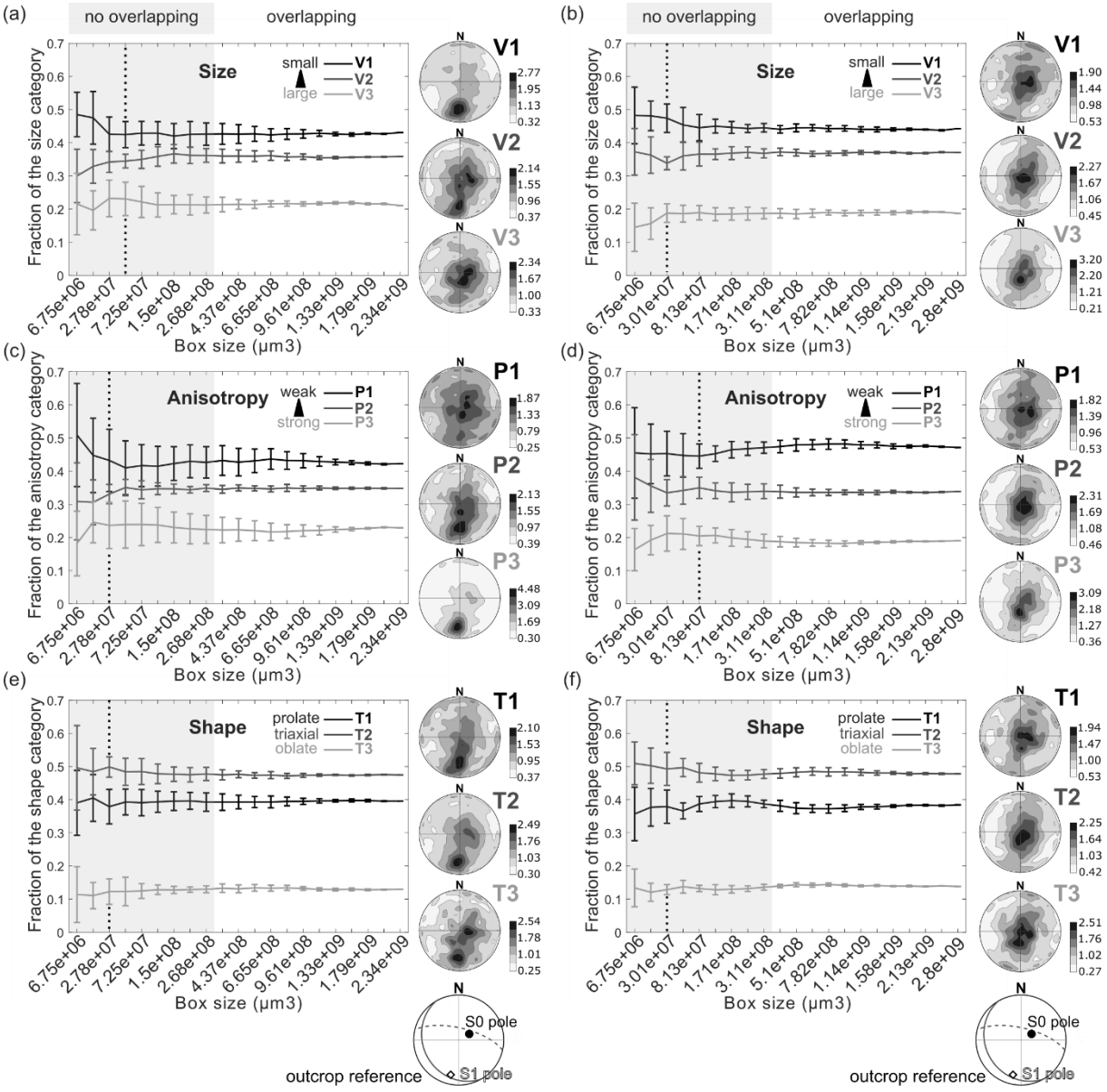

Figure 6.5: ***Results of the box-counting method for the individual grain analysis. Errorbar plot (mean and standard deviation calculated from the eight boxes) of the fraction of the three size, anisotropy and shape categories and associated stereographic projections of the*** $\mathrm{L_3}$ ***axes of grain ellipsoids for the ultimate box size, for A4-1 (a, c, e) and A4-2 (b, d, f). Dotted lines in the graphs indicate the representative size for the parameter according to the methodology explained in section 3.5.***

6.3.4.2 Bulk fabric

In this section, we analyze the evolution of the quartz volume fraction, the degree of anisotropy ($\boldsymbol{P_j}$) and the shape parameter ($\boldsymbol{T_B}$) of the mean tensors (fabric ellipsoids) as well as their directional data (principal axes $\boldsymbol{L_{1m}}$ and $\boldsymbol{L_{3m}}$) (***Figure 6.6***).

The volume fraction of quartz is highly variable in the small boxes (***Figure 6.6*a** and ***Figure 6.6*b**). After the fifth size, all boxes display a similar volume fraction of around 2% for both samples. However, it takes until the sixteenth box size (878 x 807 x 1604 µm^3 for A4-1 and 929 x 865 x 1677 µm^3 for A4-2) to reach a value that deviates less than 10% from the volume fraction of the entire VOI. As the boxes are overlapping in this region, it is possible that the true REV size is larger. Note that the drop in the volume fraction for the greater box size is due to the removal of boundary grains in the VOI.

The degree of anisotropy $\boldsymbol{P_j}$ in both samples shows a descending slope that converges to a stable value (***Figure 6.6*c** and ***Figure 6.6*d**). $\boldsymbol{P_j}$ is highly variable and greater in the small boxes. A representative value for $\boldsymbol{P_j}$ is reached at the twelfth box size for A4-1 (684 x 632 x 1256 µm^3) and at the ninth box size for A4-2 (565 x 531 x 1034 µm^3). Therefore, A4-2 shows less inter-box variability in $\boldsymbol{P_j}$ values. Even if grains are more anisotropic in A4-1, the degree of anisotropy of the mean tensor for the VOI is lower in A4-1 ($\boldsymbol{P_j} = 1.217$) than in A4-2 ($\boldsymbol{P_j} = 1.278$). The fabric is stronger in A4-2. It illustrates the difference between the $\boldsymbol{P_j}$ value of an individual ellipsoid compared to the $\boldsymbol{P_j}$ value of an ensemble of ellipsoids (Giorgis and Tikoff, 2004), which is also generally the case in magnetic fabric studies (Borradaile and Jackson, 2004, 2010).

The shape parameter $\boldsymbol{T_B}$ (***Figure 6.6*e** and ***Figure 6.6*f**) varies between prolate and oblate for the smallest box sizes. In larger boxes, $\boldsymbol{T_B}$ points at a predominantly oblate bulk fabric. A4-1 shows greater values of $\boldsymbol{T_B}$ compared to A4-2. $\boldsymbol{T_B}$ mostly stays in the oblate field for A4-1 and indicates a stronger planar orientation distribution of grains than in A4-2. In A4-2, prolate values of $\boldsymbol{T_B}$ are more represented but disappear soon after the boxes start overlapping. The median value of $\boldsymbol{T_B}$ is almost stable for the A4-1 sample (***Figure 6.6*e**). It increases slightly for A4-2 (***Figure 6.6*f**). However, we should notice that $\boldsymbol{T_B}$ values seem to stabilize for A4-1 before the overlap of boxes, after which there is a rebound in variability and curves begin to show more discrepancy. As will be shown later, this is related to the presence of heterogeneity at the scale of the VOI. This is not the case for A4-2: the shape parameter monotonously converges to an equilibrium value. A representative value for $\boldsymbol{T_B}$ is reached at the twentieth box size for A4-1 (1072 x 982 x 1952 µm^3) and at the eighteenth box size for A4-2 (1032 x 960 x 1861 µm^3).

In the lower part of ***Figure 6.6*e** and ***Figure 6.6*f** we added the directional data plotted in a geographic coordinate system for some box sizes. In each stereographic projection, the $\boldsymbol{L_{1m}}$ and $\boldsymbol{L_{3m}}$ axes of the eight mean tensors are represented. We chose not to plot the intermediate axis $\boldsymbol{L_{2m}}$to improve the readability of the diagram. For the A4-1 sample, $\boldsymbol{L_{3m}}$ in the fifth box size is heterogeneously oriented in between the S0 pole and the S1 pole. $\boldsymbol{L_{1m}}$ axes are dispersed in the S0 plane or close to the S1 plane. With increasing box size, $\boldsymbol{L_{3m}}$ axes begin to cluster. Four subvolumes appear S0 controlled and four being closer to the S1 pole. At the thirteenth box size (732 x 676 x 1343 µm^3), the influence of cleavage in the $\boldsymbol{L_{3m}}$ direction is reduced and $\boldsymbol{L_{1m}}$ axes are still dispersed horizontally towards the west. In the ultimate box size, the $\boldsymbol{L_{3m}}$ axis occupies an intermediate position that averages the orientation distribution and hides the true nature of the fabric. In A4-2, $\boldsymbol{L_{1m}}$ and $\boldsymbol{L_{3m}}$directions show very little dispersion even at the smallest box sizes. $\boldsymbol{L_{3m}}$ axes are rapidly grouped slightly oblique to the S0 pole. Note that the dispersion of $\boldsymbol{L_{1m}}$ axes and its confidence limits are related to the values of the shape parameter $\boldsymbol{T_B}$, more oblate values indicating more dispersion of $\boldsymbol{L_{1m}}$ axes.

To summarize, the greater variations of the fabric parameters ($\boldsymbol{P_j}$ and $\boldsymbol{T_B}$) for A4-1 indicate more heterogeneity in this sample. Following our criterion exposed in section ***3.5***, we found that a representative volume for the quartz volume fraction corresponds to a cubic volume of ≈1044 µm side length (an average of 4017 grains of quartz) for A4-1 and of ≈1105 µm side length (5119 grains of

quartz) for A4-2. A cube of ≈816 µm side length containing 1908 grains gives a representative value of $\boldsymbol{P_j}$ in A4-1 while a cube of ≈677 µm side length with 1151 grains provides a representative value of $\boldsymbol{P_j}$ in A4-2. A cube of ≈ 1271 µm side length containing about 7507 grains gives a representative value of $\boldsymbol{T_B}$ in A4-1 while a cube of ≈1226 µm side length with about 7017 grains provides a representative value of $\boldsymbol{T_B}$ in A4-2. These sizes are much larger than the REV dimensions obtained via the individual grain analysis, and are too close to the dimension of the VOI to claim that they are truly representative. This, complemented with the observation that both sub-samples yield a different behavior, is indicative for some larger scale heterogeneity. For oblate fabrics, while the scalar value of $\boldsymbol{T_B}$ gives an idea of the degree of dispersion of $\boldsymbol{L_{1m}}$ axes and the degree of clustering of $\boldsymbol{L_{3m}}$ axes, only the directional data can reflect the complete orientation distribution of $\boldsymbol{L_{3m}}$ axes. In particular, this makes it possible to determine whether two or more fabrics are in competition.

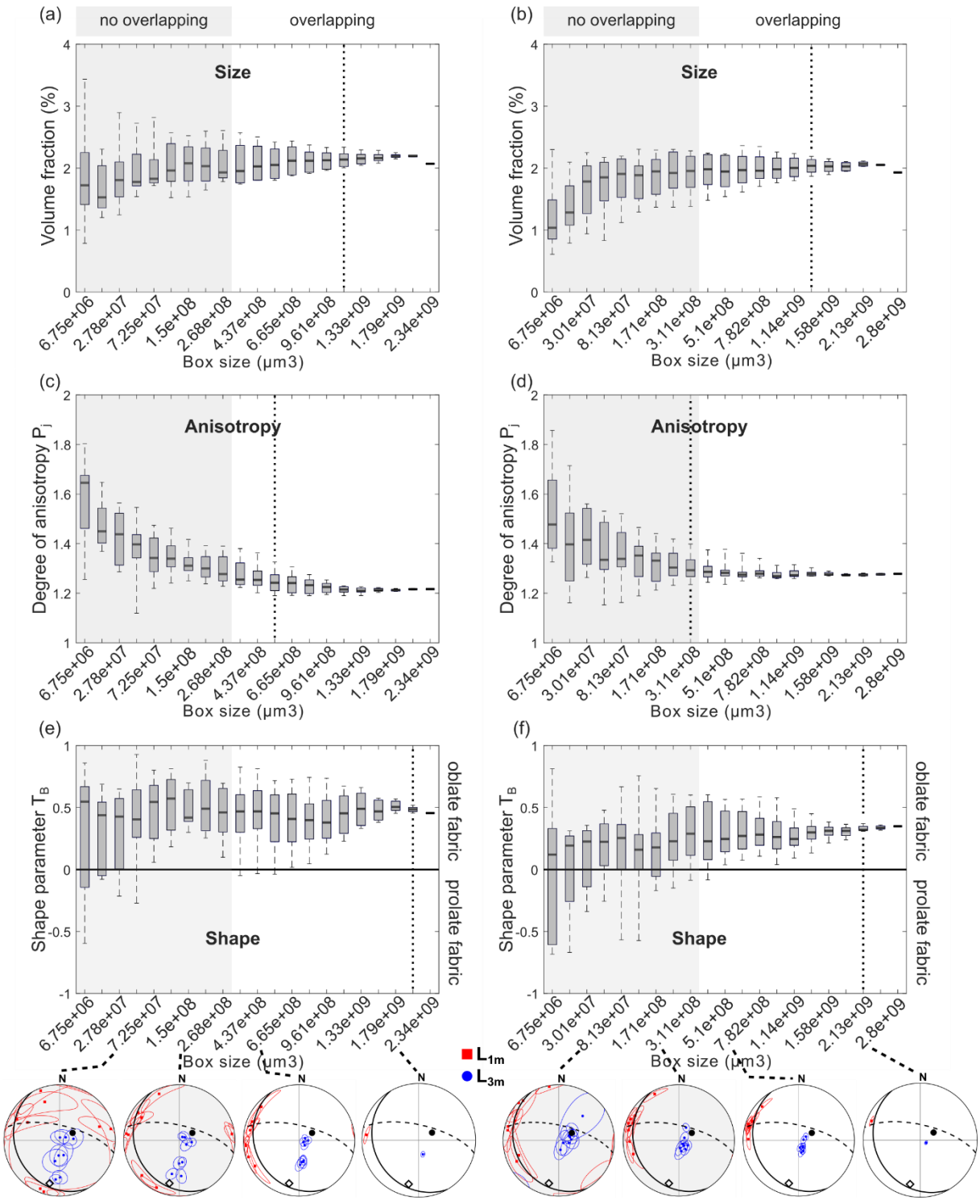

Figure 6.6: ***Results of the box-counting method for the bulk fabric analysis. Volume fraction of quartz for A4-1 (a) and A4-2 (b). Degree of anisotropy (P_j) of the mean tensors for A4-1 (c) and A4-2 (b). Shape parameter (T_B) of the mean tensors for A4-1 (e) and A4-2 (f). Dotted lines in the graphs indicate the representative size for the parameter according to the methodology explained in section 3.5. At the bottom are represented the principal axes of the fabric ellipsoids in stereographic projections for some box sizes, the bedding pole (dark circle) and the cleavage pole (diamond) are indicated.***

6.3.5 Microfabric heterogeneity and subfabrics

Figure 6.7 shows the bulk subfabric ellipsoids calculated from the subdivision of the VOI into eight compartments of the same size. These compartments are not necessarily representative of the bulk fabric parameters but the aim is to better characterize the microfabric heterogeneity. The obtained ellipsoids are represented in a geographic coordinate system both graphically (***Figure 6.7*****b** and ***Figure 6.7*****c**) and on stereographic projections (***Figure 6.7*****d** and ***Figure 6.7*****e**). The shape parameter T_B of each subfabric ellipsoid is plot against its degree of anisotropy P_j on a Jelinek diagram (***Figure 6.7*****d** and ***Figure 6.7*****e**). In A4-1, we show that the sample possesses two different localized subfabrics, four ellipsoids are controlled by the bedding plane while the other four are partially controlled by the cleavage plane as shown by the distribution of L_{3m} of each tensor. The L_{1m} axis is parallel to bedding-cleavage intersection if the ellipsoids are controlled by cleavage. The eight ellipsoids are in the oblate field and display a degree of anisotropy ranging from 1.2 to 1.4. In A4-2, an intersection lineation marked by L_{1m} seems to be better developed than for A4-1. We show a cluster of L_{3m} axes slightly oblique to the bedding pole. The subfabric ellipsoids are mainly oblate, except for two of them, and their degree of anisotropy falls in 1.2-1.4. Thus, the scalar values of the subfabric ellipsoids are not determinative for identifying subfabrics in A4-2. Size distributions of quartz associated to each subfabric ellipsoid are not plotted because differences are subtle, but small grains tend to dominate the distribution for the northern ellipsoids in A4-1, which are more cleavage dominated.

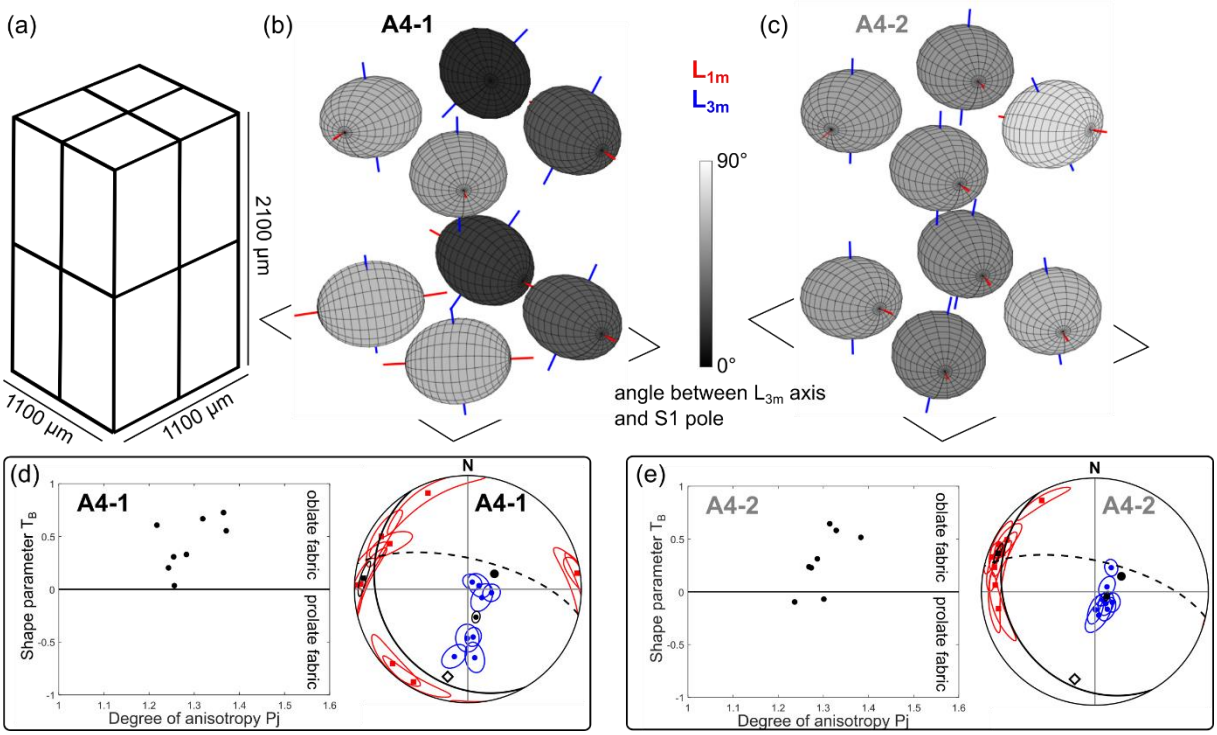

Figure 6.7: ***(a) Subdivision of the VOI into eight subvolumes. (b) Representation of the associated eight subfabric ellipsoids of A4-1 in geographic coordinate system. (c) Representation of the eight subfabric ellipsoids of A4-2. (d) Scalar data (Jelinek's diagram) and directional data of the subfabric ellipsoids represented in (b). The directional data of the whole VOI are represented in black. (e) Scalar data (Jelinek's diagram) and directional data of the subfabric ellipsoids represented in (c). The directional data of the whole VOI are represented in black. Directional data are represented in equal area and lower hemisphere projections, the bedding pole (dark circle) and the cleavage pole (diamond) are indicated.***

6.4 Discussion

6.4.1 Sample heterogeneity and microstructure

At the outcrop scale, cleavage appears continuous and dominates the rock fabric while the sedimentary fabric is hardly visible. These features characterize a slaty-cleavage fabric of the rock unit (***Figure 6.1***). XCT images obtained in this study reveal a rather spaced pattern of cleavage at the microscale (***Figure 6.3***). The two samples, extracted at 4 mm apart in very homogeneous shales, show an almost identical distribution of both quartz grain size and shape. Differences between the two samples are small and mainly arise from the directional data obtained by the individual grain analysis and the bulk fabric analysis. For both samples, the box counting method shows that individual features of quartz grains are well characterized in small rock volumes (nearly 0.08 mm^3). Therefore, the size of the two samples (nearly 2.5 mm^3) is sufficiently large to do this. On the contrary, the box-counting method applied for the bulk quartz fabric reveals a heterogeneity at the scale of the sample size. Thus, larger samples are needed to obtain a reliable REV of the bulk grain fabric. This is in accordance with the porosity analysis in slates by Akker et al. (2018). Based on Broad Ion Beam (BIB) images, they were able to estimate representative volume for porosity at the microscale whereas their bulk porosity measurements were more sensitive to larger scale heterogeneities such as the alternance of silt-rich layers and clay-rich layers, macrofractures and strain of the samples.

Our individual grain analysis reveals that clear differences do exist regarding individual quartz foliation pole ($\boldsymbol{L_3}$). As opposed to the relatively homogeneous sample A4-2 at the scale of observation, sample A4-1 shows that there is a dispersion of $\boldsymbol{L_3}$ axes between the cleavage pole and the bedding pole. It thus appears that a strong heterogeneity exists that the bulk fabric does not allow to suspect. This analysis reveals also that small grains are mostly controlled by cleavage in the A4-1 sample and are the most anisotropic. Sample A4-2 does not present such heterogeneity.

Bulk fabric analysis further shows that A4-1 is composed of two fabric domains and attests for heterogeneities at the millimeter scale. Sample A4-1 shows a mean foliation (as per the $\boldsymbol{L_{3m}}$ data) between bedding and cleavage, quite comparable to the clay fabric studied by Boiron et al. (2020) (***Figure 6.1*****e**). Rock fabric is probably partitioned by cleavage wavelength and intensity. The partitioning creates localized pressure solution seams (cleavage domains) that may have generated the smallest quartz grains. In A4-1, a deformation band of approximately 400 µm wide in which the small grains possess a strong cleavage fabric is observed. This deformation band may correspond to the subtle cleavage surface we observed in the A4 field sample (***Figure 6.1*****c**). This mixture of different fabric domains explains the average foliation of the quartz shape fabric. Sample A4-2 shows an unexpected mean foliation more dominated by bedding. Both samples show a lineation ($\boldsymbol{L_{1m}}$) that is mainly subparallel to bedding-cleavage intersection. We still observe lineations of the sedimentary fabric in A4-1.

Possible mechanisms responsible for this preferred orientation of quartz could be rigid rotation of grains and pressure solution. Surprisingly, the small grains in the A4-2 sample do not present a cleavage fabric. Multiple deformation mechanisms could yield heterogeneous fabrics. Rotation of grains may dominate in the more homogeneous part (e.g. A4-2 sample) while pressure solution may be promoted in closely-spaced cleavage domains (e.g. A4-1 sample). In the magnetic study of weakly deformed fine-grained rocks, Borradaile & Tarling (1981) also suggested that where localized cleavage surfaces developed associated to pressure solution, magnetite grains have a strong cleavage fabric. Outside of these domains, magnetite grains still have their sedimentary fabric. Our results bring geometric

evidence for such arrangements of grains and the role of the interference between sedimentary and tectonic structures in fine-grained rocks that contribute to their heterogeneity.

6.4.2 XCT grain analysis vs bulk magnetic fabric

The magnetic fabric measured on 72 cm-sized samples taken from the outcrop by Boiron et al. (2020) represents the average orientation of the clays particles and more precisely that of illite grains embedded in the rock matrix. It gives an insight in the bulk fabric over 720 cm^3 of deformed shales. The bulk magnetic fabric of the 72 samples shows an oblique foliation between bedding and cleavage (***Figure 6.8*a**). Interpreting this result would signify that illite grains are arranged obliquely between bedding and cleavage in this area. Such an arrangement would be surprising if we consider the amount of deformation of these shales, estimated to be ≈75%-80% by Boiron et al. (2020). Studies on highly deformed shales generally show that magnetic foliation is controlled by cleavage in the slaty or strong cleavage domain (Housen and van der Pluijm, 1991; Parés et al., 1999; Hirt et al., 2004). Focusing on the sample A4 (10 cm^3) from which the two mm-sized drill cores of this study have been taken, we observe a magnetic foliation subparallel to the cleavage (***Figure 6.8*a**). In the case of sample A4-1, the average quartz shape foliation is consistent with the average clay foliation of the 72 samples (***Figure 6.8*b**). This shows that results obtained at 2-3 mm^3 could be in agreement with those obtained at 10^3 cm^3 in fine-grained rocks. From the previous results, we know that the average foliation proves to be the combination of large quartz grains dominated by bedding, and small quartz grains, which are more anisotropic and preferentially oriented in the plane of cleavage (***Figure 6.8*b**). Moreover, the partitioning between bedding and cleavage domains induces this average foliation. This observation suggests that the same might be true for the illite measured by the magnetic fabric. Some illites could be controlled by cleavage and others by bedding (***Figure 6.8*c (1)**). Boiron et al. (2020) also reported this observation using Scanning Electron Microscope (SEM) images of illite. However, the average foliation of the magnetic fabric may also result from the bending and kinking of illites (***Figure 6.8*c (2)**), which are deformation mechanisms known to affect phyllosilicates in cleaved fine-grained rocks (Lüneburg et al., 1999; Chadima et al., 2004; Hirt et al., 2004; Parés, 2015).

In addition, we show that quartz lineation is remarkably stable compared to the foliation whereas one would expect to find a down-dip lineation in the cleavage plane in the most deformed domains. The quartz lineation is therefore very consistent with the magnetic lineation that also displays an intersection lineation.

We should note that the study of bulk parameters always averages out the subfabrics and are responsible, to a certain extent, to biased information. However, through the division of the VOI into subvolumes, we highlight representative subfabrics that are important to characterize the larger scale heterogeneity of these deformed shales. When such subfabrics are identified, special attention must be given to the treatment and interpretation of bulk data. Our study reveals that the study of a small volume in deformed shales by means of XCT is of interest and provides information that can be extended at larger scales. Furthermore, the study of subvolumes might answer the question: is the mm^3 quartz fabric capturing correctly the heterogeneity? The sample A4-2 is interesting in this respect, because its fabric is homogenous, both for scalar data and for directional data (***Figure 6.7***). The bulk shape fabric ($\boldsymbol{T_B} \approx 0.4$) is an element that is indicative of a competition between bedding and cleavage. In this study, this is expected because slaty cleavage is observed, but if the sample is coming from a borehole for example (cutting), it is desirable to provide additional elements of discussion. This is certainly the great variability of the shape parameter $\boldsymbol{T_B}$ measured in the box-counting method which is a clue for inferring a strong heterogeneity of the sample (***Figure 6.6*e** and ***Figure 6.6*f**).

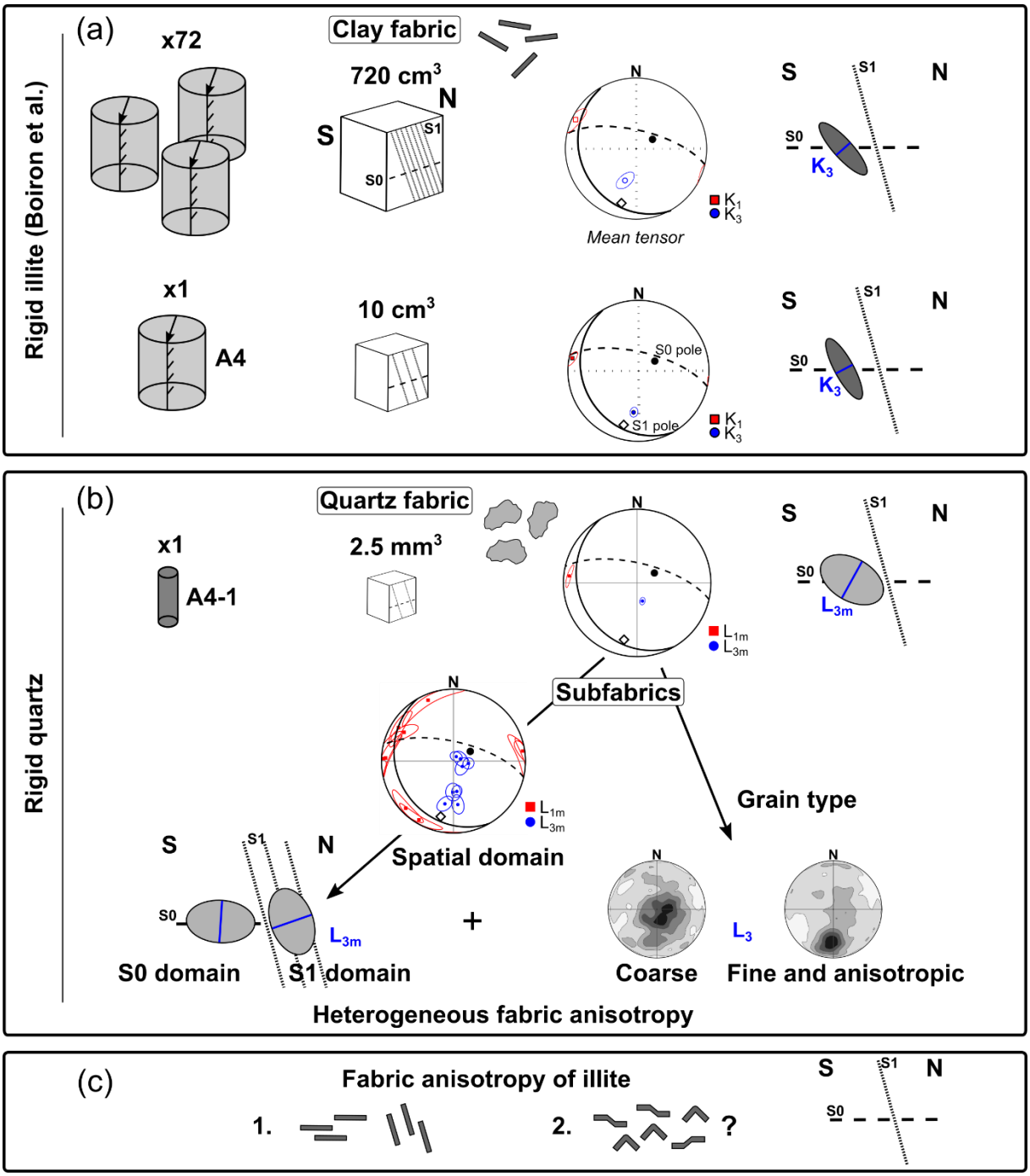

Figure 6.8: *Conceptual sketch to illustrate how small scale grain fabric heterogeneities explain bulk fabric at larger scales with specific attention to the foliation. (a) Summary of the magnetic fabric results obtained by Boiron et al., 2020. The results illustrate the geometrical arrangement of illite grains at the outcrop scale (10 m² covered by 72 measurements) and at the hand-specimen scale (A4 sample). The rightmost part represents the orientation of the* K_3 *axis of the susceptibility tensor. (b) Summary of the quartz shape fabric. Main results of the investigation of the VOI of sample A4-1 at microscale using individual grain data and bulk fabric data. The orientation of the* L_{3m} *axis of the fabric ellipsoid is represented. (c) 1. Suggested illite fabric anisotropy based on quartz shape fabric results ; 2. Folding and/or kinking of the illite platelets is not excluded.*

6.5 Conclusion

We analyzed the individual grain data and bulk data of the quartz microfabric in two XCT images of strained shales. The box-counting method was systematically used to assess the representativeness of the morphological parameters. Our results highlight the variability in the population of grains and heterogeneities in the fabric anisotropy (bedding dominated or cleavage dominated). The individual grain analysis enables to extract subfabrics related to the morphotype of each grain, regardless of their position in the VOI. The bulk fabric analysis highlights the localization of bedding domains and cleavage domains in the VOI and the variability of the scalar parameters attests for larger scale heterogeneity in the sample.

The main results obtained are:

- In strained shales, the investigation of a volume of 430 x 430 x 430 μm^3 (nearly 0.08 mm^3) captures the heterogeneity of quartz grains. A greater volume (≥ 1000 µm side length) is necessary to be representative of the grain shape fabric heterogeneity and the minimum required size depends on the studied quantity.
- In an intensely deformed rock (≈75%-80% shortening), the quartz grains can be mainly controlled by bedding because of the disjunctive nature of cleavage on observation scales of a few mm^3. This induces a matrix heterogeneity that could not have been anticipated from field observations, where the cleavage is very penetrating.
- The fine fraction of quartz, which is more anisotropic, tends to be better parallelized in the cleavage plane.

In a broader perspective, our study shows that the study of a small volume of shales can reveal key characteristics that we also found over several m^2. Our approach allowed to propose that the foliation of the clay phase measured by the magnetic fabric in the study of Boiron et al. (2020), which is on average oblique between bedding and cleavage, probably results from heterogeneous small-scale zones, where clays are both bedding-dominated and cleavage-dominated. Bending and kinking of clays cannot be ruled out as additional causes, but indistinguishable on the basis of the quartz fabric analysis at this scale. Microscale investigation allows a better understanding of shale fabric and can be transposed to larger scales. Furthermore, it helps in the interpretation of bulk measurements provided by other techniques such as AMS, and avoids the pitfall to average-out important rock fabric characteristics. In addition, it quantifies the rock fabric anisotropy and allows identifying deformation domains and microstructural relationships. It can be useful in order to infer deformation mechanisms acting at this scale.

7 Rock matrix of deformed turbiditic layers: a view from 3D clast shape fabric and magnetic fabric

7.1 Aims

We have seen in the previous chapter that the characteristic length scale of the deformation structures (millimeter scale) influences the representativeness of the rock fabric. However, in the petrofabric characterization of fine-grained rocks we are forced to make a compromise. We need a good spatial resolution and sufficient contrast in the XCT images to be able to identify the clasts and at the same time, we need a large enough volume to do a robust quantitative analysis. In this sense, the 1.5 to 2 mm diameter drill cores offer a good opportunity to address this issue. Now we desire to evaluate what could be the heterogeneity of the fabric of different clastic rocks at the outcrop scale using XCT and AMS data. In the previous chapters concerning strain gradients (chapters ***4*** and ***5***), we have examined the same (or almost the same) rock unit at different strain states. In this chapter, we intend to investigate the shape fabric of clasts in different rock units that have experienced the same deformation event(s) but that may have contrasting mechanical stiffness and thus different deformation patterns. Therefore, we are crossing the sedimentary stack in a vertical way for a common deformation event. The purpose of this chapter is to characterize both the shape fabric of quartz grains and the AMS in multiple lithologies of carbonate turbidites of the **Hecho** group (Mutti, 1977, 1983). The lithologies are displaying two macroscopic planar fabrics (bedding and cleavage).

7.2 Geological setting and samples

We have collected 36 AMS standard drill cores from multiple lithologies in two areas that are represented in the modified cross-section of Labaume et al. (1985) in ***Figure 7.1***. The locations of the sampling sites correspond to projected emplacement on the cross-section. The Roncal Valley is our main natural case study. The Sigüés outcrop of chapter ***4*** was the most external part of the fold and thrust belt represented in ***Figure 7.1***. In both new sites, we have sampled deformed rocks. The spacing and intensity of cleavage (S1) varies with the different lithologies/rock types. The first sampling area (labeled 2T or West Burgui) is located in a small canyon along the road NA-214 connecting Burgui to Navascués, approximately 10-road km west from the Roncal Valley. In total, seven samples from this site were scanned by XCT. The second and more intern sampling area (labeled 1T or North Roncal) is located on the western side of the main road NA-137 in the Roncal Valley. We have scanned eight samples coming from this site.

There are many classifications of cleavage in the literature (Alvarez et al., 1978; Powell, 1979; Borradaile et al., 1982; Engelder and Marshak, 1985; Durney and Kisch, 1994; Parés, 2004; Passchier and Trouw, 2005). For each site, we have summarized the main features concerning the spacing of the solution cleavage surfaces at the bed scale, the AMS core scale and the XCT core scale with a nomenclature taken from Durney and Kisch (1994) and Passchier and Trouw (2005). Note that this table is just a quick overview to give basic characteristics of the samples. In most cases, the cleavage surfaces are barely detectable at the AMS core scale. The cleavage spacing in the XCT images depends on the spatial resolution of the images. For some samples, there is spaced solution cleavage that can be detected at the AMS core scale. This type of cleavage can be retrieved in the XCT images and generally appears as rather thick subparallel cleavage laminae or pressure solution seams (PSS, ***Figure***

7.2). As the samples are carbonate turbidites, this spaced cleavage does not have smooth surfaces. It corresponds to the smooth to wriggly shape type of Passchier and Trouw (2005). The XCT images allow to see thinner cleavage laminae but poorly resolvable. These surfaces are generally highlighted by the truncation of carbonate bioclasts and appear as rough cleavage laminae at the given image resolution. We have subdivided the solution-cleavage surfaces (i.e. cleavage laminae or PSS) into the penetrative slaty type (thin PSS) and the non-penetrative spaced type (or disjunctive, thick PSS) for simplification. Note that this terminology is based on the scale of the field of view of the XCT images and what can be seen with the naked eye. We have also reported when heterogeneously distributed cleavage surfaces can be seen in the form of localized, high density cleavage domains or 'stripes' (Durney and Kisch, 1994).

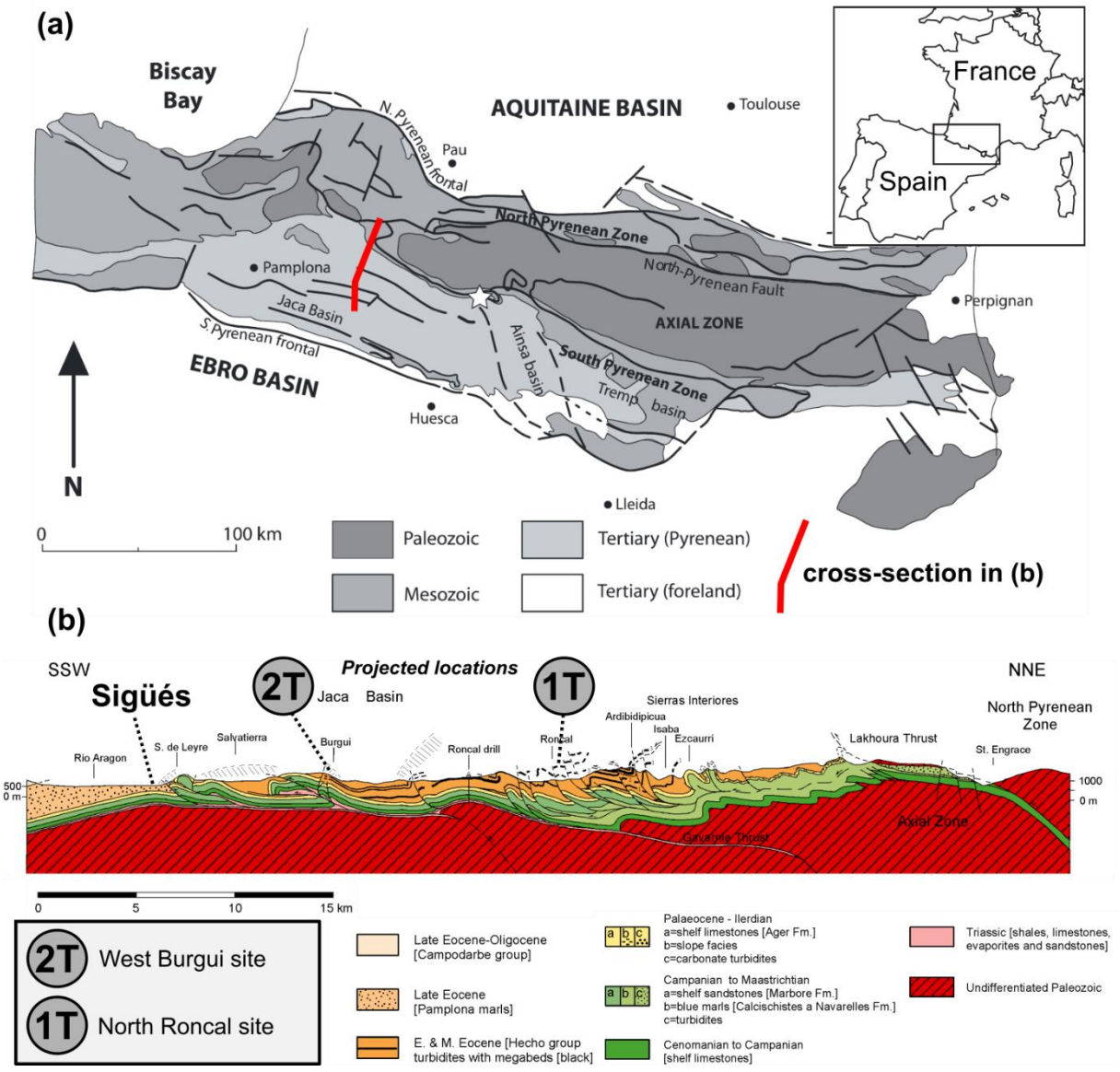

Figure 7.1: *(a) Structural map of the Pyrenees with the location of the cross-section in the Jaca basin, modified from Lacroix et al. (2014, 2015). (b) Location of the two sampling sites in the fold and thrust belt. Cross section of Schellart (2002), redrawn from Labaume et al. (1985).*

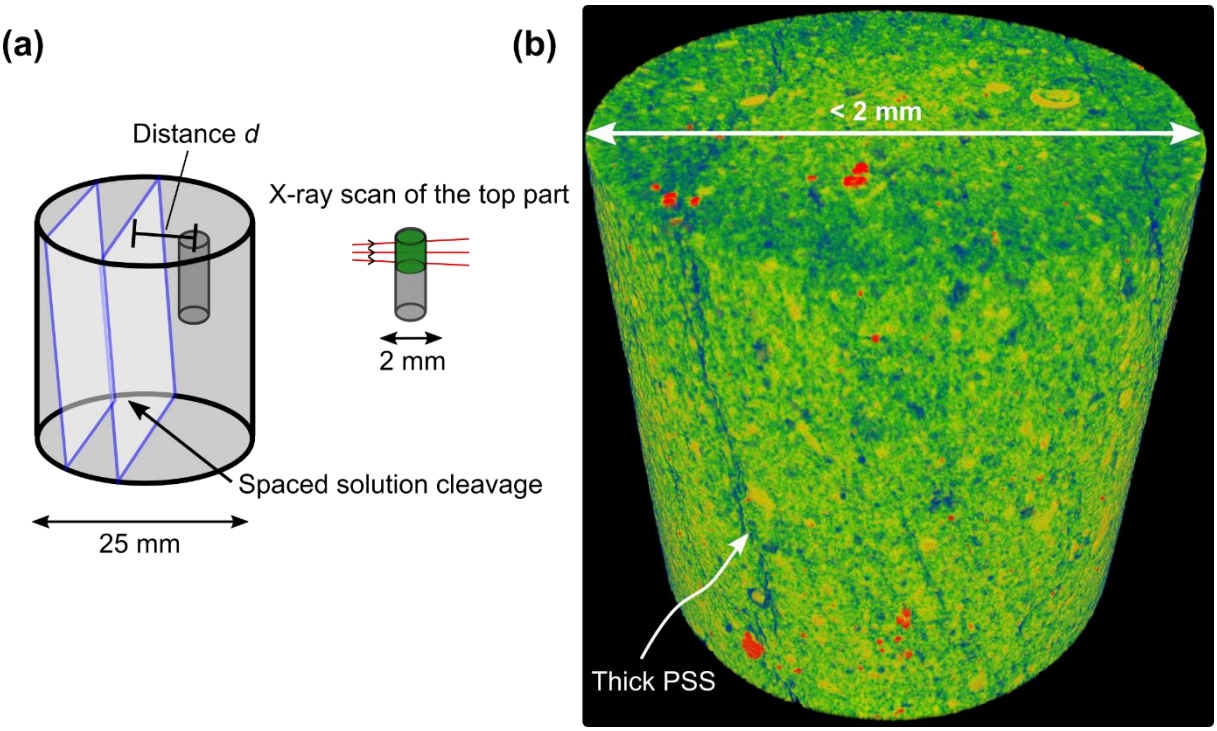

Figure 7.2: *(a) Standard AMS drill core with visible spaced cleavage surfaces. Distance d between a cleavage surface and the center of the XCT drill core. (b) Cleavage surfaces may appear as thick pressure solution seams (PSS) in the XCT image (3D view of sample 1T5A with a Look-Up Table from Dragonfly software).*

7.3 West Burgui site 2T

7.3.1 Introduction

At this outcrop, we observe a sub-horizontal bedding (S0) and a vertical cleavage (S1) that crosscut all the different beds of marlstone/calcareous turbidites (***Figure 7.3***). This high angular relationship between S0 and S1 can be attributed to an LPS deformation of the sedimentary rocks. Many pencil fragments of the surrounding rocks are found on the site that attest for a pencil state cleavage development. The macroscopic (i.e. at the bed scale) spacing of cleavage varies between 2 mm and 100 mm depending on the ductility of the rock. The bulk susceptibility measured by AMS is generally lower than or about 100 SI. These values are comparable to that of Sigüés and these rocks may have a comparable phyllosilicate content. We have subdivided the samples in two groups. The first group contains samples with a narrower cleavage spacing, at the bed scale (samples 2T7A, 2T8B and 2T8B-HR, referred to hereafter as **NCS samples**). According to the closely spaced cleavage surfaces, these samples may be less competent (i.e. less stiff). Samples 2T8B and 2T8B-HR have been drilled from the same AMS drill core but at different locations and with different voxel resolutions. The second group contains samples with a wider cleavage spacing (samples 2T12B, 2T14B, 2T16B and 2T18B, referred to hereafter as **WCS samples**) and may be more competent. ***Table 7.1*** summarizes the main characteristics of the imaged samples. ***Table 7.2*** provides the volume fraction of quartz extracted in each imaged sample. All samples from this site have been scanned at a 2 µm voxel resolution. Sample 2T8B-HR has been scanned at a 1.5 µm voxel size and one can noticed that the volume fraction of quartz is greater in this sample (***Table 7.2***).

Table 7.1: *XCT imaged samples, bedding/cleavage angle and cleavage spacing. Km = bulk magnetic susceptibility.*

	Macroscopic S0/S1 angle	Km (x 10^{-6} SI)	Macroscopic S1 spacing (mm)	Distance *d* from the XCT drill core to a major cleavage surface visible on the AMS drill core (mm)	Main structural elements in the images
2T7A (NCS)	83°	94	2 – 5	< 2	Penetrative cleavage: spacing 50-250 µm. Spaced cleavage: spacing 1200 µm. Dense array of PSS and heterogeneously distributed
2T8B (NCS)	83°	108	20 – 30	3.5	Very few PSS
2T8B-HR (NCS)	83°	108	20 – 30	3	Very few PSS
2T12B (WCS)	83°	94	60 – 80	6.5	Dense array of North-South calcite veins of 10 to 50 µm width, spacing of 250 to 500 µm.
2T14B (WCS)	83°	109	100	< 1	Penetrative cleavage: spacing 250 µm Spaced cleavage: spacing >1500 µm. Dense array of PSS.
2T16B (WCS)	83°	108	50	6	Penetrative cleavage: spacing ≈ 250 µm
2T18B (WCS)	83°	112	50	6	Penetrative cleavage: spacing ≈ 250 µm

Table 7.2: ***Volume of interest for each scanned sample collected in the West Burgui site. Number and volume fraction of quartz particles in this VOI, obtained after segmentation, cleaning and removal of boundary grains. As the XCT drill core diameter depends on the strength of the sample during the drilling operation, the size of the VOI is generally linked to the stiffness of the sample (see also Figure 7.3).***

Sample	2T7A	2T8B	2T8B-HR	2T12B	2T14B	2T16B	2T18B
Volume of interest (mm^3)	2.279	1.995	0.576	3.045	2.857	2.416	2.316
Number of quartz grains	4,795	7,693	4,628	4,177	6,051	6,859	5,363
Volume fraction of quartz	1.22 %	2.35 %	3.64 %	0.76 %	1.16 %	1.57 %	1.35 %

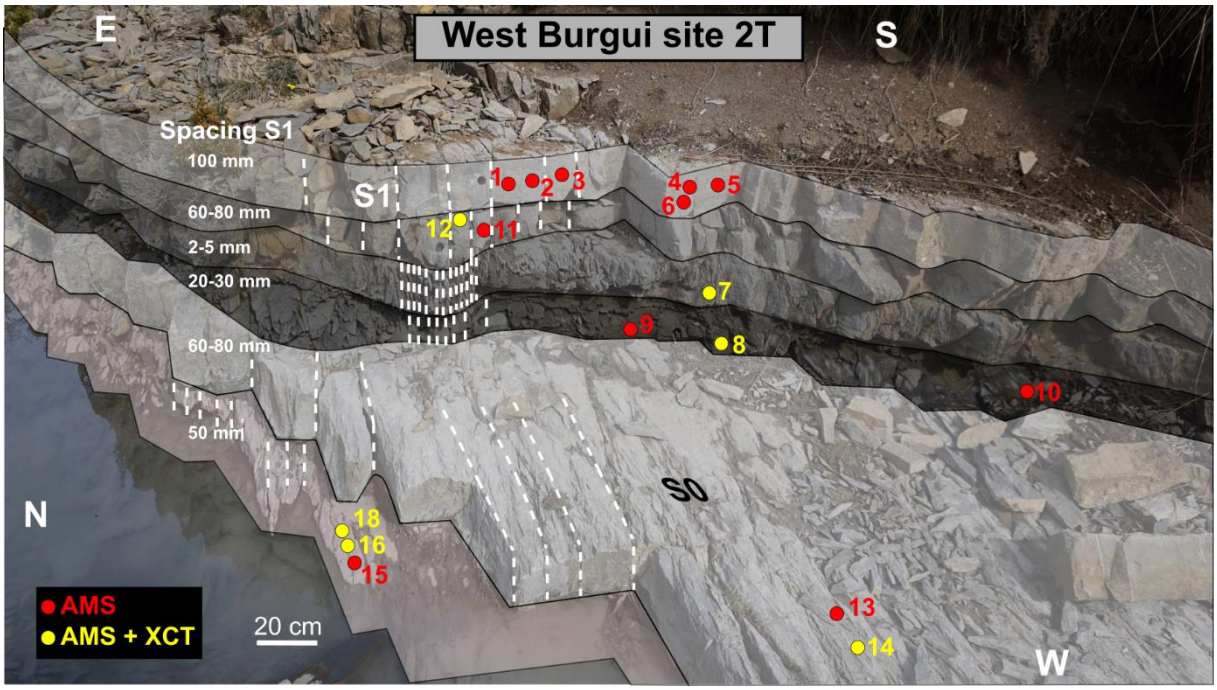

Figure 7.3: ***Photograph of the sampling area in the West Burgui site. Multiple lithologies of carbonate turbidites with similar bed thickness but various cleavage intensities at the bed scale. The NCS samples (7 and 8 on the photo) correspond to the shaly units. The WCS samples (12, 14, 16 and 18) have a higher apparent stiffness.***

7.3.2 Shape fabric of quartz and magnetic fabric

7.3.2.1 Grain shape data

The grain shape data are represented in ***Figure 7.4*** for the NCS samples and in ***Figure 7.5*** for the WCS samples. The quartz grain size distributions are not significantly different. We note a slightly steeper curve for the 2T8B-HR sample and a distribution that includes smaller grains due to its higher image resolution (voxel resolution of 1.5 µm). The distributions of the shape parameter $\boldsymbol{T_G}$ are comparable with a slightly higher proportion in triaxial prolate ellipsoids. A weak predominance for triaxial oblate ellipsoids is observed for sample 2T7A. Sample 2T8B-HR does have slightly more anisotropic grain ellipsoids compared to samples 2T7A and 2T8B.

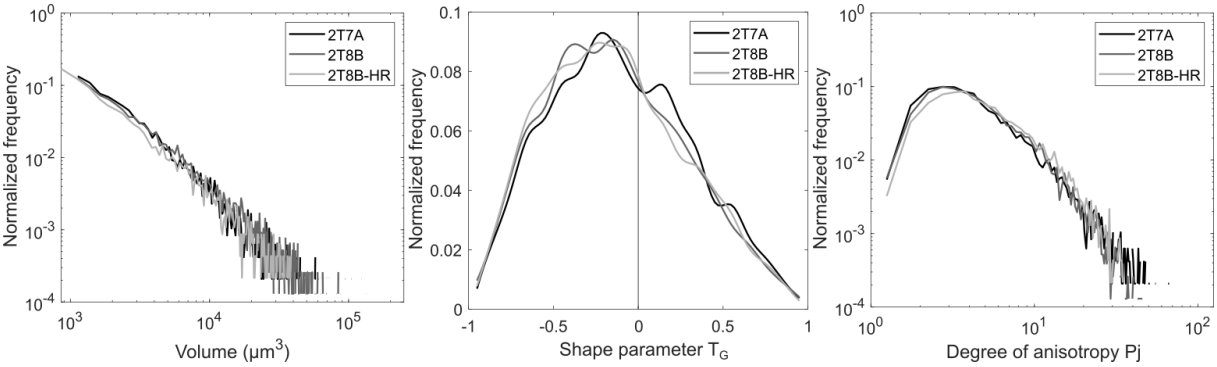

Figure 7.4: ***Normalized distributions of grain volume, shape parameter*** T_G ***and degree of anisotropy*** P_j ***of the quartz grain ellipsoids in the NCS samples.***

The distribution curves for the WCS samples are rather comparable for the three studied parameters (***Figure 7.5***). In addition, the distribution of the degree of anisotropy is comparable with the NCS samples. There are no significant differences.

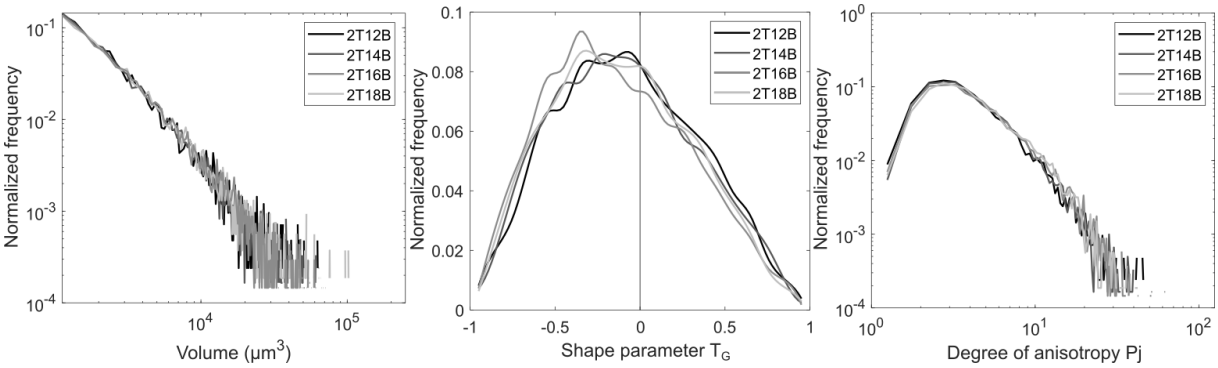

Figure 7.5: ***Normalized distributions of grain volume, shape parameter*** T_G ***and degree of anisotropy*** P_j ***of the quartz grain ellipsoids in the WCS samples.***

7.3.2.2 SPO of quartz and AMS

Directional data of the individual grain analysis and the bulk shape fabric are summarized in ***Figure 7.6*** for the NCS samples. The figure contains also the directional data of the magnetic fabric measured by means of AMS and the Jelinek diagrams for both techniques.

Firstly, the mean tensor of all AMS specimens (n = 23) is triaxial oblate ($\boldsymbol{T} \approx 0.3$) and shows a rather good orthorhombic symmetry of the confidence ellipse of the principal directions (***Figure 7.6***). The deflection of the confidence ellipse of the intermediate axis of the mean tensor is due to the imperfect oblate symmetry of the mean tensor. However, the mean AMS tensor also tells us that the orientation distribution of the susceptibility ellipsoids is more symmetric about the mean $\boldsymbol{K_3}$ axis and that this axis is on average parallel to the bedding pole. The sample 2T7A displays an intersection lineation fabric with intermediate foliation for both techniques (AMS and XCT). $\boldsymbol{L_3}$ axes in this sample depict a symmetric to slightly asymmetric girdle between the poles of bedding and cleavage. The intermediate position of $\boldsymbol{K_3}$ and $\boldsymbol{L_{3m}}$, between S0 and S1 poles, is really comparable. The shapes of the susceptibility and the fabric ellipsoids are also comparable and are in the triaxial prolate field. The degree of anisotropy of the SPO is moderate with $\boldsymbol{P_j} = 1.3$. Samples 2T8B and 2T8B-HR show an intersection lineation fabric with bedding controlled foliation in AMS and SPO. The foliation of quartz grains is more intense in the lower resolution image (2T8B) than in the higher one (2T8B-HR). The shape fabric ellipsoid is more oblate than the susceptibility ellipsoid. The shape fabric anisotropy is quite pronounced ($\boldsymbol{P_j} > 1.5$).

In these three NCS samples, directional and scalar data of quartz shape fabric and magnetic fabric are in accordance. The strength of the shape fabric is greater in the bedding-controlled foliation samples.

The data concerning the WCS samples are reported in ***Figure 7.7***. Samples 2T12B and 2T14B have contrasting directional AMS and SPO data, these two fabrics are not coaxial. Shape fabric of quartz attests for an intersection lineation fabric with girdle development of $\boldsymbol{L_3}$ axes. The foliation tend to be more bedding-controlled in 2T12B and more cleavage-controlled in 2T14B. The AMS shows an unexpected north-south lineation and west-dipping foliation. The susceptibility ellipsoid of 2T12B is prolate and its SPO ellipsoid is triaxial prolate. The susceptibility and fabric ellipsoids of 2T14B are prolate. The fabric intensity, expressed by the parameter $\boldsymbol{P_j}$, is moderate as for the previously 2T7A sample.

The AMS directional data and quartz SPO are coaxial in sample 2T16B. This sample shows a magnetic intersection lineation fabric with a north-dipping $\boldsymbol{K_3}$ axis and a large top to the north confidence region. This fabric is retrieved in the quartz shape fabric with girdle development of $\boldsymbol{L_3}$ axes and a mean $\boldsymbol{L_{3m}}$ axis dipping to the north. Sample 2T18B shows an SPO with symmetric girdle of $\boldsymbol{L_3}$ axes and a bedding-controlled $\boldsymbol{L_{3m}}$ axis. Its magnetic fabric attests for a bedding-controlled foliation.

All the four WCS samples have triaxial prolate to prolate SPO ellipsoids with anisotropy ranging from 1.25 to 1.33. The susceptibility ellipsoids are mainly prolate too with the exception of sample 2T18B which is oblate and has a stronger fabric anisotropy.

We should note that the $\boldsymbol{L_3}$ axes of the samples tend to display more symmetric girdles as opposed to the asymmetric one of Sigüés (chapter ***4***). Thus, this site may indicate a pure shear deformation event.

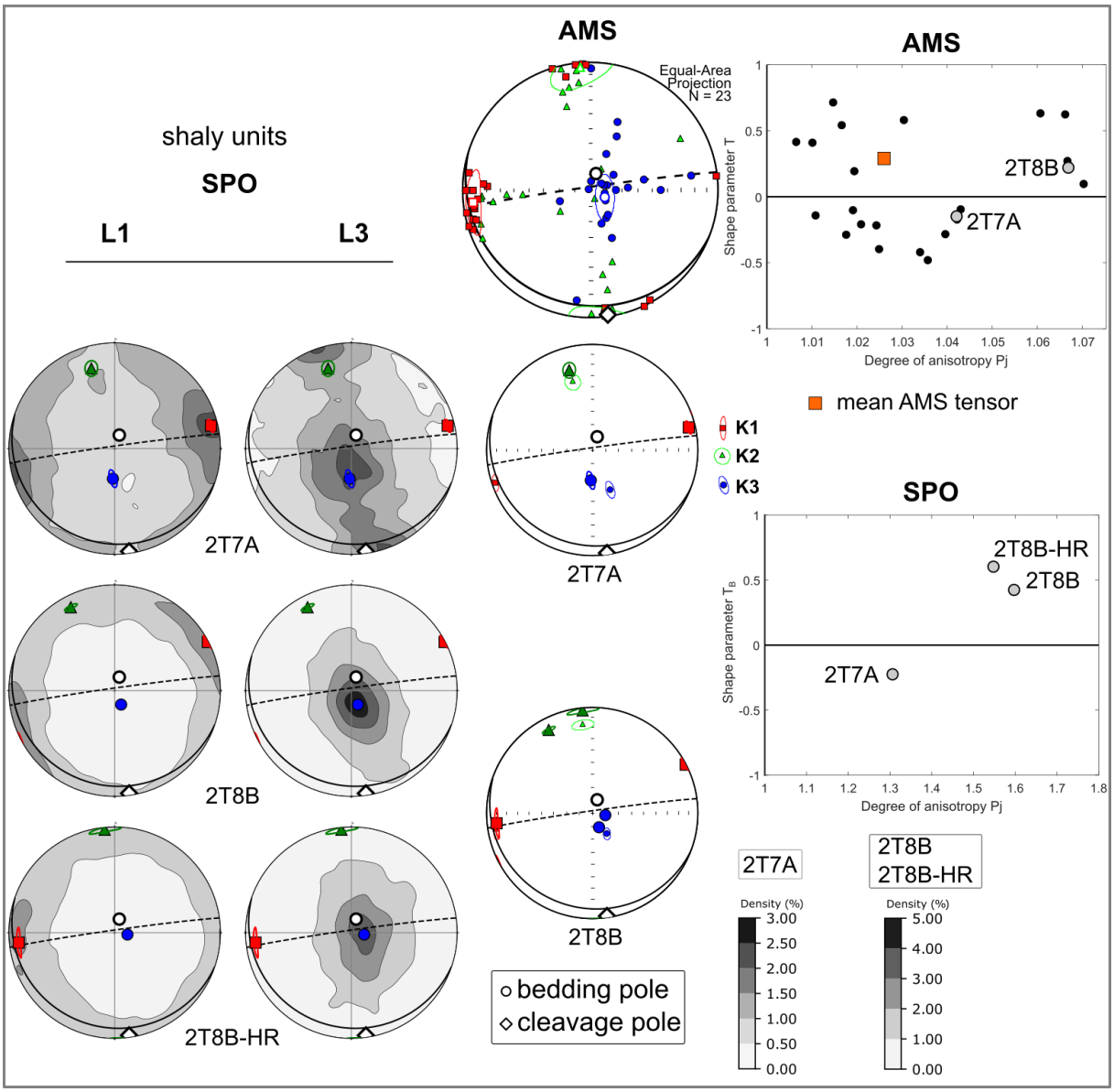

Figure 7.6: ***Quartz shape fabric and magnetic fabric data of the NCS samples of the West Burgui site.***

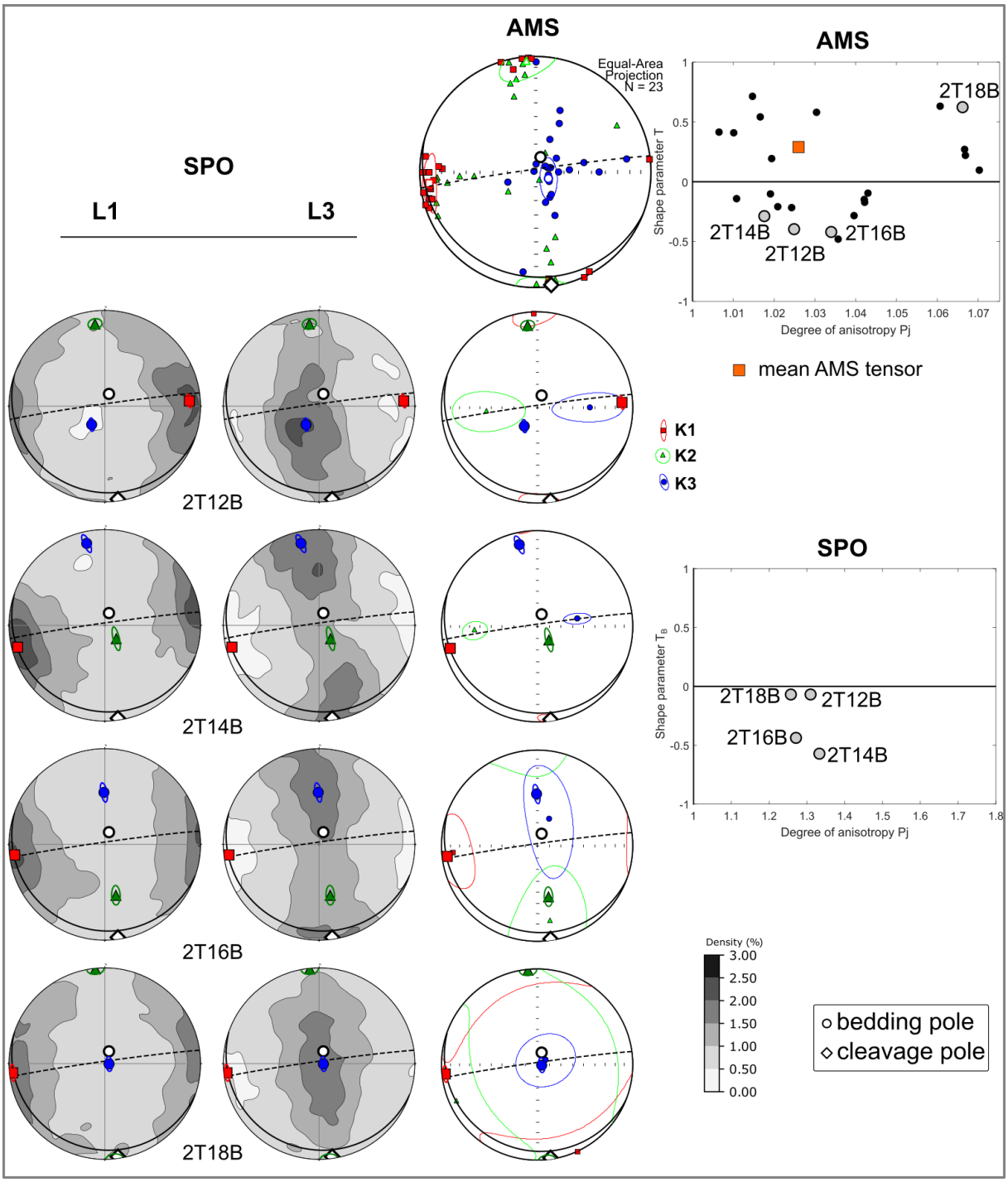

Figure 7.7: ***Quartz shape fabric and magnetic fabric data of the WCS samples of the West Burgui site.***

7.3.2.3 Representative size, sample homogeneity and subfabrics

The girdle distribution of the L_3 axes in sample **2T7A** makes it quite interesting. As such, this sample was chosen for a more in-depth analysis of its shape fabric. The XCT image of this sample reveals a striking spaced cleavage and a more penetrative one (***Table 7.1***). Moreover, the cleavage surfaces are heterogeneously distributed. XCT images of this sample are provided in ***Figure 7.8***. We can see a anastomosing to conjugated cleavage pattern connecting the thicker spaced cleavage and the thinner cleavage seams. This microscale observation is similar to the one described by Mitra and Adolph Yonkee (1985), at a slightly higher observation scale, in cleaved Jurassic micrites deformed at very low

grade ($Temperature < 200°C$). As these authors noted, we equally report that cleavage seams greatly truncate the calcite bioclasts whereas quartz grains are less affected (see e.g. ***Figure 7.8*****c**). In addition, the seams may develop increments or steps that shift the surfaces by a slight offset and give a discontinuous aspect to the seams.

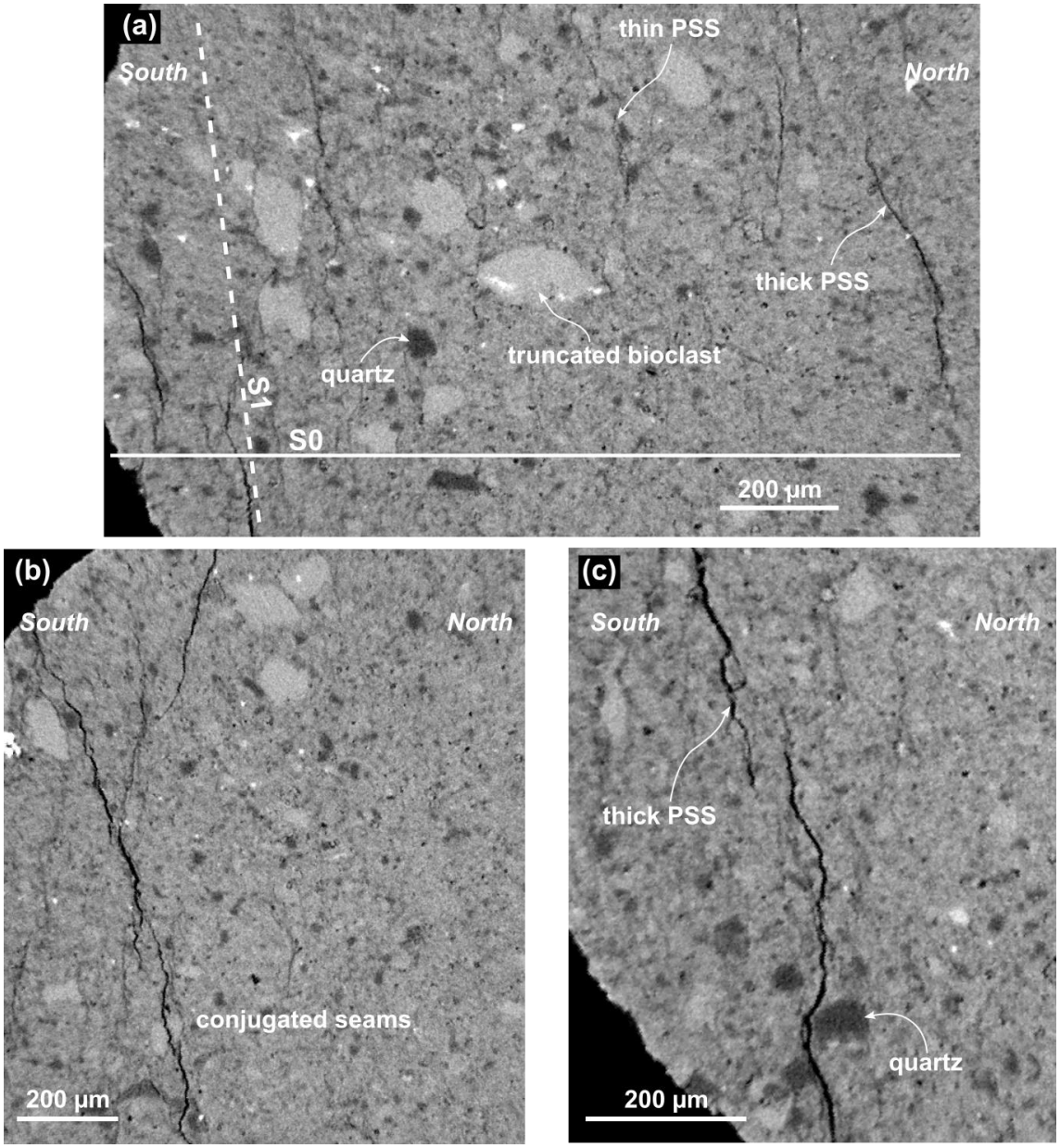

Figure 7.8: ***XCT views of sample 2T7A in a geographic coordinate system. (a) Thick PSS appear as subvertical dark laminae, thin PSS truncate the carbonate bioclasts. Note the highly flattened carbonate bioclasts on the left whereas the bigger one in the middle of the image almost retain its original shape and sedimentary fabric. Quartz grains (dark gray) are smaller. (b) Example of conjugated seams pattern formed by thick and thin PSS. (c) Example of incremental thick cleavage seam. Note the deviation of the seam around the quartz grains.***

We applied the box-counting method to estimate the representative size of the bulk quartz shape fabric and to evaluate its homogeneity. We have shown in the previous chapter that the evolution of the shape parameter of the shape fabric ellipsoid ($\boldsymbol{T_B}$) is very relevant to assess the homogeneity of the fabric. For this sample, we have represented the evolution of the degree of anisotropy $\boldsymbol{P_j}$ and the shape parameter $\boldsymbol{T_B}$ for the mean tensors computed in the box-counting method (***Figure 7.9***). Following our criterion exposed in section ***3.5***, a representative size is achieved for $\boldsymbol{P_j}$ at the tenth box

size (***Figure 7.9*a**). We remark a sinuous evolution of the bulk shape parameter $\boldsymbol{T_B}$ as the boxes are expanded (***Figure 7.9*b**). In a similar way to what was observed in chapter ***6***, we can also see a discrepancy rebound in $\boldsymbol{T_B}$ at the three quarters of the diagram while boxes are overlapping (***Figure 7.9*b**). This rebound is a marker of the inhomogeneity of the quartz shape fabric. Therefore, the representative size for $\boldsymbol{T_B}$ is only achieved at the eighteenth box size.

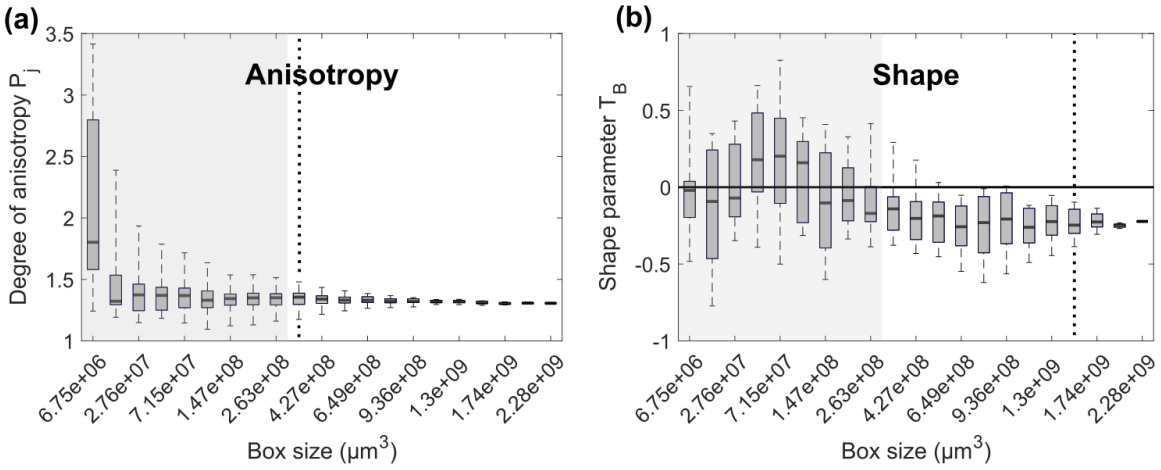

***Figure 7.9:** Results of the box-counting method (bulk fabric parameters) applied in sample 2T7A. (a) Degree of anisotropy P_j of the mean tensors. (b) Shape parameter T_B of the mean tensors. Dotted lines in the graphs indicate the representative size for the parameter.*

We have also seen in the previous chapter that subfabrics may exist such as localized subfabrics due to main deformation structures or morphological subfabrics related to the shape features of individual grains. Here we propose a global way to analyze quickly the main subfabrics of the quartz shape fabric of sample 2T7A. We only use bulk shape data. The identification of localized subfabrics is performed by subdividing the VOI into eight compartments and computation of the mean tensor (fabric ellipsoid) in these zones. Instead of using an individual grain analysis (see previous chapter) to identify morphological subfabrics, we also employ a mean tensor calculation to subdivide the quartz grains into different categories or subsets. We know that this mean tensor computation gives only an average information and must be taken with care but it is nevertheless interesting because it allows to have a quick overview of the variability of the directional data in the same stereoplot. The subfabric analysis of sample 2T7A is summarized in ***Figure 7.10***.

As shown in ***Figure 7.10***, variability in the directions of $\boldsymbol{L_{3m}}$ axes of the localized subsets are noticeable. The subfabric ellipsoids 1, 2, 5 and 6 have a bedding-controlled foliation while ellipsoids 3, 4, 7 and 8 have an intermediate foliation between bedding and cleavage. Seven out of eight ellipsoids are triaxial prolate but the intensity of their fabric anisotropy is different.

In ***Figure 7.10***, the size subsets show that as the grain size increases, the foliation of the mean subfabric ellipsoid tends to be more bedding-controlled but this is not a sharp trend. The grain size seems to influence the shape parameter $\boldsymbol{T_B}$ of the subfabric ellipsoid with prolate ellipsoids for the first subsets and triaxial ellipsoids for the last subsets. The anisotropy subsets do not induce variability in the directional data, except for very anisotropic grains (subset 10). The subset 10 of the degree of anisotropy shows a cleavage-controlled foliation. Note that you can see how the individual anisotropies of grain drive the anisotropy of the subfabric ellipsoid on the Jelinek diagram (Giorgis and Tikoff, 2004). The shape subsets illustrate the influence of $\boldsymbol{T_G}$ (individual shape parameter) on the bulk shape parameter $\boldsymbol{T_B}$. For this parameter, we remark a trend. Subsets of prolate grains provide

subfabric ellipsoids with a bedding-controlled foliation while subsets of oblate grains provide subfabric ellipsoids with a more intermediate foliation (closest to the cleavage plane).

In this sample 2T7A, it appears that the localization of the cleavage structures influence the foliation of the bulk shape fabric. This foliation may also vary with the individual shape attributes of the grain ellipsoid. In particular, oblate grains may form a foliation that is more cleavage controlled.

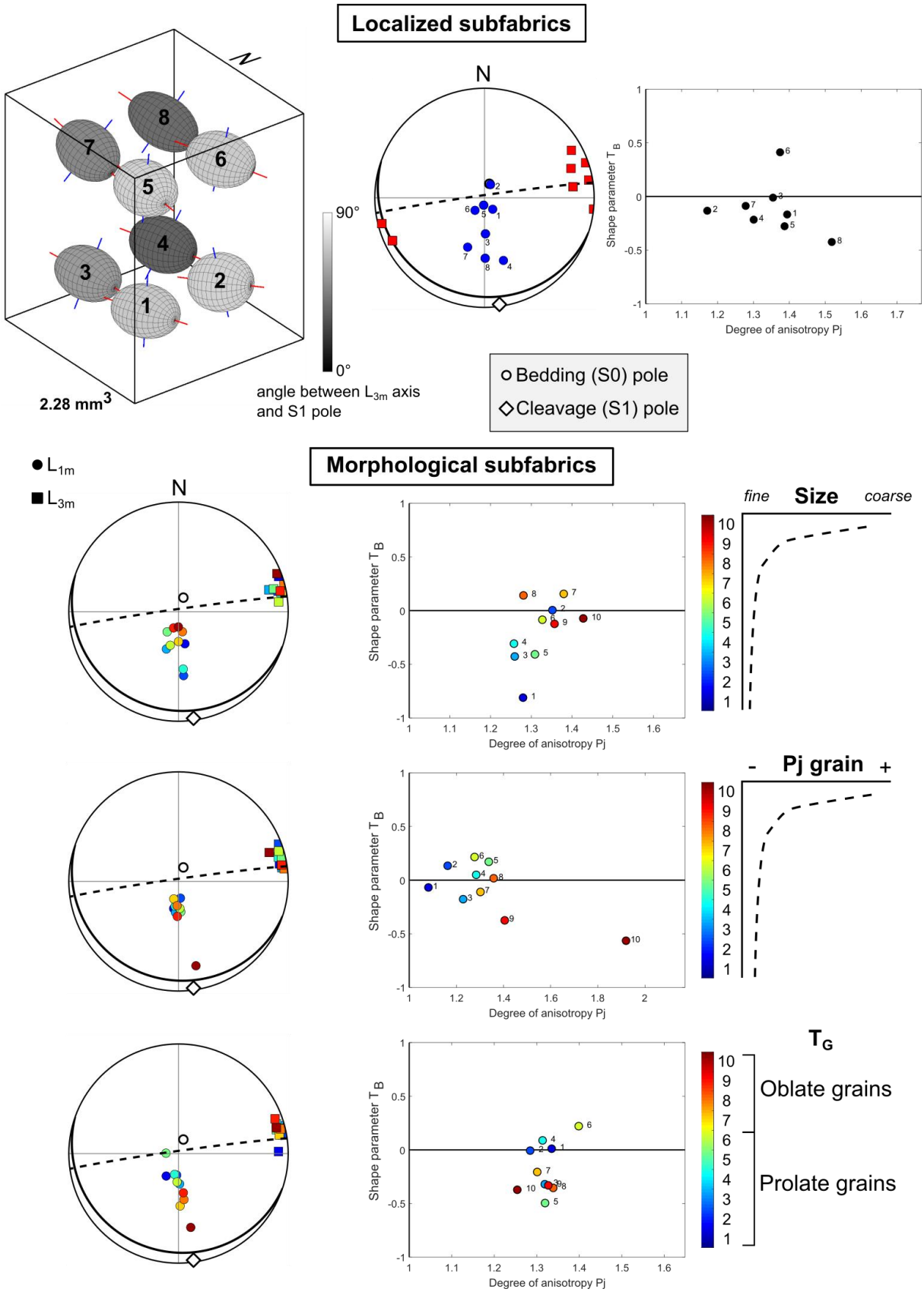

Figure 7.10: ***Subfabric analysis in sample 2T7A. Top: characterization of localized quartz subfabrics by subvolume analysis. Representation of the eight subfabric ellipsoids, in a geographic coordinate system, belonging to the eight subvolumes. Their directional and scalar data are given on the diagrams on the right. Note that these subfabric ellipsoids are computed for a different number of grains in each localized subset. Bottom: characterization of***

morphological subfabrics. Three parameters are studied (grain size, P_j, T_G). The population of quartz grains is broken down into ten subsets, which are the 10% quantiles of the considered parameter. In that case, each mean tensor or subfabric ellipsoid is an average obtained for the same number of grains.

7.3.3 Spatial distribution analysis

In this section, we give the results of the spatial distribution analysis of the segmented quartz grains of the seven samples. The results for the NCS samples are presented in ***Figure 7.11***. The results for the WCS samples are presented in ***Figure 7.12***. In sample 2T7A (***Figure 7.11***), distribution ellipsoids are very weakly anisotropic and quartz grains may be randomly distributed. The directional data suggest a lateral compaction that is not related to the cleavage development. In sample 2T8B, the distribution ellipsoid is triaxial oblate for the first three classes and then it moves to the prolate field for the subsequent classes. As the smaller grains are progressively removed, the degree of anisotropy increases but remains weak. Here again, the grains are probably randomly disposed. In the more resolved X-ray scan of sample 2T8B-HR, grains may also be randomly distributed and the directional data are considerably more variable.

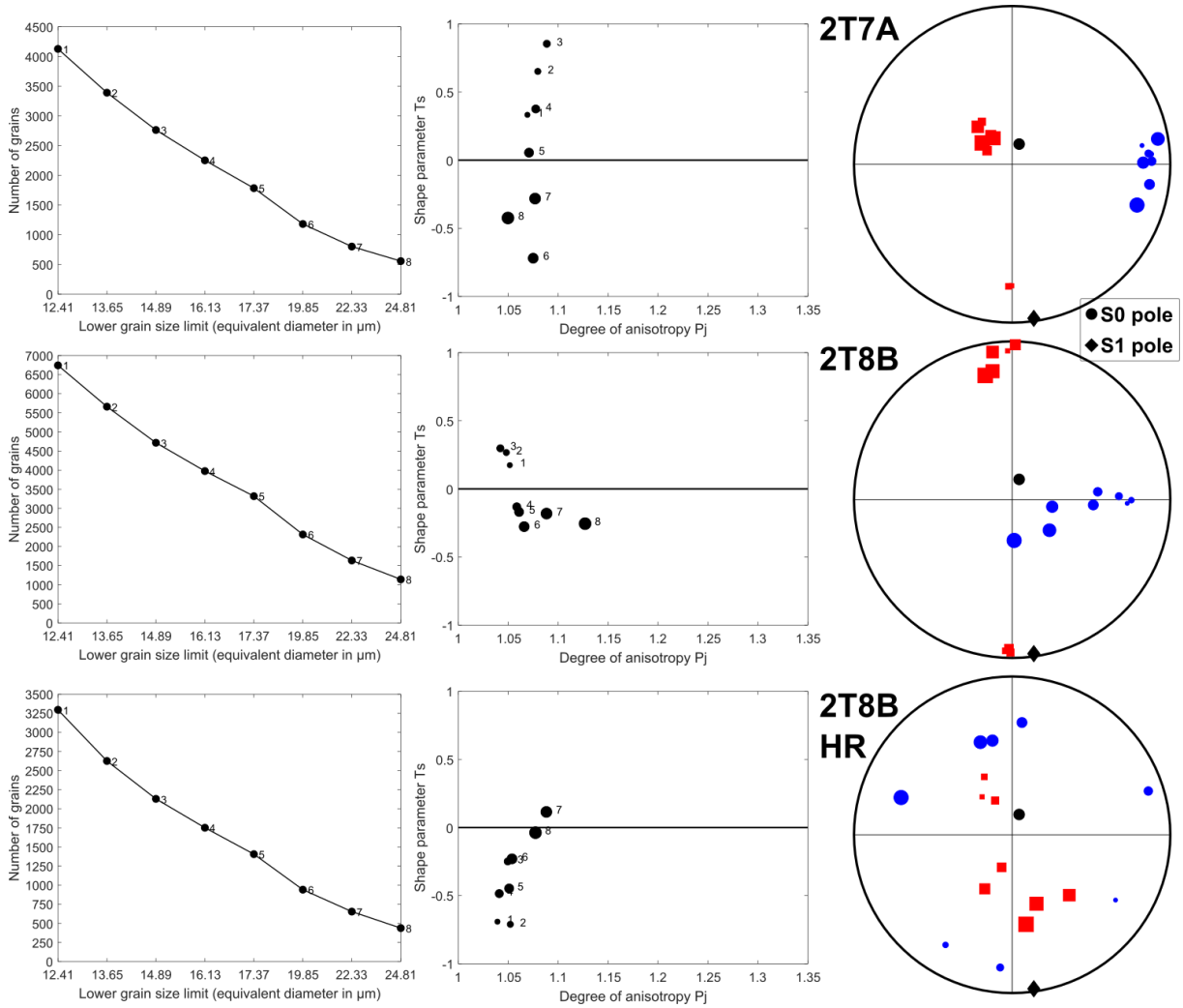

Figure 7.11: ***Spatial distribution analysis of quartz in the NCS samples (2T7A, 2T8B and 2T8B-HR). Each row is dedicated to one sample. From left to right: number of grains in the eight classes with the threshold size limit, Jelinek diagram with the eight distribution ellipsoids data points, stereoplot of the principal directions E_1 and E_3 of the eight distribution ellipsoids in geographic coordinate system.***

Concerning the WCS samples (***Figure 7.12***), the sample 2T12B emerges from the rest as the anisotropy of the distribution ellipsoids is weak to moderate ($P_j \approx 1.15$). The distribution ellipsoids are triaxial oblate to oblate. Quartz grains may be distributed along sub-horizontal planes, which are dipping to the west. As demonstrated by the E_3 axes orientation, the compaction is near vertical and possibly related to the sedimentary compaction. A similar distribution of quartz grains is reported for sample 2T16B. Samples 2T14B and 2T16b have very weak distribution intensities. The first classes of 2T14B attest for a vertical compaction and E_1 axes parallel to the bedding-cleavage intersection. These directional features are also observed for all the classes of the sample 2T18B and are that of an LPS deformation.

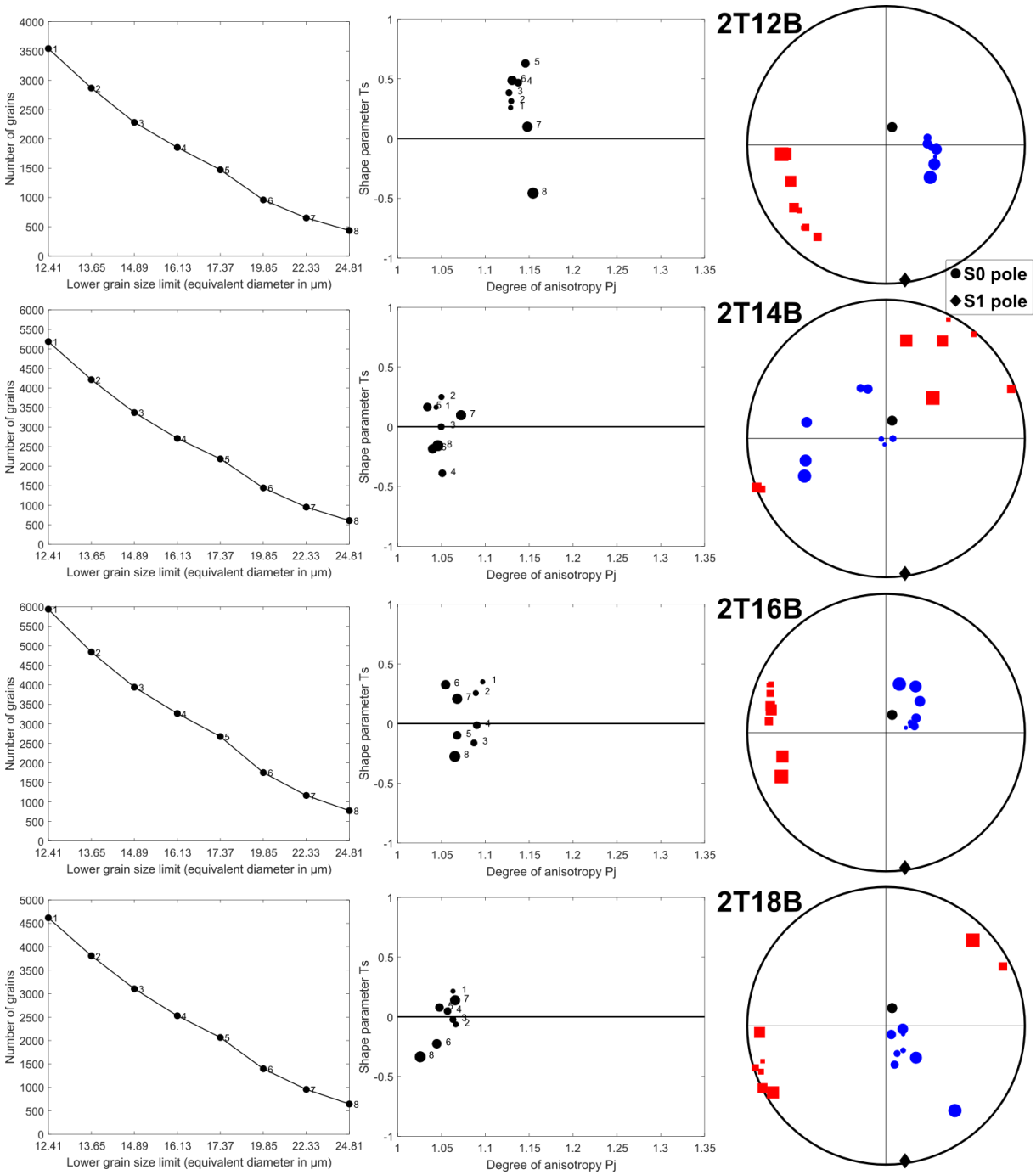

Figure 7.12: ***Spatial distribution analysis of quartz in the WCS samples (2T12B, 2T14B, 2T16B and 2T18B). Each row is dedicated to one sample. From left to right: number of grains in the eight classes with the threshold size***

limit, Jelinek diagram with the eight distribution ellipsoids data points, stereoplot of the principal directions E_1 ***and*** E_3 ***of the eight distribution ellipsoids in geographic coordinate system.***

7.3.4 Summary

In this site, we have mostly reported pencil-cleavage fabrics with moderate fabric anisotropy. The similar magnitudes of bedding and cleavages structures and their interference may be responsible for the moderate intensity of the SPO of quartz grains in most of the samples ($\boldsymbol{P_j} \approx 1.3$). When bedding fabrics are still well defined (2T8B and 2T8B-HR), the fabric anisotropy is stronger ($\boldsymbol{P_j} > 1.5$). One may note that samples 2T8B and 2T8B-HR were extracted in the darker bed observed in the field (***Figure 7.3***), suggesting a more shaly matrix. In addition, these two samples have a higher proportion of quartz grains. Overall, half of the samples exhibit coaxial magnetic and quartz shape fabrics and these samples have the lower spacing of cleavage surfaces at the bed scale.

The carbonate content of these turbidites is responsible for the development of a spaced cleavage that constitute localized deformation structures (array of subparallel cleavage seams), which are alternating with bedding domains or microlithons. At the spatial resolution of the images, these bedding domains may appear relatively undeformed or may possess a more penetrative cleavage fabric. This has been highlighted by our more detailed analysis of sample 2T7A and was demonstrated in chapter ***6***. The very penetrating cleavage at the scale of the bed, from which sample 2T7A was extracted, does not suggest such a heterogeneity of the fabric.

The spatial distribution anisotropies are weaker than the shape anisotropies. Distribution ellipsoids are not coaxial with susceptibility ellipsoids nor with shape fabric ellipsoids. One should note however, that sample 2T18B shows comparable directional data of its distribution and shape ellipsoids.

7.4 North Roncal site 1T

7.4.1 Introduction

This site is more heterogeneous at outcrop scale. It is a folded turbiditic multilayer system with alternance of clay rich rocks/siltstones and sandstones (***Figure 7.13***). The outcrop features different folds with various wavelengths in the Hecho group formation and displays cleavage refraction patterns (Hudleston and Treagus, 2010). The cleavage refraction illustrates the competence contrast between the different lithologies. Here, it is supposed to correspond to a syn-folding cleavage development. More precisely, the samples were extracted in the north limb (backlimb) of an approximately 200 m wide anticline. On this limb, tighter monoclines or parasitic folds are expressed. The bulk susceptibility of the samples is higher at this site with values around 200 x 10^{-6} SI. Considering these values, the phyllosilicate minerals are generally the main carriers of the magnetic susceptibility signal (Rochette, 1987; Rochette et al., 1992; Pueyo-Anchuela et al., 2013).

We will first present the results obtained for the coarser lithologies and will move on toward the fine-grained units. For the coarse-grained samples, we do not provide a summary of cleavage spacing as this one is significantly higher than the AMS core scale and does not provide relevant information. However, an information regarding sample 1T13 was noticed. The AMS drill core of sample 1T13 was indurated and highly cemented. This cementation was not reported in the other samples. We provide a table that summarizes the studied samples (coarse and fine) and the cleavage structures in the fine-grained samples (***Table 7.3***). ***Table 7.4*** provides the volume fraction of quartz extracted in each imaged sample.

Table 7.3: *XCT imaged coarse-grained (1T15A, 1T11B and 1T13) and fine-grained (1T1A, 1T4C, 1T5A, 1T7B and 1T17) samples, bedding/cleavage angle and cleavage spacing. Km = bulk magnetic susceptibility.*

	Macroscopic S0/S1 angle	**Km (x 10^{-6} SI)**	**Macroscopic S1 spacing (mm)**	**Distance *d* from the XCT drill core to a major cleavage surface visible on the AMS drill core (mm)**	**Main structural elements in the images**
1T15A (coarse)		197		undetectable	
1T11B (coarse)		198		undetectable	
1T13 (coarse)		102		undetectable	
1T1A (fine)	38°	247	20 – 30	undetectable	Penetrative cleavage: spacing 500 µm.
1T4C (fine)	35°	209	20 – 30	undetectable	Penetrative cleavage: spacing <100 µm
1T5A (fine)	35°	237	20 – 30	< 1	Penetrative cleavage: spacing ≈ 280 µm.

					Spaced cleavage: spacing ≈ 1400 µm.
1T7B (fine)	22°	175	2	undetectable	Spaced cleavage: spacing >1500 µm. Alternation of very fine-grained matrix and silt lenses of 400-500 µm thick.
1T17 (fine)	37°	183	10 – 20	undetectable	Spaced cleavage: spacing >1500 µm.

Table 7.4: ***Volume of interest for each sample collected in the North Roncal site. Number and volume fraction of quartz particles in this VOI, obtained after segmentation, cleaning and removal of boundary grains.***

Sample	**1T15A**	**1T11B**	**1T13**	**1T1A**	**1T4C**	**1T5A**	**1T7B**	**1T17**
Volume of interest (mm^3)	44.878	38.374	42.704	2.553	1.700	1.828	2.633	1.892
Number of quartz grains	19,682	10,915	5,837	10,219	7,502	4,625	14,792	7,879
Volume fraction of quartz	10.38 %	5.85 %	13.73 %	1.99 %	1.75 %	1.01 %	6.93 %	1.31 %

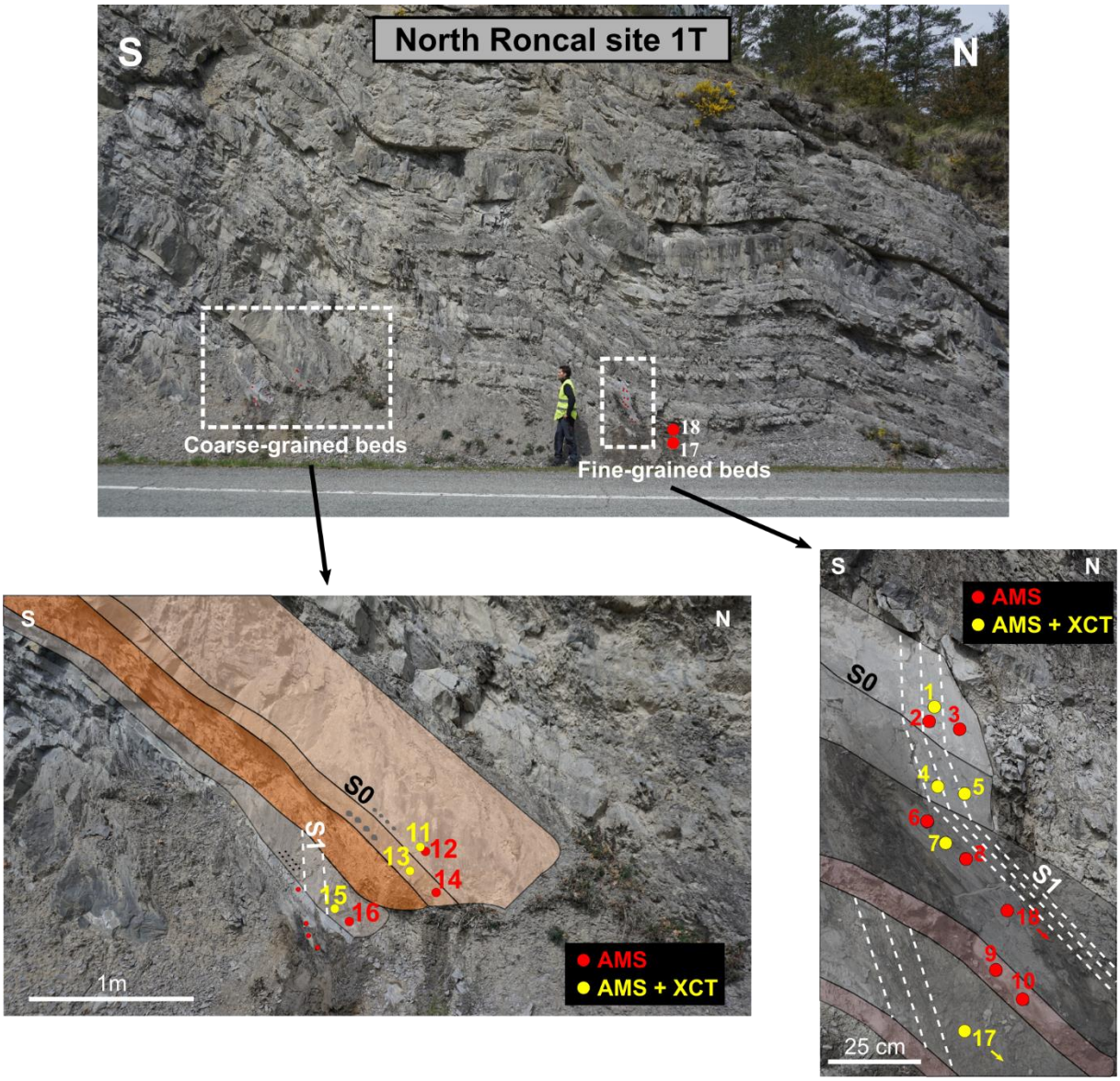

Figure 7.13: ***Photograph of the outcrop in the North Roncal site 1T and close up views of the two sub-sampling areas. Multiple lithologies of turbidites with various cleavage plunge and intensity at the bed scale due to strain refraction. 3 coarse-grained and 5 fine-grained AMS drill cores were chosen for XCT imaging.***

7.4.2 Shape fabric of quartz, spatial distribution and magnetic fabric in coarse grained lithologies

7.4.2.1 Grain shape data

The grain shape data for the coarse-grained samples are shown in ***Figure 7.14***. At the bed scale, the granulometry increases from sample 1T15A to 1T11B and to 1T13. However, the distribution curves obtained after the segmentation of quartz grains show an opposite trend. The distribution of the shape parameter T_G is similar in the three samples with a predominance of prolate grains. The grains appear to be more anisotropic in samples 1T11B and 1T13 than in 1T15A.

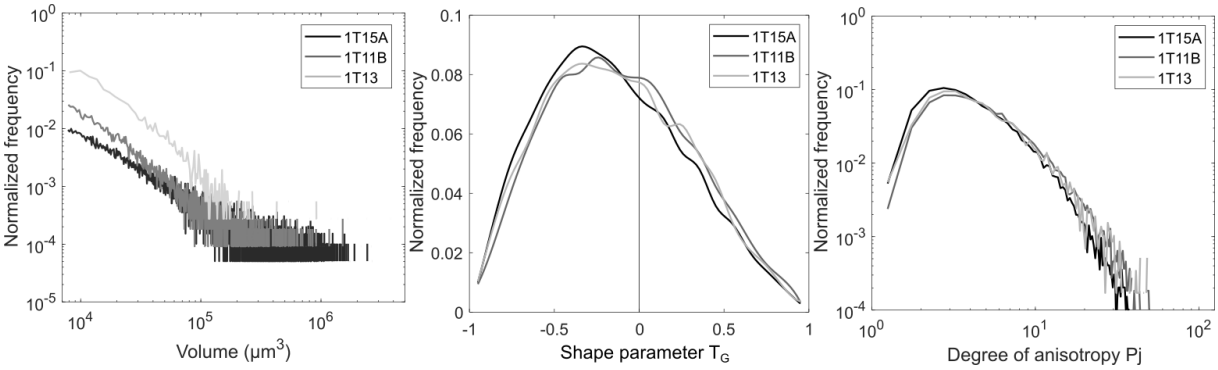

Figure 7.14: ***Normalized distributions of grain volume, shape parameter*** T_G ***and degree of anisotropy*** P_j ***of the quartz grain ellipsoids in the coarse-grained samples.***

7.4.2.2 SPO of quartz and AMS

The results concerning the shape fabric of quartz grains and the magnetic fabric are presented in ***Figure 7.15***. Firstly, we look at the mean AMS tensor of these coarse-grained samples. The mean AMS tensor is prolate with a weak anisotropy. When taking all coarse-grained AMS drill cores, the symmetry of the mean tensor is rather in relation to the longest axis or principal susceptibility axis. This axis is subparallel to the local cleavage-bedding intersection. The large confidence ellipses of the three principal axes attest for variability in the directional data but these ellipses show a sub-orthorhombic symmetry.

The individual orientation data and the bulk data show a bedding shape fabric for the sample 1T15A. The AMS directional data show that $\boldsymbol{K_3}$ axis in this sample is subparallel to $\boldsymbol{L_{3m}}$ axis but the fabrics are different. The magnetic fabric measured by AMS is prolate while the quartz shape fabric is oblate. Thus, magnetic carriers in this sample have a rotational symmetry around their maximum susceptibility axis whereas quartz grains show a rotational symmetry around their shortest axis. The shape fabric anisotropy is moderate ($\boldsymbol{P_j} > 1.3$). In sample 1T11B, $\boldsymbol{L_3}$ axes depict a north-south symmetric girdle and $\boldsymbol{L_1}$ axes are mostly parallel to bedding-cleavage intersection. We observe again the parallelism between $\boldsymbol{K_3}$ and $\boldsymbol{L_{3m}}$ axes. However, in the sample 1T11B the magnetic fabric is oblate (not related to bedding) and the quartz shape fabric is prolate. In sample 1T13, $\boldsymbol{L_{1m}}$, $\boldsymbol{L_{3m}}$, $\boldsymbol{K_1}$ and $\boldsymbol{K_3}$ axes are lying down in the bedding plane. This sample displays a weak triaxial prolate SPO.

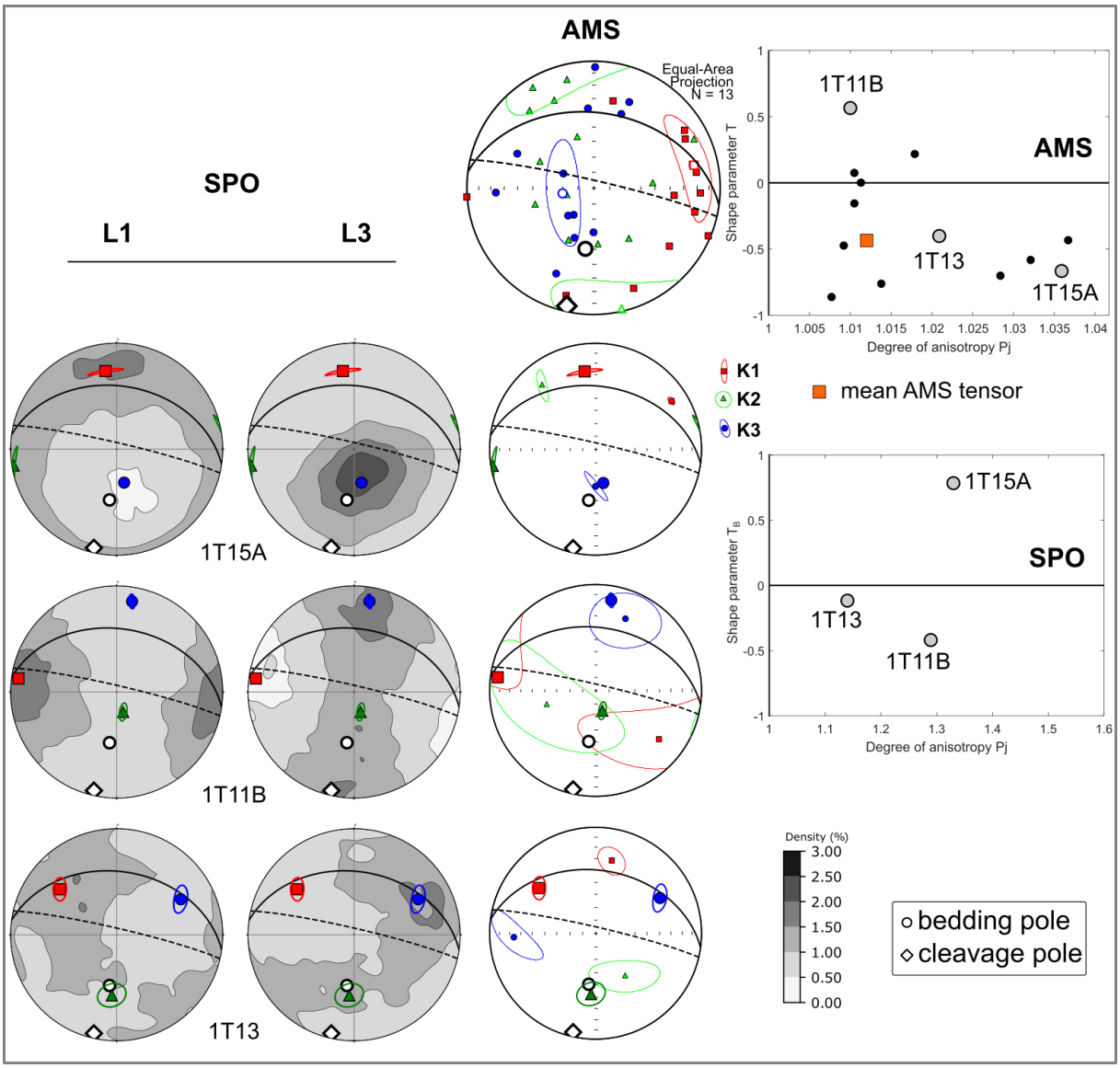

Figure 7.15: ***Quartz shape fabric and magnetic fabric data of the coarse-grained samples of the North Roncal site 1T. Coarser from 1T15A to 1T13.***

7.4.2.3 Spatial distribution analysis

The results of the spatial distribution analysis are given in ***Figure 7.16***. In sample 1T15A, which contains many grains, the scalar parameters of the Jelinek diagram suggest that no specific spatial distribution of grains is present. The path of the $\boldsymbol{E_3}$ axes on the stereoplot suggests that, when less weight is attributed to the smallest grains, the maximum compression axis moves from a lateral stress to a vertical one. However, this must be taken with care, as the degree of anisotropy of the distribution ellipsoids is too small to be representative. In sample 1T11B, the distributions are also weak as shown by the values of the degree of anisotropy. The $\boldsymbol{E_3}$ axes are heterogeneously oriented but seem to correlate with the trace of the bedding planes. The $\boldsymbol{E_1}$ axes are clustered and subparallel to the bedding pole. These directional data are unexpected and appear to be inverted. The signal of the distribution analysis is more pronounced in sample 1T13. All points fall in the prolate field and attest for a distribution of quartz grains along linear structures but with weak to moderate intensity. The directional data do not vary across the different classes of grains. $\boldsymbol{E_3}$ axes are clustered and dip slightly to the north-northeast. $\boldsymbol{E_1}$ axes orientations are in accordance with the intersection lineation

previously reported in the SPO data. These results suggest a main compression axis that is perpendicular to the fold structures and expected in the area.

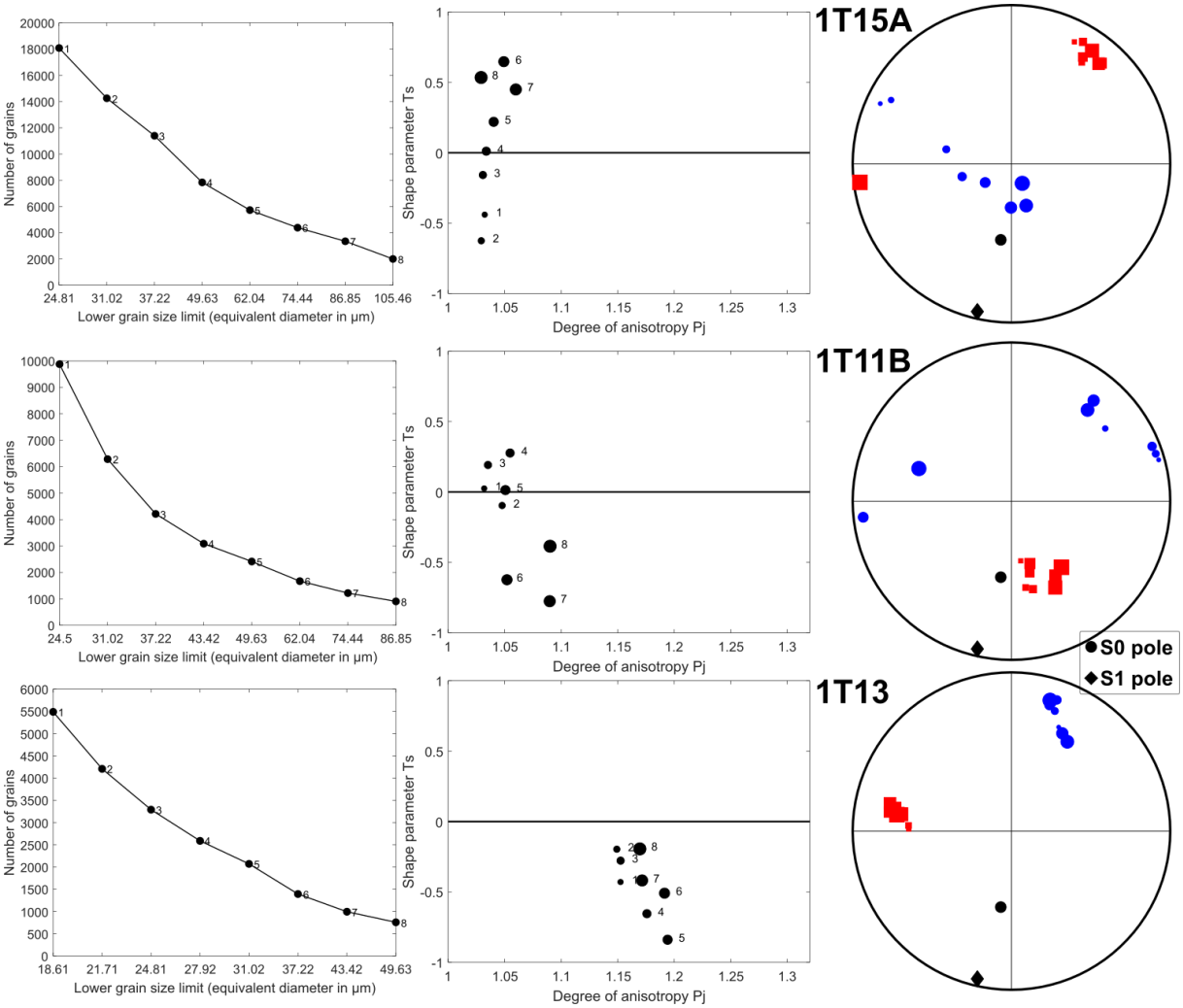

Figure 7.16: ***Spatial distribution analysis of quartz in the coarse-grained samples. Each row is dedicated to one sample. From left to right: number of grains in the eight classes with the threshold size limit, Jelinek diagram with the eight distribution ellipsoids data points, stereoplot of the principal directions*** E_1 ***and*** E_3 ***of the eight distribution ellipsoids in geographic coordinate system.***

7.4.2.4 Coarse-grained lithologies: brief summary

In the coarse-grained samples, shape fabric and magnetic fabric are contrasting. The shape and magnetic foliations are rather in agreement, $\boldsymbol{L_{3m}}$ and $\boldsymbol{K_3}$ axis being coaxial. However, the bulk shape parameters of the ellipsoids (SPO and susceptibility ellipsoids) indicate opposite arrangement/symmetry (prolate vs oblate). The sample 1T13 that has the weakest and most unexpected SPO shows the most expected stress direction in the spatial distribution analysis. This sample is highly cemented which may explain the unexpected positions of $\boldsymbol{L_1}$ and $\boldsymbol{L_3}$ axes in the bedding plane.

7.4.3 Shape fabric and magnetic fabric in fine-grained lithologies

7.4.3.1 Grain shape data

The quartz grains shape data obtained in fine-grained samples are provided in ***Figure 7.17***. The steepest curve in the grain size distribution is observed for sample 1T17. The less steep curve is observed for sample 1T7B. Otherwise, the samples show similar grain size distributions. The distributions of the shape parameter $\boldsymbol{T_G}$ do not provide any difference while the distributions of the degree of anisotropy do. The sample 1T5A contains more isotropic grains.

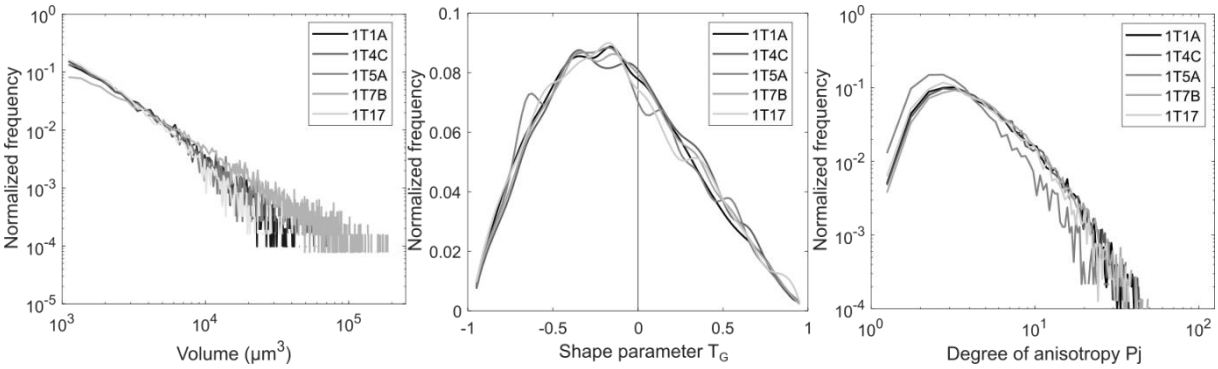

Figure 7.17: ***Normalized distributions of grain volume, shape parameter*** T_G ***and degree of anisotropy*** P_j ***of the quartz grain ellipsoids in the fine-grained samples.***

7.4.3.2 SPO of quartz and AMS

The mean AMS tensor of the 17 fine-grained samples is triaxial oblate. The non-orthorhombic symmetry of its confidence ellipses may arise from multiple or heterogeneous subfabrics or an overall unrepresentative sampling (Borradaile, 2001, 2003b). Multiple subfabrics may be due to different concentrations of the magnetic carriers, heterogeneous magnetic mineralogy and their individual preferred orientation (Borradaile, 2001).

In terms of the shape fabric of quartz grains (***Figure 7.18***), we can group samples 1T1A, 1T5A and 1T17 as an intersection lineation fabric with a bedding-controlled foliation (1T1A) or girdles of $\boldsymbol{L_3}$ axes (1T5A and 1T17). Samples 1T14C and 1T7B, which have a more pronounced SPO, display a cleavage fabric with a cleavage-controlled foliation. Their lineation displays a slight girdle of $\boldsymbol{L_1}$ axes with incipient down-dip lineation related to thrust movement. The AMS directional data are rather coaxial with the quartz directional data. A major difference is reported between the bulk shape and magnetic fabrics in sample 1T5A. The lowest shape fabric anisotropy are found in samples 1T5A and 1T17 ($\boldsymbol{P_j} < 1.3$) and the highest in samples 1T1A, 1T4C and 1T7B ($\boldsymbol{P_j} > 1.4$). Sample 1T7B is the most argillaceous one and exhibits low obliquity between bedding and cleavage foliations. This may explain its rather strong magnetic fabric. This sample also differs from the other as silt lenses can be seen in the XCT image (not shown). The matrix is partitioned into clay-rich layers and silt-rich layers. In the segmentation step, fewer grains were extracted from the fine clay-rich layers. Even from two drill cores taken 10 cm apart in the same bed, petrofabrics can be very different as suggested by quartz shape or AMS (samples 1T4C and 1T5A). Therefore, a more in-depth characterization of these two samples located in the same bed is carried out below.

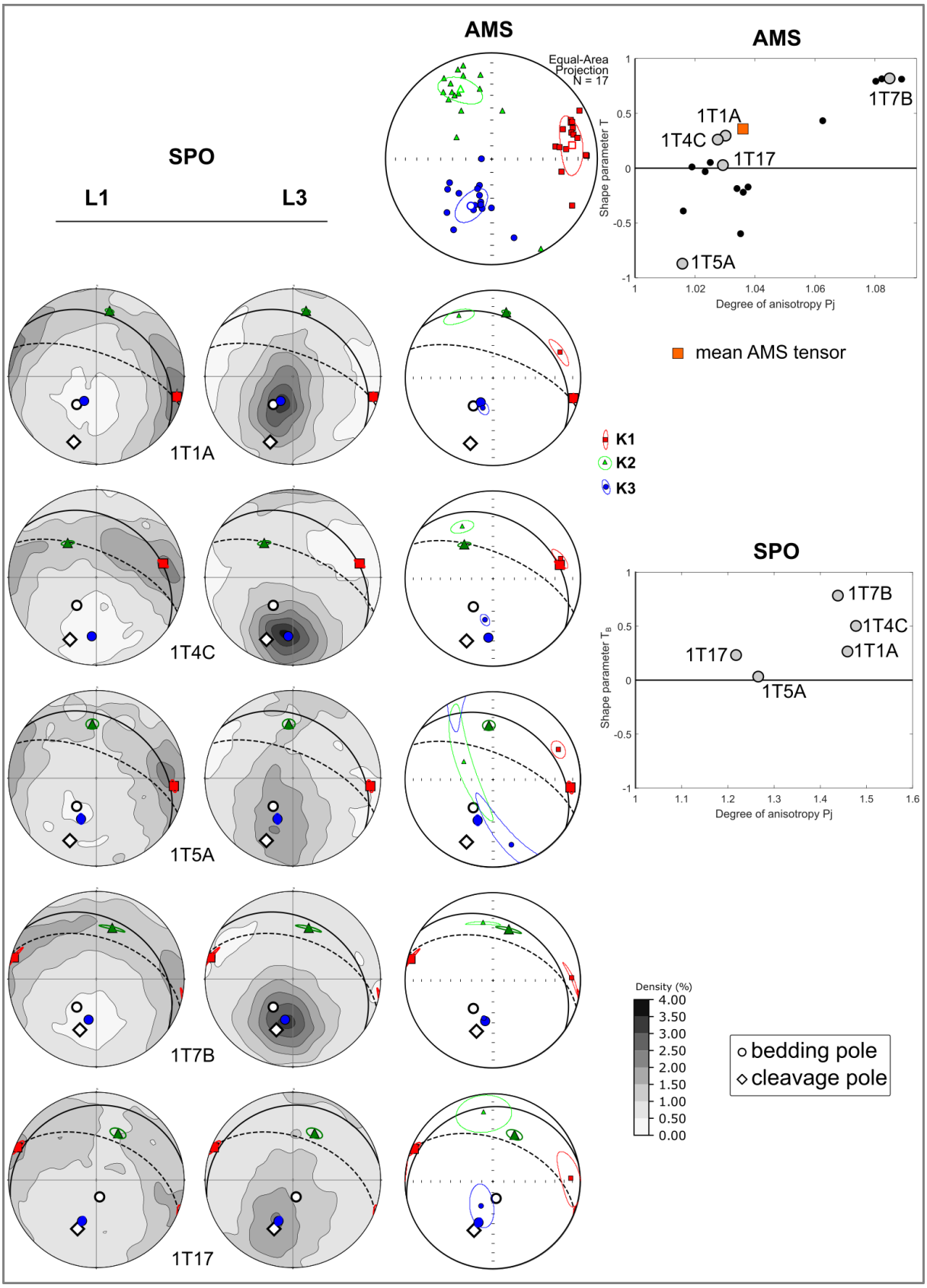

Figure 7.18: *Quartz shape fabric and magnetic fabric data of the fine-grained samples of the North Roncal site.*

7.4.3.3 Intra-bed homogeneity/inter-sample comparison and subfabrics

In this section, we perform the same analysis employed earlier for sample 2T7A (section ***7.3.2.3***). Here we are interested in two samples, 1T4C and 1T5A, extracted from the same bed only less than 10 cm apart but displaying different shape and magnetic fabrics. 2D view of their corresponding grayscale image are provided in ***Figure 7.19***. It shows a more continuous aspect of the penetrative thin pressure solution seams in 1T4C and a discontinuous spaced array of thick pressure solution seams in 1T5A.

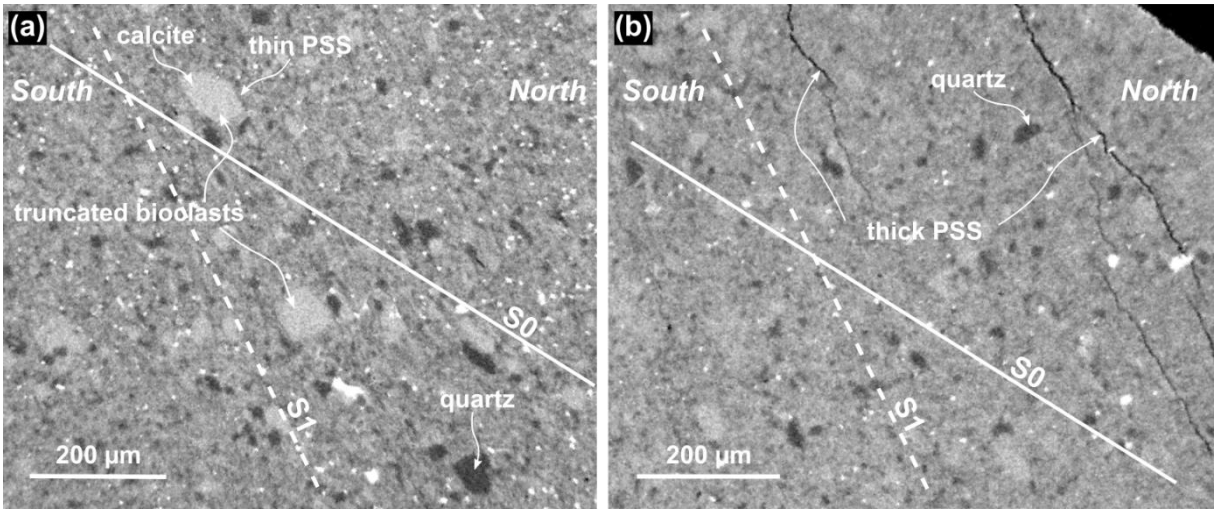

Figure 7.19: ***XCT views of samples 1T4C (a) and 1T5A (b) in a geographic coordinate system. Not the rather strong alignment of grains in (a) compared to (b). Both samples belong to the same bed.***

Using the box-counting method, we can evaluate the representative size for the bulk shape fabric parameters in the two considered samples as well as their variability (***Figure 7.20***). The representative size for the degree of anisotropy $\boldsymbol{P_j}$ is reached at the eighth box size for sample 1T4C and at the third box size for sample 1T5A. For the shape parameter $\boldsymbol{T_B}$, the representative size emerges at the fifteenth box size for 1T4C and at the seventeenth for 1T5A.

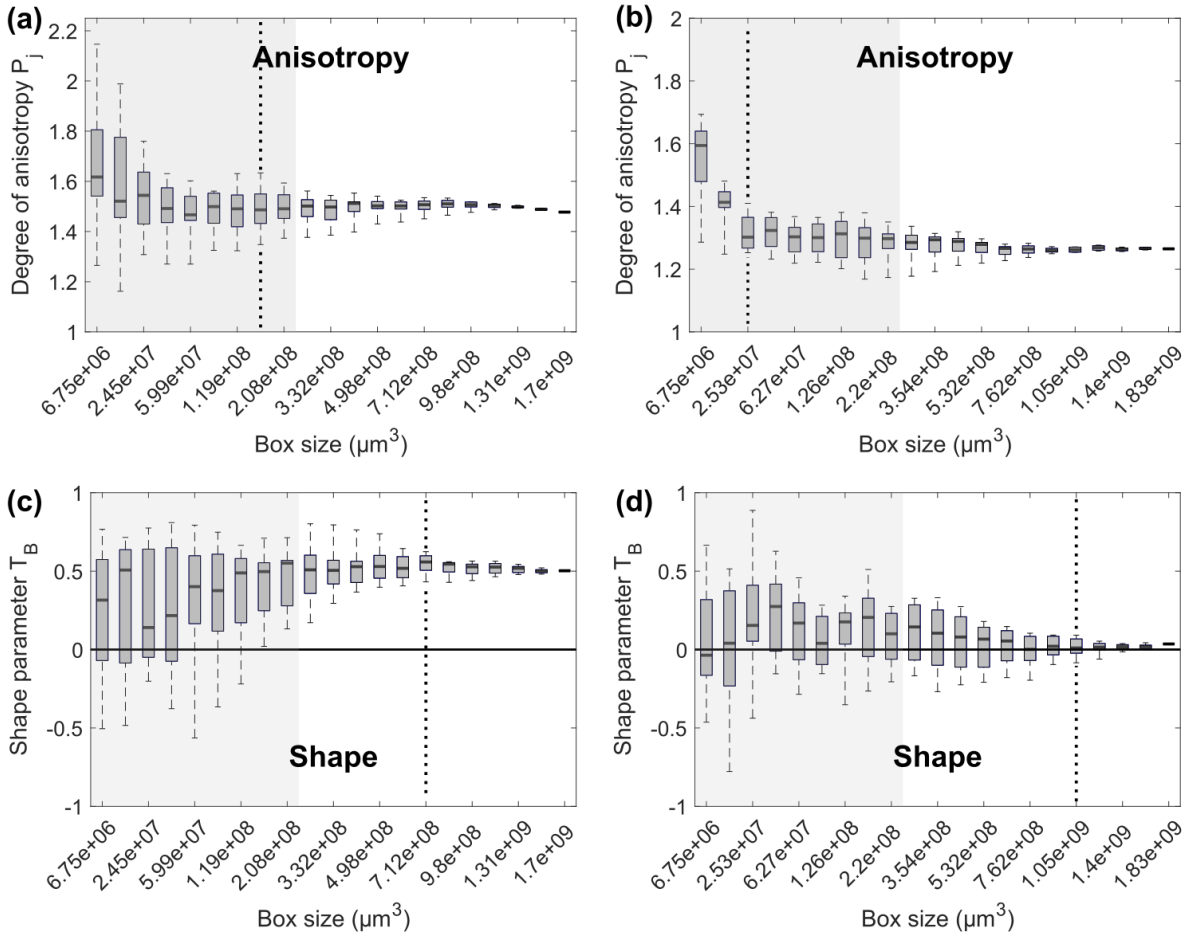

Figure 7.20: ***Results of the box-counting method (bulk fabric parameters) applied in samples 1T4C and 1T5A. Degree of anisotropy*** P_j ***of the mean tensors for 1T4C (a) and 1T5A (c). Shape parameter*** T_B ***of the mean tensors for 1T4C (b) and 1T5A (d). Dotted lines in the graphs indicate the representative size for the parameter.***

The subfabric analysis performed on both samples is presented in ***Figure 7.21***. The results concerning sample 1T4C are homogeneous (***Figure 7.21***a). Independently of the localization in the VOI and of the considered quartz grain subset, the directional data of the subfabric ellipsoids are coaxial. The scalar data of the localized subfabric ellipsoids show little variations and remain in the oblate field of the diagram with anisotropies ranging from 1.33 to 1.6. In the morphological subfabrics of sample 1T4C, the reader will notice how the individual grain anisotropies contribute to the subfabric anisotropy and how the symmetry of the individual grain ($\boldsymbol{T_G}$) may influence the subfabric symmetry ($\boldsymbol{T_B}$). These results show that the quartz shape fabric is homogeneous in this sample.

The results obtained in sample 1T5A are different (***Figure 7.21***b). Firstly, localized subfabrics emerge with subfabric ellipsoids having a bedding-controlled foliation (subsets 2, 3, 6, 7 and 8) or a cleavage-controlled foliation (subsets 1 and 4). Subfabric ellipsoid associated to localized subset 5 has an intermediate foliation ($\boldsymbol{L_{3m}}$ axis between S0 and S1 pole). These different foliations are not correlated to specific scalar parameters since a bedding-controlled foliation can be found for an oblate or prolate ellipsoid. Anisotropies of the subfabric ellipsoids are mainly clustered around 1.3. The size subsets have a slight influence on the foliation of the subfabric ellipsoid with various orientations of $\boldsymbol{L_{3m}}$ axes from subparallel to bedding pole to oblique. Interestingly, the size subset has an influence on the degree of anisotropy of the subfabric suggesting that coarser grains are the most anisotropic. The graphs below concerning the anisotropy subsets indicate that the foliation of the less anisotropic grains (subsets 1 to 5) is intermediate while the foliation is subparallel to cleavage for more anisotropic grains (subsets

5 to 10). Lastly, we report also some directional variability for the shape subsets but no clear trends emerge.

If we refer once again to ***Figure 7.13***, although the two AMS cores were taken from the same bed, they were not strictly extracted on the same stratigraphic level. However, considering the homogeneity at the bed scale, we would not have expected such difference between the two X-ray imaged samples. Small variations in the primary sedimentary fabric, on a greater length scale than the size of the VOI, may explain the different expressions of the deformation in the rock matrix.

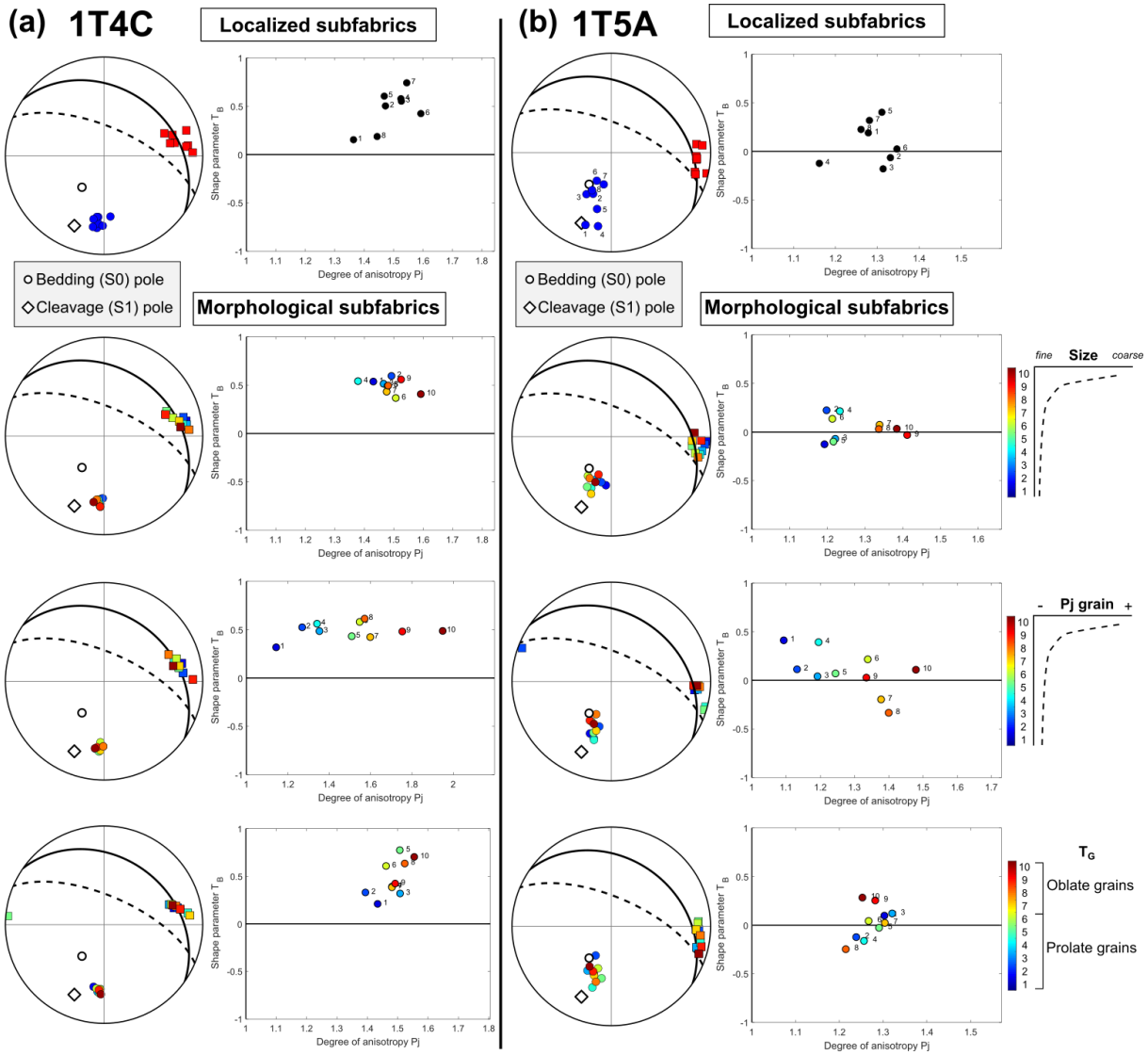

Figure 7.21: ***Subfabric analysis in samples 1T4C (a) and 1T5A (b). Characterization of localized quartz subfabrics by subvolume analysis. Note that these subfabric ellipsoids are computed for a different number of grains in each localized subset. Characterization of morphological subfabrics. Three parameters are studied (size, P_J, T_G). The population of quartz grains is broken down into ten subsets, which are the 10% quantiles of the considered parameter. In that case, each mean tensor or subfabric ellipsoid is an average obtained for the same number of grains. Please note that we do not provide a schematic representation of the subfabric ellipsoids because bedding/cleavage angle is not as important as for the sample 2T7A in section 7.3.2.3.***

7.4.4 Spatial distribution analysis in fine-grained lithologies

The results of the spatial distribution in the fine-grained sample are provided in ***Figure 7.22***. Samples 1T1A, 1T4C and 1T5A show comparable directional data of their distribution ellipsoids from very weak distribution anisotropy (1T1A and 1T5A) to weak distribution anisotropy (1T4C). The $\boldsymbol{E_3}$ axes of the different classes are dipping to the west-northwest. These directions indicate a possible lateral compaction or at least that grains are arranged in northeast-southwest directed planar, plano-linear or linear structures. A similar orientation of the $\boldsymbol{E_3}$ axes is observed for the first classes of sample 1T7B. Decreasing the influence of the smallest grains in this sample yields $\boldsymbol{E_3}$ axis dipping to the south nearly parallel to the cleavage pole. This change in orientation may be related to the coarser silt lenses observed in this sample. Another point to note here is the evolution of the shape parameter $\boldsymbol{T_S}$ of the distribution ellipsoids. This evolution suggests a change from linear structures for the most heterogeneous grain size composition to planar structures for the coarser composition. In sample 1T17, all the distribution ellipsoids are oblate with a weak anisotropy suggesting that quartz grains are slightly disposed in planes. These planes appear to dip to the south at low angle.

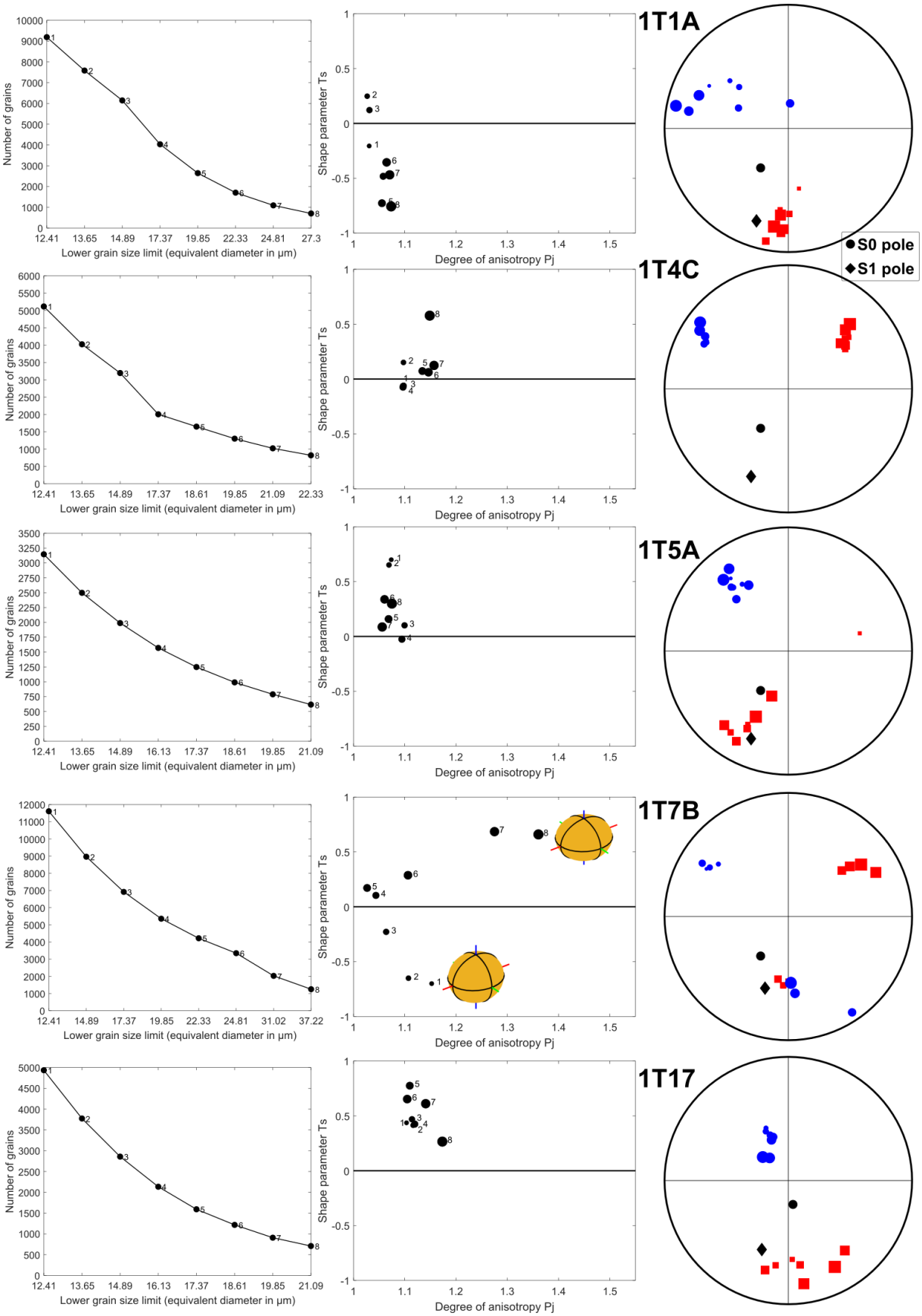

Figure 7.22: *Spatial distribution analysis of quartz in the fine-grained samples. Each row is dedicated to one sample. From left to right: number of grains in the eight classes with the threshold size limit, Jelinek diagram with the eight distribution ellipsoids data points, stereoplot of the principal directions* E_1 *and* E_3 *of the eight distribution*

ellipsoids in geographic coordinate system. Some illustration of distribution ellipsoids corresponding to data points are provided.

7.4.5 Summary

In the fine-grained samples, shape fabric and magnetic fabric show a good correlation. Intersection lineation fabric has been found in all beds, independently of the apparent ductility of the layer. Two samples (1T4C and 1T5A) extracted from the same bed, 10 cm apart, show different fabrics. One presents a homogenously cleaved fabric (1T4C) while the other presents an inhomogeneous fabric (1T5A) probably affected by the localized PSS. Hence, there is a heterogeneity at the site scale.

In the distribution analysis, four out of five samples exhibit a possible west lateral shortening direction but most distributions are weak. As previously seen in chapter ***5***, section ***5.3.4.1***, the compositional layering with silt lenses provides a significant planar distribution anisotropy in sample 1T7B.

7.5 Discussion

This chapter was devoted to the characterization of fine-grained calcareous turbiditic units that must have experienced the same deformation event(s). We wanted to investigate the rock fabric of different lithologies outcropping in two sites from the Roncal valley, or of its surroundings, by means of XCT and AMS.

In fine-grained samples, the directional and scalar data of the quartz SPO and the AMS are rather in accordance. Difference between these two types of fabrics are observed in the coarse-grained samples. Pueyo-Anchuela et al. (2010, 2011, 2012) have performed magnetic analyses on a considerable amount or rock samples (shales and sandstones) extracted in the Roncal valley and the adjacent eastern valleys, covering the main heterogeneities of the magnetic fabric in the fold-and-thrust belt. In our study, all samples have a bulk susceptibility ranging from 95 x 10^{-6} SI to 250 x 10^{-6} SI and a magnetic anisotropy lower than 35% indicating that paramagnetic clays are the main contributors to the susceptibility (Rochette, 1987; Rochette et al., 1992). However, variability in the main magnetic carriers may exist (Pueyo-Anchuela et al., 2013). In their study of the AMS of Eocene turbidites from the Jaca basin, Pueyo-Anchuela et al. (2010) identified four types of magnetic fabrics based on the relation between AMS directional data and macroscopic structures observable at outcrop scale (bedding and cleavage). They sampled folded turbiditic beds of sandstones and shales in a test site that resemble our site presented in ***Figure 7.13***. The purpose was to analyze the influence of paramagnetic and ferromagnetic contributions to the susceptibility in order to explain the changes in magnetic fabrics at outcrop scale. They found a relationship between the four fabric groups and the paramagnetic contribution to the susceptibility. In their directional data, the $\boldsymbol{K_3}$ axes of AMS showed heterogeneous orientations. The distributions of these axes indicated magnetic foliation parallel to the main foliations (bedding and cleavage) or perpendicular to the main foliations. The latter case was generally not observed in our data, except for the coarse-grained sample 1T13. In addition, Pueyo-Anchuela et al. (2010) reported $\boldsymbol{K_3}$ axes in between the bedding and cleavage poles.

An intermediate position of AMS $\boldsymbol{K_3}$ axis between bedding and cleavage poles was found in several works involving two planar fabrics in deformed sedimentary rocks (Lüneburg et al., 1999; Debacker et al., 2004, 2009; Hirt et al., 2004; Pueyo-Anchuela et al., 2010)**.** Composite magnetic fabrics due to the superposition of the cleavage fabric on the bedding fabric can explain the variable positions of $\boldsymbol{K_3}$, but also subfabrics associated to the different magnetic carriers and their relative preferred orientation and concentration in the investigated volume (Housen et al., 1993a; Debacker et al., 2009; Weil and

Yonkee, 2009). Composite magnetic fabrics with intermediate position of $\boldsymbol{K_3}$ axis have also been reported in mylonites affected by S-C structures (Aranguren et al., 1996), which are two planar fabrics. However, in the latter study, the authors found that $\boldsymbol{K_1}$ axis was mainly perpendicular to the linear intersection of the two planes. In our results, when two planar fabrics (foliations) compete, the bulk shape fabric retains a lineation ($\boldsymbol{L_{1m}}$) that is mainly parallel to the bedding-cleavage intersection and we have observed similar trends for $\boldsymbol{K_1}$ axis. This is in accordance with the numerical study of composite magnetic fabrics by Housen et al. (1993). One should note that composite magnetic fabrics may exist for linear fabrics as demonstrated by Aubourg et al. (1995). In our study, the two types of foliations (bedding and cleavage) could be distributed in a homogeneous way within the matrix or in a heterogeneous way with the preferential localization or overrepresentation of one of them in a given point. Here we have highlighted the second case. In some zones of the rock matrix, cleavage foliation replaces and destroys the bedding foliation while other domains show that the bedding foliation is intact. It indicates that ductile deformation may not propagate homogenously. It is certainly the ability of the rock matrix to permit solution flow, which explain the domainal nature of cleavage.

We have shed in light how the geometrical relationship between two foliations can explain quartz shape fabric but also AMS fabric as this process can affect phyllosilicates and other minerals. Systematically, the interference of two composite foliations weaken the fabric anisotropy of quartz measured on a 2-3 mm^3 fine-grained rock volume, especially when a spaced cleavage is reported. We have also confirmed this result based on the shape fabric of quartz (see previous chapter). The spaced or domainal cleavage has a significant influence on the bulk results obtained on the carbonates turbidites. The domainal nature of the cleavage surfaces has been put forward to explain the respective contributions of differently oriented magnetic carriers in weakly deformed sedimentary rocks (Borradaile and Tarling, 1981; Borradaile, 1988). The advantage of our analysis is that it focuses on one main mineralogical phase and on more simple data. Thus, we can investigate precisely the variation in the preferred orientation of this phase. The bulk AMS signal is more complex and integrates many parameters (magnetic mineralogy, concentration of magnetic carriers, intrinsic susceptibility, anisotropies and preferred orientations), even if the paramagnetic clays are the main contributors. The concentration of spaced cleavage domains, at the AMS core scale, may have a strong influence on the final picture. In addition, more pervasive mechanisms may explain composite or multiple magnetic fabrics such as the bending and kinking of detrital phyllosilicates at a finer scale (Lüneburg et al., 1999; Chadima et al., 2004; Debacker et al., 2004; Hirt et al., 2004; Weil and Yonkee, 2009; Haerinck et al., 2013).

The investigation of subfabrics in some selected samples (2T7A, 1T4C and 1T5A) has shown that localized spaced cleavage laminae have a great influence on the principal directions of the bulk shape fabric. This is particularly the case for samples 2T7A and 1T5A. When the cleavage is penetrative and hardly visible in the XCT image such as in sample 1T4C, the principal directions of the subsets are almost invariant. The morphological subfabrics have less influence of the bulk preferred orientation, although there are slight trends.

The expected microfabric (i.e. shape fabric at microscale) may be different from the macroscopic fabric (outcrop) because of the heterogeneities at microscale. For example, the cleavage at the bed scale of sample 2T7A was highly penetrative whereas the XCT image has revealed a more domainal type of cleavage. The contrary was observed for sample 2T16B which has a much more penetrative microscopic cleavage than its mesoscopic scale suggests. However, the microscopic cleavage is sometimes barely detectable in the X-ray images. As the cleavage seams appear as air-filled surfaces in our X-ray images, the use of high-contrast gases could help to better visualize them (Vega et al.,

2014; Withers et al., 2021). Another possibility is to use dark-field X-ray imaging to access to a sub-voxel resolution and better identify the more penetrative cleavage.

In these deformed turbidites, the results of the spatial distribution analysis are more complex. The distribution anisotropy are weaker than the shape anisotropy in all the studied samples. In both studied sites, we almost never find coaxiality of the principal directions between the distribution ellipsoid and the bulk shape fabric ellipsoid. In the West Burgui site, samples 2T12B and 2T18B have shown some closeness in these directions. In the North Roncal site, there is no clear example. This is probably due to more complex deformation mechanisms recorded by the rocks in the limb of a fold from the internal part of the fold and thrust belt.

The different fabric types reported by Pueyo-Anchuela et al. (2010, 2012) along the entire fold and thrust belt are also found on a much finer scale such that of a fold limb when dealing with the microstructure of a particular mineral phase (here quartz clasts) in a millimeter-sized rock volume.

7.6 Conclusion

From two sites of Eocene turbidites where multiple lithologies outcrop and are affected by two macroscopic foliations, AMS and XCT techniques have been applied on drill core samples. AMS gives a bulk magnetic fabric, more or less representing the true petrofabric, in a 10 cm^3. XCT provides individual and bulk shape fabric results for a specific phase of interest that is extracted in a 2-3 mm^3 sample. The paramagnetic minerals may drive AMS in most cases, especially in fine-grained rocks, thus the principal directions of the magnetic susceptibility tensor are strongly governed by the preferred orientation of clay minerals (illite and/or mica and/or chlorite). We have studied the shape fabric of the diamagnetic quartz that influences the bulk magnetic susceptibility but the preferred orientation of quartz grains cannot be evaluated from the directional data of the susceptibility ellipsoid. Therefore, the two techniques are complementary for the investigation of the 3D petrofabric and its subfabrics.

8 Mechanical simulation of the lateral shortening of a fine-grained rock matrix at the microscopic scale

8.1 Aims

The main goal here is to use a Finite Element Method (FEM) simulation to model the mechanical compression of a fine-grained matrix with inclusions, to analyze the changes in inclusion shape, orientation and spatial distribution. As described in the methodology chapter (see section ***3.8***), we employ the Cast3M software and MATLAB to perform this task.

8.2 Introduction

3D simulations are less frequent in literature because they are time consuming and required advanced workstations. Finite element method simulations based on 3D microstructure have been done for particle-reinforced composites for example (Chawla and Chawla, 2006). In this study, they employed a 2D sectioning process to reconstruct a 3D microstructure based on 2D images. Robinet et al. (2012) have employed segmented XCT images of a clay-rich rock to perform diffusion simulations. In their model, the geometry was partitioned into voxels belonging to the clay matrix and voxels belonging to the nonporous minerals. Specific diffusion properties were assigned to each voxel. However, 2D simulations are more common. For example, a recent paper by Griffiths et al. (2017) focuses on the influence of the morphology of pores and their preferred orientation on the compressive strength and stiffness of porous rocks. They made numerical simulations from synthetic binarized images (ellipsoidal pores and matrix were discretized into pixels) generated with MATLAB and used a specific two-dimensional rock failure code.

8.3 Initial parameters

We generated an initial synthetic binary image, using a MATLAB script, of 100 x 100 x 100 voxels with a voxel size of 2 µm thus representing a rock volume of 200 µm side length (***Figure 8.1*****a**). 56 ellipsoidal particles were randomly distributed in the matrix but following a normal distribution along the z-axis to simulate an initial degree of compaction. The 56 particles could not overlap but could be in contact. This synthetic image is intended to simulate a representative population of quartz grains based on the binary XCT image of quartz of sample A1 (see chapter ***4***). To this end, we subdivided the population of grains into three representative grain types generated with average size, shape parameter and degree of anisotropy as per the data of sample A1. To simplify, we have the small, medium and large grains.

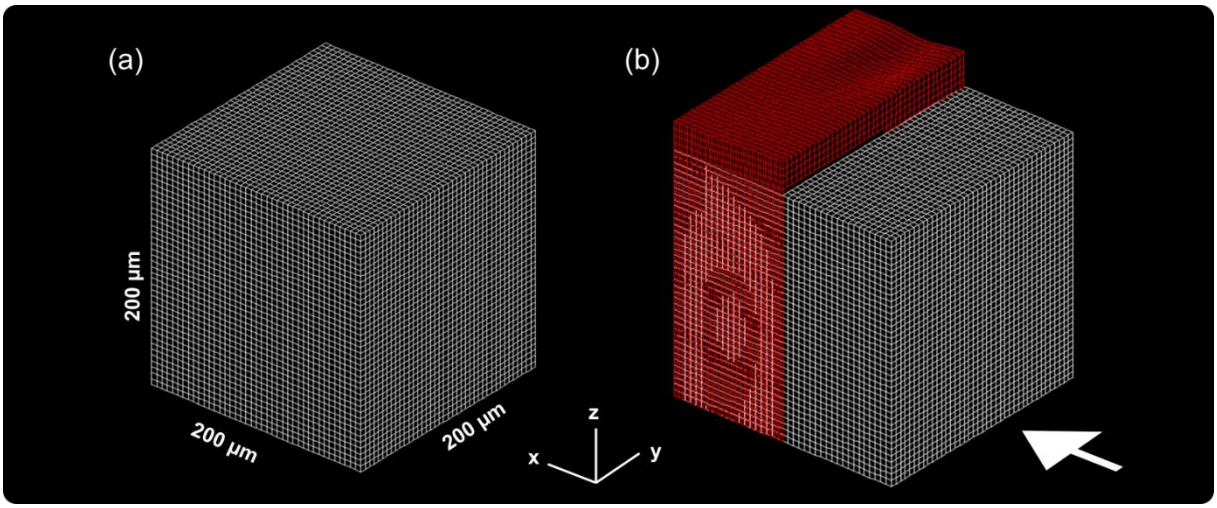

Figure 8.1: ***(a) Initial cubic mesh. (b) Superimposition of the deformed mesh (red) on the initial mesh (white). Deformation of 50 % along x-axis.***

We assumed an isotropic elastic behavior for both phases (clay matrix and silt grains of quartz). Different values of Young's modulus for quartz can be found in the literature. In this simulation, we took a Young modulus of 87 GPa for the inclusions which is the value for "stiff" components (i.e. mixture of quartz and calcite) used in Sone and Zoback (2013). Young modulus of quartz is usually close to this value. Similarly, we used their value of 11 GPa for the "soft" components that correspond to the clay matrix. Poisson's ratio for quartz was taken from Gercek (2007). Typical ranges of values for Poisson's ratio of some rock types were also indicated in this publication and we took an intermediate value for the clay matrix. The initial parameters used for this simulation are summarized in ***Table 8.1***. We slightly overrepresented the number of quartz particles to have a sufficient number of grains. We applied a horizontal shortening (pure shear) of 50 % to this initial mesh along the x-axis (***Figure 8.1*****b**).

Table 8.1: ***Mechanical parameters used.***

	Density (kg/m³)	**Young's modulus (GPa)**	**Poisson's ratio**	**Volume fraction (%)**
Clay matrix	2650	11	0.20	96.65
Quartz inclusions	2650	87	0.08	3.35

8.4 Results

Figure 8.2**a** shows the displacement of the initial ellipsoidal quartz grains to their deformed state. In this figure, the raw voxelized ellipsoids are shown (represented here as an isosurface). In ***Figure 8.2*****b**, the size distributions of the grains in the two states are provided. The deformation induces a decrease in grain size.

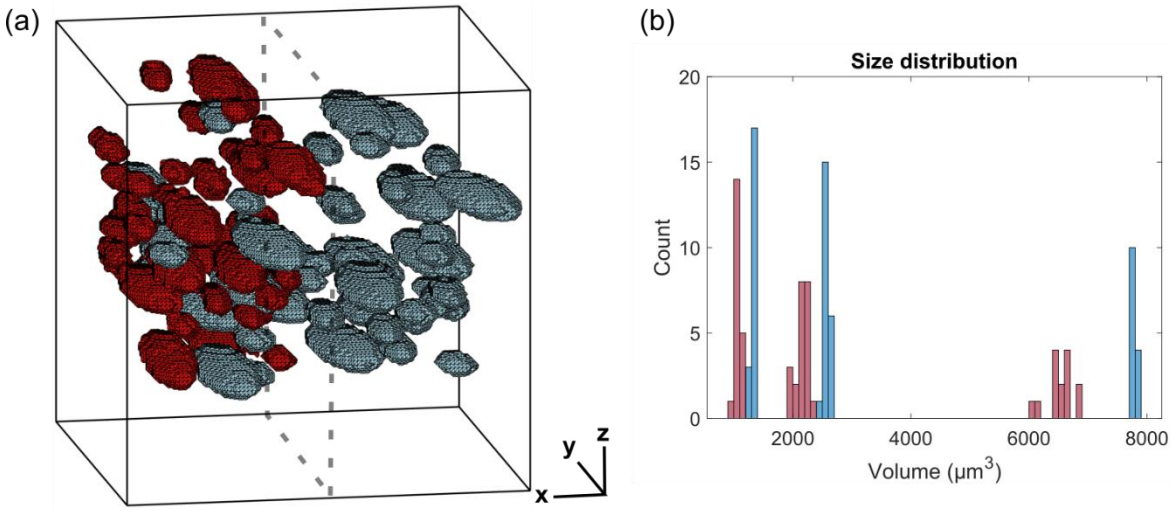

Figure 8.2: *(a) Initial grains (blue) and deformed grains (red). N = 56 grains. (b) Size distribution of the initial grains (blue) and the deformed grains (red).*

We used the calculation of second-order central moments to have smoother ellipsoid shapes and to investigate the directional data. The summary of the changes in the shape fabric and spatial distribution of the grains is presented in ***Figure 8.3***. The shape attributes of the ellipsoids are represented in the Flinn and Jelinek diagrams and their directional data in lower-hemisphere stereonets. Scalar and directional data of the bulk fabric ellipsoid and the distribution ellipsoid are given as well. The x-axis is implied to represent the north in the Sigüés framework. Initially (***Figure 8.3***), grains have southwest lineations and near vertical poles of foliation. They are mostly constrictional ellipsoids in the Flinn diagram or trixial prolate ellipsoids in the Jelinek diagram with anisotropies ranging from 3 (small grains) to 7 (large grains). These individual ellipsoids were arranged to define a common foliation (fabric ellipsoid) and common planar structures (distribution ellipsoid). In the deformed state (***Figure 8.3***), lineations of grains mainly become subparallel to a horizontal east-west trend (y-axis). Poles of foliation depict a slight asymmetric north extended girdle. The lineations of the fabric and distribution ellipsoids are in agreement with the individual lineations. The foliation of the fabric ellipsoid is plunging to the south at ≈20° while the foliation of the distribution ellipsoid is dipping more strongly in that same direction. The scalar parameters indicate that ellipsoids of small grains become more triaxial and less anisotropic whereas ellipsoids of medium and large grains become more cigar-shaped (especially true for the medium-sized grains) with slight variations in their anisotropy. The grains now share a common east-west directed line rather than a common plane as shown by the scalar data of the fabric ellipsoid. The distribution ellipsoid has significantly changed its shape, now becoming almost perfectly prolate. The included grains are distributed along lines with a comparable magnitude to the initial state.

The results show that starting from the initial state characterized by a bedding fabric with compaction strain, the attributes of the included grains in the deformed state indicate the loss of the sedimentary fabric. The fabric is more triaxial and a bit less anisotropic in the deformed state. The grains initially arranged in planes now form lines. To this end, the strain would be constrictional.

8.5 Discussion and conclusion

This study presents a one-step compressive stress applied to a fine-grained matrix with inclusions. We illustrate the elastic response of such system in which the matrix and the inclusions have different mechanical properties. The initial purpose of this numerical simulation was to better constrain the

results of the 3D spatial distribution of the natural case studies in order to evaluate finite strain. This 3D aspect is poorly documented in rocks. Additionally, the model results would have help to constrain the shape fabric of our field results. This theme is extensively developed in the literature. Comparison of shape fabric data and model can be found e.g. in Cladouhos (1999) and Giorgis and Tikoff (2004), among many others.

We recall that our methodology is not limited to a two-phase medium and can be applied to a complete segmented XCT dataset with multiple phases having specific properties.

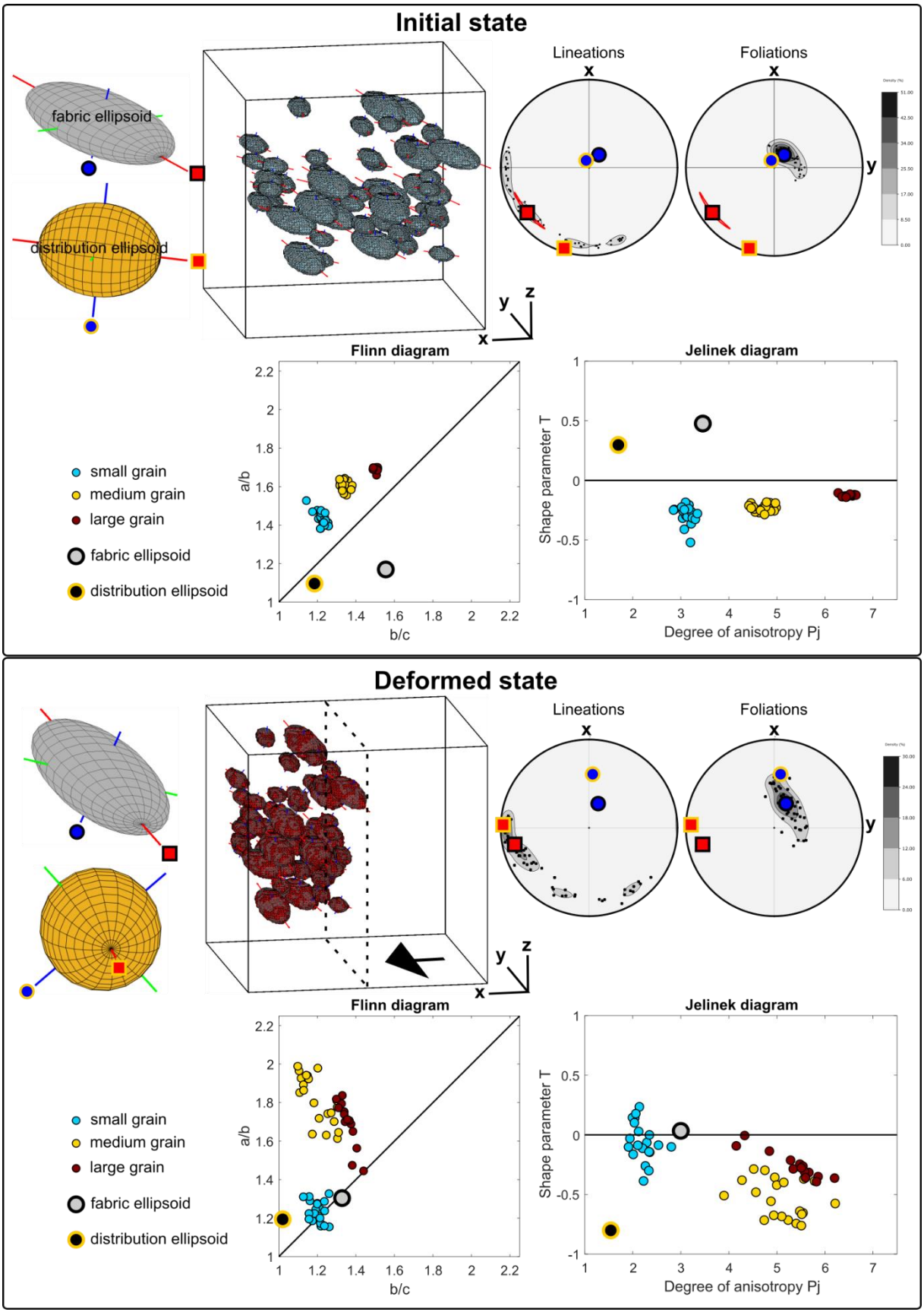

Figure 8.3: ***Summary of the shape fabric and spatial distribution of ellipsoidal inclusions embedded in a weaker matrix, obtained in the case of a homogeneously distributed 50 % shortening. (a) Initial state. (b) Deformed state.***

9 Discussion, conclusion and perspectives

The goal of this thesis was to develop methodologies to study and quantify microstructures but also to evaluate finite strain based on three-dimensional XCT images. At the same time, the application of these developed tools on several case studies of naturally deformed and consolidated fine-grained rocks was paramount. In the following lines are presented elements of discussion and conclusion. Ultimately, we provide perspectives related to this work. We will first focus on the methodological axis implemented during this thesis to characterize the microstructures. We will then discuss the results of the application axis of this thesis.

9.1 Methodology

The tools developed during this thesis concern the analyses of the SPO, the grain fabric and the spatial distribution of minerals and pores in rocks in general. The set of tools implemented in the *SPO*, *Intercept* and *Ellipsoid* programs to study 2D images have largely contributed to improve the quantitative approach of mesostructures and microstructures since the 90s (Launeau and Robin, 1996, 2005; Launeau and Cruden, 1998; Launeau, 2004; Launeau et al., 2010) and more specifically in igneous materials. Similarly, other authors have implemented comparable programs under *Mathematica* in which 2D quantitative data can be extrapolated in 3D (Mookerjee and Nickleach, 2011). In addition, 2D shape data and spatial distribution of grains can be studied by the methods of Mulchrone (2003); Mulchrone et al. (2003). Since the rise of XCT, it has been shown that 3D-SPO of grains can be extracted directly in a non-destructive manner (Ketcham, 2005a; Jerram and Higgins, 2007; Voltolini et al., 2011). A typical example of the popularity of XCT for the study of petrofabrics is shown by the work of Petri et al. (2020).

However, throughout this thesis we bring a unique methodology to study the true 3D-SPO of individual clasts in fine-grained rocks with extensive investigations based on carefully acquired lab-based XCT images. These investigations include the characterization of shape anisotropy, fabric anisotropy, subsets, subfabrics and assessing the heterogeneity of the results. On the other hand, we have chosen fine-grained rocks in which 3D-SPO analysis is rare. From this point of view, our study is a novelty. Moreover, we have varied the study sites to validate our approach. We thus propose a large panel of applications, which may be of academic or industrial interest.

We set up methodological tools to analyze shape-based data and point distribution data, in three-dimensional space, of clasts and pores extracted from a fine clastic rock matrix imaged by XCT. This extraction involved segmentation of our image. In some cases, complementary techniques have been used (EDS and EBSD). The petrofabric analysis and deformation quantification strategies that have been developed can be routinely applied to XCT images. These tools are not limited to the analysis of minerals and pores but can also be adapted to any type of medium containing inclusions/particles wishing to have a quantitative tool for microstructure analysis. For example during this thesis, I had the opportunity to apply these tools to the study of dense inclusions in activated carbons beads. We also proposed a way to evaluate the representativeness of our morphological and directional data, both individual and bulk, obtained from segmented grains. Finally, we have proposed a way to combine numerical models with real 3D microstructures that could better constrain the deformation analysis.

An overview of the methods developed in this thesis in fine-grained clastic rocks is proposed in ***Figure 9.1***. After the image processing step, we base our analysis on the binarized image. Each individual clast or pore has an equivalent ellipsoid using the inertia tensor method and is replaced in a geographic

coordinate system. It is the starting point of our shape-based analysis. Individual morphological parameters include grain size (i.e. volume), symmetry and eccentricity of its equivalent ellipsoid. Bulk fabric can be obtained by combining the individual measurements and gives access to the orientation distribution of the particles and their degree of alignment. Further investigations can be done by looking at individual or bulk subsets and subfabrics. Subset analysis is particularly interesting in providing information on the grain-scale deformation mechanisms. Subvolume analysis is useful to determine strain localization patterns. Variability in the data can be critically evaluated using our box-counting approach. The second aspect of the methodology deals with the distribution of the centroids of each particle. It is used to quantify distribution anisotropy of the particles and to evaluate deformation state of the rock matrix. Constraining the natural data is envisaged using Finite Element Method simulation.

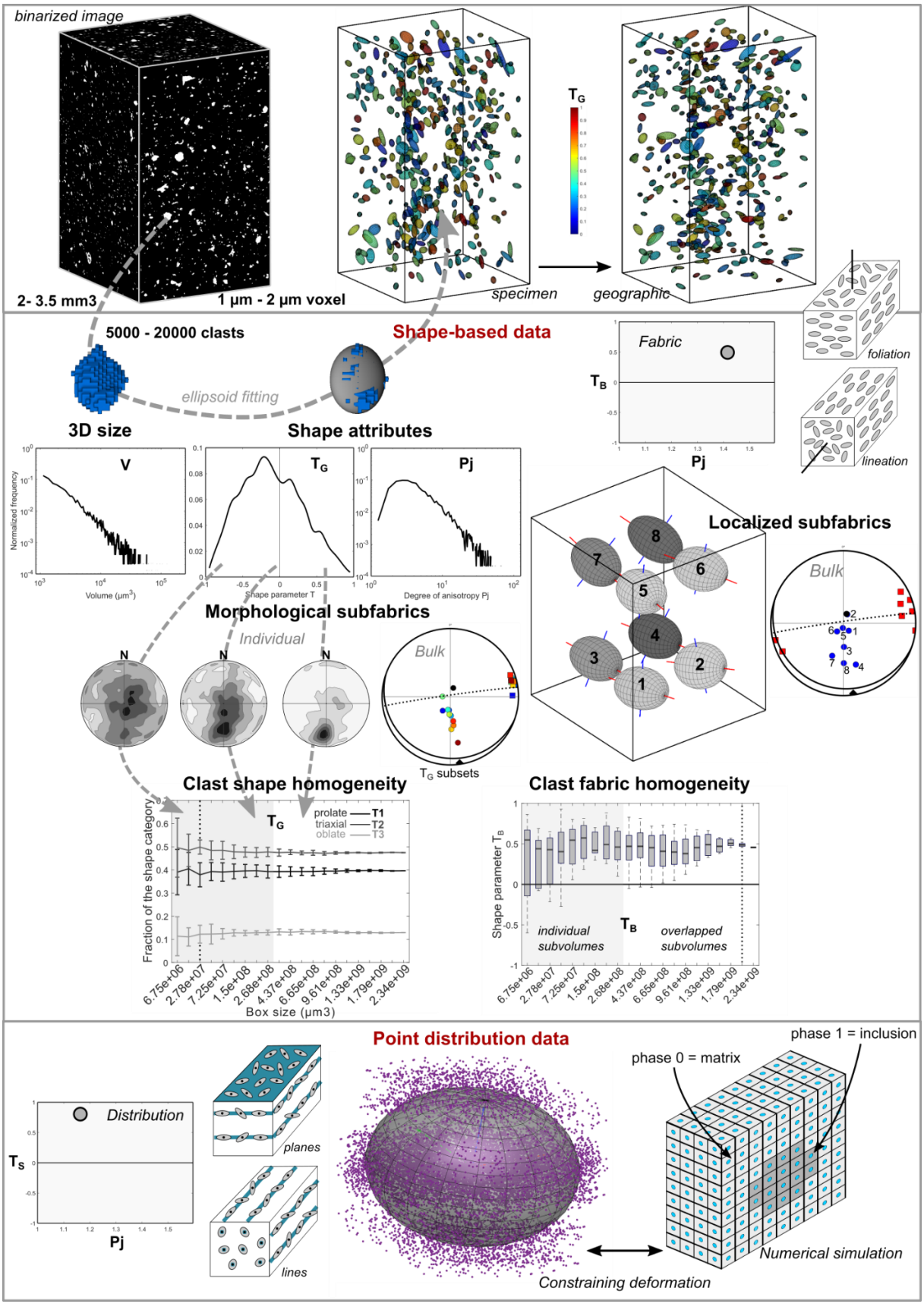

Figure 9.1 : ***Review of the different methodological contributions. As an example, we emphasize on the individual shape parameter*** T_G ***but other parameters can be equally addressed. Please note that the figures are not necessarily from the same dataset. Small sketches for lineation and foliation redrawn from*** (Borradaile, 2003b; Archanjo et al., 2006)***.***

9.2 Applications

9.2.1 The same fine-grained clastic matrix with different deformation states

In this section, we discuss the results concerning the evolution of a fine-grained matrix with cleavage development. We studied the cleaved calcareous shales of Sigüés (chapter ***4***) and the shale to slate transition of Lehigh Gap (chapter ***5***). These two sites show an uncleaved domain, a pencil-cleavage domain and a slaty cleavage domain. This is the first time that naturally deformed fine-grained rocks are investigated by means of XCT.

The two studied outcrops are characterized by different metamorphic conditions for cleavage development. The rocks of Sigüés may have experienced a peak burial temperature of ≈180°C to 215°C maximum at which cleavage development may have occurred (Izquierdo-Llavall et al., 2013). New Raman spectroscopy data of carbonaceous material obtained on samples from a surrounding area indicate ≈200°C (R. Stokes, personal communication). As previously discussed in chapter ***5***, temperatures for the Martinsburg shale were higher. Some of our newly collected samples have been analyzed by Raman technique and indicate ≈280°C (R. Stokes, personal communication).

Both studies show some common results:

- The grain shape fabric inferred from a 2-3 mm^3 sample imaged by XCT is representative to the macroscopic fabric and its structural elements (bedding and cleavage). We repeated the measurement for the Sigüés samples and the results between the two sets of samples are in accordance for all the studied mineral phases (calcite, quartz and pyrite) and pore space.

- Fabric anisotropy of all phases is weak in the transition domain (pencil-cleavage). This is in agreement with AMS studies in deformed fine-grained rocks (Parés et al., 1999; Parés, 2004).

- Pore fabric is mainly disorganized in the transition domain (pencil-cleavage) and the porosity is generally low.

- In terms of shape anisotropy, the deformation state of the fine-grained matrix does not influence the average shape parameter ($\boldsymbol{T_G}$) of the calcite and quartz grains. The evolution of the aspect ratio of grains gives another information that we discuss below.

In order to highlight some differences, we sum up the morphological results of calcite and quartz in the two sets of samples of Sigüés and the set of Lehigh Gap in ***Figure 9.2***. At low temperature (≈ 200°C), calcite is more mobile than quartz (Gratier et al., 2013) and this may explain the different average aspect ratios of both phases in the most deformed samples of Sigüés. Quartz aspect ratio is higher at Lehigh Gap (up to 2.61) compared to Sigüés (max 2.36). We suggest that dissolution-precipitation of quartz is discrete at Sigüés (high for calcite) and pronounced at Lehigh Gap (temperature ≈280°C). In the XCT image of a slate from the Ardennes, probably having experienced higher temperatures than the slates of Lehigh Gap, Wenk et al. (2019) provided an average aspect ratio of 2.7 for quartz and suggested that dissolution-precipitation was responsible for this high aspect ratio. This value would be in agreement with our 3D shape data.

The summary of the shape fabric results are provided in ***Figure 9.3***. This figure indicates that in low temperature environments and slower strain rates (Sigüés), quartz shape fabric is less affected by the intensity of the lateral compressive regime. In these conditions, calcite shape fabric is far more expressive. At Lehigh Gap, quartz shape fabric tends to have similarities with the calcite shape fabric

of Sigüés. In particular, we report strong values of P_J. Note that the degree of anisotropy of the shape fabric depends on the degree of alignment of the grains and on their individual shape anisotropy.

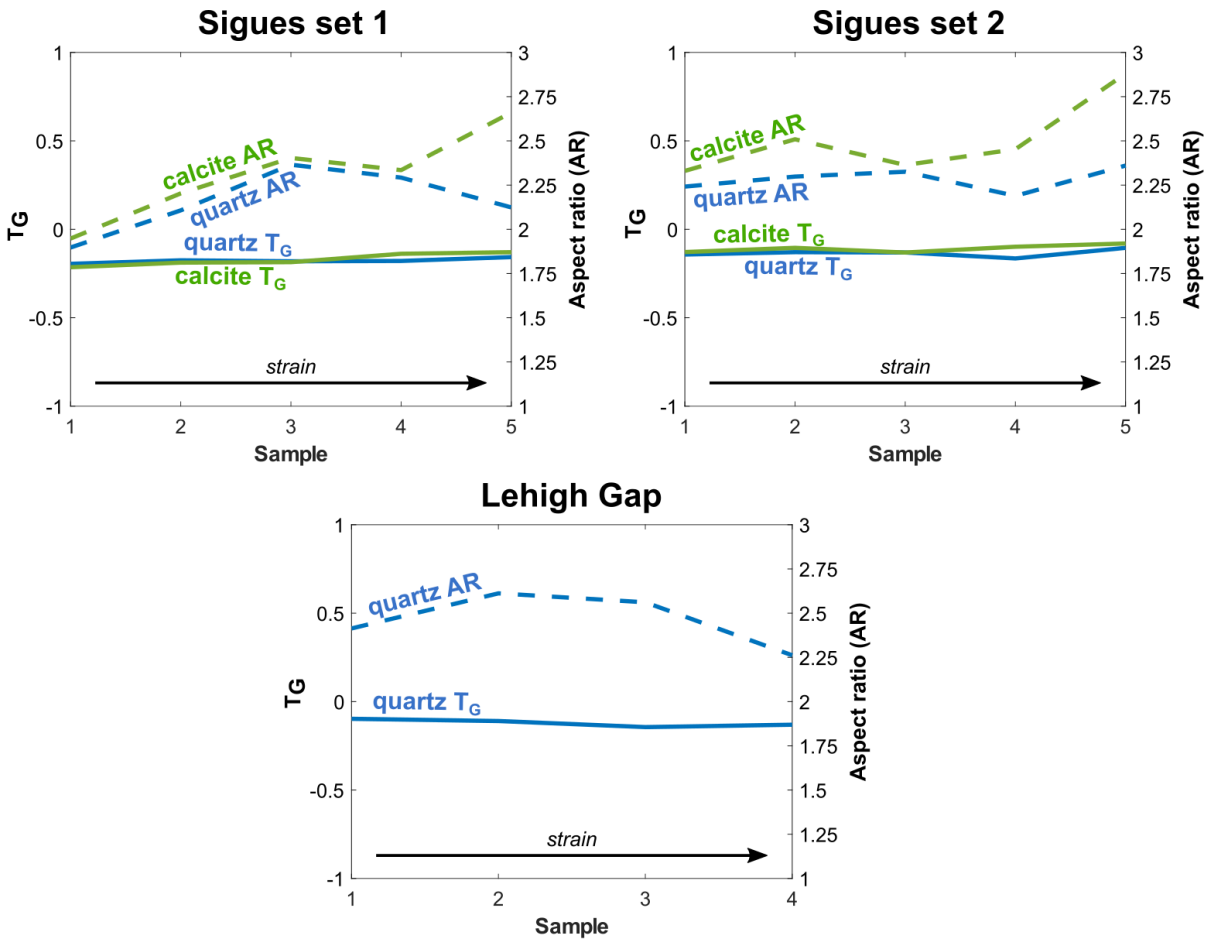

Figure 9.2 : ***Evolution of the average individual shape parameter T_G and the average aspect ratio (AR) of calcite and quartz grains in the samples of Sigüés (top two diagrams). Strain increases from sample 1 to 5 at Sigüés. Evolution of the same parameters for quartz in the Lehigh Gap samples (bottom diagram). As per the macroscopic fabric, strain is expected to increase from sample 1 to 4 at Lehigh Gap.***

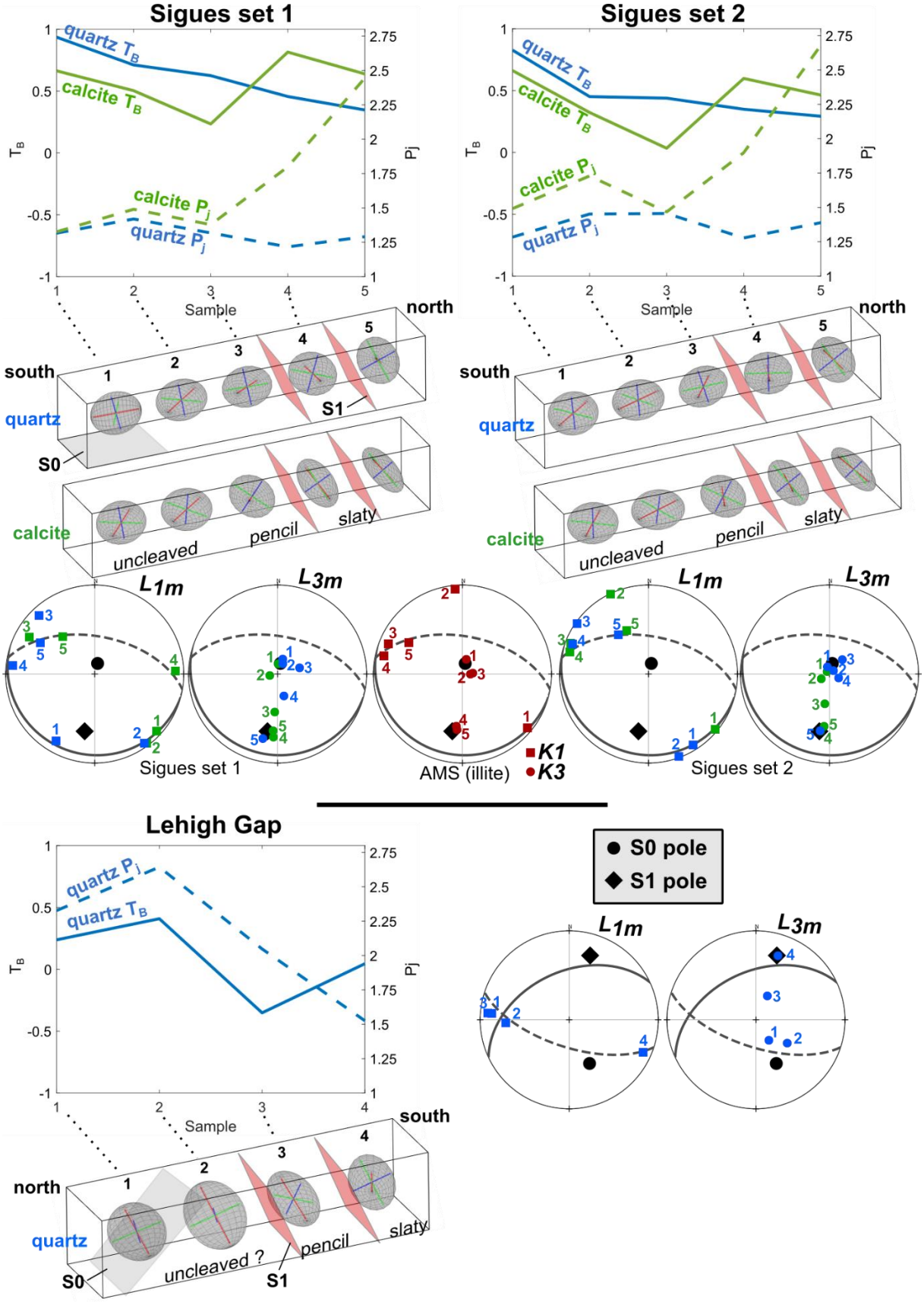

***Figure 9.3** : Evolution of the shape fabrics of calcite and quartz at Sigüés. Strain increases from sample 1 to 5 at Sigüés. Evolution of the shape fabric of quartz at Lehigh Gap. As per the macroscopic fabric, strain is expected to increase from sample 1 to 4 at Lehigh Gap.*

In the case of Sigüés, compaction strain inferred from the spatial distribution analysis of quartz grains is retrieved only in the uncleaved samples. Complexity emerges from this analysis in the samples associated to an increase in cleavage development. The sum of all strain increments and the multiple deformation mechanisms make the analysis more delicate to interpret (Passchier and Trouw, 2005; Burmeister et al., 2009). At Lehigh Gap, the strain associated to the vertical compaction is recorded across the four samples.

9.2.2 Heterogeneous clastic matrices subjected to the same deformation regime

In this section, we discuss the results concerning different fine-grained (and some coarse) matrices subjected to the same deformation regime. We have worked on samples collected in the Hecho group turbidites from two sites of the Roncal valley. Crognier (2016) performed a detailed analysis in this area combining analytical measurements and thermal modeling to study the spatial distribution of paleotemperatures in the Jaca basin. They estimated burial temperatures of around 200°C maximum in the Roncal area. This is not different from the Sigüés site although burial temperatures may have been superior in the eastern part of the basin and the Internal Sierras, up to 240-250°C in the Torla area (Lacroix et al., 2011; Crognier, 2016; Labaume et al., 2016; Oliva-Urcia, 2018).

A review of the main results is provided in ***Figure 9.4***. The orientation distribution of the clasts (i.e. shape parameter $\boldsymbol{T_B}$ and directional data) are more pertinent to characterize the heterogeneity of the multiple rock matrices. We show that there is an important variability in the orientation distribution of clasts at the bed scale. The clast shape fabric appears to depend on their supporting matrix and local variations within the same bed may exist. One should note that the high angle relationship between bedding and cleavage at site 2T (LPS type) favored prolate shape fabrics while the lower angle at site 1T (shearing type) does not. This is in line with the results obtained on magnetic fabrics (Housen et al., 1993a; Debacker et al., 2004).

One should note that the average aspect ratio of quartz measured in the samples from the two sites is comparable to the values obtained for Sigüés. This is also true for the intensity of the quartz shape fabric. This would be in accordance with relatively low temperature at the time of deformation in this area.

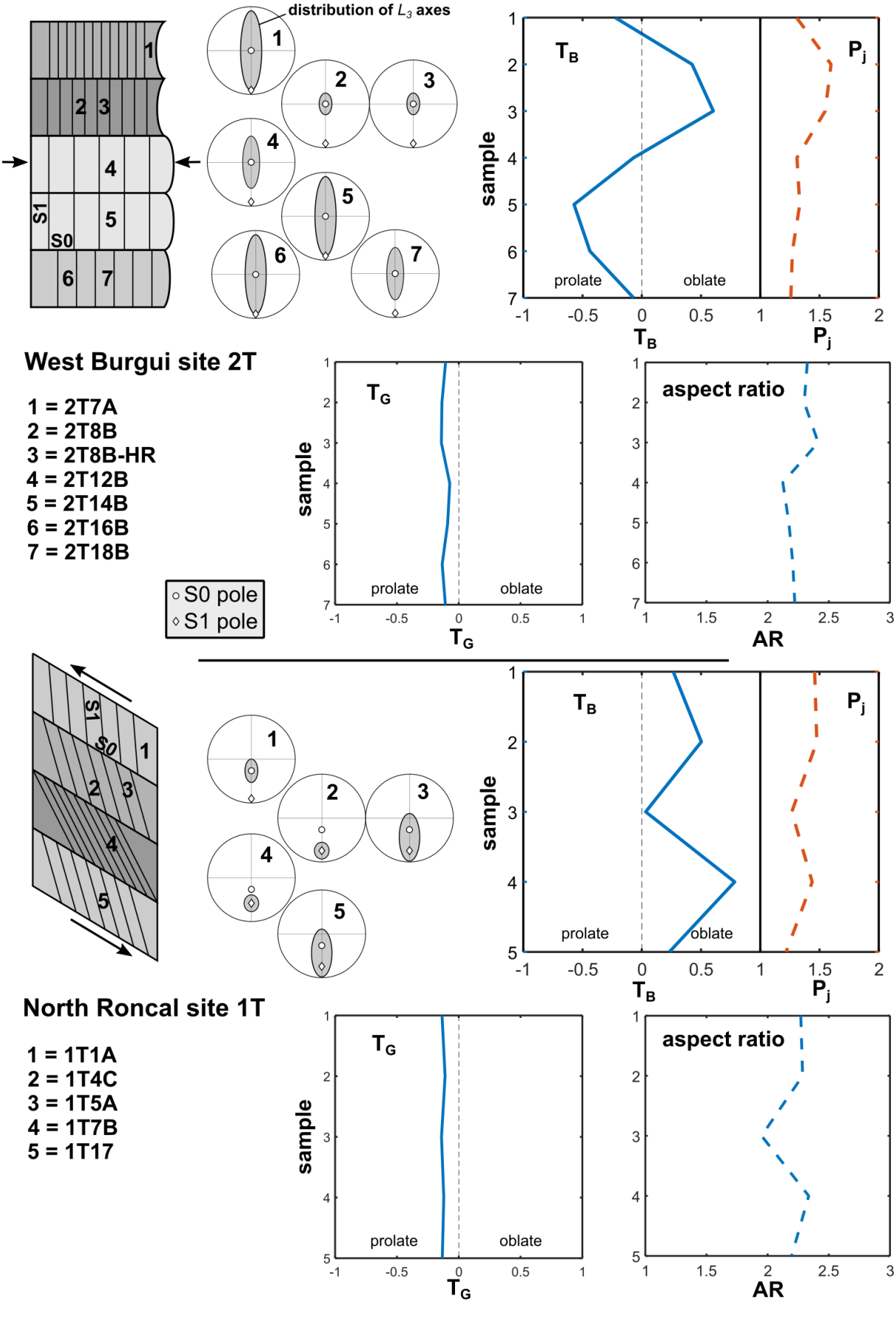

West Burgui site 2T

1 = 2T7A
2 = 2T8B
3 = 2T8B-HR
4 = 2T12B
5 = 2T14B
6 = 2T16B
7 = 2T18B

North Roncal site 1T

1 = 1T1A
2 = 1T4C
3 = 1T5A
4 = 1T7B
5 = 1T17

Figure 9.4 : ***Schematic overview of the shape anisotropies and shape fabrics of clasts in multiple deformed lithologies (Hecho turbidites). Site 2T is an LPS type deformed system. Site 1T may combine pre and/or syn-folding LPS and shearing associated to fold growth. Note that we have simplified the main results obtained in chapter 7.***

9.2.3 Petrofabric techniques used (XCT and AMS)

A short discussion on the two techniques is necessary because AMS has been widely used to characterize deformed fine-grained rocks. Our work on X-ray images is a first on such a panel of fine-grained rocks presenting different deformation state and we bring new insights.

XCT provides a rather simple signal (at the first order, considering spatial variations in attenuation) and gives direct information on the petrofabric. Moreover, it gives access to individual measurements of the components of the imaged medium. This technique is non-destructive but requires significantly more time than AMS and does not have the cost advantage with it. The volume of fine-grained rock analyzed is about 2 to 3.5 mm^3, much smaller than the AMS cylinder but much larger than volumes observed by Focused Ion Beam-Scanning Electron Microscope (FIB-SEM) for example. This volume is suitable for the study of silt grains and relatively large pores in shale rocks.

AMS is a complex convoluted signal providing indirect information about the petrofabric. This measurement is bulk, non-destructive and fast (less than 2 min with the 3D rotator, Studýnka et al., 2014). The measurement is very cheap and provides information on a volume of 10 cm^3 very useful for laboratory scale analysis.

We have seen that XCT can be an alternative technique to identify subfabrics. Separating mineral subfabrics from bulk petrophysical measurements is always essential to better understand the deformation history of rocks. In fine-grained rocks, XCT has allowed us to focus on the shape fabric of diamagnetic minerals (calcite and quartz) that do not contribute significantly to the magnetic fabric. In addition, for one mineral phase (e.g. quartz), X-ray imaging allowed us to characterize multiple preferred orientations that may also exist for magnetic carriers and can contribute to the formation of composite magnetic fabrics (Borradaile and Tarling, 1981; Housen et al., 1993a; Debacker et al., 2004). On the contrary, AMS fabric will average out multiple fabrics. This is to be linked to the work of Martín-Hernández et al. (2005). For their mathematical simulation, they compared the preferred orientation of phyllosilicates measured by AMS and X-ray goniometry on slates with different kink wavelengths.

Some studies have shown significant variability in AMS directional data in the Jaca basin and the Internal Sierras of the Pyrenees (Oliva-Urcia et al., 2009; Pueyo-Anchuela et al., 2010), which is not always easy to relate to geological structures and deformation state. Our results on rocks in the Jaca basin have shown that XCT provides information, sometimes unexpected and measured on a small volume of rock, but always consistent with macroscopic structures such as bedding or cleavage. Because AMS is based on both physico-chemical and geometric properties, the measurement integrates several parameters. The direct geometric measurement allowed by the XCT is an advantage. We have also shown in this thesis that the overprinting of the original sedimentary fabric by the tectonic fabric in cleaved fine-grained rocks from the Jaca basin is not widespread. This is in agreement with the observations on electronic images of Bauluz et al. (2012) that studied fine-grained turbiditic samples in the valleys further west of the basin. The intensity of the original sedimentary fabric, the lithology and the degree of deformation may explain this feature (Parés and van der Pluijm, 2002; Robion et al., 2007).

In shales from fold-and-thrust belts, the dispersion of AMS $\boldsymbol{K_3}$ axes often describes an asymmetric girdle distribution (Parés et al., 1999; Pueyo-Anchuela et al., 2011; Parés, 2015; Parés and Anastasio, 2018). This type of distribution is generally associated to layer-parallel shearing (Parés, 2015). We were

able to confirm, through X-ray imaging, a top-to-the south shear at Sigüés and a top-to-the north-northwest shear at Lehigh Gap, both recorded by the shape fabrics of the studied grains. In our shape fabric results, the intersection lineation was often well expressed, in accordance with magnetic fabric data in the cleaved rocks from the southern Pyrenean basin (Pueyo-Anchuela et al., 2010, 2012).

9.2.4 Limitations

The spatial resolution of the XCT images and the contrast between components are the main limitations. In the Sigüés case study, XCT images had a voxel resolution of 1 to 1.5 µm. At this voxel resolution, detrital silt grains can be well distinguished and the structure of micrometric pores can be characterized. On the other hand, we also come closer to more intimate relationships such as polyphasic micro aggregates, possible mineralogical replacements and new growths inherited from diagenesis and/or metamorphism. Indeed, it is good to recall that the same mineral phase can be represented by different generations of appearance during the burial of the rock and its tectonic history. Generally, we distinguish the detrital grains from the authigenic grains. These relationships between minerals were further revealed by EBSD with a combination of authigenic, recrystallized and/or replaced grains that XCT can hardly distinguish. An alternative 2D analytical method to discriminate the generations of crystallization of the grains is the scanning electron microscopy-based cathodoluminescence imaging (SEM-CL). This technique is efficient for quartz grains (Hart et al., 2013; Milliken, 2014). In terms of contrast between components, the pores can sometimes be confused with carbonaceous materials because of the comparable weak attenuations of air and carbon. In some cases, the morphology of the particles can allow distinguishing the two types. A more robust solution is to inject high-contrast gases such as Xenon in the rock sample to highlight porosity (Vega et al., 2014). Furthermore, the complete characterization of the pore space, which spans several length scales, was beyond the scope of this thesis and requires advanced multi-scale imaging (Ma et al., 2016, 2017). In this thesis, we have provided important data concerning the porosity at a millimeter scale. This porosity is mostly unconnected and can be found in the form of microcracks.

There is a physical limit inherent to the XCT, which remains the volume of data obtained. The three-dimensional aspect is always generating large volumes of data. Thus, it is common to convert the images obtained in 16-bit to 8-bit or to resample the dataset (down sampling) to a coarser voxel size. In this thesis, we have always treated the 16-bit datasets. On the other hand, the post-processing workflow can be quite long, especially image processing. The time spent on image processing was important during this thesis. It is important to clearly identify the major structures and heterogeneities of each sample by carefully scanning the entire volume. Thus, we then worked on X-ray images having a 2 µm voxel resolution to facilitate post-processing and to cover more lithologies (in the Lehigh Gap and Hecho case studies).

9.3 General conclusion

The main conclusive elements of this thesis are as followed:

→ We have developed robust tools to thoroughly investigate shape-based and point distribution data of individual particles in a porous medium imaged by means of X-ray computed tomography. In this thesis, the particles that serve as example are clasts and pores embedded in a clay rock matrix.

→ We propose a method to evaluate the homogeneity of the clast population and the homogeneity of their orientation distribution. In our rock samples, the characteristic length of

the deformation structures is a key factor to the representativeness of the orientation distribution of the clasts.

→ Among the first investigations of naturally deformed fine-grained rocks in fold-and-thrust belt systems by means of X-ray computed tomography. The 3D images cover a voxel size range between 1 and 2 µm.

→ Shape-based data characterize the deformation orientation and intensity of the rock matrix and point distribution data characterize the clustering of grains on layering or bedding.

→ Among the shape-based data, orientation distributions of the clasts (i.e. shape fabrics) appear more discriminating to characterize the deformation state of the matrix compared to the individual clast shapes.

→ Contrasting 3D shape anisotropies and shape fabrics of calcite and quartz clasts as deformation increases in fine-grained cleaved rocks. New opportunity is presented to characterize microstructures in deformed rocks with these 3D data.

→ Subset and subvolume analysis provide key information on grain-scale deformation mechanisms and strain localization patterns in the matrix, respectively, which is the main advantage of the technique.

→ A spatial distribution analysis (similar to a 3D Fry method) provides interesting results in the uncleaved samples. It records the primary structures and the vertical compaction of the sedimentary load. This is best expressed in the siltstones facies in which the compositional layering is significant. Tectonic strain and cleavage development tend to erase the primary structures. Thus, further investigations are needed to constrain the influence of the heterogeneous deformation mechanisms affecting the clasts. Additional data on other deformed rocks at very low-grade metamorphic conditions would help. Overall, our approach mostly reveals spatial organization of the grains with local patchy clustering or anti-clustering or more regular layering due to sedimentary processes.

→ A methodology to constrain the natural 3D point distribution data with finite element simulation is given.

9.4 Perspectives

The methodology developed in this thesis can be coupled with in situ mechanical experiments. We have characterized the shape anisotropy, orientation distribution and spatial distribution of particles in 3D XCT images. We have presented a way to use these structural data in a finite element simulation. Thus, the characterization of deformed particles may help to predict quantitative data of structural anisotropy and mechanical behavior of any medium with inclusions.

The obtained data in fine-grained rocks throughout this thesis may also serve as input parameters for microstructure based modeling of shales. If we stack all the data concerning the shape parameter ($\boldsymbol{T_G}$) of individual quartz grains extracted from X-ray imaging during this thesis, the average grain in a fine-grained rock is triaxial prolate ($\boldsymbol{T_G} \approx -0.25$). Its eccentricity varies with the deformation state of the rock.

Our approach to evaluate the 3D clast fabric and its homogeneity in rocks can be of interest in the case of drilling operations and can be applied on recovered drill cores or drill cuttings. This will provide useful information on the microstructural deformation mechanisms in fault zone for example.

References

Adams, B.L., Wright, S.I., Kunze, K., 1993. Orientation imaging: The emergence of a new microscopy. Metallurgical Transactions A 24, 819–831. https://doi.org/10.1007/BF02656503

Ailleres, L., Champenois, M., 1994. Refinements to the Fry method (1979) using image processing. Journal of Structural Geology 16, 1327–1330. https://doi.org/10.1016/0191-8141(94)90073-6

Ailleres, L., Champenois, M., Macaudiere, J., Bertrand, J.M., 1995. Use of image analysis in the measurement of finite strain by the normalized Fry Method: geological implications for the 'Zone Houillère' (Briançonnais zone, French Alps). Mineralogical Magazine 59, 179–187. https://doi.org/10.1180/minmag.1995.059.395.02

Akker, I. V, Kaufmann, J., Desbois, G., Klaver, J., Urai, J.L., Berger, A., Herwegh, M., 2018. Multiscale porosity changes along the pro- and retrograde deformation path: an example from Alpine slates. Solid Earth 9, 1141–1156. https://doi.org/10.5194/se-9-1141-2018

Al-Raoush, R., 2007. Microstructure characterization of granular materials. Physica A: Statistical Mechanics and Its Applications 377, 545–558. https://doi.org/10.1016/j.physa.2006.11.090

Allan, A.M., Kanitpanyacharoen, W., Vanorio, T., 2015. A multiscale methodology for the analysis of velocity anisotropy in organic-rich shale. GEOPHYSICS 80, C73–C88. https://doi.org/10.1190/geo2014-0192.1

Allard, B., Benn, K., 1989. Shape preferred-orientation analysis using digitized images on a microcomputer. Computers & Geosciences 15, 441–448. https://doi.org/https://doi.org/10.1016/0098-3004(89)90049-6

Almqvist, B.S.G., Mainprice, D., 2017. Seismic properties and anisotropy of the continental crust: Predictions based on mineral texture and rock microstructure. Reviews of Geophysics 55, 367–433. https://doi.org/https://doi.org/10.1002/2016RG000552

Alvarez, W., Engelder, T., Geiser, P.A., 1978. Classification of solution cleavage in pelagic limestones. Geology 6, 263–266. https://doi.org/10.1130/0091-7613(1978)6<263:COSCIP>2.0.CO;2

Aranguren, A., Cuevas, J., Tubía, J.M., 1996. Composite magnetic fabrics from S-C mylonites. Journal of Structural Geology 18, 863–869. https://doi.org/https://doi.org/10.1016/0191-8141(96)00013-2

Arbaret, L., Bystricky, M., Launeau, P., 2019. Crystal clustering in magmas: Insights from HP–HT experiments. Comptes Rendus Geoscience 351, 574–585. https://doi.org/https://doi.org/10.1016/j.crte.2019.10.004

Archanjo, C.J., 2002. Fabric of the Rio Ceará–Mirim mafic dike swarm (northeastern Brazil) determined by anisotropy of magnetic susceptibility and image analysis. Journal of Geophysical Research 107, 2046. https://doi.org/10.1029/2001JB000268

Archanjo, C.J., Launeau, P., 2004. Magma flow inferred from preferred orientations of plagioclase of the Rio Ceará-Mirim dyke swarm (NE Brazil) and its AMS significance. Geological Society Special Publication 238, 285–298. https://doi.org/10.1144/GSL.SP.2004.238.01.17

Archanjo, C.J., Silva, M.G., Castro, J.C., Launeau, P., Trindade, R.I.F., Macedo, J.W.P., 2006. AMS and grain shape fabric of the Late Palaeozoic diamictites of the Southeastern Paraná Basin, Brazil. Journal of the Geological Society 163, 95–106. https://doi.org/10.1144/0016-764904-155

Arganda-Carreras, I., Kaynig, V., Rueden, C., Eliceiri, K.W., Schindelin, J., Cardona, A., Sebastian Seung,

H., 2017. Trainable Weka Segmentation: a machine learning tool for microscopy pixel classification. Bioinformatics 33, 2424–2426. https://doi.org/10.1093/bioinformatics/btx180

Arif, M., Mahmoud, M., Zhang, Y., Iglauer, S., 2021. X-ray tomography imaging of shale microstructures: A review in the context of multiscale correlative imaging. International Journal of Coal Geology 233, 103641. https://doi.org/https://doi.org/10.1016/j.coal.2020.103641

Aubourg, C., Rochette, P., Bergmüller, F., 1995. Composite magnetic fabric in weakly deformed black shales. Physics of the Earth and Planetary Interiors 87, 267–278. https://doi.org/https://doi.org/10.1016/0031-9201(94)02962-B

Aubourg, C., Rochette, P., Vialon, P., 1991. Subtle stretching lineation revealed by magnetic fabric of Callovian-Oxfordian black shales (French Alps). Tectonophysics 185, 211–223. https://doi.org/10.1016/0040-1951(91)90445-X

Averbuch, O., Frizon de Lamotte, D., Kissel, C., 1992. Magnetic fabric as a structural indicator of the deformation path within a fold-thrust structure: a test case from the Corbières (NE Pyrenees, France). Journal of Structural Geology 14, 461–474. https://doi.org/https://doi.org/10.1016/0191-8141(92)90106-7

Backeberg, N.R., Iacoviello, F., Rittner, M., Mitchell, T.M., Jones, A.P., Day, R., Wheeler, J., Shearing, P.R., Vermeesch, P., Striolo, A., 2017. Quantifying the anisotropy and tortuosity of permeable pathways in clay-rich mudstones using models based on X-ray tomography. Scientific Reports 7, 14838. https://doi.org/10.1038/s41598-017-14810-1

Bailey, J.J., Heenan, T.M.M., Finegan, D.P., Lu, X., Daemi, S.R., Iacoviello, F., Backeberg, N.R., Taiwo, O.O., Brett, D.J.L., Atkinson, A., Shearing, P.R., 2017. Laser-preparation of geometrically optimised samples for X-ray nano-CT. Journal of Microscopy 267, 384–396. https://doi.org/10.1111/jmi.12577

Baker, D.R., Mancini, L., Polacci, M., Higgins, M.D., Gualda, G.A.R., Hill, R.J., Rivers, M.L., 2012. An introduction to the application of X-ray microtomography to the three-dimensional study of igneous rocks. Lithos 148, 262–276. https://doi.org/10.1016/J.LITHOS.2012.06.008

Baud, P., Louis, L., David, C., Rawling, G.C., Wong, T.-F., 2005. Effects of bedding and foliation on mechanical anisotropy, damage evolution and failure mode., High-Strain Zones: Structure and Physical Properties. https://doi.org/10.1144/GSL.SP.2005.245.01.11

Bauluz, B., Yuste, A., Mayayo, M.J., Rodríguez-Navarro, A.B., González-López, J.M., 2012. Microtexture and genesis of clay minerals from a turbiditic sequence in a Southern Pyrenees foreland basin (Jaca basin, Eocene). Clay Minerals 47, 303–318. https://doi.org/10.1180/claymin.2012.047.3.02

Bear, J., 1988. Dynamics of Fluids in Porous Media, Dover Civil and Mechanical Engineering Series. Dover.

Benn, K., Allard, B., 1989. Preferred mineral orientations related to magmatic flow in ophiolite layered gabbros. Journal of Petrology 30, 925–946. https://doi.org/10.1093/petrology/30.4.925

Bernard, D., Guillon, O., Combaret, N., Plougonven, E., 2011. Constrained sintering of glass films: Microstructure evolution assessed through synchrotron computed microtomography. Acta Materialia 59, 6228–6238. https://doi.org/10.1016/J.ACTAMAT.2011.06.022

Bésuelle, P., Viggiani, G., Lenoir, N., Desrues, J., Bornert, M., 2006. X-ray Micro CT for Studying Strain Localization in Clay Rocks under Triaxial Compression., Advances in X-ray Tomography for Geomaterials, Wiley Online Books. https://doi.org/https://doi.org/10.1002/9780470612187.ch2

Beucher, S., Lantuejoul, C., 1979. Use of Watersheds in Contour Detection, International Workshop on

Image Processing: Real-time Edge and Motion Detection/Estimation.

Beutner, E.C., 1978. Slaty cleavage and related strain in Martinsburg Slate, Delaware Water Gap, New Jersey. American Journal of Science 278, 1 LP – 23. https://doi.org/10.2475/ajs.278.1.1

Beutner, E.C., Diegel, F.A., 1985. Determination of fold kinematics from syntectonic fibers in pressure shadows, Martinsburg slate, New Jersey. American Journal of Science 285, 16–50. https://doi.org/10.2475/ajs.285.1.16

Biedermann, A.R., 2018. Magnetic Anisotropy in Single Crystals: A Review., Geosciences . https://doi.org/10.3390/geosciences8080302

Bjorkum, P.A., 1996. How important is pressure in causing dissolution of quartz in sandstones? Journal of Sedimentary Research 66, 147–154. https://doi.org/10.1306/D42682DE-2B26-11D7-8648000102C1865D

Blott, S.J., Pye, K., 2008. Particle shape: A review and new methods of characterization and classification. Sedimentology 55, 31–63. https://doi.org/10.1111/j.1365-3091.2007.00892.x

Boiron, T., Aubourg, C., Grignard, P.A., Callot, J.P., 2020. The clay fabric of shales is a strain gauge. Journal of Structural Geology 138, 104130. https://doi.org/10.1016/j.jsg.2020.104130

Bons, P.D., Den Brok, B., 2000. Crystallographic preferred orientation development by dissolution-precipitation creep. Journal of Structural Geology 22, 1713–1722. https://doi.org/10.1016/S0191-8141(00)00075-4

Borradaile, G.J., 2003a. Spherical Orientation Data:Tensors. In: Borradaile, G. (Ed.), Statistics of Earth Science Data. Springer Berlin Heidelberg, Berlin, Heidelberg, 293–326. https://doi.org/10.1007/978-3-662-05223-5_11

Borradaile, G.J., 2003b. Spherical-Orientation Data. In: Borradaile, G. (Ed.), Statistics of Earth Science Data. Springer Berlin Heidelberg, Berlin, Heidelberg, 247–292. https://doi.org/10.1007/978-3-662-05223-5_10

Borradaile, G.J., 2001. Magnetic fabrics and petrofabrics: their orientation distributions and anisotropies. Journal of Structural Geology 23, 1581–1596. https://doi.org/https://doi.org/10.1016/S0191-8141(01)00019-0

Borradaile, G.J., 1988. Magnetic susceptibility, petrofabrics and strain. Tectonophysics 156, 1–20. https://doi.org/https://doi.org/10.1016/0040-1951(88)90279-X

Borradaile, G.J., Bayly, M.B., Powell, C.M., 1982. Introduction. In: Borradaile, Graham J, Bayly, M.B., Powell, C.M. (Eds.), Atlas of Deformational and Metamorphic Rock Fabrics. Springer Berlin Heidelberg, Berlin, Heidelberg, 1–6. https://doi.org/10.1007/978-3-642-68432-6_1

Borradaile, G.J., Jackson, M., 2010. Structural geology, petrofabrics and magnetic fabrics (AMS, AARM, AIRM). Journal of Structural Geology 32, 1519–1551. https://doi.org/https://doi.org/10.1016/j.jsg.2009.09.006

Borradaile, G.J., Jackson, M., 2004. Anisotropy of magnetic susceptibility (AMS): magnetic petrofabrics of deformed rocks. Geological Society, London, Special Publications 238, 299 LP – 360. https://doi.org/10.1144/GSL.SP.2004.238.01.18

Borradaile, G.J., Tarling, D.H., 1981. The influence of deformation mechanisms on magnetic fabrics in weakly deformed rocks. Tectonophysics 77, 151–168. https://doi.org/https://doi.org/10.1016/0040-1951(81)90165-7

Brabant, L., 2013. Latest developments in the improvement and quantification of high resolution X-ray

tomography data.

Brabant, L., Vlassenbroeck, J., De Witte, Y., Cnudde, V., Boone, M.N., Dewanckele, J., Van Hoorebeke, L., 2011. Three-Dimensional Analysis of High-Resolution X-Ray Computed Tomography Data with Morpho+. Microscopy and Microanalysis 17, 252–263. https://doi.org/DOI: 10.1017/S1431927610094389

Brosch, F.J., Schachner, K., Blümel, M., Fasching, A., Fritz, H., 2000. Preliminary investigation results on fabrics and related physical properties of an anisotropic gneiss. Journal of Structural Geology 22, 1773–1787. https://doi.org/https://doi.org/10.1016/S0191-8141(00)00106-1

Brun, F., Mancini, L., Kasae, P., Favretto, S., Dreossi, D., Tromba, G., 2010. Pore3D: A software library for quantitative analysis of porous media. Nuclear Instruments and Methods in Physics Research, Section A: Accelerators, Spectrometers, Detectors and Associated Equipment 615, 326–332. https://doi.org/10.1016/j.nima.2010.02.063

Burmeister, K.C., Harrison, M.J., Marshak, S., Ferré, E.C., Bannister, R.A., Kodama, K.P., 2009. Comparison of Fry strain ellipse and AMS ellipsoid trends to tectonic fabric trends in very low-strain sandstone of the Appalachian fold-thrust belt. Journal of Structural Geology 31, 1028–1038. https://doi.org/10.1016/j.jsg.2009.03.010

Cárdenes, V., Lopez-Sanchez, M.A., Barou, F., Olona, J., Llana-Fúnez, S., 2021. Crystallographic preferred orientation, seismic velocity and anisotropy in roofing slates. Tectonophysics 808, 228815. https://doi.org/https://doi.org/10.1016/j.tecto.2021.228815

Cárdenes, V., Merinero, R., De Boever, W., Rubio-Ordóñez, Á., Dewanckele, J., Cnudde, J.-P., Boone, M.N., Van Hoorebeke, L., Cnudde, V., 2016. Characterization of micropyrite populations in low-grade metamorphic slate: A study using high-resolution X-ray tomography. Palaeogeography, Palaeoclimatology, Palaeoecology 441, 924–935. https://doi.org/https://doi.org/10.1016/j.palaeo.2015.10.044

Carlson, W.D., 2006. Three-dimensional imaging of earth and planetary materials. Earth and Planetary Science Letters 249, 133–147. https://doi.org/10.1016/j.epsl.2006.06.020

Chadima, M., Hansen, A., Hirt, A.M., Hrouda, F., Siemes, H., 2004. Phyllosilicate preferred orientation as a control of magnetic fabric: evidence from neutron texture goniometry and low and high-field magnetic anisotropy (SE Rhenohercynian Zone of Bohemian Massif). Geological Society, London, Special Publications 238, 361 LP – 380. https://doi.org/10.1144/GSL.SP.2004.238.01.19

Chadima, M., Jelínek, V., 2008. Anisoft 4.2.–Anisotropy data browser. Contributions to Geophysics and Geodesy 38, 38–41.

Chatzaras, V., Kruckenberg, S.C., Cohen, S.M., Medaris Jr., L.G., Withers, A.C., Bagley, B., 2016. Axial-type olivine crystallographic preferred orientations: The effect of strain geometry on mantle texture. Journal of Geophysical Research: Solid Earth 121, 4895–4922. https://doi.org/https://doi.org/10.1002/2015JB012628

Chawla, N., Chawla, K.K., 2006. Microstructure-based modeling of the deformation behavior of particle reinforced metal matrix composites. Journal of Materials Science 41, 913–925. https://doi.org/10.1007/s10853-006-6572-1

Cifelli, F., Mattei, M., Chadima, M., Hirt, A.M., Hansen, A., 2005. The origin of tectonic lineation in extensional basins: Combined neutron texture and magnetic analyses on “undeformed” clays. Earth and Planetary Science Letters 235, 62–78. https://doi.org/https://doi.org/10.1016/j.epsl.2005.02.042

Cifelli, F., Mattei, M., Chadima, M., Lenser, S., Hirt, A.M., 2009. The magnetic fabric in “undeformed

clays": AMS and neutron texture analyses from the Rif Chain (Morocco). Tectonophysics 466, 79–88. https://doi.org/https://doi.org/10.1016/j.tecto.2008.08.008

Cladouhos, T.T., 1999. Shape preferred orientations of survivor grains in fault gouge. Journal of Structural Geology 21, 419–436. https://doi.org/10.1016/S0191-8141(98)00123-0

Cnudde, V., Boone, M.N., 2013. High-resolution X-ray computed tomography in geosciences: A review of the current technology and applications. Earth-Science Reviews 123, 1–17. https://doi.org/10.1016/J.EARSCIREV.2013.04.003

Cnudde, V., Boone, M.N., Dewanckele, J., Dierick, M., Van Hoorebeke, L., Jacobs, P., 2011a. 3D characterization of sandstone by means of X-ray computed tomography. Geosphere 7, 54–61. https://doi.org/10.1130/GES00563.1

Cnudde, V., Cwirzen, A., Masschaele, B., Jacobs, P., 2009. Porosity and microstructure characterization of building stones and concretes. Engineering Geology 103, 76–83. https://doi.org/https://doi.org/10.1016/j.enggeo.2008.06.014

Cnudde, V., Dewanckele, J., Boone, M.N., de Kock, T., Brabant, L., Dusar, M., de Ceukelaire, M., de Clercq, H., Hayen, R., Jacobs, P., 2011b. High-resolution X-ray CT for 3D petrography of ferruginous sandstone for an investigation of building stone decay. Microscopy Research and Technique 74, 1006–1017. https://doi.org/https://doi.org/10.1002/jemt.20987

Cosenza, P., Prêt, D., Fauchille, A.-L., Hedan, S., 2019. Representative elementary area of shale at the mesoscopic scale. International Journal of Coal Geology 216, 103316. https://doi.org/https://doi.org/10.1016/j.coal.2019.103316

Coster, M., Chermant, J.-L., 2001. Image analysis and mathematical morphology for civil engineering materials. Cement and Concrete Composites 23, 133–151. https://doi.org/https://doi.org/10.1016/S0958-9465(00)00058-5

Crognier, N., 2016. Évolution Thermique, Circulation De Fluides Et Fracturation Associées À La Structuration Du Bassin D'Avant-Pays Sud-Pyrénéen., Universite De Pau Et Des Pays De L'Adour .

Crognier, N., Hoareau, G., Aubourg, C., Dubois, M., Lacroix, B., Branellec, M., Callot, J.P., Vennemann, T., 2018. Syn-orogenic fluid flow in the Jaca basin (south Pyrenean fold and thrust belt) from fracture and vein analyses. Basin Research 30, 187–216. https://doi.org/10.1111/bre.12249

Cross, A.J., Prior, D.J., Stipp, M., Kidder, S., 2017. The recrystallized grain size piezometer for quartz: An EBSD-based calibration. Geophysical Research Letters 44, 6667–6674. https://doi.org/10.1002/2017GL073836

David, C., Robion, P., Menéndez, B., 2007. Anisotropy of elastic, magnetic and microstructural properties of the Callovo-Oxfordian argillite. Physics and Chemistry of the Earth, Parts A/B/C 32, 145–153. https://doi.org/10.1016/j.pce.2005.11.003

De Boever, W., Derluyn, H., Van Loo, D., Van Hoorebeke, L., Cnudde, V., 2015. Data-fusion of high resolution X-ray CT, SEM and EDS for 3D and pseudo-3D chemical and structural characterization of sandstone. Micron 74, 15–21. https://doi.org/10.1016/j.micron.2015.04.003

de Pascalis, F., Nacucchi, M., 2019. Relationship between the anisotropy tensor calculated through global and object measurements in high-resolution X-ray tomography on cellular and composite materials. Journal of Microscopy 273, 65–80. https://doi.org/10.1111/jmi.12762

Debacker, T.N., Hirt, A.M., Sintubin, M., Robion, P., 2009. Differences between magnetic and mineral fabrics in low-grade, cleaved siliciclastic pelites: A case study from the Anglo-Brabant Deformation Belt (Belgium). Tectonophysics 466, 32–46.

https://doi.org/https://doi.org/10.1016/j.tecto.2008.09.039

Debacker, T.N., Robion, P., Sintubin, M., 2004. The anisotropy of magnetic susceptibility (AMS) in low-grade, cleaved pelitic rocks: influence of cleavage/bedding angle and type and relative orientation of magnetic carriers. Geological Society, London, Special Publications 238, 77 LP – 107. https://doi.org/10.1144/GSL.SP.2004.238.01.08

Dewers, T., Ortoleva, P., 1991. Influences of clay minerals on sandstone cementation and pressure solution. Geology 19, 1045–1048. https://doi.org/10.1130/0091-7613(1991)019<1045:IOCMOS>2.3.CO;2

Dong, P., Haupert, S., Hesse, B., Langer, M., Gouttenoire, P.-J., Bousson, V., Peyrin, F., 2014. 3D osteocyte lacunar morphometric properties and distributions in human femoral cortical bone using synchrotron radiation micro-CT images. Bone 60, 172–185. https://doi.org/https://doi.org/10.1016/j.bone.2013.12.008

Doube, M., Kłosowski, M.M., Arganda-Carreras, I., Cordelières, F.P., Dougherty, R.P., Jackson, J.S., Schmid, B., Hutchinson, J.R., Shefelbine, S.J., 2010. BoneJ: Free and extensible bone image analysis in ImageJ. Bone 47, 1076–1079. https://doi.org/https://doi.org/10.1016/j.bone.2010.08.023

Dunne, W.M., Onasch, C.M., Williams, R.T., 1990. The problem of strain-marker centers and the fry method. Journal of Structural Geology 12, 933–938. https://doi.org/https://doi.org/10.1016/0191-8141(90)90067-9

Durney, D.W., Kisch, H.J., 1994. A field classification and intensity scale for first-generation cleavages. AGSO Journal of Australian Geology and Geophysics 15, 257–295.

Dürrast, H., Siegesmund, S., 1999. Correlation between rock fabrics and physical properties of carbonate reservoir rocks. International Journal of Earth Sciences 88, 392–408. https://doi.org/10.1007/s005310050274

Egan, C.K., Jacques, S.D.M., Wilson, M.D., Veale, M.C., Seller, P., Beale, A.M., Pattrick, R.A.D., Withers, P.J., Cernik, R.J., 2015. 3D chemical imaging in the laboratory by hyperspectral X-ray computed tomography. Scientific Reports 5, 15979.

Elhanati, D., Issachar, R., Levi, T., Weinberger, R., 2021. A Practical Approach for Identification of Magnetic Fabric Carriers in Rocks. Journal of Geophysical Research: Solid Earth 126, e2020JB021105. https://doi.org/10.1029/2020JB021105

Ellis, B.R., Peters, C.A., 2016. 3D Mapping of calcite and a demonstration of its relevance to permeability evolution in reactive fractures. Advances in Water Resources 95, 246–253. https://doi.org/https://doi.org/10.1016/j.advwatres.2015.07.023

Engelder, T., Engelder, R., 1977. Fossil distortion and décollement tectonics of the Appalachian Plateau. Geology 5, 457–460. https://doi.org/10.1130/0091-7613(1977)5<457:FDADTO>2.0.CO;2

Engelder, T., Marshak, S., 1985. Disjunctive cleavage formed at shallow depths in sedimentary rocks. Journal of Structural Geology 7, 327–343. https://doi.org/https://doi.org/10.1016/0191-8141(85)90039-2

Epstein, A.G., Epstein, J.B., Harris, L.D., 1977. Conodont color alteration - an index to organic metamorphism, USGS Professional Paper. https://doi.org/10.3133/pp995

Epstein, J.B., 2006. Geology of Delaware Water Gap National Recreation Area, New Jersey–Pennsylvania., Excursions in Geology and History: Field Trips in the Middle Atlantic States. https://doi.org/10.1130/2006.fld008(04)

Epstein, J.B., 1980. Geology of the Ridge and Valley province, northwestern New Jersey and eastern Pennsylvania. Field Studies of New Jersey Geology and Guide to Field Trips: Newark, New Jersey, Rutgers University 70–91.

Epstein, J.B., Epstein, A.G., 1969. Geology of the valley and ridge province between Delaware Water Gap and Lehigh Gap, Pennsylvania. Geology of Selected Areas in New Jersey and Pennsylvania. Edited by S. Subitzky. Rutgers University Press, New Brunswick, NJ 132–205.

Epstein, J.B., Lyttle, P.T., 1993. Geology of the New Tripoli quadrangle, Lehigh, Berks, Schuylkill, and Carbon Counties, Pennsylvania, US Geological Survey Bulletin. https://doi.org/10.3133/b1994

Epstein, J.B., Sevon, W.D., Glaeser, J.D., 1974. Geology and mineral resources of the Lehighton and Palmerton quadrangles, Carbon and Northampton Counties, Pennsylvania.

Erdogan, S.T., Quiroga, P.N., Fowler, D.W., Saleh, H.A., Livingston, R.A., Garboczi, E.J., Ketcham, P.M., Hagedorn, J.G., Satterfield, S.G., 2006. Three-dimensional shape analysis of coarse aggregates: New techniques for and preliminary results on several different coarse aggregates and reference rocks. Cement and Concrete Research 36, 1619–1627. https://doi.org/https://doi.org/10.1016/j.cemconres.2006.04.003

Erslev, E.A., 1988. Normalized center-to-center strain analysis of packed aggregates. Journal of Structural Geology 10, 201–209. https://doi.org/https://doi.org/10.1016/0191-8141(88)90117-4

Esteban, L., Géraud, Y., Bouchez, J.-L., 2006. Pore network geometry in low permeability argillites from magnetic fabric data and oriented mercury injections. Geophysical Research Letters 33. https://doi.org/https://doi.org/10.1029/2006GL026908

Falvard, S., Paris, R., 2017. X-ray tomography of tsunami deposits: Towards a new depositional model of tsunami deposits. Sedimentology 64, 453–477. https://doi.org/https://doi.org/10.1111/sed.12310

Feldkamp, L.A., Davis, L.C., Kress, J.W., 1984. Practical cone-beam algorithm. Journal of the Optical Society of America A 1, 612. https://doi.org/10.1364/josaa.1.000612

Fielitz, W., Mansy, J.L., 1999. Pre- and synorogenic burial metamorphism in the Ardenne and neighbouring areas (Rhenohercynian zone, central European Variscides). Tectonophysics 309, 227–256. https://doi.org/10.1016/S0040-1951(99)00141-9

Figueroa Pilz, F., Dowey, P.J., Fauchille, A.-L., Courtois, L., Bay, B., Ma, L., Taylor, K.G., Mecklenburgh, J., Lee, P.D., 2017. Synchrotron tomographic quantification of strain and fracture during simulated thermal maturation of an organic-rich shale, UK Kimmeridge Clay. Journal of Geophysical Research: Solid Earth 122, 2553–2564. https://doi.org/10.1002/2016JB013874

Fisher, R., 1953. Dispersion on a Sphere. Proceedings of the Royal Society A: Mathematical, Physical and Engineering Sciences 217, 295–305. https://doi.org/10.1098/rspa.1953.0064

Flusser, J., Suk, T., Zitová, B., 2016. 3D Moment Invariants to Translation, Rotation, and Scaling., 2D and 3D Image Analysis by Moments, Wiley Online Books. https://doi.org/10.1002/9781119039402.ch4

Friese, K.-I., Blanke, P., Wolter, F.-E., 2011. YaDiV—an open platform for 3D visualization and 3D segmentation of medical data. The Visual Computer 27, 129–139. https://doi.org/10.1007/s00371-010-0539-6

Fry, N., 1979. Random point distributions and strain measurement in rocks. Tectonophysics 60, 89–105. https://doi.org/10.1016/0040-1951(79)90135-5

Fusseis, F., Xiao, X., Schrank, C., De Carlo, F., 2014. A brief guide to synchrotron radiation-based

microtomography in (structural) geology and rock mechanics. Journal of Structural Geology 65, 1–16. https://doi.org/https://doi.org/10.1016/j.jsg.2014.02.005

Gaillot, P., Darrozes, J., Bouchez, J.-L., 1999. Wavelet transform: a future of rock fabric analysis? Journal of Structural Geology 21, 1615–1621. https://doi.org/https://doi.org/10.1016/S0191-8141(99)00073-5

Garboczi, E.J., 2002. Three-dimensional mathematical analysis of particle shape using X-ray tomography and spherical harmonics: Application to aggregates used in concrete. Cement and Concrete Research 32, 1621–1638. https://doi.org/https://doi.org/10.1016/S0008-8846(02)00836-0

Garboczi, E.J., Bullard, J.W., 2004. Shape analysis of a reference cement. Cement and Concrete Research 34, 1933–1937. https://doi.org/https://doi.org/10.1016/j.cemconres.2004.01.006

Gercek, H., 2007. Poisson's ratio values for rocks. International Journal of Rock Mechanics and Mining Sciences 44, 1–13. https://doi.org/https://doi.org/10.1016/j.ijrmms.2006.04.011

Giorgis, S., Tikoff, B., 2004. Constraints on kinematics and strain from feldspar porphyroclast populations. Geological Society, London, Special Publications 224, 265 LP – 285. https://doi.org/10.1144/GSL.SP.2004.224.01.17

Golab, A.N., Knackstedt, M.A., Averdunk, H., Senden, T., Butcher, A.R., Jaime, P., 2010. 3D porosity and mineralogy characterization in tight gas sandstones. The Leading Edge 29, 1476–1483. https://doi.org/10.1190/1.3525363

Golab, A.N., Romeyn, R., Averdunk, H., Knackstedt, M.A., Senden, T.J., 2013. 3D characterisation of potential CO2 reservoir and seal rocks. Australian Journal of Earth Sciences 60, 111–123. https://doi.org/10.1080/08120099.2012.675889

Goldstein, A., Knight, J., Kimball, K., 1998. Deformed graptolites, finite strain and volume loss during cleavage formation in rocks of the taconic slate belt, New York and Vermont, U.S.A. Journal of Structural Geology 20, 1769–1782. https://doi.org/10.1016/S0191-8141(98)00083-2

Goldstein, J., Newbury, D.E., Michael, J.R., Ritchie, N.W.M., Scott, J.H.J., Joy, D.C., 2018. Scanning electron microscopy and x-ray microanalysis. Springer, New York, NY.

Goral, J., Andrew, M., Olson, T., Deo, M., 2020. Correlative core- to pore-scale imaging of shales. Marine and Petroleum Geology 111, 886–904. https://doi.org/https://doi.org/10.1016/j.marpetgeo.2019.08.009

Goral, J., Walton, I., Andrew, M., Deo, M., 2019. Pore system characterization of organic-rich shales using nanoscale-resolution 3D imaging. Fuel 258, 116049. https://doi.org/https://doi.org/10.1016/j.fuel.2019.116049

Gratier, J.-P., Dysthe, D.K., Renard, F., 2013. Chapter 2 - The Role of Pressure Solution Creep in the Ductility of the Earth's Upper Crust. In: Dmowska, R.B.T.-A. in G. (Ed.), Advances in Geophysics. Elsevier, 47–179. https://doi.org/https://doi.org/10.1016/B978-0-12-380940-7.00002-0

Gray, D.R., 1997. Volume loss and slaty cleavage development. In: Sengupta, S. (Ed.), Evolution of Geological Structures in Micro- to Macro-Scales. Springer Netherlands, Dordrecht, 273–291. https://doi.org/10.1007/978-94-011-5870-1_17

Gray, M.B., Mitra, G., 1993. Migration of deformation fronts during progressive deformation: evidence from detailed structural studies in the Pennsylvania Anthracite region, U.S.A. Journal of Structural Geology 15, 435–449. https://doi.org/https://doi.org/10.1016/0191-8141(93)90139-2

Gray, M.B., Stamatakos, J., 1997. New model for evolution of fold and thrust belt curvature based on

integrated structural and paleomagnetic results from the Pennsylvania salient. Geology 25, 1067–1070. https://doi.org/10.1130/0091-7613(1997)025<1067:NMFEOF>2.3.CO;2

Grégoire, V., Darrozes, J., Gaillot, P., Nédélec, A., Launeau, P., 1998. Magnetite grain shape fabric and distribution anisotropy vs rock magnetic fabric: a three-dimensional case study. Journal of Structural Geology 20, 937–944. https://doi.org/10.1016/S0191-8141(98)00022-4

Griffiths, L., Heap, M.J., Xu, T., Chen, C. feng, Baud, P., 2017. The influence of pore geometry and orientation on the strength and stiffness of porous rock. Journal of Structural Geology 96, 149–160. https://doi.org/10.1016/j.jsg.2017.02.006

Grohmann, C.H., Campanha, G.A., 2010. OpenStereo: Open Source, Cross-Platform Software for Structural Geology Analysis. American Geophysical Union, Fall Meeting 2010, Abstract Id. IN31C-06.

Gualda, G.A.R., Pamukcu, A.S., Claiborne, L.L., Rivers, M.L., 2010. Quantitative 3D petrography using X-ray tomography 3: Documenting accessory phases with differential absorption tomography. Geosphere 6, 782–792. https://doi.org/10.1130/GES00568.1

Gualda, G.A.R., Rivers, M.L., 2006. Quantitative 3D petrography using x-ray tomography: Application to Bishop Tuff pumice clasts. Journal of Volcanology and Geothermal Research 154, 48–62. https://doi.org/10.1016/J.JVOLGEORES.2005.09.019

Haerinck, T., Adriaens, R., Debacker, T.N., Hirt, A.M., Sintubin, M., 2013. Paramagnetic metamorphic mineral assemblages controlling AMS in low-grade deformed metasediments and the implications with respect to the use of AMS as a strain marker. Journal of the Geological Society 170, 263–280. https://doi.org/10.1144/jgs2012-062

Hamid, R., Hossein, M., Yihuai, Z., Zarzor, A.-Y.A., Stefan, I., Maxim, L., Mohammad, S., 2018. Microstructural Effects on Mechanical Properties of Shaly Sandstone. Journal of Geotechnical and Geoenvironmental Engineering 144, 6017019. https://doi.org/10.1061/(ASCE)GT.1943-5606.0001831

Hanna, R.D., Ketcham, R.A., 2017. X-ray computed tomography of planetary materials: A primer and review of recent studies. Geochemistry 77, 547–572. https://doi.org/https://doi.org/10.1016/j.chemer.2017.01.006

Haralick, R.M., Shapiro, L.G., 1985. Image segmentation techniques. Computer Vision, Graphics, and Image Processing 29, 100–132. https://doi.org/10.1016/S0734-189X(85)90153-7

Hart, B.S., Macquaker, J.H.S., Taylor, K.G., 2013. Mudstone ("shale") depositional and diagenetic processes: Implications for seismic analyses of source-rock reservoirs. Interpretation 1, B7–B26. https://doi.org/10.1190/INT-2013-0003.1

Hastie, W.W., Watkeys, M.K., Aubourg, C., 2013. Characterisation of grain-size, shape and orientation of plagioclase in the Rooi Rand dyke swarm, South Africa. Tectonophysics 583, 145–157. https://doi.org/10.1016/J.TECTO.2012.10.035

Hastie, W.W., Watkeys, M.K., Aubourg, C., 2011. Significance of magnetic and petrofabric in Karoo-feeder dykes, northern Lebombo. Tectonophysics 513, 96–111. https://doi.org/10.1016/J.TECTO.2011.10.008

Heilbronner, R.P., 1992. The autocorrelation function: an image processing tool for fabric analysis. Tectonophysics 212, 351–370. https://doi.org/https://doi.org/10.1016/0040-1951(92)90300-U

Hemes, S., Desbois, G., Urai, J.L., Schröppel, B., Schwarz, J.-O., 2015. Multi-scale characterization of porosity in Boom Clay (HADES-level, Mol, Belgium) using a combination of X-ray μ-CT, 2D BIB-

SEM and FIB-SEM tomography. Microporous and Mesoporous Materials 208, 1–20. https://doi.org/https://doi.org/10.1016/j.micromeso.2015.01.022

Hirt, A.M., Julivert, M., Soldevila, J., 2000. Magnetic fabric and deformation in the Navia-Alto Sil slate belt, northwestern Spain. Tectonophysics 320, 1–16. https://doi.org/10.1016/S0040-1951(00)00047-0

Hirt, A.M., Lowrie, W., Lüneburg, C., Lebit, H., Engelder, T., 2004. Magnetic and mineral fabric development in the Ordovician Martinsburg Formation in the Central Appalachian Fold and Thrust Belt, Pennsylvania. Geological Society, London, Special Publications 238, 109–126. https://doi.org/10.1144/GSL.SP.2004.238.01.09

Ho, N.-C., Peacor, D.R., van der Pluijm, B.A., 1996. Contrasting roles of detrital and authigenic phyllosilicates during slaty cleavage development. Journal of Structural Geology 18, 615–623. https://doi.org/10.1016/S0191-8141(96)80028-9

Ho, N.-C., Peacor, D.R., van der Pluijm, B.A., 1995. Reorientation mechanisms of phyllosilicates in the mudstone-to-slate transition at Lehigh Gap, Pennsylvania. Journal of Structural Geology 17, 345–356. https://doi.org/10.1016/0191-8141(94)00065-8

Hobbs, B.E., 1985. The geological significance of microfabric analysis. Preferred Orientation in Deformed Metals and Rocks: An Introduction to Modern Texture Analysis.

Hogan, P.J., Burbank, D.W., 1996. Evolution of the Jaca piggyback basin and emergence of the External Sierra, southern Pyrenees. In: Dabrio, C.J., Friend, P.F. (Eds.), Tertiary Basins of Spain: The Stratigraphic Record of Crustal Kinematics, World and Regional Geology. Cambridge University Press, Cambridge, 153–160. https://doi.org/DOI: 10.1017/CBO9780511524851.023

Holeywell, R.C., Tullis, T.E., 1975. Mineral reorientation and slaty cleavage in the martinsburg formation, Lehigh Gap, Pennsylvania. Bulletin of the Geological Society of America 86, 1296–1304. https://doi.org/10.1130/0016-7606(1975)86<1296:MRASCI>2.0.CO;2

Houben, M.E., Desbois, G., Urai, J.L., 2013. Pore morphology and distribution in the Shaly facies of Opalinus Clay (Mont Terri, Switzerland): Insights from representative 2D BIB–SEM investigations on mm to nm scale. Applied Clay Science 71, 82–97. https://doi.org/https://doi.org/10.1016/j.clay.2012.11.006

Houseknecht, D.W., 1988. Intergranular pressure solution in four quartzose sandstones. Journal of Sedimentary Research 58, 228–246. https://doi.org/10.1306/212F8D64-2B24-11D7-8648000102C1865D

Houseknecht, D.W., 1984. Influence of grain size and temperature on intergranular pressure solution, quartz cementation, and porosity in a quartzose sandstone. Journal of Sedimentary Research 54, 348–361. https://doi.org/10.1306/212F8418-2B24-11D7-8648000102C1865D

Housen, B.A., Richter, C., van der Pluijm, B.A., 1993a. Composite magnetic anisotropy fabrics: experiments, numerical models and implications for the quantification of rock fabrics. Tectonophysics 220, 1–12. https://doi.org/10.1016/0040-1951(93)90219-A

Housen, B.A., van der Pluijm, B.A., 1991. Slaty cleavage development and magnetic anisotropy fabrics. Journal of Geophysical Research 96, 9937–9946. https://doi.org/10.1029/91JB00605

Housen, B.A., van der Pluijm, B.A., 1990. Chlorite control of correlations between strain and anisotropy of magnetic susceptibility. Physics of the Earth and Planetary Interiors 61, 315–323. https://doi.org/https://doi.org/10.1016/0031-9201(90)90114-D

Housen, B.A., van der Pluijm, B.A., Van Der Voo, R., 1993b. Magnetite dissolution and neocrystallization

during cleavage formation: paleomagnetic study of the Martinsburg Formation, Lehigh Gap, Pennsylvania. Journal of Geophysical Research 98, 13799–13813. https://doi.org/10.1029/93jb01088

Hrouda, F., 2007. Magnetic Susceptibility, Anisotropy. In: Gubbins, D., Herrero-Bervera, E. (Eds.), Encyclopedia of Geomagnetism and Paleomagnetism. Springer Netherlands, Dordrecht, 546–560. https://doi.org/10.1007/978-1-4020-4423-6_185

Hu, M.-K., 1962. Visual pattern recognition by moment invariants. IRE Transactions on Information Theory 8, 179–187. https://doi.org/10.1109/TIT.1962.1057692

Hudleston, P.J., Treagus, S.H., 2010. Information from folds: A review. Journal of Structural Geology 32, 2042–2071. https://doi.org/10.1016/j.jsg.2010.08.011

Iassonov, P., Gebrenegus, T., Tuller, M., 2009. Segmentation of X-ray computed tomography images of porous materials: A crucial step for characterization and quantitative analysis of pore structures. Water Resources Research 45. https://doi.org/https://doi.org/10.1029/2009WR008087

Ikeda, S., Nakano, T., Nakashima, Y., 2000. Three-dimensional study on the interconnection and shape of crystals in a graphic granite by X-ray CT and image analysis. Mineralogical Magazine 64, 945–959. https://doi.org/10.1180/002646100549760

Issachar, R., Levi, T., Marco, S., Weinberger, R., 2018. Separation of Diamagnetic and Paramagnetic Fabrics Reveals Strain Directions in Carbonate Rocks. Journal of Geophysical Research: Solid Earth 123, 2035–2048. https://doi.org/10.1002/2017JB014823

Izquierdo-Llavall, E., Aldega, L., Cantarelli, V., Corrado, S., Gil-Peña, I., Invernizzi, C., Casas-Sainz, A.M., 2013. On the origin of cleavage in the Central Pyrenees: Structural and paleo-thermal study. Tectonophysics 608, 303–318. https://doi.org/10.1016/J.TECTO.2013.09.027

Jelínek, V., 1981. Characterization of the magnetic fabric of rocks. Tectonophysics 79, T63–T67. https://doi.org/https://doi.org/10.1016/0040-1951(81)90110-4

Jelínek, V., 1977. The statistical theory of measuring anisotropy of magnetic susceptibility of rocks and its application. Geofyzika Brno, Czech Republic.

Jelínek, V., Kropáček, V., 1978. Statistical processing of anisotropy of magnetic susceptibility measured on groups of specimens. Studia Geophysica et Geodaetica 22, 50–62. https://doi.org/10.1007/BF01613632

Jerram, D.A., Higgins, M.D., 2007. 3D Analysis of Rock Textures: Quantifying Igneous Microstructures. Elements 3, 239–245. https://doi.org/10.2113/gselements.3.4.239

Jowett, E.C., Robin, P.-Y.F., 1988. Statistical significance of clustered orientation data on the sphere: an empirical derivation. Journal of Geology 96, 591–599. https://doi.org/10.1086/629254

Kaarsberg, E.A., 1959. Introductory Studies of Natural and Artificial Argillaceous Aggregates by Sound-Propagation and X-ray Diffraction Methods. The Journal of Geology 67, 447–472. https://doi.org/10.1086/626597

Kaestner, A., Lehmann, E., Stampanoni, M., 2008. Imaging and image processing in porous media research. Advances in Water Resources 31, 1174–1187. https://doi.org/10.1016/J.ADVWATRES.2008.01.022

Kahl, W.A., Dilissen, N., Hidas, K., Garrido, C.J., LÓpez-SÁnchez-Vizcaíno, V., RomÁn-Alpiste, M., 2017. 3-D microstructure of olivine in complex geological materials reconstructed by correlative X-ray μ-CT and EBSD analyses. Journal of Microscopy 268, 193–207. https://doi.org/10.1111/jmi.12598

Kameda, A., Dvorkin, J., Keehm, Y., Nur, A., Bosl, W., 2006. Permeability-porosity transforms from small sandstone fragments. GEOPHYSICS 71, N11–N19. https://doi.org/10.1190/1.2159054

Kanitpanyacharoen, W., Kets, F.B., Wenk, H.-R., Wirth, R., 2012. Mineral Preferred Orientation and Microstructure in the Posidonia Shale in Relation to Different Degrees of Thermal Maturity. Clays and Clay Minerals 60, 315–329. https://doi.org/10.1346/CCMN.2012.0600308

Kanitpanyacharoen, W., Parkinson, D.Y., De Carlo, F., Marone, F., Stampanoni, M., Mokso, R., MacDowell, A., Wenk, H.-R., 2013. A comparative study of X-ray tomographic microscopy on shales at different synchrotron facilities: ALS, APS and SLS. Journal of Synchrotron Radiation 20, 172–180.

Kanitpanyacharoen, W., Wenk, H.-R., Kets, F.B., Lehr, C., Wirth, R., 2011. Texture and anisotropy analysis of Qusaiba shales. Geophysical Prospecting 59, 536–556. https://doi.org/https://doi.org/10.1111/j.1365-2478.2010.00942.x

Kaufhold, A., Gräsle, W., Plischke, I., Dohrmann, R., Siegesmund, S., 2013. Influence of carbonate content and micro fabrics on the failure strength of the sandy facies of the Opalinus Clay from Mont Terri (Underground Rock Laboratory). Engineering Geology 156, 111–118. https://doi.org/https://doi.org/10.1016/j.enggeo.2013.01.014

Keller, L.M., 2016. Pore geometry effects on elastic properties of Opalinus Clay. GEOPHYSICS 81, D543–D551. https://doi.org/10.1190/geo2015-0452.1

Keller, L.M., Holzer, L., Wepf, R., Gasser, P., 2011. 3D geometry and topology of pore pathways in Opalinus clay: Implications for mass transport. Applied Clay Science 52, 85–95. https://doi.org/https://doi.org/10.1016/j.clay.2011.02.003

Keller, L.M., Schuetz, P., Erni, R., Rossell, M.D., Lucas, F., Gasser, P., Holzer, L., 2013. Characterization of multi-scale microstructural features in Opalinus Clay. Microporous and Mesoporous Materials 170, 83–94. https://doi.org/https://doi.org/10.1016/j.micromeso.2012.11.029

Kern, H., Ivankina, T.I., Nikitin, A.N., Lokajíček, T., Pros, Z., 2008. The effect of oriented microcracks and crystallographic and shape preferred orientation on bulk elastic anisotropy of a foliated biotite gneiss from Outokumpu. Tectonophysics 457, 143–149. https://doi.org/https://doi.org/10.1016/j.tecto.2008.06.015

Ketcham, R.A., 2005a. Three-dimensional grain fabric measurements using high-resolution X-ray computed tomography. Journal of Structural Geology 27, 1217–1228. https://doi.org/10.1016/J.JSG.2005.02.006

Ketcham, R.A., 2005b. Computational methods for quantitative analysis of three-dimensional features in geological specimens. Geosphere 1, 32–41. https://doi.org/10.1130/GES00001.1

Ketcham, R.A., Carlson, W.D., 2001. Acquisition, optimization and interpretation of X-ray computed tomographic imagery: applications to the geosciences. Computers & Geosciences 27, 381–400. https://doi.org/10.1016/S0098-3004(00)00116-3

Ketcham, R.A., Ryan, T.M., 2004. Quantification and visualization of anisotropy in trabecular bone. Journal of Microscopy 213, 158–171. https://doi.org/https://doi.org/10.1111/j.1365-2818.2004.01277.x

Klaver, J., Desbois, G., Urai, J.L., Littke, R., 2012. BIB-SEM study of the pore space morphology in early mature Posidonia Shale from the Hils area, Germany. International Journal of Coal Geology 103, 12–25. https://doi.org/https://doi.org/10.1016/j.coal.2012.06.012

Klinkenberg, M., Kaufhold, S., Dohrmann, R., Siegesmund, S., 2009. Influence of carbonate microfabrics

on the failure strength of claystones. Engineering Geology 107, 42–54. https://doi.org/https://doi.org/10.1016/j.enggeo.2009.04.001

Knackstedt, M.A., Kelly, J., Saadatfar, M., Senden, T., Sok, R.M., 2005. Rock fabric and texture from Digital Core Analysis., SPWLA 46th Annual Logging Symposium.

Kristiansen, K., Valtiner, M., Greene, G.W., Boles, J.R., Israelachvili, J.N., 2011. Pressure solution – The importance of the electrochemical surface potentials. Geochimica et Cosmochimica Acta 75, 6882–6892. https://doi.org/10.1016/J.GCA.2011.09.019

Kuehn, R., Hirt, A.M., Biedermann, A.R., Leiss, B., 2019. Quantitative comparison of microfabric and magnetic fabric in black shales from the Appalachian plateau (western Pennsylvania, U.S.A.). Tectonophysics 765, 161–171. https://doi.org/10.1016/j.tecto.2019.04.013

Kyle, J.R., Ketcham, R.A., 2015. Application of high resolution X-ray computed tomography to mineral deposit origin, evaluation, and processing. Ore Geology Reviews 65, 821–839. https://doi.org/https://doi.org/10.1016/j.oregeorev.2014.09.034

Labaume, P., Meresse, F., Jolivet, M., Teixell, A., Lahfid, A., 2016. Tectonothermal history of an exhumed thrust-sheet-top basin: An example from the south Pyrenean thrust belt. Tectonics 35, 1280–1313. https://doi.org/10.1002/2016TC004192

Labaume, P., Séguret, M., Seyve, C., 1985. Evolution of a turbiditic foreland basin and analogy with an accretionary prism: Example of the Eocene South-Pyrenean Basin. Tectonics 4, 661–685. https://doi.org/10.1029/TC004i007p00661

Lacroix, B., Buatier, M., Labaume, P., Travé, A., Dubois, M., Charpentier, D., Ventalon, S., Convert-Gaubier, D., 2011. Microtectonic and geochemical characterization of thrusting in a foreland basin: Example of the South-Pyrenean orogenic wedge (Spain). Journal of Structural Geology 33, 1359–1377. https://doi.org/10.1016/j.jsg.2011.06.006

Lacroix, B., Tesei, T., Oliot, E., Lahfid, A., Collettini, C., 2015. Early weakening processes inside thrust fault. Tectonics 34, 1396–1411. https://doi.org/10.1002/2014TC003716

Lacroix, B., Travé, A., Buatier, M., Labaume, P., Vennemann, T., Dubois, M., 2014. Syntectonic fluid-flow along thrust faults: Example of the South-Pyrenean fold-and-thrust belt. Marine and Petroleum Geology 49, 84–98. https://doi.org/10.1016/j.marpetgeo.2013.09.005

Lai, P., Moulton, K., Krevor, S., 2015. Pore-scale heterogeneity in the mineral distribution and reactive surface area of porous rocks. Chemical Geology 411, 260–273. https://doi.org/https://doi.org/10.1016/j.chemgeo.2015.07.010

Landis, E.N., Keane, D.T., 2010. X-ray microtomography. Materials Characterization 61, 1305–1316. https://doi.org/https://doi.org/10.1016/j.matchar.2010.09.012

Larrasoaña, J.C., Pueyo, E.L., Parés, J.M., 2004. An integrated AMS, structural, palaeo- and rock-magnetic study of Eocene marine marls from the Jaca-Pamplona basin (Pyrenees, N Spain); new insights into the timing of magnetic fabric acquisition in weakly deformed mudrocks. Geological Society, London, Special Publications 238, 127 LP – 143. https://doi.org/10.1144/GSL.SP.2004.238.01.10

Lash, G.G., 1978. The structure and stratigraphy op the pen argyl member of the Martinsburg formation in Lehigh and Berks Counties, Pennsylvania.

Latham, S., Varslot, T., Sheppard, A., 2008. Image registration: enhancing and calibrating X-ray micro-CT imaging. Proc. of the Soc. Core Analysts, Abu Dhabi, UAE 1–12.

Launeau, P., 2004. Evidence of magmatic flow by 2-D image analysis of 3-D shape preferred orientation

distributions. Bulletin de La Société Géologique de France 175, 331–350. https://doi.org/10.2113/175.4.331

Launeau, P., Archanjo, C.J., Picard, D., Arbaret, L., Robin, P.-Y.F., 2010. Two- and three-dimensional shape fabric analysis by the intercept method in grey levels. Tectonophysics 492, 230–239. https://doi.org/https://doi.org/10.1016/j.tecto.2010.06.005

Launeau, P., Bouchez, J.-L., Benn, K., 1990. Shape preferred orientation of object populations: automatic analysis of digitized images. Tectonophysics 180, 201–211. https://doi.org/10.1016/0040-1951(90)90308-U

Launeau, P., Cruden, A.R., 1998. Magmatic fabric acquisition mechanisms in a syenite: Results of a combined anisotropy of magnetic susceptibility and image analysis study. Journal of Geophysical Research: Solid Earth 103, 5067–5089. https://doi.org/10.1029/97JB02670

Launeau, P., Robin, P.-Y.F., 2005. Determination of fabric and strain ellipsoids from measured sectional ellipses—implementation and applications. Journal of Structural Geology 27, 2223–2233. https://doi.org/10.1016/J.JSG.2005.08.003

Launeau, P., Robin, P.-Y.F., 1996. Fabric analysis using the intercept method. Tectonophysics 267, 91–119. https://doi.org/10.1016/S0040-1951(96)00091-1

Lee, J.H., Ahn, J.H., Peacor, D.R., 1985. Textures in layered silicates; progressive changes through diagenesis and low-temperature metamorphism. Journal of Sedimentary Research 55, 532–540. https://doi.org/10.1306/212F871F-2B24-11D7-8648000102C1865D

Lee, J.H., Peacor, D.R., Lewis, D.D., Wintsch, R.P., 1986. Evidence for syntectonic crystallization for the mudstone to slate transition at Lehigh gap, Pennsylvania, U.S.A. Journal of Structural Geology 8, 767–780. https://doi.org/https://doi.org/10.1016/0191-8141(86)90024-6

Lee, J.H., Peacor, D.R., Lewis, D.D., Wintsch, R.P., 1984. Chlorite-illite/muscovite interlayered and interstratified crystals: A TEM/STEM study. Contributions to Mineralogy and Petrology 88, 372–385. https://doi.org/10.1007/BF00376762

Lin, C.L., Miller, J.D., 2005. 3D characterization and analysis of particle shape using X-ray microtomography (XMT). Powder Technology 154, 61–69. https://doi.org/10.1016/j.powtec.2005.04.031

Lloyd, G.E., Butler, R.W.H., Casey, M., Tatham, D.J., Mainprice, D., 2011. Constraints on the seismic properties of the middle and lower continental crust. Geological Society Special Publication 360, 7–32. https://doi.org/10.1144/SP360.2

Lüneburg, C., Lampert, S.A., Lebit, H., Hirt, A.M., Casey, M., Lowrie, W., 1999. Magnetic anisotropy, rock fabrics and finite strain in deformed sediments of SW Sardinia (Italy). Tectonophysics 307, 51–74. https://doi.org/https://doi.org/10.1016/S0040-1951(99)00118-3

Ma, L., Fauchille, A.-L., Ansari, H., Chandler, M., Ashby, P., Taylor, K.G., Pini, R., Lee, P.D., 2021. Linking multi-scale 3D microstructure to potential enhanced natural gas recovery and subsurface CO2 storage for Bowland shale, UK. Energy & Environmental Science 14, 4481–4498. https://doi.org/10.1039/D0EE03651J

Ma, L., Fauchille, A.-L., Dowey, P.J., Figueroa Pilz, F., Courtois, L., Taylor, K.G., Lee, P.D., 2017. Correlative multi-scale imaging of shales: a review and future perspectives. Geological Society, London, Special Publications 454, 175–199. https://doi.org/10.1144/SP454.11

Ma, L., Taylor, K.G., Lee, P.D., Dobson, K.J., Dowey, P.J., Courtois, L., 2016. Novel 3D centimetre-to nano-scale quantification of an organic-rich mudstone: The Carboniferous Bowland Shale,

Northern England. Marine and Petroleum Geology 72, 193–205. https://doi.org/https://doi.org/10.1016/j.marpetgeo.2016.02.008

Macente, A., Fusseis, F., Menegon, L., Xiao, X., John, T., 2017. The strain-dependent spatial evolution of garnet in a high-P ductile shear zone from the Western Gneiss Region (Norway): a synchrotron X-ray microtomography study. Journal of Metamorphic Geology 35, 565–583. https://doi.org/10.1111/jmg.12245

Martín-Hernández, F., Kunze, K., Julivert, M., Hirt, A.M., 2005. Mathematical simulations of anisotropy of magnetic susceptibility on composite fabrics. Journal of Geophysical Research: Solid Earth 110, 1–12. https://doi.org/10.1029/2004JB003505

Maxwell, J.C., 1962. Origin of Slaty and Fracture Cleavage in the Delaware Water Gap Area, New Jersey and Pennsylvania., Petrologic Studies. https://doi.org/10.1130/Petrologic.1962.281

McBeck, J., Kobchenko, M., Hall, S.A., Tudisco, E., Cordonnier, B., Meakin, P., Renard, F., 2018. Investigating the Onset of Strain Localization Within Anisotropic Shale Using Digital Volume Correlation of Time-Resolved X-Ray Microtomography Images. Journal of Geophysical Research: Solid Earth 123, 7509–7528. https://doi.org/https://doi.org/10.1029/2018JB015676

McCarthy, D.J., Meere, P.A., Petronis, M.S., 2015. A comparison of the effectiveness of clast based finite strain analysis techniques to AMS in sandstones from the Sevier Thrust Belt, Wyoming. Tectonophysics 639, 68–81. https://doi.org/https://doi.org/10.1016/j.tecto.2014.11.014

Mendelson, K.S., Cohen, M.H., 1982. The effect of grain anisotropy on the electrical properties of sedimentary rocks. GEOPHYSICS 47, 257–263. https://doi.org/10.1190/1.1441332

Meyer, E.E., Greene, G.W., Alcantar, N.A., Israelachvili, J.N., Boles, J.R., 2006. Experimental investigation of the dissolution of quartz by a muscovite mica surface: Implications for pressure solution. Journal of Geophysical Research: Solid Earth 111. https://doi.org/10.1029/2005JB004010

Milliken, K.L., 2014. A compositional classification for grain assemblages in fine-grained sediments and sedimentary rocks. Journal of Sedimentary Research 84, 1185–1199. https://doi.org/10.2110/jsr.2014.92

Milliken, K.L., Rudnicki, M., Awwiller, D.N., Zhang, T., 2013. Organic matter-hosted pore system, Marcellus Formation (Devonian), Pennsylvania. AAPG Bulletin 97, 177–200. https://doi.org/10.1306/07231212048

Mitra, G., Yonkee, A., 1985. Relationship of spaced cleavage to folds and thrusts in the Idaho-Utah-Wyoming thrust belt. Journal of Structural Geology 7, 361–373. https://doi.org/10.1016/0191-8141(85)90041-0

Mokhtari, M., Honarpour, M.M., Tutuncu, A.N., Boitnott, G.N., 2016. Characterization of Elastic Anisotropy in Eagle Ford Shale: Impact of Heterogeneity and Measurement Scale. SPE Reservoir Evaluation & Engineering 19, 429–439. https://doi.org/10.2118/170707-PA

Montoya-Araque, E.A., Suarez-Burgoa, L., 2018. Application software in Python 3 for calculating the second-order tensors Jelínek's statistics in anisotropy of magnetic susceptibility data - Software de aplicación en Python 3 para el cálculo de la estadística de tensores de segundo orden de Jelinek en . Boletín de Ciencias de La Tierra 44, 49–58. https://doi.org/10.15446/rbct.n43.70973

Mookerjee, M., Nickleach, S., 2011. Three-dimensional strain analysis using Mathematica. Journal of Structural Geology 33, 1467–1476. https://doi.org/https://doi.org/10.1016/j.jsg.2011.08.003

Morley, C.K., von Hagke, C., Hansberry, R.L., Collins, A.S., Kanitpanyacharoen, W., King, R., 2017.

Review of major shale-dominated detachment and thrust characteristics in the diagenetic zone: Part I, meso- and macro-scopic scale. Earth-Science Reviews 173, 168–228. https://doi.org/10.1016/j.earscirev.2017.07.019

Mulchrone, K.F., 2003. Application of Delaunay triangulation to the nearest neighbour method of strain analysis. Journal of Structural Geology 25, 689–702. https://doi.org/https://doi.org/10.1016/S0191-8141(02)00067-6

Mulchrone, K.F., Choudhury, K.R., 2004. Fitting an ellipse to an arbitrary shape: implications for strain analysis. Journal of Structural Geology 26, 143–153. https://doi.org/https://doi.org/10.1016/S0191-8141(03)00093-2

Mulchrone, K.F., O'Sullivan, F., Meere, P.A., 2003. Finite strain estimation using the mean radial length of elliptical objects with bootstrap confidence intervals. Journal of Structural Geology 25, 529–539. https://doi.org/https://doi.org/10.1016/S0191-8141(02)00049-4

Mutti, E., 1983. The Hecho Eocene submarine fan system, south-central Pyrenees, Spain. Geo-Marine Letters 3, 199–202. https://doi.org/10.1007/BF02462468

Mutti, E., 1977. Distinctive thin-bedded turbidite facies and related depositional environments in the Eocene Hecho Group (South-central Pyrenees, Spain). Sedimentology 24, 107–131. https://doi.org/10.1111/j.1365-3091.1977.tb00122.x

Nichols, G., 2009. Sedimentology and stratigraphy. John Wiley & Sons.

Oertel, G., 1983. The relationship of strain and preferred orientation of phyllosilicate grains in rocks—a review. Tectonophysics 100, 413–447. https://doi.org/https://doi.org/10.1016/0040-1951(83)90197-X

Oliva-Urcia, B., 2018. Thirty years (1988-2018) of advances in the knowledge of the structural evolution of the south-central Pyrenees during the Cenozoic collision, a summary. Revista de La Sociedad Geologica de Espana 31, 51–68.

Oliva-Urcia, B., Larrasoaña, J.C., Pueyo, E.L., Gil Imaz, A., Mata, P., Parés, J.M., Schleicher, A.M., Pueyo-Anchuela, Ó., 2009. Disentangling magnetic subfabrics and their link to deformation processes in cleaved sedimentary rocks from the Internal Sierras (west central Pyrenees, Spain). Journal of Structural Geology 31, 163–176. https://doi.org/10.1016/j.jsg.2008.11.002

Ollion, J., Cochennec, J., Loll, F., Escudé, C., Boudier, T., 2013. TANGO: A generic tool for high-throughput 3D image analysis for studying nuclear organization. Bioinformatics 29, 1840–1841. https://doi.org/10.1093/bioinformatics/btt276

Otsu, N., 1979. Threshold Selection Method From Gray-Level Histograms. IEEE Trans Syst Man Cybern SMC-9, 62–66. https://doi.org/10.1109/tsmc.1979.4310076

Ougier-Simonin, A., Renard, F., Boehm, C., Vidal-Gilbert, S., 2016. Microfracturing and microporosity in shales. Earth-Science Reviews 162, 198–226. https://doi.org/https://doi.org/10.1016/j.earscirev.2016.09.006

Parés, J.M., 2015. Sixty years of anisotropy of magnetic susceptibility in deformed sedimentary rocks ., Frontiers in Earth Science .

Parés, J.M., 2004. How deformed are weakly deformed mudrocks? Insights from magnetic anisotropy. Geological Society Special Publication 238, 191–203. https://doi.org/10.1144/GSL.SP.2004.238.01.13

Parés, J.M., Anastasio, D.J., 2018. The extent of penetrative pyrenean deformation in the ebro foreland basin: Magnetic fabric data from the eastern sector. Geologica Acta 16, 375–390.

https://doi.org/10.1344/GeologicaActa2018.16.4.3

Parés, J.M., Dinarès-Turell, J., 1993. Magnetic Fabric in Two Sedimentary Rock-Types from the Southern Pyrenees. Journal of Geomagnetism and Geoelectricity 45, 193–205. https://doi.org/10.5636/jgg.45.193

Parés, J.M., van der Pluijm, B.A., 2002. Evaluating magnetic lineations (AMS) in deformed rocks. Tectonophysics 350, 283–298. https://doi.org/10.1016/S0040-1951(02)00119-1

Parés, J.M., van der Pluijm, B.A., Dinarès-Turell, J., 1999. Evolution of magnetic fabrics during incipient deformation of mudrocks (Pyrenees, northern Spain). Tectonophysics 307, 1–14. https://doi.org/https://doi.org/10.1016/S0040-1951(99)00115-8

Paris, R., Falvard, S., Chagué, C., Goff, J., Etienne, S., Doumalin, P., 2020. Sedimentary fabric characterized by X-ray tomography: A case-study from tsunami deposits on the Marquesas Islands, French Polynesia. Sedimentology 67, 1207–1229. https://doi.org/https://doi.org/10.1111/sed.12582

Passchier, C.W., Trouw, R.A.J., 2005. Microtectonics. Springer Berlin Heidelberg.

Patterson, B.M., Escobedo-Diaz, J.P., Dennis-Koller, D., Cerreta, E., 2012. Dimensional Quantification of Embedded Voids or Objects in Three Dimensions Using X-Ray Tomography. Microscopy and Microanalysis 18, 390–398. https://doi.org/DOI: 10.1017/S1431927611012554

Perona, P., Malik, J., 1990. Scale-space and edge detection using anisotropic diffusion. IEEE Transactions on Pattern Analysis and Machine Intelligence 12, 629–639. https://doi.org/10.1109/34.56205

Peternell, M., Hasalová, P., Wilson, C.J.L., Piazolo, S., Schulmann, K., 2010. Evaluating quartz crystallographic preferred orientations and the role of deformation partitioning using EBSD and fabric analyser techniques. Journal of Structural Geology 32, 803–817. https://doi.org/10.1016/j.jsg.2010.05.007

Petri, B., Almqvist, B.S.G., Pistone, M., 2020. 3D rock fabric analysis using micro-tomography: An introduction to the open-source TomoFab MATLAB code. Computers & Geosciences 138, 104444. https://doi.org/https://doi.org/10.1016/j.cageo.2020.104444

Pokorný, J., Pokorný, P., Suza, P., Hrouda, F., 2011. A Multi-Function Kappabridge for High Precision Measurement of the AMS and the Variations of Magnetic Susceptibility with Field, Temperature and Frequency. In: Petrovský, E., Ivers, D., Harinarayana, T., Herrero-Bervera, E. (Eds.), The Earth's Magnetic Interior. Springer Netherlands, Dordrecht, 293–301. https://doi.org/10.1007/978-94-007-0323-0_20

Porter, M.L., Wildenschild, D., 2010. Image analysis algorithms for estimating porous media multiphase flow variables from computed microtomography data: A validation study. Computational Geosciences 14, 15–30. https://doi.org/10.1007/s10596-009-9130-5

Powell, C.M., 1979. A morphological classification of rock cleavage. Tectonophysics 58, 21–34. https://doi.org/10.1016/0040-1951(79)90320-2

Přikryl, R., 2001. Some microstructural aspects of strength variation in rocks. International Journal of Rock Mechanics and Mining Sciences 38, 671–682. https://doi.org/https://doi.org/10.1016/S1365-1609(01)00031-4

Prior, D.J., Boyle, A.P., Brenker, F., Cheadle, M.C., Austin, D., Lopez, G., Peruzzo, L., Potts, G.J., Reddy, S., Spiess, R., Timms, N.E., Trimby, P., Wheeler, J., Zetterström, L., 1999. The application of electron backscatter diffraction and orientation contrast imaging in the SEM to textural problems

in rocks. American Mineralogist 84, 1741–1759. https://doi.org/10.2138/am-1999-11-1204

Prior, D.J., Mariani, E., Wheeler, J., 2009. EBSD in the earth sciences: Applications, common practice, and challenges. In: Schwartz, A.J., Kumar, M., Adams, B.L., Field, D.P. (Eds.), Electron Backscatter Diffraction in Materials Science. Springer US, Boston, MA, 345–360. https://doi.org/10.1007/978-0-387-88136-2_26

Pueyo-Anchuela, Ó., Casas-Sainz, A.M., Pueyo, E.L., Juan, A.P., Imaz, A.G., 2013. Analysis of the ferromagnetic contribution to the susceptibility by low field and high field methods in sedimentary rocks of the Southern Pyrenees and Northern Ebro foreland basin (Spain). Terra Nova 25, 307–314. https://doi.org/10.1111/ter.12037

Pueyo-Anchuela, Ó., Gil Imaz, A., Pocoví Juan, A., 2012. Factors affecting the record of strain fabrics at the anisotropy of magnetic susceptibility: West-Central South-Pyrenean cleavage domain (Southern Pyrenees; NE Spain). Tectonophysics 554–557, 1–17. https://doi.org/10.1016/j.tecto.2012.05.028

Pueyo-Anchuela, Ó., Gil Imaz, A., Pocoví Juan, A., 2010. Significance of AMS in multilayer systems in fold-and-thrust belts. A case study from the Eocene turbidites in the Southern Pyrenees (Spain). Geological Journal 45, 544–561. https://doi.org/10.1002/gj.1194

Pueyo-Anchuela, Ó., María Casas-Sainz, A., Pocoví Juan, A., Gil Imaz, A., 2011. Lithology-dependent reliability of AMS analysis: A case study of the Eocene turbidities in the southern Pyrenees (Aragón, Spain). Comptes Rendus Geoscience 343, 11–19. https://doi.org/https://doi.org/10.1016/j.crte.2010.11.003

Puigdefábregas, C., 1975. La sedimentación molásica en la cuenca de Jaca. Pirineos, Jaca Monografía, 1–188.

Ramachandran, G.N., Lakshminarayanan, A. V., 1971. Three-dimensional Reconstruction from Radiographs and Electron Micrographs: Application of Convolutions instead of Fourier Transforms. Proceedings of the National Academy of Sciences 68, 2236–2240. https://doi.org/10.1073/PNAS.68.9.2236

Ramos, M.J., Espinoza, D.N., Goldfarb, E.J., Tisato, N., Laubach, S.E., Torres-Verdín, C., 2019. Microstructural controls on elastic anisotropy of finely laminated Mancos Shale. Geophysical Journal International 216, 991–1004. https://doi.org/10.1093/gji/ggy474

Raynaud, S., Fabre, D., Mazerolle, F., Geraud, Y., Latière, H.J., 1989. Analysis of the internal structure of rocks and characterization of mechanical deformation by a non-destructive method: X-ray tomodensitometry. Tectonophysics 159, 149–159. https://doi.org/https://doi.org/10.1016/0040-1951(89)90176-5

Renard, F., Ortoleva, P., Gratier, J.-P., 1997. Pressure solution in sandstones: Influence of clays and dependence on temperature and stress. Tectonophysics 280, 257–266. https://doi.org/10.1016/S0040-1951(97)00039-5

Robin, P.-Y.F., 2002. Determination of fabric and strain ellipsoids from measured sectional ellipses — theory. Journal of Structural Geology 24, 531–544. https://doi.org/10.1016/S0191-8141(01)00081-5

Robin, P.-Y.F., Jowett, E.C., 1986. Computerized density contouring and statistical evaluation of orientation data using counting circles and continuous weighting functions. Tectonophysics 121, 207–223. https://doi.org/10.1016/0040-1951(86)90044-2

Robinet, J.-C., Sardini, P., Coelho, D., Parneix, J.-C., Prêt, D., Sammartino, S., Boller, E., Altmann, S., 2012. Effects of mineral distribution at mesoscopic scale on solute diffusion in a clay-rich rock:

Example of the Callovo-Oxfordian mudstone (Bure, France). Water Resources Research 48. https://doi.org/https://doi.org/10.1029/2011WR011352

Robion, P., Grelaud, S., Frizon de Lamotte, D., 2007. Pre-folding magnetic fabrics in fold-and-thrust belts: Why the apparent internal deformation of the sedimentary rocks from the Minervois basin (NE — Pyrenees, France) is so high compared to the Potwar basin (SW — Himalaya, Pakistan)? Sedimentary Geology 196, 181–200. https://doi.org/https://doi.org/10.1016/j.sedgeo.2006.08.007

Rochette, P., 1988. Inverse magnetic fabric in carbonate-bearing rocks. Earth and Planetary Science Letters 90, 229–237. https://doi.org/https://doi.org/10.1016/0012-821X(88)90103-3

Rochette, P., 1987. Magnetic susceptibility of the rock matrix related to magnetic fabric studies. Journal of Structural Geology 9, 1015–1020. https://doi.org/https://doi.org/10.1016/0191-8141(87)90009-5

Rochette, P., Jackson, M., Aubourg, C., 1992. Rock magnetism and the interpretation of anisotropy of magnetic susceptibility. Reviews of Geophysics 30, 209–226. https://doi.org/https://doi.org/10.1029/92RG00733

Russ, J., Neal, F., Neal, F.B., 2015. The Image Processing Handbook, Seventh Edition. CRC Press. https://doi.org/10.1201/b18983

Safonov, I., Yakimchuk, I., Abashkin, V., 2018. Algorithms for 3D Particles Characterization Using X-Ray Microtomography in Proppant Crush Test., Journal of Imaging . https://doi.org/10.3390/jimaging4110134

Sak, P.B., McQuarrie, N., Oliver, B.P., Lavdovsky, N., Jackson, M.S., 2012. Unraveling the central Appalachian fold-thrust belt, Pennsylvania: The power of sequentially restored balanced cross sections for a blind fold-thrust belt. Geosphere 8, 685–702. https://doi.org/10.1130/GES00676.1

Saur, H., Moonen, P., Aubourg, C., 2021. Grain Fabric Heterogeneity in Strained Shales: Insights From XCT Measurements. Journal of Geophysical Research: Solid Earth 126, e2021JB022025. https://doi.org/https://doi.org/10.1029/2021JB022025

Saur, H., Sénéchal, P., Boiron, T., Aubourg, C., Derluyn, H., Moonen, P., 2020. First investigation of quartz and calcite shape fabrics in strained shales by means of X-ray tomography. Journal of Structural Geology 130. https://doi.org/10.1016/j.jsg.2019.103905

Sayab, M., Miettinen, A., Aerden, D., Karell, F., 2017. Orthogonal switching of AMS axes during type-2 fold interference: Insights from integrated X-ray computed tomography, AMS and 3D petrography. Journal of Structural Geology 103, 1–16. https://doi.org/10.1016/J.JSG.2017.09.002

Sayab, M., Suuronen, J.-P., Hölttä, P., Aerden, D., Lahtinen, R., Kallonen, A.P., 2015. High-resolution X-ray computed microtomography: A holistic approach to metamorphic fabric analyses. Geology 43, 55–58. https://doi.org/10.1130/G36250.1

Schellart, W., 2002. Alpine deformation at the western termination of the axial zone, Southern Pyrenees. Journal of The Virtual Explorer 08. https://doi.org/10.3809/jvirtex.2002.00055

Schindelin, J., Arganda-Carreras, I., Frise, E., Kaynig, V., Longair, M., Pietzsch, T., Preibisch, S., Rueden, C., Saalfeld, S., Schmid, B., Tinevez, J.-Y., White, D.J., Hartenstein, V., Eliceiri, K.W., Tomancak, P., Cardona, A., 2012. Fiji: an open-source platform for biological-image analysis. Nature Methods 9, 676–682. https://doi.org/10.1038/nmeth.2019

Schlüter, S., Sheppard, A., Brown, K., Wildenschild, D., 2014. Image processing of multiphase images obtained via X-ray microtomography: A review. Water Resources Research 50, 3615–3639.

https://doi.org/10.1002/2014WR015256

Schmidt, V., Hirt, A.M., Rosselli, P., Martín-Hernández, F., 2007. Separation of diamagnetic and paramagnetic anisotropy by high-field, low-temperature torque measurements. Geophysical Journal International 168, 40–47. https://doi.org/10.1111/j.1365-246X.2006.03202.x

Schmidt, W., 1925. XXIII. Gefügestatistik. Tschermaks Mineralogische Und Petrographische Mitteilungen 38, 392–423. https://doi.org/10.1007/BF02993943

Schöpa, A., Floess, D., de Saint Blanquat, M., Annen, C., Launeau, P., 2015. The relation between magnetite and silicate fabric in granitoids of the Adamello Batholith. Tectonophysics 642, 1–15. https://doi.org/https://doi.org/10.1016/j.tecto.2014.11.022

Schuster, V., Rybacki, E., Bonnelye, A., Herrmann, J., Schleicher, A.M., Dresen, G., 2021. Experimental Deformation of Opalinus Clay at Elevated Temperature and Pressure Conditions: Mechanical Properties and the Influence of Rock Fabric. Rock Mechanics and Rock Engineering 54, 4009–4039. https://doi.org/10.1007/s00603-021-02474-3

Schwarz, S., Stöckhert, B., 1996. Pressure solution in siliciclastic HP-LT metamorphic rocks — constraints on the state of stress in deep levels of accretionary complexes. Tectonophysics 255, 203–209. https://doi.org/https://doi.org/10.1016/0040-1951(95)00137-9

Serra, J., Vincent, L., 1992. An overview of morphological filtering. Circuits Systems and Signal Processing 11, 47–108. https://doi.org/10.1007/BF01189221

Siegesmund, S., Dürrast, H., 2014. Physical and mechanical properties of rocks. In: Siegesmund, Siegfried, Snethlage, R. (Eds.), Stone in Architecture: Properties, Durability: Fifth Edition. Springer Berlin Heidelberg, Berlin, Heidelberg, 97–224. https://doi.org/10.1007/978-3-642-45155-3_3

Siegesmund, S., Török, Á., 2014. Building stones. In: Siegesmund, Siegfried, Snethlage, R. (Eds.), Stone in Architecture: Properties, Durability: Fifth Edition. Springer Berlin Heidelberg, Berlin, Heidelberg, 11–95. https://doi.org/10.1007/978-3-642-45155-3_2

Sittner, J., Godinho, J.R.A., Renno, A.D., Cnudde, V., Boone, M.N., De Schryver, T., Van Loo, D., Merkulova, M., Roine, A., Liipo, J., 2021. Spectral X-ray computed micro tomography: 3-dimensional chemical imaging. X-Ray Spectrometry 50, 92–105. https://doi.org/https://doi.org/10.1002/xrs.3200

Sok, R.M., Knackstedt, M.A., Varslot, T., Ghous, A., Latham, S., Sheppard, A., 2010. Pore Scale Characterization of Carbonates At Multiple Scales: Integration of Micro-CT, BSEM, And FIBSEM. Petrophysics - The SPWLA Journal of Formation Evaluation and Reservoir Description 51.

Sone, H., Zoback, M.D., 2013. Mechanical properties of shale-gas reservoir rocks — Part 1: Static and dynamic elastic properties and anisotropy. GEOPHYSICS 78, D381–D392. https://doi.org/10.1190/geo2013-0050.1

Stallard, A., Shelley, D., 1995. Quartz c-axes parallel to stretching directions in very low-grade metamorphic rocks. Tectonophysics 249, 31–40. https://doi.org/10.1016/0040-1951(95)00040-T

Stamatakos, J., Hirt, A.M., Lowrie, W., 1996. The age and timing of folding in the central Appalachians from paleomagnetic results. GSA Bulletin 108, 815–829. https://doi.org/10.1130/0016-7606(1996)108<0815:TAATOF>2.3.CO;2

Stephenson, A., 1994. Distribution anisotropy: two simple models for magnetic lineation and foliation. Physics of the Earth and Planetary Interiors 82, 49–53. https://doi.org/https://doi.org/10.1016/0031-9201(94)90101-5

Studýnka, J., Chadima, M., Suza, P., 2014. Fully automated measurement of anisotropy of magnetic susceptibility using 3D rotator. Tectonophysics 629, 6–13. https://doi.org/https://doi.org/10.1016/j.tecto.2014.02.015

Suuronen, J.-P., Sayab, M., 2018. 3D nanopetrography and chemical imaging of datable zircons by synchrotron multimodal X-ray tomography. Scientific Reports 8, 4747. https://doi.org/10.1038/s41598-018-22891-9

Tarling, D., Hrouda, F., 1993. Magnetic anisotropy of rocks. Springer Science & Business Media.

Thissen, C.J., Brandon, M.T., 2015. An autocorrelation method for three-dimensional strain analysis. Journal of Structural Geology 81, 135–154. https://doi.org/https://doi.org/10.1016/j.jsg.2015.09.001

Tournier, F., 2010. Mécanismes et contrôle des phénomènes diagénétiques en milieu acide dans les grès de l'Ordovicien glaciaire du bassin de Sbaa, Algérie.

Trepmann, C.A., Stöckhert, B., 2009. Microfabric of folded quartz veins in metagreywackes: Dislocation creep and subgrain rotation at high stress. Journal of Metamorphic Geology 27, 555–570. https://doi.org/10.1111/j.1525-1314.2009.00842.x

Tsai, W.H., 1985. Moment-preserving thresholding: a new approach. Computer Vision, Graphics, & Image Processing 29, 377–393. https://doi.org/10.1016/0734-189x(85)90133-1

Ulm, F.J., Delafargue, A., Constantinides, G., 2005. Experimental Microporomechanics. In: Dormieux, L., Ulm, F.-J. (Eds.), CISM International Centre for Mechanical Sciences, Courses and Lectures. Springer Vienna, Vienna, 207–288. https://doi.org/10.1007/3-211-38046-9_7

Valcke, S.L.A., Casey, M., Lloyd, G.E., Kendall, J.M., Fisher, Q.J., 2006. Lattice preferred orientation and seismic anisotropy in sedimentary rocks. Geophysical Journal International 166, 652–666. https://doi.org/10.1111/j.1365-246X.2006.02987.x

van der Pluijm, B.A., Ho, N.-C., Peacor, D.R., 1994. High-resolution X-ray texture goniometry. Journal of Structural Geology 16, 1029–1032. https://doi.org/https://doi.org/10.1016/0191-8141(94)90084-1

van der Pluijm, B.A., Ho, N.-C., Peacor, D.R., Merriman, R.J., 1998. Contradictions of slate formation resolved? Nature 392, 348.

Vasin, R.N., Wenk, H.-R., Kanitpanyacharoen, W., Matthies, S., Wirth, R., 2013. Elastic anisotropy modeling of Kimmeridge shale. Journal of Geophysical Research: Solid Earth 118, 3931–3956. https://doi.org/https://doi.org/10.1002/jgrb.50259

Vega, B., Dutta, A., Kovscek, A.R., 2014. CT Imaging of Low-Permeability, Dual-Porosity Systems Using High X-ray Contrast Gas. Transport in Porous Media 101, 81–97. https://doi.org/10.1007/s11242-013-0232-0

Vernik, L., Liu, X., 1997. Velocity anisotropy in shales: A petrophysical study. GEOPHYSICS 62, 521–532. https://doi.org/10.1190/1.1444162

Vincent, L., Vincent, L., Soille, P., 1991. Watersheds in Digital Spaces: An Efficient Algorithm Based on Immersion Simulations. IEEE Transactions on Pattern Analysis and Machine Intelligence 13, 583–598. https://doi.org/10.1109/34.87344

Voltolini, M., Ajo-Franklin, J., 2020. Evolution of propped fractures in shales: The microscale controlling factors as revealed by in situ X-Ray microtomography. Journal of Petroleum Science and Engineering 188, 106861. https://doi.org/https://doi.org/10.1016/j.petrol.2019.106861

Voltolini, M., Wenk, H.-R., Mondol, N.H., Bjørlykke, K., Jahren, J., 2008. Anisotropy of experimentally compressed kaolinite-illite-quartz mixtures. GEOPHYSICS 74, D13–D23. https://doi.org/10.1190/1.3002557

Voltolini, M., Zandomeneghi, D., Mancini, L., Polacci, M., 2011. Texture analysis of volcanic rock samples: Quantitative study of crystals and vesicles shape preferred orientation from X-ray microtomography data. Journal of Volcanology and Geothermal Research 202, 83–95. https://doi.org/https://doi.org/10.1016/j.jvolgeores.2011.02.003

Wadell, H., 1932. Volume, Shape, and Roundness of Rock Particles. The Journal of Geology 40, 443–451. https://doi.org/10.1086/623964

Wang, L., Park, J.Y., Fu, Y., 2007. Representation of real particles for DEM simulation using X-ray tomography. Construction and Building Materials 21, 338–346. https://doi.org/10.1016/j.conbuildmat.2005.08.013

Weil, A.B., Yonkee, A., 2009. Anisotropy of magnetic susceptibility in weakly deformed red beds from the Wyoming salient, Sevier thrust belt: Relations to layer-parallel shortening and orogenic curvature. Lithosphere 1, 235–256. https://doi.org/10.1130/L42.1

Wenk, H.-R., Houtte, P. Van, 2004. Texture and anisotropy. Reports on Progress in Physics 67, 1367–1428. https://doi.org/10.1088/0034-4885/67/8/r02

Wenk, H.-R., Kanitpanyacharoen, W., Ren, Y., 2019. Slate – A new record for crystal preferred orientation. Journal of Structural Geology 125, 319–324. https://doi.org/https://doi.org/10.1016/j.jsg.2017.12.009

Wenk, H.-R., Kanitpanyacharoen, W., Voltolini, M., 2010. Preferred orientation of phyllosilicates: Comparison of fault gouge, shale and schist. Journal of Structural Geology 32, 478–489. https://doi.org/https://doi.org/10.1016/j.jsg.2010.02.003

Wenk, H.-R., Lonardelli, I., Franz, H., Nihei, K., Nakagawa, S., 2007. Preferred orientation and elastic anisotropy of illite-rich shale. Geophysics 72, E69–E75. https://doi.org/10.1190/1.2432263

Wenk, H.-R., Voltolini, M., Mazurek, M., Van Loon, L.R., Vinsot, A., 2008. Preferred orientations and anisotropy in shales: Callovo-oxfordian shale (France) and opalinus clay (Switzerland). Clays and Clay Minerals 56, 285–306. https://doi.org/10.1346/CCMN.2008.0560301

Wenk, H.-R., Yu, R., Cárdenes, V., Lopez-Sanchez, M.A., Sintubin, M., 2020. Fabric and anisotropy of slates: From classical studies to new results. Journal of Structural Geology 138, 104066. https://doi.org/https://doi.org/10.1016/j.jsg.2020.104066

Wennberg, O.P., Rennan, L., 2018. A brief introduction to the use of X-ray computed tomography (CT) for analysis of natural deformation structures in reservoir rocks. Geological Society, London, Special Publications 459, 101 LP – 120. https://doi.org/10.1144/SP459.10

Weyl, P.K., 1959. Pressure solution and the force of crystallization: a phenomenological theory. Journal of Geophysical Research 64, 2001–2025. https://doi.org/10.1029/JZ064i011p02001

Wildenschild, D., Sheppard, A., 2013. X-ray imaging and analysis techniques for quantifying pore-scale structure and processes in subsurface porous medium systems. Advances in Water Resources 51, 217–246. https://doi.org/https://doi.org/10.1016/j.advwatres.2012.07.018

Wildenschild, D., Vaz, C.M.P., Rivers, M.L., Rikard, D., Christensen, B.S.B., 2002. Using X-ray computed tomography in hydrology: systems, resolutions, and limitations. Journal of Hydrology 267, 285–297. https://doi.org/https://doi.org/10.1016/S0022-1694(02)00157-9

Wintsch, R.P., 1978. A chemical approach to the preferred orientation of mica. Bulletin of the

Geological Society of America 89, 1715–1718. https://doi.org/10.1130/0016-7606(1978)89<1715:ACATTP>2.0.CO;2

Wintsch, R.P., Kunk, M.J., Epstein, J.B., 1996. 40Ar/39Ar whole-rock data constraints on Acadian diagenesis and Alleghanian cleavage in the Martinsburg Formation, eastern Pennsylvania. American Journal of Science 296, 766–788.

Wintsch, R.P., Kvale, C.M., Kisch, H.J., 1991. Open-system, constant-volume development of slaty cleavage, and strain-induced replacement reactions in the Martinsburg Formation, Lehigh Gap, Pennsylvania. Geological Society of America Bulletin 103, 916–927. https://doi.org/10.1130/0016-7606(1991)103<0916:OSCVDO>2.3.CO;2

Wirjadi, O., 2007. Survey of 3d image segmentation methods, Berichte des Fraunhofer-Instituts für Techno- und Wirtschaftsmathematik (ITWM Report) - 123 .

Withers, P.J., Bouman, C., Carmignato, S., Cnudde, V., Grimaldi, D., Hagen, C.K., Maire, E., Manley, M., Du Plessis, A., Stock, S.R., 2021. X-ray computed tomography. Nature Reviews Methods Primers 1, 18. https://doi.org/10.1038/s43586-021-00015-4

Woodland, B.G., 1982. Gradational development of domainal slaty cleavage, its origin and relation to chlorite porphyroblasts in the Martinsburg Formation, eastern Pennsylvania. Tectonophysics 82, 89–124. https://doi.org/https://doi.org/10.1016/0040-1951(82)90090-7

Wright, S.I., Nowell, M.M., Field, D.P., 2011. A review of strain analysis using electron backscatter diffraction. Microscopy and Microanalysis 17, 316–329. https://doi.org/10.1017/S1431927611000055

Wright, T.O., Platt, L.B., 1982. Pressure dissolution and cleavage in the Martinsburg Shale. American Journal of Science 282, 122 LP – 135. https://doi.org/10.2475/ajs.282.2.122

Yun, T.S., Jeong, Y.J., Kim, K.Y., Min, K.B., 2013. Evaluation of rock anisotropy using 3D X-ray computed tomography. Engineering Geology 163, 11–19. https://doi.org/10.1016/j.enggeo.2013.05.017

Zhao, B., Wang, J., 2016. 3D quantitative shape analysis on form, roundness, and compactness with μCT. Powder Technology 291, 262–275. https://doi.org/10.1016/j.powtec.2015.12.029

Zucali, M., Voltolini, M., Ouladdiaf, B., Mancini, L., Chateigner, D., 2014. The 3D quantitative lattice and shape preferred orientation of a mylonitised metagranite from Monte Rosa (Western Alps): Combining neutron diffraction texture analysis and synchrotron X-ray microtomography. Journal of Structural Geology 63, 91–105. https://doi.org/10.1016/J.JSG.2014.02.011

Supplementary information

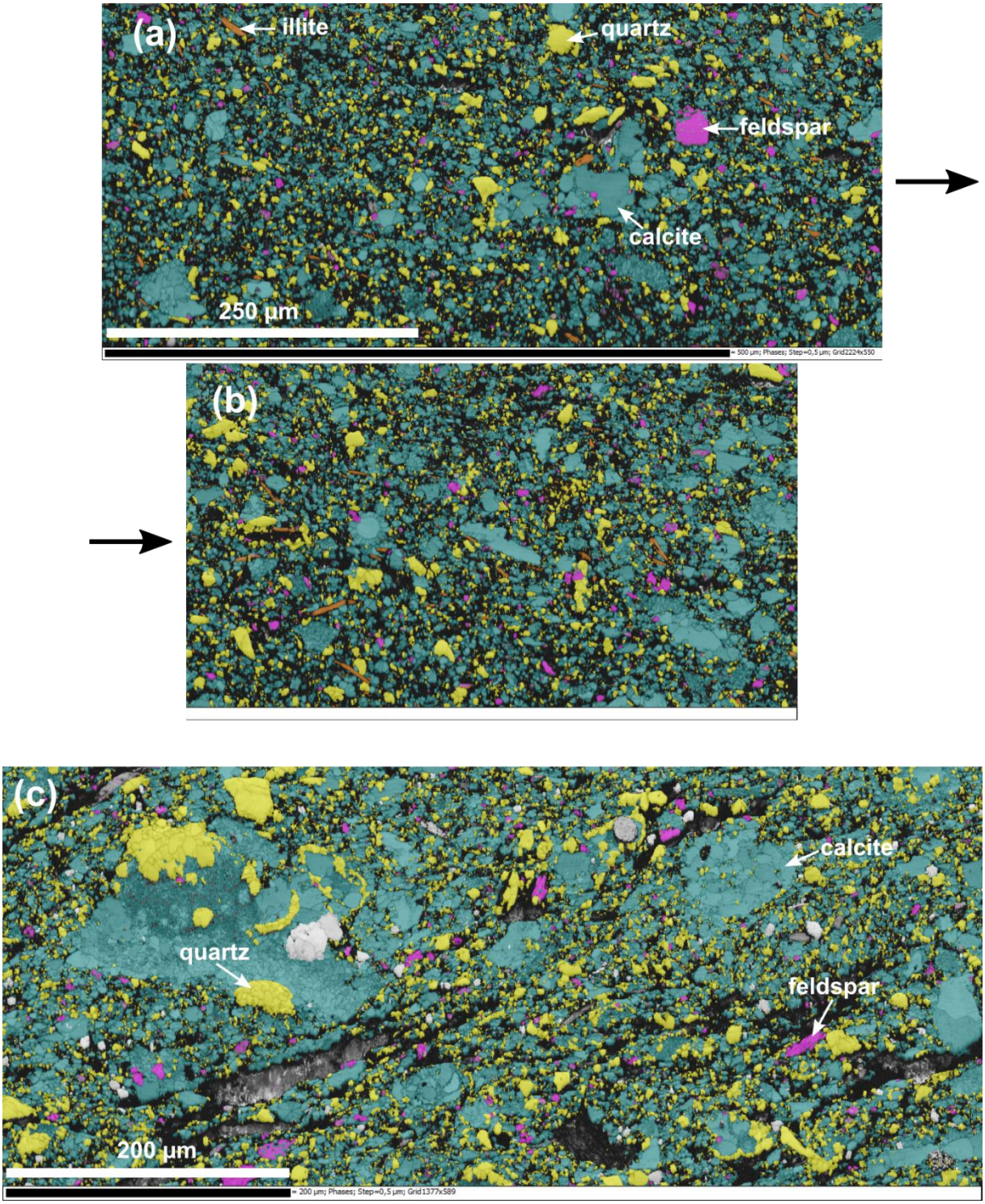

Figure supp 1 : *(a) and (b) EBSD phase map of sample A2. (c) EBSD phase map of sample A5.*

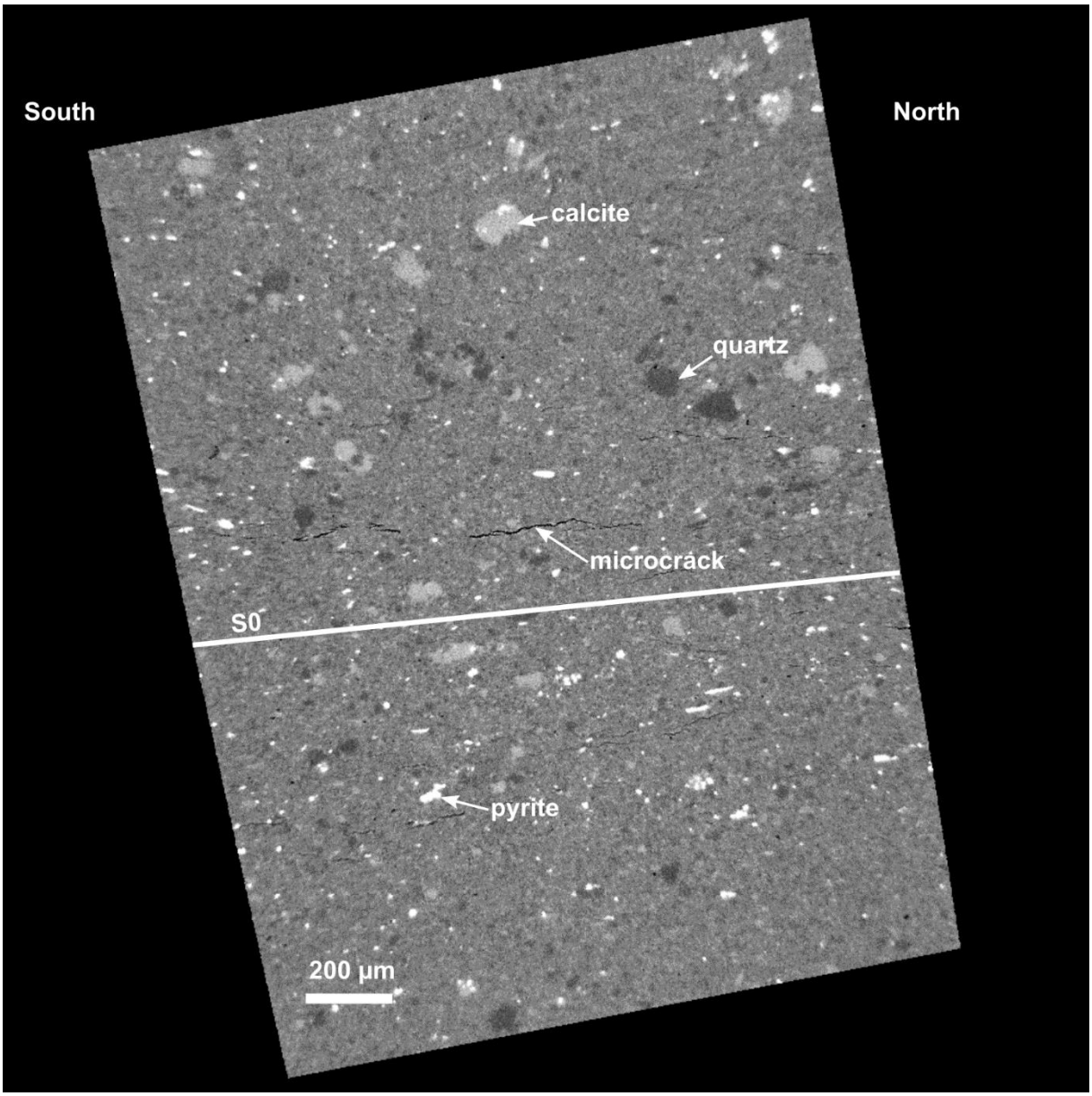

Figure supp 2 : *2D slice view of sample A1-2 in geographic coordinate system. S0 = bedding.*

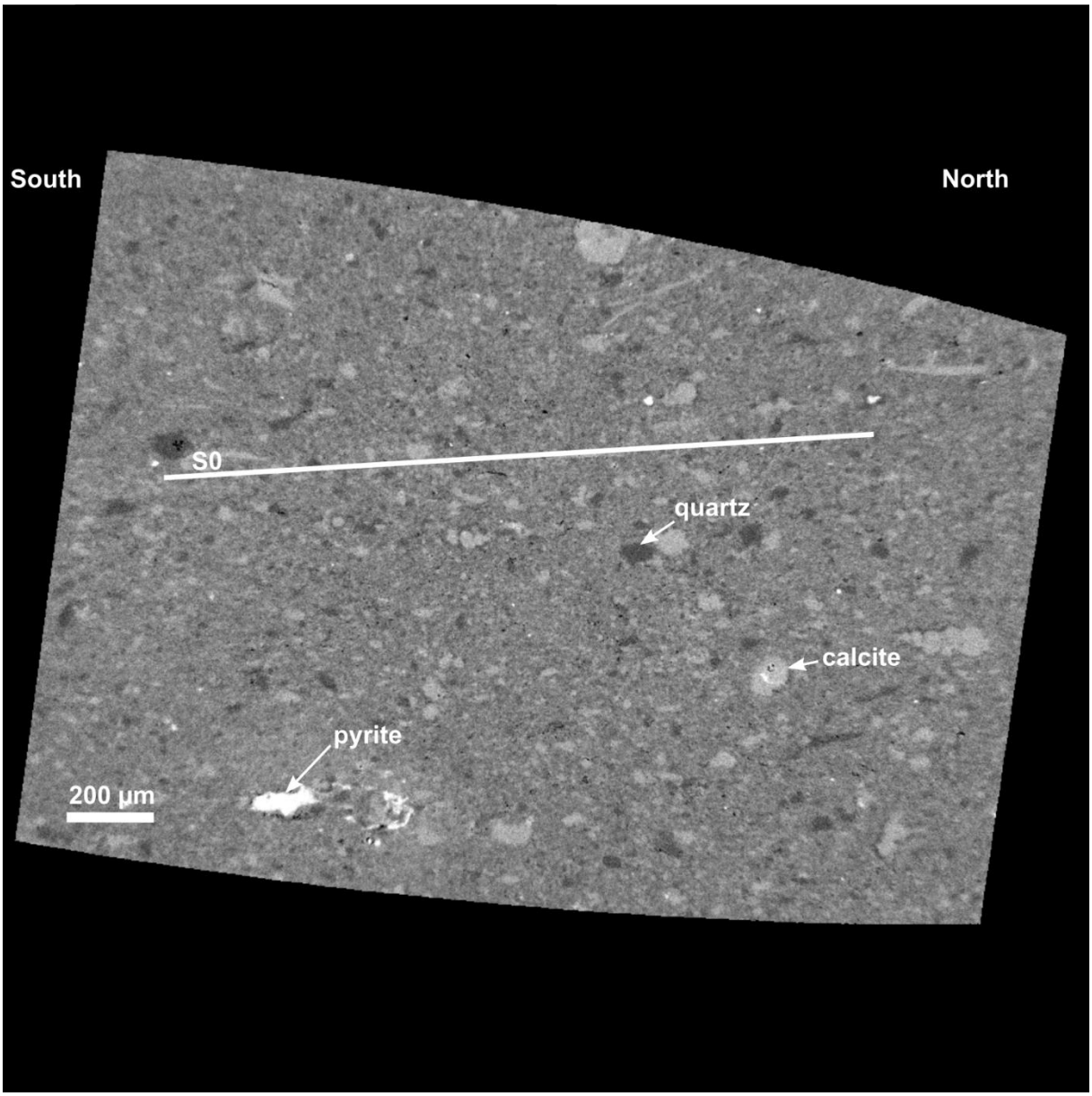

Figure supp 3 : *2D slice view of sample A2-2 in geographic coordinate system. S0 = bedding.*

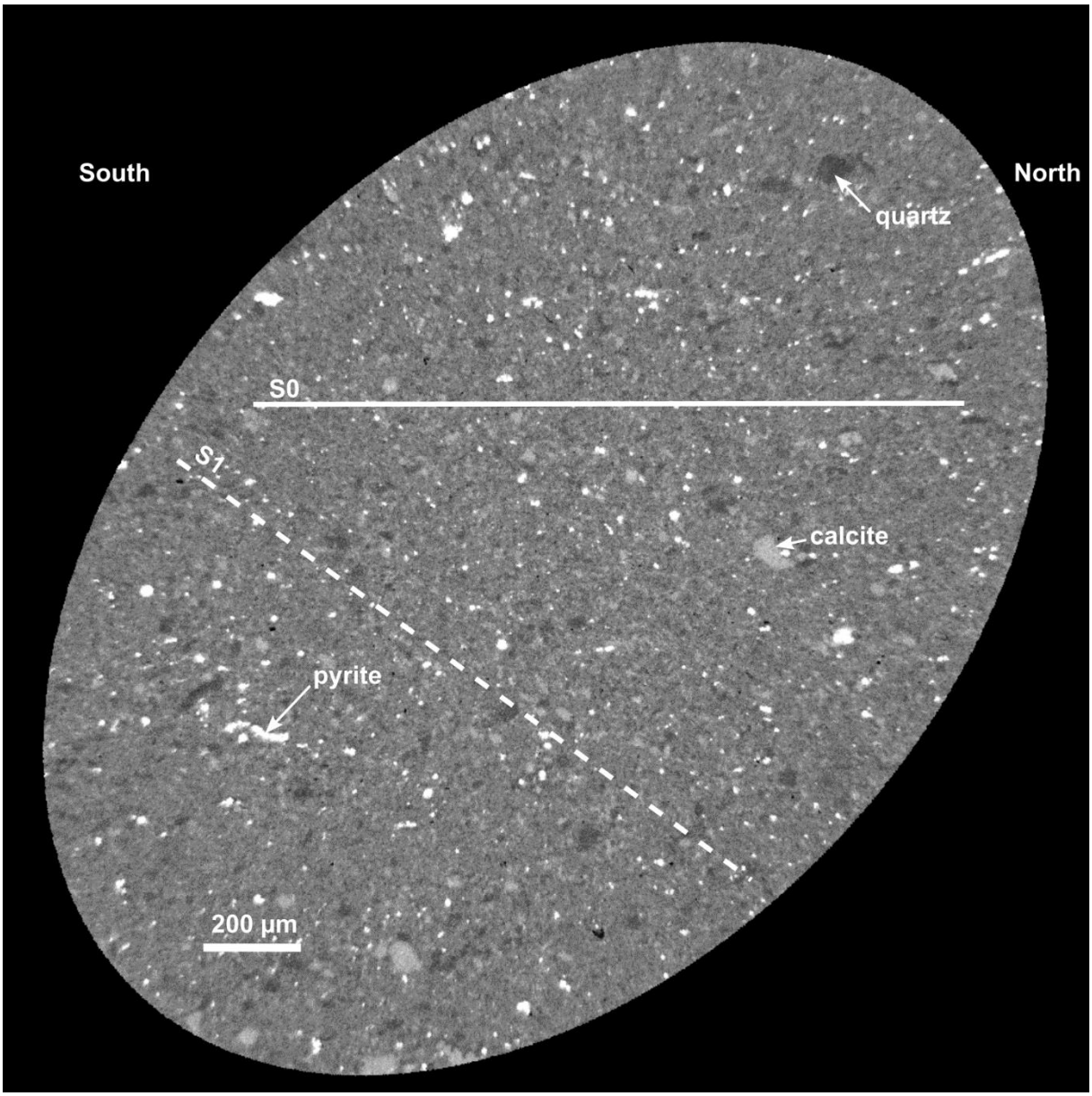

Figure supp 4 : *2D slice view of sample A3-2 in geographic coordinate system. S0 = bedding, S1 = cleavage.*

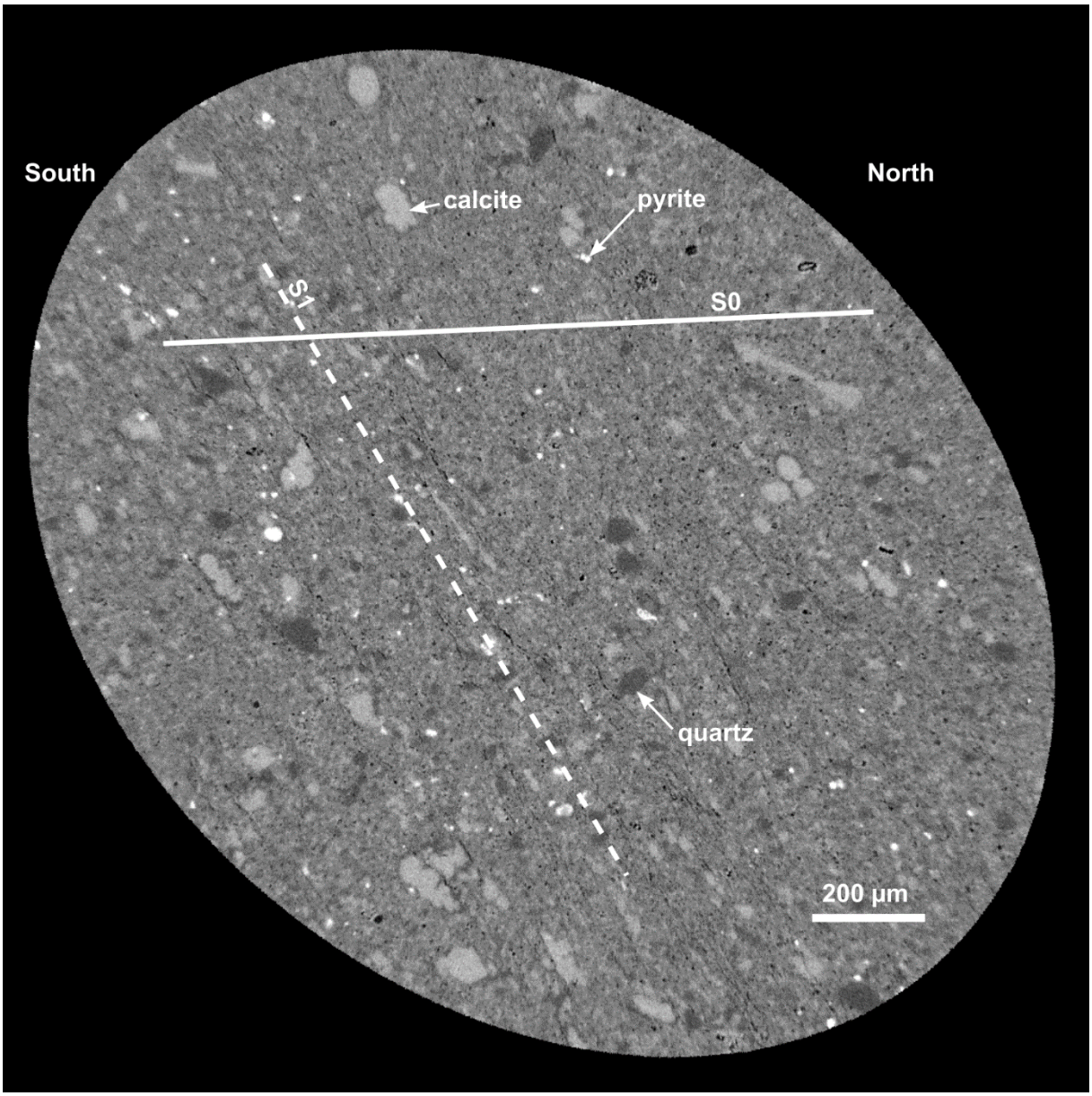

Figure supp 5 : *2D slice view of sample A4-2 in geographic coordinate system. S0 = bedding, S1 = cleavage.*

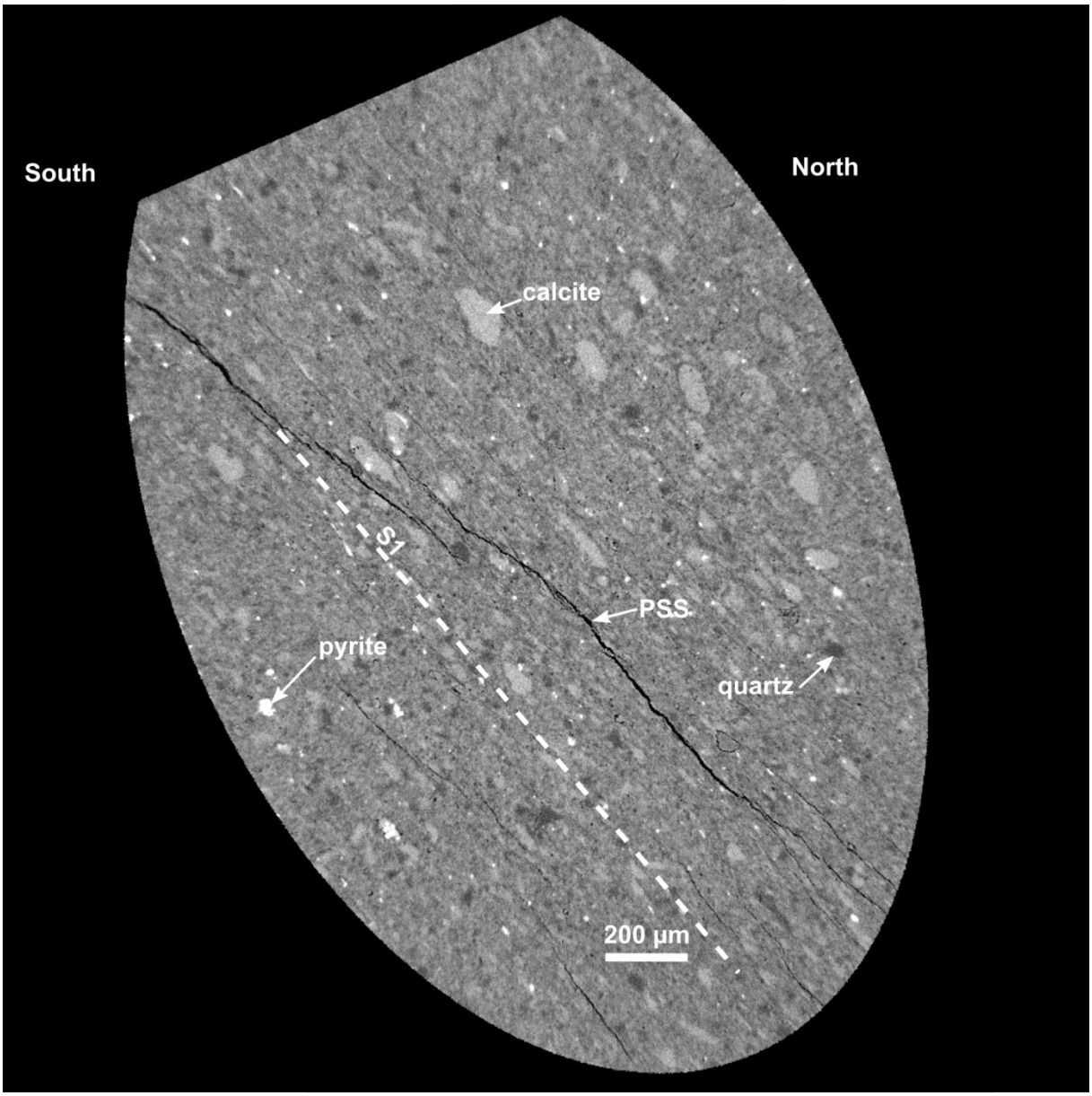

Figure supp 6 : *2D slice view of sample A5-2 in geographic coordinate system. PSS = pressure solution seam, S0 = bedding, S1 = cleavage.*